Investigations of a Closed-Loop Thermosyphon Operating with Slurries of a Microencapsulated Phase-Change Material

by

Alexandre Lamoureux

Department of Mechanical Engineering
McGill University
Montreal, Quebec, Canada

A thesis submitted to McGill University
in partial fulfillment of the requirements for the degree of
Doctor of Philosophy

Abstract

Complementary computational and experimental investigations of steady, laminar, fluid flow and heat transfer in a vertical closed-loop thermosyphon operating with slurries of a microencapsulated phase-change material (MCPCM) suspended in distilled water are presented.

The MCPCM particles consisted of a solid-liquid phase-change material (PCM) encapsulated in a polymer resin shell. Their effective diameter was in the range 0.5 μm to 12.5 μm, and had a mean value of 2.5 μm. Tests conducted with a differential scanning calorimeter (DSC) yielded the following data: starting with the PCM in its solid state, during monotonic heating, its melting starts gradually at about 20.0 °C, occurs mainly between 25.8 °C to 28.6 °C, and is completed by about 32.5 °C; during cooling after complete melting, supercooling of the liquid PCM to a temperature of about 18.1 °C is required for the initiation of freezing, which is then completed by about 15.0 °C; if cooling is started after only partial melting, no supercooling is required to start the freezing process; and the latent heat of fusion of the encapsulated PCM is 129.5 kJ/kg. The DSC data were used to deduce the variation of the effective specific heat of the MCPCM with temperature during both heating (melting) and cooling (freezing) processes. The effective density of the MCPCM during these processes was also determined, and the rheological behavior of the slurries was characterized. In the range of parameters considered, the slurries exhibited non-Newtonian behavior. The related experimental equipment, procedures, findings, and correlations for the aforementioned effective properties (for temperatures between 5°C and 55°C) are presented and discussed. The effective thermal conductivity of the slurries was determined using a correlation available in the literature.

A thermosyphon was designed, built, instrumented, and used in the experimental investigation. It consisted of two vertical straight pipes (ID = 10.21 mm, OD = 12.70 mm and height of 2.198 m) made of stainless steel (316), joined together by two vertical semi-circular 180° bends made of the same pipe (mean bend radius of 0.229 m). On a portion of one of the vertical pipes, a Teflon-insulated nichrome wire was tightly wound on the outer surface and electrically heated to provide a thermal boundary condition of essentially constant heat flux, ranging from 150 W/m^2 to 1850 W/m^2. A portion of the other vertical pipe was cooled using a concentric annular heat exchanger, and its wall temperature was maintained at 13 °C and 19.5 °C. The outer surfaces of these various components of the thermosyphon were very well insulated. Calibrated thermocouples were used to measure outer-wall-surface temperature at numerous points over the heated portion and the bulk temperature of the slurry at four different locations. A special procedure was formulated, benchmarked, and used to deduce the mass flow rate of the slurries in the thermosyphon. The experimental investigation was conducted with slurries of MCPCM mass concentration 0% (pure distilled water), 7.5%, 10%, 12.5%, 15%, and 17.5%.

In the computational investigation, a cost-effective homogeneous mathematical model was proposed and used for simulations of the laminar fluid flow and heat transfer. A control-volume finite element method was formulated (with several novel features) and employed to solve the two-dimensional, steady, axisymmetric fluid flow and thermal problems in the vertical heating and cooling sections of the thermosyphon, where local buoyancy effects were significant. In the remaining portions of the thermosyphon, a quasi-one-dimensional thermofluid model was used and solved using a segmented numerical method. This 1-D/2-D model and the numerical methods are described with special attention being given to the treatment of highly variable properties.

Finally, the numerical and experimental results obtained in this investigation are presented, compared, and discussed.

Résumé

Cette thèse présente des études numériques et expérimentales complémentaires d'écoulements laminaires et de transfert de chaleur en régime permanent au sein d'un thermosiphon à boucle fermée verticale opérant avec des suspensions de microcapsules d'un matériau à changement de phase (MCMCP) dispersées dans de l'eau distillée.

Les MCMCP sont formées d'un matériau à changement de phase (MCP) encapsulé dans une enveloppe de résine polymérique. Leur diamètre équivalent est compris entre 0,5 μm et 12,5 μm et possède une valeur moyenne de 2,5 μm. Des études menées à l'aide d'un calorimètre différentiel à balayage (CDB) ont permis d'obtenir les données suivantes : lorsque soumis à un réchauffement continu à partir de l'état solide, la fusion du MCP s'amorce autour de 20,0 °C, se produit principalement entre 25,8 °C et 28,6 °C et se termine autour de 32,5 °C ; lorsqu'un refroidissement est entamé suite à une fusion complète, un abaissement de la température du MCP liquide à 18,1 °C est nécessaire afin d'amorcer la solidification qui se conclut alors à 15,0 °C ; si le refroidissement est entamé suite à une fusion partielle, le phénomène de surfusion décrit précédemment est absent ; finalement, la chaleur latente de fusion du MCP encapsulé est de 129,5 kJ/kg. Les données obtenues à l'aide du CDB ont permis d'évaluer la chaleur massique équivalente des MCMCP en fonction de la température lors d'un chauffage (fusion) et d'un refroidissement (solidification). La masse volumique équivalente des MCMCP fut aussi mesurée pour ces deux processus et le comportement rhéologique des MCMCP fut caractérisé comme étant non newtonien. Le matériel expérimental, les procédures, les résultats ainsi que les corrélations décrivant les propriétés équivalentes énumérées ci-haut (pour des températures allant de 5 °C à 55 °C) sont présentés.

Un thermosiphon a été conçu, construit, instrumenté et utilisé afin de mener les expériences. Il est composé de deux tuyaux verticaux (diamètres interne et externe de 10,21 mm et 12,70 mm) faits d'acier inoxydable (316) et joints par deux coudes de 180° (rayon de courbure de 0.229 m) de sections transversales identiques. Un fil de nichrome recouvert d'une gaine isolante de Téflon embobiné autour d'une portion de la surface extérieure de l'un des tuyaux verticaux et ensuite chauffé à l'aide d'un courant électrique permit d'appliquer une condition aux limites s'apparentant à un flux thermique essentiellement constant (allant de 150 W/m^2 à 1850 W/m^2). Une portion de l'autre tuyau vertical a été refroidie à l'aide d'un échangeur de chaleur annulaire grâce auquel la température de sa paroi externe fut maintenue à 13 °C et 19.5 °C. Les surfaces externes des composants formant le thermosiphon ont été recouvertes d'un isolant. Des thermocouples étalonnés ont permis de mesurer la température de la surface externe de la section chauffante à de multiples endroits ainsi que la température de mélange à quatre emplacements de la boucle. Une procédure permettant de mesurer le débit massique des suspensions au sein du thermosiphon a été formulée et validée. Les études expérimentales ont été menées avec des suspensions ayant des concentrations massiques de 0% (eau distillée), 7.5%, 10%, 12.5%, 15% et 17.5%.

Un modèle homogène a été proposé et utilisé lors des simulations d'écoulements et de transfert de chaleur en régime laminaire. Une méthode des éléments finis à volumes de contrôle a été formulée ainsi qu'améliorée avant d'être ultimement utilisée afin de résoudre les problèmes stationnaires et axisymétriques au sein des sections de chauffage et de refroidissement, où les effets de convection mixte sont significatifs. Une approche quasi unidimensionnelle, résolue à l'aide d'une méthode numérique segmentée, a été utilisée dans les autres sections du thermosiphon afin d'y résoudre les problèmes d'écoulements et de transfert de chaleur.

Finalement, les résultats des simulations et des expériences sont présentés, comparés puis discutés.

Acknowledgements

I am grateful to Professor B. Rabi Baliga for his unfaltering guidance and support throughout this journey. I would also like to thank him for his dedicated training efforts and, especially, for being an example of noble-spiritedness one can hope to follow.

The research work presented in this thesis was financially supported by the Natural Sciences and Engineering Research Council of Canada through individual operating and equipment grants to Prof. B.R. Baliga. I have received a doctoral research scholarship from the Fonds québécois de la recherche sur la nature et les technologies (FQRNT) which was very appreciated. I was also awarded the Vadasz Doctoral Fellowship by the Faculty of Engineering and additional financial support was provided by the Department of Mechanical Engineering, in the form of scholarships and teaching assistantships. Lastly, I was offered instructorships in the Department of Mechanical Engineering at Université de Sherbrooke throughout the course of my PhD studies.

I would like to thank Professor Pascal Hubert and Jonathan Laliberté for granting me access to a differential scanning calorimeter that enabled measurements of the effective specific heat of the slurries used in this work. Many thanks also to James Kratz for his valuable help in determining the rheological behavior of these slurries. I also am very grateful to Professor Laurent Mydlarski, Professor Evgeny Timofeev and Professor Arun Misra (Department Chair) for offering teaching assistantships and for their support.

I am grateful to the Mechanical Engineering Department staff for their assistance and advice. I would like to thank Georges Twefik and Mario Iacobaccio for their technical support. I would to also like to convey my thanks to the secretaries, Della Maharajh, Joyce Nault, Mary Fiorilli, and Nozomi Kanekatsu for their precious help with the paperwork and financial assistance.

I would like to thank Samer Afara and Nirma Jesuthasan and the other members of the Heat Transfer Laboratory for their company, encouragement and help during my doctoral studies. I would also like to thank my former colleagues Nima Atabaki, Éric Duplain and David Scott for their companionship and assistance in the early years of my graduate studies.

Special thanks are due to Alain Batailly and Biru Zhou whose kindness and friendship are treasured by my fiancée and I. I also owe thanks to my friends Mathieu Bock-Côté and André Leclerc.

I am infinitely indebted to my parents for their love and support. Without them, my academic endeavors would not have been conceivable. For your unwavering encouragement throughout my undergraduate and graduate studies, thank you.

Finally, I would like to thank my fiancée Karine Dubois for her unequaled support and patience during my graduate studies. Her love and presence made every day a blessed one.

Table of Contents

List of Figures

List of Tables

Nomenclature

$A_{c.s.}$	cross-sectional area of pipe [m^2]
$a_i^{\Phi}, a_{nb}^{\Phi}, b_i^{\Phi}$	coefficients of the discretized equations for scalar dependent variable Φ and node *i*
C_D	drag coefficient
C_{visc}	glass capillary tube viscometer constant [m^2/s^2]
c_p	specific heat at constant pressure [J/(kgºC)]
d_p	solid particle diameter [m]
D_i, D_o	internal and external pipe diameters [m]
d^w, d^v	coefficients of pressure in equations for mass-conserving velocity components
De	Dean number
E^{S_Φ}, G^{S_Φ}	coefficients of the dependent variable and constant term in linearized source term
Ec	Eckert number
$f_{Fanning}$	Fanning friction factor
Fac_{corr}	factor for correcting calculated velocity components at outflow boundaries
g	magnitude of the grativational acceleration constant [m/s^2]
Gr	Grashof number
i	specific enthalpy [J/kg]
$\vec{J}$	combined advection plus diffusion flux vector

k	thermal conductivity [W/mºC]
l_1, l_2	half-lengths of element edges associated with a boundary node [m]
L	lengths of various portions of the calculation domains, characteristic length in dimensionless Grashof number or cavity height in Test Problem 1 [m]
m	relative consistency index [s^{n-1}]
$\dot{m}$	mass flow rate of working fluid in the thermosyphon [kg/s]
n	flow behavior index
$\vec{n}$	unit vector normal to control-volume face
N	thermocouple number
Nu	Nusselt number
p	static pressure [$\mathrm{N/m^2}$]
P	reduced pressure [$\mathrm{N/m^2}$]
Pe	Péclet number
$\dot{Q}$	volumetric flow rate [$\mathrm{m^3/s}$]
$q_{heating,total}$	power input to the nichrome wire heater [W]
q_{in}	net rate of heat transfer to the fluid in 1D fluid element [W]
q'	rate of power input per unit length [W/m]
$q_{in}^{'}$	net rate of heat transfer to the fluid per unit length [W/m]
$q_{loss}^{'}$	rate of heat loss per unit length [W/m]
R	cavity radius in Test Problem 1 [m]

R_{bend}	radius of pipe bends [m]
Re	Reynolds number
r_i, r_o	radial positions at inner and outer pipe wall surfaces [m]
$\Re^{\Phi}_{advec,i}$	rate of advection transport of Φ across the boundary of the calculation domain into or out of control volume associated with boundary node *i*
$\Re^{\Phi}_{D,i}$	rate of diffusion transport of Φ across the boundary of the calculation domain into or out of control volume associated with boundary node *i*
$\Re_{mass,i}$	mass flow rate across the boundary of the calculation domain into or out of control volume associated with boundary node *i* [kg/s]
$\Re^{\Phi}_{total,i}$	total (advection plus diffusion) rate of transport of Φ across the boundary of the calculation domain into or out of control volume associated with boundary node *i*
s	axial coordinate around closed-loop [m]
S_{Φ}	volumetric (per unit volume) source term associated with scalar independent variable Φ
St_{w_p}	momentum Stokes number of particle
St_{T_p}	thermal Stokes number of particle
t	time [s]
T	temperature [ºC]
$T_{b,in,heating}$	inlet bulk temperature of the vertical heating section[ºC]
$T_{b,out,heating}$	outlet bulk temperature of the vertical heating section [ºC]

$T_{b,in,cooling}$	inlet bulk temperature of the vertical cooling section [ºC]
$T_{b,out,cooling}$	outlet bulk temperature of the vertical cooling section [ºC]
T_{cool}	cooling water temperature [ºC]
T_H, T_C	temperatures of hot and cold faces of cavity in Test Problem 1 [ºC]
$\overline{T}_{b,\Delta s}$	average bulk temperature value over 1D fluid segment [ºC]
$U^{'}$	overall heat transfer coefficient per unit length [W/mºC]
$v,\ w$	velocity components in the *r*- and *z*-directions [m/s]
$\hat{v},\ \hat{w}$	pseudo-velocities in the *r*- and *z*-directions [m/s]
v^m, w^m	mass-conserving velocity components in the *r*- and *z*-directions [m/s]
V	voltage output of a thermocouple [mV]
V_i	volume of control volume associated with node *i* [m^3]
Vol	volume of the glass capillary tube viscometer upper bulb [m^3]
w_{av}	average working fluid velocity in the thermosyphon [m/s]
r, z	radial and axial coordinates [m]
z^+	dimensionless axial coordinate in Test Problem 1

Greek symbols

α_Φ	under relaxation factor for Φ
β	volumetric thermal expansion coefficient [K^{-1}]
Γ_Φ	diffusion coefficient associated with scalar dependent variable Φ

$\dot{\gamma}$	magnitude of the local rate of strain [s^{-1}]
Δr	node spacing in the r-direction [m]
Δs	length of 1D fluid element [m]
Δz	effective elevation of the cooling section vs. heating section or node spacing in the z-direction [m]
ε	specified convergence criterion for iterative solution procedure
η	relative viscosity (with respect to that of the conveying liquid)
θ	angle with respect to the horizontal [rad]
λ	latent heat of fusion [kJ/kg]
μ	dynamic viscosity [kg/(m-s)]
ρ	mass density [kg/m^3]
τ	shear stress [N/m^2]
τ_f	characteristic time scale of the flow [s]
τ_{T_p}	thermal response time of particle [s]
τ_{w_p}	momentum response time of particle [s]
υ	kinematic viscosity [m^2/s]
Φ	scalar dependent variable (w, v, P, T, …)
ϕ	mass concentration of the MCPCM in the slurries;
φ	volume concentration of the MCPCM in the slurries

Subscripts

∞	ambient value
abs	absolute value
$advec$	pertaining to advection
b	bulk value or based on bulk temperature
c	cooling section
cap	capillary tube of viscometer
$calc$	calculated
D	pertaining to diffusion
d	pertaining to or based on particle diameter
exp	pertaining to the experimental apparatus dimensions
gen	generalized non-Newtonian fluid approach or definition
h	heating section
H_2O	pertaining to distilled water
i	pertaining to or based on inner pipe diameter or pertaining to node i
ins	pertaining to the loop insulation
l	pertaining to the liquid (water in this work)
o	pertaining to or based on outer pipe diameter
p	pertaining to a suspended particle
pre	pertaining to the pre-heating or cooling section
$post$	pertaining to the post-heating or cooling section

ref	reference value
s	pertaining to the slurries
w	pertaining to the pipe wall or evaluated at the inner pipe wall surface
Δ	element-based

Acronyms

DSC	differential scanning calorimeter
FMSCWFH	full-melting-supercooling-with-freezing-and-hysteresis
FMNSCFNH	full-melting-no-supercooled-freezing-no-hysteresis
LMTD	log mean temperature difference
MCPCM	microencapsulated phase-change material
PCM	phase-change material
PMNSCNH	partial-melting-no-supercooling-no-hysteresis

1. Introduction

1.1 Motivation and Main Goals

Liquid-vapor and solid-liquid phase-change phenomena are the basis of a wide range of energy conversion, storage, exchange, and control systems. For example, liquid-vapor phase-change phenomena are pivotal to the Rankine cycle which is the basis of the majority of large thermal power plants in use today; ice-water phase-change is used in so-called ice boxes to keep food products cool; salt- and paraffin-based solid-liquid latent-heat storage devices are used to enhance the efficiency of solar energy systems and thermal-control systems for buildings [Lee et al. (2006); Shilei et al. (2007)]; liquid-vapor and solid-liquid phase-change phenomena are employed for the thermal management of high-heat-flux devices in electronics [Mudawar (2003); Bergles (2003)]; and in heat pipes, capillary pumped loops, and loop heat pipes, liquid-vapor phase-change phenomena are used to achieve very high rates of heat transfer with relatively low temperature drops over large distances [Maydanik (2005)]. Also, over the last 40 years, there has been increasing research interest in the enhancement of convective heat transfer using slurries of solid-liquid phase-change materials (PCMs) suspended in a carrier liquid. The work presented in this thesis involves investigations of a closed-loop thermosyphon operating with slurries of a microencapsulated solid-liquid phase-change material suspended in distilled water. The tasks undertaken in this work include the formulation and implementation of a cost-effective mathematical model of such closed-loop thermosyphons, improvements to a numerical method for solving this model, experiments to determine the effective properties of the aforementioned slurries, and a complementary experimental study of the above-mentioned closed-loop thermosyphon.

The main benefit of introducing a PCM in a carrier or conveying liquid is the following: when the PCM undergoes melting or freezing, the effective specific heat of the resulting suspension or slurry is increased due to the latent heat of fusion. As a result, the rate of convective heat transfer can also be increased (relative to that obtained with just the conveying liquid with no change of phase) if the PCM and the slurry are suitably chosen for the application of interest. It is advantageous in practice to use slurries of microencapsulated phase-change materials (MCPCMs) suspended in the conveying liquid, as they provide the following desirable characteristics: no drastic changes in the effective viscosity of the slurry during the phase-change process; no mixing of the molten PCM with the conveying liquid; no clumping or agglomeration of the PCM; and, with the proper choice of the encapsulation material and size of the particles, no agglomeration and no significant separation of the MCPCM from the conveying liquid.

The concept of adding encapsulated PCM particles to a carrier liquid to augment convective heat transfer was first proposed by Katz (1967). He conducted an experimental investigation of natural convection heat transfer in a cubical enclosure filled with slurries of disk-shaped capsules containing wax and found that the rate of heat transfer for a given temperature difference could be doubled relative to that achieved with just the liquid (without the encapsulated PCM). Another experimental investigation of natural convection in a cubical enclosure with slurries of MCPCM particles suspended in a liquid was carried out by Datta et al. (1992): they too discovered an appreciable increase of the average Nusselt number relative to the value obtained when only the liquid was used as the working fluid. The vast majority of past experimental and numerical investigations of convective heat transfer with MCPCM slurries pertain to forced convection in tubes of circular cross-section: some of the important works in this area include the contributions of Charunyakorn et al. (1991), Zhang and Faghri (1995), Yamagishi et al. (1999), and Alvarado et al. (2006, 2007). Scott (2006), who worked in the Heat Transfer Laboratory of the Department of Mechanical Engineering at McGill University, conducted the first study of steady, laminar, *mixed* convection with MCPCM slurries. A review of the published literature on these and related topics is provided in Section 1.4.

Closed-loop thermosyphons are employed in numerous heat transfer systems and have many engineering applications: examples include solar water heaters, geothermal heat pumps, cooling systems for large electrical transformers, cooling systems for electronics, emergency cooling of nuclear reactor cores, chillers used in HVAC (heating, ventilating, and air-conditioning) systems, and natural circulation loops for heating buildings [Japikse (1973); Zvirin (1981); Grief (1988); Parent et al. (1990)]. A closed-loop thermosyphon operating with suitably chosen and designed MCPCM slurries would transfer heat at a higher rate with a fixed driving temperature difference, or achieve a desired rate of heat transfer with a smaller temperature difference, than if it were operated with the carrier liquid alone. The proposal of cost-effective mathematical models, numerical simulations, and experimental investigations of a closed-loop thermosyphon akin to that illustrated schematically in Figure 1.1 are the main goals of the research presented in this thesis. This research involves topics of fundamental interest, provides opportunities for some novel original contributions, and fits in well with a desire (on the part of the author and his supervisor) to contribute to ongoing worldwide efforts to develop improved (next generation) heat exchange devices and systems.

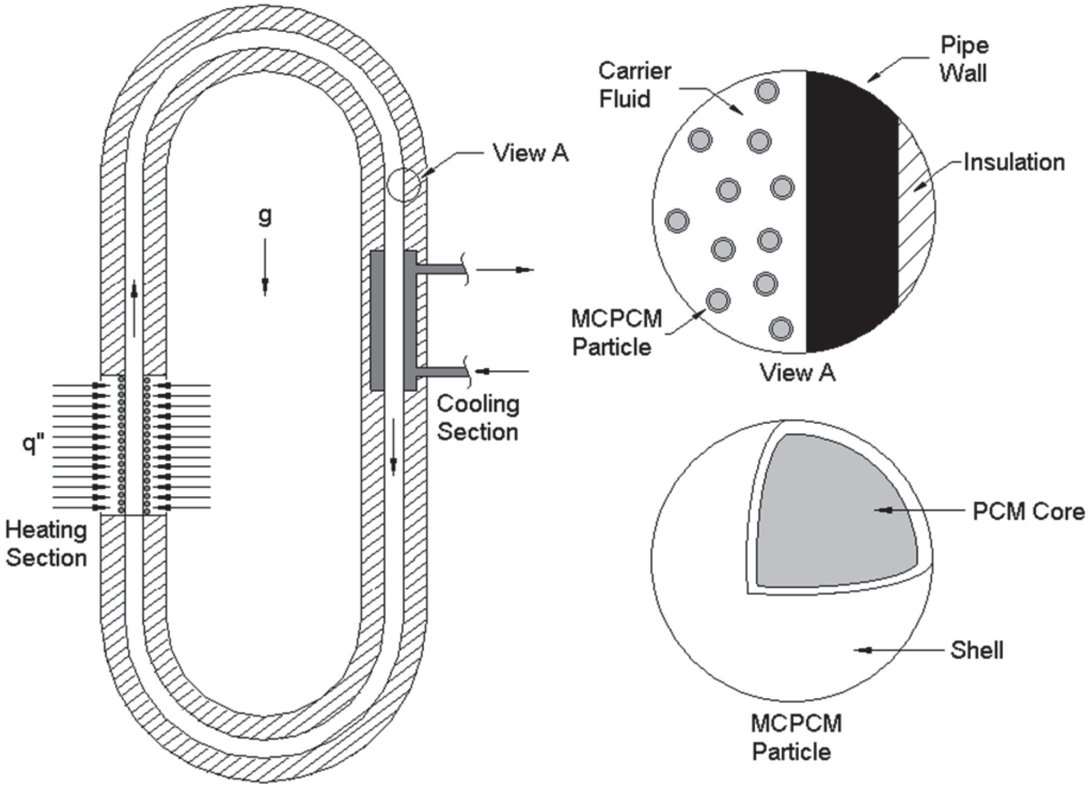

Figure 1.1: Schematic representation of a closed-loop thermosyphon, the MCPCM slurry, and an MCPCM particle.

1.2 Overview of the Microencapsulated Phase-Change Material and the Slurries

The microencapsulated phase-change material (MCPCM) used in this work consists of particles of a solid-liquid phase-change material (PCM) enclosed in a solid shell, as shown in Fig. 1.1. This MCPCM was manufactured by Outlast Ventures Inc., which is located in Boulder, Colorado. The encapsulation process and the precise composition of the PCM and the shell are proprietary information belonging to the manufacturer. Scott (2006), who used the same MCPCM in his research, determined that the PCM is similar to octadecane (a paraffin) and the shell is made of a polymer resin. When disseminated in distilled water (the conveying liquid used in this work) at moderate mass concentrations (less than or equal to 20%), this MCPCM forms a homogeneous suspension or slurry. These slurries have the appearance of a dilute white paint. In the temperature range of interest (13 °C to 50 °C), the density of this MCPCM was slightly lower than that of distilled water. However, experimental observations indicated that a considerable amount of time, normally more than 48 hours, was required for discernable separation of the MCPCM particles from the conveying liquid.

Scott (2006) determined that the effective diameter of the MCPCM particles used in this work was in the range 0.5 μm to 12.5 μm, and had a mean value of 2.5 μm. As the PCM used was not a pure substance, its solid-liquid (melting) and liquid-solid (freezing) phase-change processes did not occur at a single temperature, but over a range of temperatures. Tests conducted in this work with a differential scanning calorimeter (DSC) yielded the following data: starting with the PCM in its solid state, during monotonic heating, its melting gets initiated gradually at about 20.0 °C, occurs mainly between 25.8 °C to 28.6 °C, and is completed by about 32.5 °C; during cooling after complete melting (temperature equal to or exceeding 32.5 °C), supercooling of the liquid PCM to a temperature of about 18.1 °C is required for the initiation of freezing, which is then completed by about 15.0 °C; if cooling is started after only partial melting with all temperatures less than 28.0°C, no supercooling is required to start the freezing process; and the latent heat of fusion of the encapsulated PCM is 129.5 kJ/kg. The DSC data also showed that if the melting process of a slurry is halted at temperatures between 28.0°C and 32.5°C, and it is then cooled, part of the PCM freezes between 25.8 °C to 28.6 °C, but supercooling to about 18.1 °C is required to complete the solidification process: this type of process, that is, partial melting, with temperatures between 28.0°C and 32.5°C, followed by the aforementioned two-stage freezing, was not investigated in the thermosyphon experiments and computer simulations undertaken in this work.

The variations of the effective mass density of the MCPCM slurries with temperature were measured using a specially designed and constructed apparatus, during both monotonic heating (melting) and monotonic cooling (freezing) processes. The rheological behavior of the slurries was also characterized by performing experiments with capillary-tube viscometers. These experiments revealed that in the range of flow rates encountered in the thermosyphon experiments undertaken in this work, the slurries exhibit a slight shear-thinning behavior: their effective or apparent dynamic viscosity decreases with increasing rate of strain. Correlations that allow calculations of the effective properties of the slurries for temperatures ranging between 5°C and 55°C were formulated using the measured property data. Full descriptions and discussions of the experiments for determining these effective properties, their results, and the proposed correlations are presented in Chapter 3.

In the main experiments, a closed-loop thermosyphon, similar to that illustrated schematically in Figure 1.1, was operated with slurries having the following MCPCM mass concentrations: 0% (pure distilled water), 7.5%, 10%, 12.5%, 15% and 17.5%. The maximum and minimum operating temperatures during these experiments were 50°C and 13°C, respectively. Visual inspections of the slurries (with the help of an optical microscope) before and after the aforementioned operations of the thermosyphon showed that there were no perceptible degradations of the MCPCM shells or leaking of the PCM core. Thus, it was concluded that the integrity of the MCPCM particles was preserved in these experiments. In addition, the MCPCM mass concentration in the aforementioned slurries was considered to remain spatially uniform throughout the loop over the full duration of each experiment, as every one of the experimental runs was completed in less than 12 hours, a time period that is much shorter than the above-mentioned particle separation time. In this context, it should also be noted that slurry motion in the closed-loop thermosyphon helps to delay particle separation or agglomeration.

Using the above-mentioned properties of the MCPCM slurries in some theoretical considerations, it was determined that a simple homogeneous model can be used for accurate mathematical descriptions of their flow and the associated heat transfer in the closed-loop thermosyphon. Details of such theoretical aspects of this work are discussed in Chapter 2, and descriptions of the thermosyphon apparatus and related experimental procedures are provided in Chapter 4.

1.3 Objectives

The specific objectives of the numerical and experimental investigations carried out in this work are the following:

1. Formulate and implement a hybrid model that iteratively couples a segmented quasi one-dimensional network thermofluid model (referred to in the remainder of this thesis as the 1-D model) with an axisymmetric, two-dimensional, mathematical model and numerical solutions of steady, laminar, fluid flow and heat transfer phenomena in the heating and cooling sections of vertical thermosyphons akin to that shown in Figure 1.1 (in the remainder of this thesis, this hybrid model is referred to as the 1-D/2-D model). This objective also involves the formulation, implementation, and validation of a control-volume finite element method (CVFEM), with several novel features, for the detailed axisymmetric, two-dimensional simulations required in the proposed 1-D/2-D model.
2. Set up and conduct experiments to determine the effective or apparent viscosity, the effective mass density, and the effective specific heat at constant pressure of the above-mentioned MCPCM slurries over a temperature range of 5°C to 55°C, during both heating (which involves melting of the PCM) and cooling (which involves freezing of the PCM) processes, and propose suitable correlations for these effective properties. The variations of the aforementioned effective properties with temperature during the heating and cooling processes are different when supercooling effects come into play during the freezing of the MCPCM particles [Scott (2006)]: in this work, one of the objectives is to explore the characteristics, degree, and impact of this supercooling.

3. Design and set-up a closed-loop thermosyphon for steady-state operation with the above-mentioned slurries of MCPCM particles dispersed in distilled water. Conduct experiments with this thermosyphon operating with slurries of different MCPCM mass concentrations, and obtain data that could be used to check and refine the aforementioned 1-D/2-D model.
4. Using the aforementioned 1-D/2-D model, perform simulations of the thermosyphon operated with distilled water (for benchmarking) and the above-mentioned slurries, and compare the numerical predictions with the corresponding experimental results. Review and discuss the numerical and experimental results.

Attention in this work is limited to vertical thermosyphons akin to that shown in Figure 1.1, operating with either pure distilled water or MCPCM slurries, under steady-state conditions and in the laminar flow regime. The study of transient operations of thermosyphons, and transitional or turbulent fluid flow and heat transfer phenomena, are not within the scope of this investigation, but are suggested extensions of it. As stated earlier, the focus of this work is to propose and validate cost-effective and accurate models of the thermosyphon. Ultimately, the proposed model could be used as part of a computational optimization procedure to design thermosyphons and tailor properties of the slurries for specific applications. These and other suggested extensions of this work are given in Chapter 7.

1.4 Literature Review

This literature review is limited to publications that are directly relevant to or provide the basis of the research work presented in this thesis. It is divided into the following five subsections: 1) textbooks and handbooks offering comprehensive and broad discussions of convective heat transfer; 2) numerical methods employed to solve fluid flow and heat transfer problems; 3) publications on laminar convective heat transfer in ducts and thermosyphons operating with single-phase fluids; 4) investigations of thermophysical properties of liquid-solid particle slurries with and without change of phase; and 5) past works and contributions on convective heat transfer in ducts and closed-loop thermosyphons with MCPCM slurries as the working fluid.

1.4.1 Textbooks and Handbooks on Convective Heat Transfer

Detailed discussions of the basic and more advanced aspects of the vast subject of convective heat transfer in ducts are available in numerous textbooks, handbooks, and specialized collections of articles by leading researchers: a few examples of the pivotal works include those of Eckert and Drake (1972), White (1991), Kays and Crawford (1993), Rohsenow et al. (1998), Incropera and DeWitt (2002), Bird et al. (2002) and Hartnett et al. (1964 – 2010). Shah and London (1978) extensively covered single-phase laminar flow and heat transfer in ducts. The topic of single-phase, laminar and turbulent, flow and heat transfer in compact heat exchangers and interrupted-surface geometries was investigated in depth by Kays and London (1964). A comprehensive discussion of the rheology of non-Newtonian fluids and related fluid flow and convective heat transfer aspects can be found in the book of Bird et al. (1987), *Dynamics of Polymeric Liquids (Vol. 1)*. Authoritative reviews and discussions of multiphase flows and heat transfer can be found in the works of Fan and Zhu (1998), Brennen (2005), and Crowe (2006).

1.4.2 Numerical Methods for Fluid Flow and Heat Transfer

There are three main groups of numerical methods for the solution of mathematical models of fluid flow and heat transfer: finite difference methods, finite volume methods, and finite element methods. Boundary element, spectral, and control-volume finite element methods form other important categories. Authoritative discussions of these methods can be found in the works of Patankar (1980), Reddy and Gartling (1994), Tannehil et al. (1997), Roache (1998), Ferziger and Perić (1999), Gresho and Sani (2000), Zienkiewicz and Taylor (2000a, 2000b), Peyret (2002), Gaul et al. (2003), and Karniadakis and Sherwin (2005), among others. In this work, the aforementioned 1-D/2-D thermosyphon model involves the formulation and implementation of a control-volume finite element method (CVFEM) for the solution of the two-dimensional axisymmetric fluid flow and heat transfer in the vertical heated and cooled sections. The numerical method used in this work was formulated by borrowing and extending ideas from the works of Patankar (1980), Masson et al. (1994), Baliga (1997), Baliga and Atabaki (2006), Acharya et al. (2007) and Lamoureux and Baliga (2011). Lastly, useful review articles pertaining to various topics of computational fluid dynamics and heat transfer can be found in the *Handbook of Numerical Heat Transfer* edited by Minkowycz et al. (2006) and in volumes 1 and 2 of *Advances in Numerical Heat Transfer* edit by Minkowycz and Sparrow (1997, 2000).

1.4.3 Single-Phase Laminar Convective Heat Transfer in Ducts and Thermosyphons

A review of the key works pertaining to single-phase, laminar, convective heat transfer in ducts is presented first in this subsection. Emphasis is then given to investigations pertaining to thermosyphons in single-phase operation.

Forced Convection

Authoritative discussions and reviews of the broad topic of forced convection in ducts can be found in the works of Kays and Perkins (1973), Shah (1975) and Shah and London (1978). Comprehensive overviews of this subject can also be found in the textbooks of Kays and Crawford (1993), Oosthuizen and Naylor (1999), Incropera and DeWitt (2002), and Bird et al. (2002), to name a few. For additional discussions and review articles, the reader is referred to the *Handbook of Single-Phase Convective Heat Transfer* edited by Kakac et al. (1987) and the *Handbook of Heat Transfer Fundamentals* edited by Rohsenow et al. (1998).

Natural Convection

A few pivotal contributions to the topic of natural convection in ducts are presented in this subsection. Elenbaas (1942a) is generally credited for publishing the first investigation of single-phase natural convection in ducts. In this study, the author experimentally studied natural convection occurring between two parallel isothermal plates aligned vertically to form a channel of uniform cross-section with open ends. Elenbaas (1942a) then proposed a model based on a blending of asymptotic solutions for fully-developed and developing flow and heat transfer. Predictions obtained with this model agreed well with his experimental data. In an extension of his original work, Elenbaas (1942b) conducted more experiments on natural convection in additional duct geometries and refined his analytical model with this new data. Extensions of the model proposed by Elenbaas (1942a, 1942b) have been proposed by Churchill and Usagi (1972), Churchill (1977), Raithby and Hollands (1975, 1985) and Yovanovich et al. (2002).

A numerical investigation of laminar, natural convection in a heated, vertical open tube maintained at a uniform temperature was conducted by Davis and Perona (1971). The numerical results showed that the developing flow and thermal lengths were relatively large for the investigated geometry and parameters. Thus, they deduced that analytical models should take into account the important flow and thermal development lengths. Lastly, the authors discovered that transverse velocity components (in the plane normal to the streamwise direction) significantly influenced the numerical results.

Dyer (1975) carried out numerical and experimental investigations of laminar natural convection occurring in open-ended vertical pipes of circular cross-section, subjected to a uniform wall heat flux. He studied the influence of the inlet conditions, the Rayleigh number, and the Prandtl number on the overall thermal results, such as the Nusselt number. Two limiting cases were discovered: a fully-developed flow at low Rayleigh number values and a boundary layer-type flow at high values of Rayleigh number. The results obtained by using a finite difference method to solve the governing equations were in good agreement with the experimental data. A few years later, Dyer (1978) conducted additional complementary numerical and experimental investigations of natural convection in the same geometry. However, in this new study, a section of the tube inlet was not heated and acted as a resistance to fluid motion. The author discussed that a sufficiently long unheated section hindered flow in the pipe to a point where it behaved like a thermosyphon with an open top surface.

Mixed Convection

A review of mixed (combined natural and forced) convection in vertical circular tubes was published by Eckert and Diaguila (1954). In this review, the authors focused on past works pertaining to turbulent mixed convection, but also included a few studies pertaining to the laminar regime. One of the most important contributions of this review article consisted in the elaboration of a flow-regime map which provides the parameter-space boundaries of natural, mixed and forced convection, in both laminar and turbulent regimes.

Hallman (1958) conducted analytical and experimental investigations of laminar mixed-convection heat transfer in vertical tubes. He derived analytical solutions for the constant-wall-heat-flux and uniform-wall-temperature boundary conditions, for both assisting and opposing flows. The author proposed a correlation for predicting the average Nusselt number as a function of the Rayleigh number over the following range: $100 \leq Ra \leq 10000$. For Rayleigh numbers less than 100, he found that the buoyancy effects were negligibly small, and the average Nusselt number could be predicted with well-known solutions for forced convection heat transfer.

Metais and Eckert (1964) published an important review of natural, forced, and mixed convection heat transfer in both vertical and horizontal pipes. Using experimental data available in the literature, the authors designed new flow-regime maps, delimiting natural, forced, and mixed convection regimes, and also transition from laminar to turbulent flow. The parameters used to delimit the flow regimes are the following: i) the Reynolds number and ii) the product of the Grashof number, the Prandtl number, and the pipe diameter-to-length ratio $[GrPr(D/L)]$. These maps are discussed further in Chapter 2.

Zeldin and Schmidt (1972) conducted a numerical investigation of laminar mixed convection in an isothermal vertical pipe of circular cross-section. They solved the fully-elliptic forms of the governing equations, using a finite difference method, and validated their numerical results with complementary experimental data.

Bernier and Baliga (1992a) conducted an experimental investigation of laminar mixed convection heat transfer in vertical pipes. A semi-transparent gold-film heater was glued on the inside surface of a circular Plexiglas tube, thereby allowing the authors to make flow visualization studies using a dye-injection technique. Numerical studies were also performed, and the predicted flow patterns compared qualitatively well with those observed in the experiments.

A numerical investigation of mixed convection heat transfer in vertical pipes of circular cross-section was carried out by Wang et al. (1994). The authors focused their attention on the impact of buoyancy and axial conduction on the numerical results, for both assisting and opposing flows. Flow reversal was found to occur at high values of the Grashof-to-Reynolds number ratio.

Lagana (1997) conducted an experimental investigation of laminar mixed convection heat transfer in pipes of circular cross-section, inclined at several different angles to the vertical direction. A semi-transparent thin gold-film heater was used to apply an essentially constant wall heat flux. The heating section was insulated from the environment by enclosing it in a larger, concentric, transparent Plexiglas cylinder casing, with a partial vacuum inside it. This design allowed flow visualization over the entire length of the heated section, using a dye injection technique. Some attention in this work was also devoted to laminar-to-turbulent transition in mixed convection flows.

Thermosyphons in Single-Phase Operation

A comprehensive review of thermosyphon applications was proposed by Zvirin (1981), in which he discussed past studies of different configurations such as vertical loops, toroidal loops, nuclear reactor heat sinks, and solar collectors. He also reviewed so-called oscillatory-flow modes and possible flow reversal causes, but a definitive flow-reversal criterion was not provided or defined. The author reviewed available one-dimensional (1-D) analytical and numerical models for the simulation of both steady-state and transient operations, as well as various empirical data obtained with either scaled experiments or actual operating systems, such as nuclear reactor heat sinks. Zvirin (1981) also stated that the shortcomings of available 1-D numerical models are caused by the inadequate assumptions of fully-developed flow and heat transfer in some sections of the thermosyphons, thereby making detailed two-dimensional (2-D) or three-dimensional (3-D) simulations desirable.

Greif (1988) presented a review of loop thermosyphons used in different applications. Existing analytical and numerical models were discussed, along with published experimental investigations. A large portion of the review was dedicated to studies of flow instability and oscillations occurring in both closed- and open-loop thermosyphons. Investigations pertaining to loops operating with liquid-vapor phase-change were also reviewed.

A novel numerical model for the simulation of closed-loop thermosyphons with vertical heat transfer sections was proposed by Bernier and Baliga (1992b). This model couples a 1-D model with detailed 2-D axisymmetric simulations of fluid flow and heat transfer in the heating and cooling sections, where buoyancy effects are important. Since the detailed analysis is limited to the vertical heat-exchange sections, not only is this new model is more accurate than traditional 1-D models, which neglect local buoyancy effects, but it is also computationally less expensive than either full 2-D or 3-D simulations of the entire loop. These authors also built and instrumented a thermosyphon, and obtained experimental data for model validation purposes. The experimental apparatus consisted of vertical heating and cooling sections connected by top and bottom semicircular 180º pipe bends. Distilled water was used as the heat exchange fluid. A constant-wall-heat-flux boundary condition was imposed in the heating section using a thin heated gold film attached to the inner surface of the pipe. The cooling section consisted of a concentric annular heat exchanger, which was designed to provide an essentially constant and uniform temperature on the outer surface of the thermosyphon pipe. Thermocouples were installed on the outer surface of the pipe in the heating section to obtain local wall-temperature distributions. The mass flow rate inside the thermosyphon was calculated using an energy balance across the heating section. Since the specific heat of water is well known and the amount of heat added to the fluid was accurately measured, the mass flow rate and the average loop velocity (in steady-state operation) could be deduced by measuring the bulk temperatures at entry and exit planes of the heating section. The proposed model accurately predicted the average loop velocity, and the numerically predicted wall-temperature distributions along the heating section agreed well with the experimental measurements, especially at lower power levels. The authors also demonstrated that simulations with a traditional 1-D model yielded inaccurate results when mixed-convection effects were important in the heating and cooling sections, and when heat losses (or gains) in the insulated portion of the loop were significant.

Fichera and Pagano (2002) conducted a complementary numerical and experimental investigation of the dynamic behavior of closed-loop thermosyphons. The authors used a neural-network method to predict fluid temperatures at multiple locations in the loop. This method does not involve solutions of the governing differential equations, but instead relies on experimental data which it assimilates and processes in what could be described as a *training* period. According to the authors, the trained algorithm can successfully predict local temperatures if initial conditions are provided along with the operating parameters. As the authors themselves admit, such a method does not provide physical insight into the flow and heat transfer phenomena occurring in the thermosyphon, and it can only be used to predict the performance of the system it was trained on. They argued that classical methods relying on solutions of the governing equations do not describe the dynamic behavior of thermosyphons with acceptable accuracy. The model proposed in the work of Fichera et al. (2002) was then used by Cammarata et al. (2004) in an effort to develop a heater controller for preventing flow oscillations and flow-direction reversal that may occur under certain conditions in closed-loop thermosyphons. This controller, also based on a neural network method, was trained with the aforementioned thermosyphon model instead of the actual loop, as the authors feared that the experimental apparatus could endure some damage during the controller training period. The trained controller was not validated by applying it to stabilize the experimental apparatus, but instead was tested with simulations only. Also, the proposed controller might have limited applications, as it regulated the heating-power input to avoid flow oscillations and flow-direction reversal. In actual applications, the heating power (or component cooling requirements) might not be an adjustable parameter.

A numerical investigation of laminar flow and heat transfer in closed-loop thermosyphons was carried out by Desrayaud et al. (2006). The authors studied the dynamic behavior of an annular (non-toroidal) loop operating with water. A constant-wall-heat-flux boundary condition was imposed on the bottom half of the geometry while the surface of the top-half was maintained at a constant temperature. The authors investigated values of the outer-to-inner diameter ratio ranging between 1.08 and 2. A two-dimensional finite volume method was used to solve a mathematical model of the unsteady flow and heat transfer phenomena in the loop. A dimensionless parameter, based on a Rayleigh number, was proposed to correlate the dimensionless heat transfer data and mass flow rate. The following three loop dynamic behaviors were found to exist: a steady-flow operation at low Rayleigh numbers, followed by a periodic oscillatory flow regime, and finally Lorenz-like flow reversals and oscillations at higher Rayleigh number values. The numerical results were not compared to the experimental data.

Küçüka and Başaran (2007) performed a complementary numerical and experimental study of closed-loop thermosyphons having vertical heat exchange sections. In this study, the wall temperatures in both the heating and cooling sections were maintained at uniform values. The numerical simulations were performed by assuming that the flow and heat transfer phenomena are two-dimensional axisymmetric in these heat-exchange sections. Their mathematical model was then validated using experimental data obtained with an instrumented thermosyphon. The authors proposed a correlation, based on the Prandtl and Grashof numbers, for predicting the dimensionless heat transfer rates. However, the constants in the proposed correlation are strongly dependent on the thermosyphon geometrical parameters and dimensions, thus limiting its potential uses for design purposes.

Benne and Homan (2008) conducted a numerical study of closed-loop thermosyphons for thermal storage applications. One of the vertical sections of the studied thermosyphon acted as a reservoir, while the other included the heating section and a flow restrictor to optimize the system performance. The authors used a quasi-one-dimensional model and a finite-difference method to predict the unsteady flow and heat transfer phenomena in the whole system. The best transient (storage) performance of the studied thermosyphon was found to occur when the heating-section length was small relative to the loop height. Practical thermal-storage applications suggested by the authors include solar domestic hot water (SDHW) heating systems and novel thermosyphon-based electric resistance water heaters (ERWH).

For the sake of conciseness, the focus in this subsection was on publications pertaining to thermosyphons in single-phase operation. For some discussions of recent investigations of thermosyphons with liquid-vapor phase-change, the reader is referred to the experimental work of Na et al. (2001), and also the complementary analytical and experimental investigations of Haider and Nakayama (2002). A review of publications on thermosyphons operating with MCPCM slurries is presented in Section 1.4.5.

1.4.4 Thermophysical Properties of Liquid-Solid Particle Slurries with and without Change of Phase

The thermosyphon model proposed in this work requires accurate predictions of the effective properties of MCPCM slurries. In this subsection, some pivotal studies of the effective properties of liquid-solid particle slurries are presented first, with a focus on the effective thermal conductivity and dynamic viscosity. Next, key investigations pertaining to other properties and characteristics of MCPCM slurries are discussed.

Effective Thermal Conductivity

While studying the electrical properties of heterogeneous media, Maxwell (1954) derived a relation for predicting the effective electrical resistance of a medium containing uniformly disseminated spherical particles having different electrical properties. This equation can be adapted to predict the effective thermal conductivity of a static suspension of approximately spherical solid particles dispersed in a liquid carrier fluid. If the volume concentration of the MCPCM is denoted as φ and the thermal conductivities of the carrier fluid and particles are represented as k_f and k_p, respectively, the effective thermal conductivity of the slurry, k_s, can be predicted using the following relation:

$$\frac{k_s}{k_f} = \frac{2k_f + k_p + 2\varphi\left(k_p - k_f\right)}{2k_f + k_p - \varphi\left(k_p - k_f\right)} \qquad (1.1)$$

This equation is strictly applicable only to suspensions having the following characteristics: an essentially uniform particle distribution, a relatively low particle volume concentration, and a particle size which is relatively small compared to the characteristic length scale of the thermal problem.

Another important investigation of the effective thermal conductivity of suspensions of spherical particles in a carrier liquid was conducted by Sohn and Chen (1981). The authors investigated the enhancement of the effective thermal conductivity of suspensions due to particle micro-convection effects induced by viscous shear. They designed a Couette flow apparatus in which heat is exchanged between a uniformly heated rotating inner cylinder and a fixed, concentric, outer cylindrical casing maintained at a uniform temperature. Sohn and Chen (1981) conducted their investigation using the following two neutrally-buoyant suspensions: (i) polyethylene beads introduced in volume concentrations of 15% and 30% in a mixture of silicone oil and kerosene; and (ii) polystyrene particles in a mixture of silicone oil and Freon-113. The diameters of the polyethylene and polystyrene beads were of 2.9 mm and 0.3 mm, respectively, while the gap width between the concentric test cylinders was maintained at 23.8 mm. Before performing the final experiments, the authors measured the thermal conductivity of single-phase fluids subjected to a shear rate and noticed no change with respect to the static fluid results. However, an enhancement of the effective thermal conductivity was observed for sheared suspensions, and it was found to increase as a function of a modified particle Péclet number based on the fluid velocity gradient, as defined below:

$$Pe_p = \frac{ed_p^2}{\dfrac{k_f}{\rho_f c_{p,f}}} \tag{1.2}$$

In this equation, e represents the fluid velocity gradient in the vicinity of a particle, and d_p denotes the particle diameter. Modest enhancements of the effective thermal conductivity of the slurries were observed for particle Péclet numbers values less that 50, while for values greater than 300, micro-convection effects considerably augmented this effective property of the slurry. Though these authors were not able to fully correlate data obtained with the two above-mentioned slurries, they suggested the following relationship to predict the enhancement of the effective thermal conductivity with respect to its static value, for a given (fixed) volume concentration (φ) of the particles in the slurries:

$$\frac{k_s}{k_{s,static}} = f\left(\varphi\right) Pe_p^n \qquad \text{where}\, n = 1/2 \text{ for}\, Pe_p \geq 300 \tag{1.3}$$

Charunyakorn et al. (1991) formulated a new expression to predict the effective thermal conductivity of sheared slurries following an inspection of the analytical works of

Leal (1973), and Nir and Acrivos (1976), and the experimental investigation of Sohn and Chen (1981). They proposed the following relation:

$$\frac{k_s}{k_{s,static}} = 1 + B\varphi Pe_p^m \tag{1.4}$$

In the above expression, the values of B and m depend on the particle Péclet number and are assigned as follows: for $Pe_p < 0.67$, $B = 3.0$ and $m = 1.5$; for $0.67 < Pe_p < 250$, $B = 1.8$ and $m = 0.18$; and for $Pe_p > 250$, $B = 3.0$ and $m = 1/11$.

In his numerical and experimental investigation, Scott (2006) used the adapted relation of Maxwell (1954), given in Eq. (1.1), to compute the effective thermal conductivity of MCPCM slurries. Micro-convection effects were neglected, as the maximum estimated particle Péclet number was found to be negligibly small.

Effective Dynamic Viscosity

One of the first analytical models for the prediction of the dynamic viscosity of dilute suspensions or slurries of rigid spheres disseminated in a carrier fluid was proposed by Einstein (1906). He suggested the following relation relating the dynamic viscosity of the suspension to that of the pure carrier fluid:

$$\mu_s = \mu_f \left(1 + \kappa\varphi\right) \tag{1.5}$$

In Eq. (1.5), μ_s denotes the dynamic viscosity of the slurry, μ_f is the dynamic viscosity of the carrier fluid, φ is the volume concentration of the spherical particles, and κ is a constant with an assigned value of 2.5.

A pivotal extension of the model of Einstein (1906) was conducted by Vand (1945), who modified Eq. (1.5) to accurately predict the dynamic viscosity of slurries having higher particle concentrations. The proposed relation is considered to remain valid as long as the particle concentration of the slurry is still sufficiently low to allow the effects of particle interactions, such as collisions, to be neglected. The dynamic viscosity model formulated by Vand (1945) can be expressed as follows:

$$\mu_s = \mu_f \left(1 - \varphi - B\varphi^2\right)^{-k} \tag{1.6}$$

Here, μ_s, μ_f, and φ denote the dynamic viscosity of the slurry, the dynamic viscosity of the carrier fluid, and the particle volume concentration, respectively. The constants B and k need to be empirically determined. Vand (1945) experimentally investigated the dynamic viscosity of slurries composed of 0.13 mm diameter glass beads immersed in a zinc iodide solution in water and glycerin. The results, obtained with capillary viscometers, were curve-fitted and the values of the constants B and k were determined to be 1.16 and 2.5, respectively, for the studied slurries. The agreement between the predicted viscosity values and the experimental data was very good up to particle volume concentrations of 37%. Above this value, the author stated that the suspensions were characterized by a non-Newtonian behavior. The relation proposed by Vand (1945) has often been modified by other researchers for predicting the dynamic viscosity of specific suspensions with greater accuracy. For example, Mulligan et al. (1996) modified the value of B to 3.4, and Yamagishi et al. (1999) used $B = 3.7$.

An important review of rheological studies of suspensions was provided by Stein (1986). Along with many related subjects, the author reviewed the experimental techniques and challenges commonly encountered when investigating the rheological behavior of suspensions. The analytical works of Einstein (1906) and Batchelor (1974) were discussed critically, as well as the semi-empirical relations of Mooney (1951) and Krieger and Dougherty (1959) [as discussed in Krieger (1972)]. Batchelor (1974) analytically derived the following relation to predict the relative viscosity of a suspension, including particle interactions:

$$\eta_r = \frac{\mu_s}{\mu_f} = 1 + 2.5\varphi + 5.2\varphi^2 \tag{1.7}$$

In this equation, η_r denotes the relative viscosity. It should be noted that the value of the last coefficient in this equation is incorrectly reported as 6.2 (instead of 5.2) in the review article of Stein (1986).

In an effort to provide an expression for predicting the relative viscosity of suspensions with high particle concentrations, Mooney (1951) proposed the following semi-empirical relation based on analytical derivations and experimental inputs:

$$\eta_r = \frac{\mu_s}{\mu_f} = \exp\left(\frac{2.5\varphi}{1-k\varphi}\right) \tag{1.8}$$

The agreement between predictions obtained with this relation and the corresponding experimental data was very good for particle volume concentrations less than 40%. A variant of Mooney's equation is presented in the review of Stein (1986), in which the constant *k* is removed and a maximum concentration limit $\varphi_{\max}$ is introduced:

$$\eta_r = \frac{\mu_s}{\mu_f} = \exp\left(\frac{2.5\varphi}{1-\varphi/\varphi_{\max}}\right) \tag{1.9}$$

A similar relation was proposed by Krieger and Dougherty (1959) [as discussed in Krieger (1972)]:

$$\eta_r = \frac{\mu_s}{\mu_f} = \left(1-\frac{\varphi}{\varphi_{\max}}\right)^{-\eta_{intrinsic}\,\varphi_{\max}} \tag{1.10}$$

The value of the maximum concentration, $\varphi_{\max}$, in this equation is interpreted as that at which motion of the solid spheres in the slurry is no longer possible. Its value is not uniquely established. For example, a $\varphi_{\max}$ value of 0.74, which corresponds to an array of hexagonal close-packed spheres of equal diameter, is sometimes used. A $\varphi_{\max}$ value of 0.52 has also been proposed, which pertains to close-packed spheres of equal diameter in a simple cubic lattice. However, since motion of the spheres in the suspension may occur without all lattice layers being in motion, an intermediate $\varphi_{\max}$ value of 0.63 is often adopted.

Scott (2006) used capillary viscometers to determine the dynamic viscosity of MCPCM slurries over a temperature range of 6 ºC to 60 ºC and for particle concentrations up to 15%. His study confirmed that the relative viscosity of the slurry, $\eta_r = \mu_s / \mu_f$, is essentially a function only of the MCPCM mass concentration, and can be considered to be independent of temperature. Scott (2006) curve-fitted the relative viscosity measurements as a function of the MCPCM mass concentration, ϕ, and presented a correlation of the following form:

$$\eta_r = \frac{\mu_s}{\mu_f} = a_3\phi^3 + a_2\phi^2 + a_1\phi + 1.0 \tag{1.11}$$

In this equation, the values of the coefficients a_3, a_2, and a_1 are determined experimentally, and are specific to the slurries investigated. Scott (2006) assumed that the slurries used in his investigation of mixed convection heat transfer in a vertical pipe were characterized by an essentially Newtonian behavior for concentrations less than 20%. More thorough rheological studies were performed on the same MCPCM slurries in the course of the work presented in this thesis. These studies showed that for the shear rates expected in the thermosyphon flows of interest here, the slurries have a slightly non-Newtonian, shear thinning, behavior, even at relatively low concentrations. A description of the rheological study conducted in this work is presented in Chapter 3.

Other Properties and Characteristics of MCPCM Slurries

Roy and Sengupta (1991) studied the thermophysical properties of MCPCM slurries and also tested the resistance of the microcapsule shells to thermal cycling fatigue. Two phase-change materials were tested, n-eicosane and stearic acid, and these PCMs were encapsulated in shells having diameters ranging between 50 μm and 250 μm. The thermal cycling tests were performed using a differential scanning calorimeter, and it was found that the stearic acid microcapsules could not withstand numerous heating and cooling cycles due to their thinner shells (which accounted for 15% of the total particle volume). Interestingly, their experimental data also showed that the latent heat of fusion of the MCPCM slurries drifted slightly after a few thermal cycles. However, the maximum variation of this property during the aforementioned thermal cycling studies was less than 10% in all cases, even after a hundred cycles.

Yamagishi et al. (1996) obtained experimental data on the properties of MCPCM slurries that could be used for design purposes. They conducted an extensive investigation of the thermal, rheological, and resiliency properties of multiple suspensions. Two different paraffins (n-tetradecane and n-dodecane) were encapsulated in particles having mean effective diameters of 5, 30, 250 and 1000 μm. Differential scanning calorimetry studies were performed. They revealed that capsules having diameters smaller than 100 μm required a high degree of supercooling for the PCM solidification to occur. However, addition of a 1-tetradecanol nucleating agent into the n-tetradecane PCM efficiently suppressed the PCM supercooling phenomena. Yamagishi et al. (1996) then examined capsule shell resistance capabilities by circulating the slurry in a closed circuit for long periods. They discovered that only the 5 μm diameter capsules successfully withstood the mechanical pumping and also the numerous thermal cycles. In contrast to the observation of Roy and Sengupta (1991) that the latent heat of fusion of the slurry was modified by thermal cycling, Yamagishi et al. (1996) did not witness any difference in this property of cycled and non-cycled suspensions. Rheological studies performed with a Couette rheometer revealed that slurries having 20% and 30% particle concentrations were characterized by a non-Newtonian behavior. However, adding 1% (by mass) of ionic surfactants in the slurries successfully modified their rheological behavior to Newtonian, while also reducing their effective dynamic viscosity.

A similar investigation of MCPCM slurry properties was carried out by Yang et al. (2003), who encapsulated tetradecane with four different types of shell materials. The authors used a differential scanning calorimeter to obtain the MCPCM melting and freezing temperatures, and also the slurry latent heat of melting for different particle concentrations and crust materials.

Fan et al. (2004) attempted to suppress the supercooling requirements of encapsulated n-octadecane by adding nucleating agents to the PCM. The authors investigated the effects of adding sodium chloride, 1-octadecnol, and a paraffin in multiple concentrations with respect to the PCM. Adding sodium chloride in mass concentrations of 6% to the n-octadecane prior to the encapsulation process essentially neutralized the supercooling phenomena. However, the resulting microcapsules had rougher shell surfaces and were found to agglomerate easily. The paraffin, added in a mass concentration of 20%, proved to be a better nucleating agent, as it almost completely suppressed supercooling without inducing any significant undesirable effects.

Another study for characterizing MCPCM slurries was carried out by Alvarado et al. (2006). The authors aimed at reducing the undesirable supercooling requirements of the encapsulated PCM by introducing a nucleating agent in it. The MCPCM capsules employed in this study had a diameter range of 90 to 125 μm, and n-tetradecane ($C_{14}H_{30}$) was used as the PCM. Tetradecanol ($C_{14}H_{30}O$) was added to the PCM as a nucleating agent in mass concentrations of 1, 2 and 4 %. On average, the capsules were formed of 88.3% tetradecane (and its nucleating agent) and 11.7% crust material. Differential scanning calorimetry studies revealed that adding 2% of the nucleating agent almost suppressed the supercooling phenomena entirely. However, the addition of tetradecanol also decreased the latent heat of fusion of the MCPCM capsules noticeably.

Studies have also been conducted on ways to increase the effective thermal conductivity of the slurries. The effective thermal conductivity of MCPCM suspensions in water is generally less than that of the conveying liquid alone, due to the lower thermal conductivity values of the PCM and the usual polymer-resin encapsulation shell. In an attempt to overcome this undesirable effect, Zhang et al. (2010) manufactured MCPCM particles of encapsulated n-octadecane in higher-conductivity inorganic silica shells. The thermal conductivity of the silica shell material was measured to be 1.296 W/m°C, a value that is many times higher than that of generic polymeric shell materials (≈ 0.2 W/m°C). However, relatively thick particle shells were needed to obtain overall MCPCM thermal conductivity values equivalent to that of water. Thicker shells reduce the latent-heat storage capacity of the particles, as the proportion of the PCM within the particle is reduced.

Ho et al. (2010) also investigated ways to augment of the effective thermal conductivity of MCPCM slurries. To that end, they introduced Al_2O_3 “nano” particles in slurries of encapsulated n-eicosane particles dispersed in water. Slurries having MCPCM mass concentrations of 3.7, 9.1, and 18.2% were studied, and the Al_2O_3 particles were introduced in mass concentrations ranging between 0 to 10%. As was expected, the addition of the Al_2O_3 particles had no effect on the melting and freezing behaviors of the MCPCM particles. However, the Al_2O_3 particles did have a beneficial effect on the effective thermal conductivity of the slurries. For example, adding Al_2O_3 particles in a mass concentration of 10% to slurry having an MCPCM mass concentration of 10% increased the effective thermal conductivity value by 9.6%. However, the authors observed that when the Al_2O_3 particles were introduced, they slightly lowered the effective specific heat of the slurry in temperature ranges corresponding to sensible heating.

1.4.5 MCPCM Slurry Flow and Heat Transfer in Ducts, Enclosures, and Thermosyphons

Numerous analytical, numerical, and experimental investigations of fluid-solid particle flow and heat transfer (with and without phase-change) in ducts and enclosures have been published. Many of these investigations are devoted to one or more of the following topics: complete local descriptions or exact formulations; discussions of averaging procedures; kinetic theory models; various practical mathematical models (such as Eulerian-Lagrangian, two-fluid Eulerian-Eulerian, and homogenous models) that employ suitably averaged governing equations; dimensional analyses; particle-wall interactions; appropriate boundary conditions; experimental techniques and measurements; effective thermophysical properties and techniques to measure them; numerical solution methods; and results of analytical, numerical, and experimental investigations, and their interpretations. Examples of such investigations include the works of Bagnold (1954; 1956), Karnis et al. (1966), Cox and Mason (1971), Crapiste et al. (1973), Whitaker (1973), Jeffrey and Acrivos (1976), Spalding (1978), Slattery (1981), Bouré and Delhaye (1982), Crowe (1982), Drew (1983), Savage (1984), Durst et al. (1984), Stewart and Wendroff (1984), Stein (1986), Darby (1986), Zimmels (1986), Jiang et al. (1986), Johnson and Jackson (1987), Campbell (1990), Crowe (1991), Drew and Lahey Jr. (1993), Masson and Baliga (1994), Gidaspow (1994), Acrivos (1995), Schaflinger (1996), Masson and Baliga (1998), Fan and Zhu (1998), Crowe et al. (1998), Savage (1998), Whitaker (1999), Sommerfeld and Huber (1999), Ottino and Khakhar

(2000), Inaba (2000), Kaviany (2001), Naterer (2003), Brennen (2005), and Crowe (2006).

The review in the next subsection is focused on MCPCM slurry flow and heat transfer in ducts and enclosures, with melting and freezing of the encapsulated PCM. To the author's knowledge, only one study of closed-loop thermosyphons operating with MCPCM slurries has been published to date. That study is reviewed in the second of the two following subsections.

Ducts and Enclosures

As was mentioned earlier, the concept of adding encapsulated PCM particles to a carrier liquid to augment convective heat transfer was first proposed by Katz (1967). He conducted an experimental investigation of natural convection heat transfer in a cubical enclosure filled with slurries of disk-shaped capsules (containing wax) dispersed in water. He found that the rate of heat transfer for a given temperature difference could be doubled relative to that achieved with just the conveying liquid (without the encapsulated PCM).

Colvin and Mulligan (1987), in a study sponsored by NASA, investigated the possibilities offered by MCPCM slurries for enhancing the performance of spacecraft thermal systems. They examined MCPCMs with mean effective diameters of 20 μm, and cores of octadecane or eicosane as the PCM. Their investigation showed that MCPCM slurries could be used to obtain enhancements of the overall heat transfer coefficient. The authors observed that one of the main difficulties encountered in the use of such slurries in thermal systems is related to the manufacturing of capsule shells that can withstand the wear-and-tear effects of mechanical pumping.

A numerical investigation of laminar forced convection heat transfer with MCPCM slurries flowing in straight tubes was conducted by Charunyakorn et al. (1991). They assumed that the slurries could be treated as a homogeneous Newtonian fluid. The authors simplified the flow and heat transfer problems by imposing a fully-developed velocity profile in the heat-exchange section and by fixing the slurry entry temperature to the melting-onset temperature of the phase-change material. A general correlation, based on a particle Péclet number, was devised to model the effective thermal conductivity and its enhancement due to local shear. The phase-change process was modeled by a heat source/sink function introduced in the energy equation. This function was assessed at each grid node by solving a one-dimensional radial Stefan problem, consisting of a spherical mass of PCM in a shell of negligible thickness subjected to convective heat transfer on its exterior. The energy equation was solved using a finite difference method, which solved iteratively for the temperature field and the local melting process of the encapsulated PCM. The parameters investigated included the following: the MCPCM volume concentration (up to 25 %); a bulk Stefan number; the pipe-to-particle radius ratio; and the particle-to-carrier-fluid thermal conductivity ratio. The authors first validated their model by solving the thermal problem with MCPCM slurries not undergoing phase change, and comparing their results with the experimental investigation of Ahuja (1975). The results of the main simulations (with phase change) showed an increase of the local Nusselt number and a reduction of the maximum wall temperature when a constant-wall-heat-flux thermal boundary condition was applied. These authors also stated that the bulk Stefan number is the dominant parameter, and the effect of the pipe-to-particle radius ratio is negligible for values ranging between 200 and 400. The results of the main simulations with MCPCM slurries were not checked against any experimental data.

An experimental study of natural convection in a cubical enclosure containing MCPCM slurries was carried by Datta et al. (1992). In their experimental setup, the side-walls of the enclosure were insulated, a constant heat flux was applied at the bottom wall, and the top surface was maintained at a constant temperature. The authors investigated the effects of a suitably defined Rayleigh number, the volume concentration of the MCPCM particles, the bulk Stefan number, and the particle size. The slurries consisted of microencapsulated n-eicosane ($C_{20}H_{42}$) disseminated in Mobiltherm-603 mineral oil, with values of volumetric concentration in the range 0.5% to 20%. The values of Rayleigh number ranged from 9×10^7 to 5×10^8, and the effective diameter of the MCPCM particles was between 50 μm and 300 μm. The authors discerned three different flow regimes: (i) for particle concentrations up to 1%, the slurry remained homogeneous, and the addition of MCPCMs resulted in increases of the overall Nusselt number; (ii) for higher concentrations, particle clumping was observed and the potential benefits of using the MCPCMs (for example, increases in Nusselt number) were not fully achieved; and (iii) for MCPCM concentrations greater than 5%, the particles coagulated on the hot and cool enclosure walls, and thereby acted as an insulating layer and hindered heat transfer. As was expected, decreasing the bulk Stefan number increased the overall Nusselt number. Finally, the authors indicated that the disappointing results obtained with slurries having particle concentrations greater than 1% could be improved by preventing particle clumping with dispersing agents.

Goel et al. (1994) conducted an experimental investigation on forced convection heat transfer of MCPCM slurries flowing in a horizontal pipe subjected to a constant heat flux on its wall. Prior to entering the heated section, the laminar slurry flow first traveled into an entrance section and reached the fully-developed condition. Additionally, a water jacket was installed around this entry section to maintain the slurry slightly below the PCM melting-onset temperature. The effective thermophysical properties of the slurry were obtained using the following approaches and equations: a mass balance requirement to obtain the effective density; an energy balance condition to determine the effective specific heat; an adapted form of the equation proposed by Maxwell (1954), as shown in Eq. (1.1), for the effective thermal conductivity; and model of Vand (1945), as expressed by Eq. (1.6), for the effective dynamic viscosity. The slurries were prepared by mixing the MCPCMs (n-eicosane PCM encapsulated in an amino-formaldehyde resinous shell wall) in water. The authors investigated the influence of the following four parameters: the particle concentration; the bulk Stefan number; the pipe-to-particle diameter ratio; and the degree of homogeneity of the suspension. To validate their experimental set-up and procedures, they first measured wall-temperature distributions in the heating section for conditions in which there was no solid-liquid phase-change in the encapsulated PCM, and checked these experimental results against a well-established solution for single-phase flow. A relatively poor agreement was found in the middle portion of the heating section. So the authors introduced a correction factor to the temperature measurements, thereby casting some doubts on the reliability of the results of their main experimental study, for which there was solid-liquid phase-change of the encapsulated PCM. Nevertheless, the results of their main experimental studies revealed that the bulk Stefan number was the dominant parameter. Reductions in the wall temperatures of up to 50% were obtained when the MCPCMs were added to the conveying fluid. Finally, the authors stated that if the objective is to maintain the maximum temperature of the pipe wall below a given value, then introducing MCPCMs into the conveying fluid could be used to reduce the required flow rate by a factor of ten and the related pumping power by a factor of 100.

Zhang and Faghri (1995) performed a numerical investigation of laminar forced convection of MCPCM slurries in a horizontal pipe, and aimed to overcome the shortcomings of the model proposed by Charunyakorn et al. (1991). A constant-heat-flux condition was applied at the pipe wall, and a fully developed flow velocity profile was assumed. The proposed mathematical model was based on the assumption that the slurries behaved as homogeneous Newtonian fluids for MCPCM concentrations less than 20%. The effects of the thermal resistance of the MCPCM shell and the “initial subcooling” (defined in this paper as the difference between the slurry temperature at the inlet of the heating section and the PCM melting-onset temperature) were taken into account, in addition to the PCM melting temperature range (as the melting did not occur at a single or unique value of temperature). Inclusion of the thermal resistance of the MCPCM shell and the “initial subcooling” in the model improved the agreement of the predicted results with the experimental results of Goel et al. (1994), but large discrepancies were observed when the melting of the PCM was considered to occur at a single or unique value. Better agreement was yielded by simulations performed when the melting of the PCM was considered to occur over a suitable temperature range. However, since Goel et al. (1994) did not specify a precise melting temperature range for the PCM employed in their experiments, no direct comparison was possible to fully assess this feature of the model.

The improved heat transfer performance provided by MCPCM slurries in the above-mentioned works encouraged Mulligan et al. (1996) to investigate their potential use in spacecraft thermal systems. They conducted analytical and experimental studies of laminar forced convection with MCPCM slurries flowing in a pipe with a constant heat flux imposed on its outer surface. The effective diameter of the MCPCM particles ranged from 10 to 30 μm, and they contained four different phase-change materials: n-heptadecane, n-octadecane, n-nonadecane, and n-eicosane. All four of these MCPCMs were shown to diminish the pipe wall temperatures in the heated section, increase the local heat transfer coefficient, and augment the effective specific heat of the working fluid (the slurries). Their analytical predictions only showed qualitative agreement with the experimental results since, as the authors point out, many of the assumptions in their model were not accurate. Mulligan et al. (1996) also claimed that classical correlations that are commonly used to predict Nusselt numbers for single-phase fully-developed turbulent forced convection in pipes, such as the correlation of Sieder and Tate (1936), are also applicable to turbulent flows of MCPCM slurries, provided the effective specific heat values used for the slurries correctly incorporate the effects of the latent heat of fusion of the PCM. To support this statement, the authors attempted to formulate a relation analogous to the Sieder-Tate correlation. However, the scatter of the experimental data about the predictions obtained with this correlation was significant.

An experimental study of forced convection heat transfer with MCPCM slurries flowing in a horizontal pipe subjected to a constant wall heat flux was performed by Yamagishi et al. (1999). In addition to investigating the laminar flow regime, the authors also sought to obtain empirical data for the turbulent regime. The slurries used in their experiments consisted of an octadecane ($C_{18}H_{38}$) MCPCM mixed in pure water. The effective diameter of the MCPCM particles ranged from 2 to 10 μm, and particle volumetric concentrations of up to 30% were investigated. The slurries were assumed to have a Newtonian behavior over the investigated Reynolds number range, as no contradicting evidence was observed in the rheological studies performed by the authors. Thermophysical properties were calculated with the same relations as those used by Goel et al. (1994), except that the value of coefficient B in Eq. (1.6) proposed by Vand (1945) was changed to 3.7 (from the earlier value of 1.16). The authors provided measurements of the friction factor and also local heat transfer coefficients. To obtain the local heat transfer data, the heated-pipe section was divided into multiple contiguous heating segments, each insulated from the environment and fitted with a thermocouple on the outer wall. Local data was then obtained by progressively activating these segments in the downstream direction and assuming that the heat losses from the slurries flowing in the unheated sections were negligibly small, thereby allowing the values of the local bulk temperature to be obtained from measurements in a mixing chamber located downstream. As was expected, the values of the local heat transfer coefficient were increased when the

MCPCMs underwent phase-change, and also when the MCPCM concentration was augmented. However, the measured heat transfer coefficients for turbulent flows of the MCPCM slurries did not surpass those obtained with pure water for identical volume flow rates. The authors attributed such results to the phase-change benefits of the slurries not being fully exploited during their turbulent flow experiments.

A numerical investigation of laminar forced convection heat transfer with MCPCM slurries flowing in a pipe was performed by Bai and Lu (2003). They combined a finite difference method with a boundary element method in an iterative procedure that alternatively solved the temperature of the conveying liquid and the temperature distribution within the particles, which were considered as spheres undergoing solid-liquid change of phase. In this study, the slurry was considered to be a Newtonian fluid and the problem was solved for a constant-wall-heat-flux boundary condition. The mathematical model was validated by comparing the predicted distributions of a dimensionless wall temperature to those experimentally obtained by Goel et al. (1994). The agreement between these results was relatively good. The particle diameter, volume concentration, and bulk Stefan number were found to be the dominant parameters.

Zhang et al. (2003) conducted a numerical investigation of laminar forced convective heat transfer in a pipe conveying MCPCM slurries. In this study, the pipe wall temperature was maintained at a constant value. The authors employed an effective-specific-heat model in their analysis to account for the effects of the latent heat of the phase-change material. The influences of the bulk Stefan number, the MCPCM concentration, and a dimensionless “degree of subcooling”, were investigated, and their impact on the values of a local heat transfer coefficient was assessed. This local heat transfer coefficient was based on the wall-to-entry temperature difference, instead of the conventional wall-to-bulk temperature difference, at a given streamwise location. In their conclusions, the authors state that the bulk Stefan number and MCPCM concentration are the most important parameters. Intriguingly, they also claimed that the heat transfer enhancement due to the presence of MCPCM is also observed in the thermally fully developed region, once the PCM has melted. This is counterintuitive as the benefits of the MCPCM slurries are expected when the PCM undergoes melting. Indeed, once the melting process is completed and the thermally fully developed condition is reestablished, the local Nusselt number value (based on the conventional definition) should be almost identical to the well-known value for a single-phase fluid with the same effective properties as those of the slurry (with no change of phase of the PCM). It is possible that the aforementioned conclusion in this paper is caused by the above-mentioned unconventional definition of the local heat transfer coefficient. This modified heat transfer coefficient does not asymptote to a constant value when the thermally developed condition is reached. Thus its values in the fully-developed region are affected by upstream effects, including the PCM latent heat of fusion, making a direct comparison between heat transfer coefficients in the thermally developed region potentially misleading. With this study, the authors sought to extend the earlier work of Hu and Zhang (2002), in which the same problem was solved for the constant-wall-heat-flux boundary condition. Finally, Zhang et al. (2003) varied the *shape* of the function that was used to model the effective specific heat of the slurries when the PCM undergoes phase change, while maintaining the latent heat of fusion constant. They concluded that the assumed shape of this function has a significant impact on the computed results.

An experimental investigation of laminar and turbulent forced convective heat transfer with MCPCM slurries flowing in a pipe subjected to a constant wall heat flux was conducted by Inaba et al. (2004). In this study, the slurries were composed of a mixture of two different types of MCPCMs: one contained n-tetradecane ($C_{14}H_{30}$) as the phase-change material, and had a mean effective diameter of 1.5 μm; in the other, the phase-change material was n-docosane ($C_{22}H_{46}$), and the mean effective diameter was 17 μm. The slurries had the following mass concentrations of the MCPCMs: 20% of the small particles and 0 to 50% of the larger ones. Intriguingly, the experimental settings were chosen such that only the smaller MCPCMs underwent phase-change, as the maximum fluid temperature in the apparatus was maintained well below the melting temperature of the larger MCPCMs, thereby deliberately not exploiting their phase-change benefits. The authors claimed that the addition of the larger MCPCMs in the slurries generated desirable micro-convection effects. Interestingly, the addition of these larger capsules did result in an increase of the local Nusselt numbers: the local Nusselt number values in the laminar regime increased by a factor of 2.8 with respect to those obtained for the pure carrier liquid. The authors also measured velocity profiles using an ultrasonic velocity profiler (UVP) technique for different MCPCM concentrations and compositions. In the laminar flow regime, the velocity profiles had a non-parabolic shape, which the author ascribed to non-Newtonian slurry behavior and uneven capsule distribution in the radial direction. Distributions of the friction factor were also obtained for multiple values of MCPCM concentrations and for Reynolds number values up to 7000. The results revealed that the presence of the smaller MCPCMs suppressed transitional flow instabilities and delayed the onset of turbulence.

Wang et al. (2004) conducted a numerical investigation of turbulent forced convection heat transfer with MCPCM slurries flowing in a pipe with a constant heat flux imposed on its wall. The turbulence model employed in the problem was based on an eddy-diffusivity approach. Some of the results were compared to the experimental results of Roy and Avanic (2001) and showed reasonably good agreement. The particle bulk Stefan number was found to be the dominant parameter.

A volume-averaged Eulerian-Eulerian model for the simulation of flow and heat transfer with MCPCM slurries as the working fluid was proposed by Ho (2004). In his model, the liquid and solid particles are treated as interpenetrating continua. Two sets of volume-averaged governing equations are proposed: one for the carrier liquid and the other for the MCPCM particles; and special relations are prescribed for the momentum and energy balances at the interfaces between them. This model was benchmarked by simulating forced convection heat transfer in a pipe of circular cross-section. The results displayed only qualitative agreement with the experimental data of Goel et al. (1994). The author attributed the quantitative discrepancies between these numerical and empirical results to axial conduction in the wall of the instrumented copper pipe. It is also apparent that the proposed model relies on numerous approximations that are necessary to obtain problem closure. This model was later used by Ho et al. (2005) in a numerical investigation of a closed-loop thermosyphon using MCPCM slurries as the heat transfer fluid. This last study will be discussed further in the next subsection.

Complementary numerical and experimental studies of laminar mixed convection heat transfer with water-based slurries flowing in a vertical pipe subjected to a constant wall heat flux was carried out by Scott (2006), in the Heat Transfer Laboratory at McGill University. The author proposed a homogeneous model with effective thermophysical properties for the slurries. Differential scanning calorimetry (DSC) was used to measure the effective specific heat of the slurries at temperatures between 6 ^{o}C to 60 ^{o}C. Scott (2006) also designed and constructed a special apparatus for measuring the effective thermal conductivity of the slurries in the aforementioned range of temperatures. Additionally, experiments were conducted to determine the effective dynamic viscosity and mass density of the slurries. These experimental data were then used to propose correlations that allow calculations of the effective properties of the slurries as functions of the temperature and the MCPCM concentration. One of the major contributions of Scott (2006) is the definition of a modified bulk temperature of the slurries (related details are presented in Section 2.7) which resolves shortcomings of the classical definition when the phase-change effects are significant. The MCPCM used by Scott (2006) was the same as that used in this work (see Section 1.2 for an overview of the properties of this MCPCM). The mixed-convection heat transfer experiments were conducted by Scott (2006) for the following values of MCPCM mass concentration: 5%, 10%, 15% and 20%. Two different values of the volume flow rate of the slurries were investigated for a range of values of the imposed wall heat flux. The results showed that at corresponding volume flow rates, the addition of the MCPCM to the distilled water successfully reduced the temperature of the pipe wall. A finite volume method (FVM) for the solution of two-dimensional axisymmetric flow and heat transfer problems was implemented. The numerical predictions of the pipe-wall temperatures displayed relatively good agreement with the experimental data.

An experimental study of turbulent forced convection heat transfer in horizontal pipes carrying MCPCM slurries was conducted by Alvarado et al. (2007). In their experimental setup, the external surface of the pipe wall was subjected to an essentially constant heat flux. In addition to obtaining friction factors and heat transfer data, the authors provided many insights on the thermophysical properties of the slurries. They attempted to suppress the PCM supercooling requirement by adding a nucleating agent, tetradecanol, to the phase-change material. They also investigated the relation between the supercooling requirement and capsule size. In addition, capsule durability experiments were performed, and the authors concluded that the smallest capsules, having an effective diameter less than 10 μm, had the best durability. Rheological studies were performed and they showed that the slurries used in the experiments exhibited essentially Newtonian behavior up to an MCPCM mass concentration of 17.7%. The authors also found that the MCPCM particle they used had a turbulence-suppression effect, as shown by reductions in the measured pressure drops. Finally, the authors observed an increase in the values of the local heat transfer coefficient in the section of the pipe in which the MCPCMs underwent phase-change. However, the heat transfer coefficient values obtained with the MCPCM slurries did not surpass those measured with only the carrier fluid (water) at matching volume flow rates. It is likely that the aforementioned turbulence-suppressing effect of the MCPCM particles caused this reduction in the overall heat transfer performance.

Wang et al. (2007) performed a comprehensive experimental investigation of laminar and turbulent forced convection heat transfer with MCPCM slurries flowing in a heated pipe, and also conducted an in-depth examination of the thermophysical properties of the slurries. The slurries were composed of water and microencapsulated 1-bromohexadecane ($C_{16}H_{33}Br$), with mass fractions ranging between 5 % and 27.6 %. The MCPCM crust thickness was approximately equal to 0.3 μm, and the mean effective diameter of the MCPCM particles was estimated to be 10.1 μm. An adapted version of a relation proposed by Maxwell (1954), as expressed in Eq. (1.1), was employed to calculate the effective thermal conductivity of the slurries, and mass and energy balances were used to determine the effective mass density and specific heat of the slurries, respectively. Rheological studies were also performed by these authors, and it was found that the slurries displayed Newtonian behavior up to mass concentrations of 27.6%. The authors proposed a correlation for predicting the dynamic viscosity of the slurries as a function of particle concentration, slightly modifying the model of Vand (1945), as expressed in Eq. (1.6), to fit their experimental data. Friction factor and local heat transfer coefficient data were obtained and used by the authors to propose modification to the correlations proposed for laminar flows by Shah and London (1978). In all of the investigated cases, the measured heat transfer coefficients with the MCPCM slurries were higher than those obtained with pure water, at equivalent heat inputs and flow rates.

More recently, an experimental study of laminar flow and heat transfer with MCPCM slurries flowing in a pipe of circular cross-section, subjected to a constant wall heat flux, was conducted by Chen et al. (2008). The encapsulated PCM used by the authors was 1-bromohexadecane, the conveying fluid was water, and the mean effective diameter of the MCPCM particles was 8.2 μm. Differential scanning calorimetry (DSC) studies revealed that the melting and freezing temperatures of the encapsulated PCM were of 14.3°C and 4.3°C, respectively, and the latent heat of fusion was 129.8 kJ/kg. Rheological investigations revealed that the slurries displayed Newtonian behavior for mass concentrations less than 15.8% and rates of strain higher than 600 s^{-1}. The heated section of the pipe measured 1.46 m in length, had an inner diameter of 4 mm, and a pipe-wall thickness of 1 mm. It was instrumented with eight thermocouples on its outer wall. The authors obtained pressure-drop measurements, wall temperature distributions, and local Nusselt number data. These experimental data revealed for an MCPCM mass concentration of 15.8%, the maximum reduction of the dimensionless inner-wall temperature, with respect to that obtained with only the conveying fluid (water), was 30%. The authors also showed that the pumping power required to achieve a desired rate of heat transfer for a specified maximum value of the wall temperature was reduced when the MCPCM slurries were used, even though the dynamic viscosity of the slurries was significantly higher that that of water. Additional experiments with similar MCPCM slurries were performed by Wang et al. (2008) using the same apparatus as that employed by Chen et al. (2008). Average Nusselt numbers were measured and correlations (based on the Reynolds, Stefan, and Prandtl numbers) were proposed to allow their prediction in both laminar and lower-transitional flow regimes.

Closed-Loop Thermosyphons Operating with MCPCM Slurries

The previously discussed volume-averaged Eulerian-Eulerian model proposed by Ho (2004) was later used by Ho et al. (2005) in a numerical investigation of a closed-loop thermosyphon operating with MCPCM slurries. In this study, the values of a Rayleigh number in the heated and cooled sections ranged from 10^9 to 10^{13}, the range of values of the bulk Stefan number was 0.05 to 0.5, and the volume concentration of the MCPCM particles was varied between 0 to 20%. The complete thermosyphon loop was modeled by considering the flow and heat transfer as being two-dimensional axisymmetric throughout, and a pseudo-transient approach was employed to obtain a steady-state solution. For a fixed value of the Rayleigh number, the presence of MCPCMs in the conveying liquid reduced the dimensionless wall temperatures of the heating section slightly. The authors found that for Rayleigh number values ranging between 10^{10} and 10^{12}, the use of MCPCM slurries increased the average Nusselt number in the cooling section above the values obtained with the conveying liquid alone. The proposed model was not validated by comparing the numerical predictions with experimental data.

To the author’s knowledge, no other investigation pertaining to closed-loop thermosyphons operating with MCPCM slurries has been published. The work presented in this thesis is an attempt at fulfilling the need for an accurate and relatively inexpensive (computationally), or cost-effective, mathematical model for the simulation of flow and heat transfer phenomena in such systems. It should also be noted that research reported in this thesis includes the first experimental study of a closed-loop thermosyphon operating with MCPCM slurries. Finally, the experimental data obtained was used for the validation of the proposed mathematical model and the numerical solutions, a crucial task that was not performed in the above-mentioned numerical study of Ho et al. (2005).

1.5 Survey of the Thesis

This thesis has seven chapters. In the earlier sections of this first chapter, the motivation and main goals of this work, an overview of the MCPCM slurries, the specific objectives, and a literature review were presented. The proposed 1-D/2-D mathematical model used for the simulations of the flow and heat transfer phenomena in closed-loop thermosyphons operating with slurries of MCPCM particles dispersed in distilled water is presented in Chapter 2, along with discussions of some of its key theoretical aspects. The experimental investigations that were conducted to measure the effective thermophysical properties of the slurries, such as the mass density, the specific heat, and the dynamic viscosity, during both heating (melting) and cooling (freezing) processes, are described in Chapter 3, along with the results. The closed-loop thermosyphon apparatus, which was designed and fabricated in this work, and the experimental procedures, which were used to run this apparatus, are described in Chapter 4. A description of the control-volume finite element method (CVFEM) that was used to solve the proposed mathematical model of the two-dimensional axisymmetric flow and thermal problems in the vertical heating and cooling sections of the thermosyphon is presented in Chapter 5. In addition, the following topics are also presented and discussed in Chapter 5: some novel aspects of the proposed CVFEM; test problems that were used to validate the proposed CVFEM; and an overall iterative procedure for solving the axisymmetric two-dimensional (2-D) model, for the fluid flow and heat transfer in the heating and cooling sections (numerical solved using the abovementioned CVFEM), and a segmented quasi-one-dimensional network thermofluid model, of the fluid flow and heat transfer in the remaining portions of the closed-loop thermosyphon. The results of the main experimental and numerical investigations of the closed-loop thermosyphon operating with the MCPCM slurries are presented, compared, and discussed in Chapter 6. Lastly, a summary of the main contributions of this thesis and recommendations for potential extensions of this work are presented in Chapter 7.

2. Theoretical Considerations

As was mentioned in the first chapter, the complementary computational and experimental investigations presented in this thesis pertain to steady, laminar, fluid flow and heat transfer phenomena in a vertically oriented closed-loop thermosyphon operating with slurries of a microencapsulated phase-change material (MCPCM) suspended in distilled water. One of the objectives of this research was to formulate a cost-effective mathematical model of these fluid flow and heat transfer phenomena. The proposed mathematical model involves an amalgamation of two-dimensional axisymmetric and quasi-one-dimensional models of the fluid flow and heat transfer in the vertical (heating and cooling) sections and the remaining portions of the closed-loop thermosyphon, respectively. This cost-effective model is referred to as the 1-D/2-D model in the remainder of this thesis. It was formulated by borrowing and extending ideas put forward by Bernier and Baliga (1992b) in the context of single-phase closed-loop thermosyphons operating with Newtonian liquids. The theoretical considerations and aspects on which the proposed 1-D/2-D model is based are reviewed and discussed in this chapter.

A brief review of multiphase flows and related modeling issues is presented first in this chapter. Next, expressions for the momentum and thermal Stokes numbers of the particle are derived, along with an expression for the terminal settling velocity of the particle. The values of these Stokes numbers demonstrate that the MCPCM slurries used in this work can be considered as homogeneous fluids and modeled accordingly. Next, brief overviews of the closed-loop thermosyphon and the proposed 1-D/2-D model are presented. Following that, the assumptions, governing equations, and boundary conditions for the two-dimensional axisymmetric fluid flow and heat transfer phenomena in the vertical heating and cooling sections of the closed-loop thermosyphon are presented and discussed. Then, the quasi-one-dimensional models of fluid flow and heat transfer in the remaining portions of the closed-loop thermosyphon are presented and discussed. An overall momentum balance, which allows the calculation of the average velocity of the working fluid in the loop, is subsequently derived. The definition of a modified bulk temperature, originally proposed by Scott (2006), is then presented. It overcomes shortcomings of the standard definition of bulk temperature [Incropera and DeWitt

(2002)] when strong variations of the fluid specific heat are encountered. Finally, using a flow-regime map [Metais and Eckert (1964)], it is shown that the flows of distilled water (and by inference, also the flows of the MCPCM slurries) within the heating section, cooling section, and the other portions of the closed-loop thermosyphon are all laminar.

2.1 Background

As is suggested by its name, a *multiphase flow* involves more than a single phase. Traditionally, such flows have been denoted as either *disperse flows* or *separated flows* [Brennen (2005)]. *Separated flows* are composed of two (or more) different, non-mingling, continuous fluid phases separated by interfaces. *Disperse flows* consist of a disperse, non-continuous, phase (either a solid, liquid, or gas) disseminated in a connected volume of a continuous phase. *Disperse flows* of solid-particles in a fluid are further characterized as *dilute* or *dense*. In the first category, the particle motion is mainly governed by the fluid forces acting on it; whereas in *dense* flows, it is dominated by inter-particle collisions [Crowe et al. (1998); Crowe (2006)].

As was mentioned previously, the slurries considered in this work consist of MCPCM particles suspended in distilled water. The mean effective diameter of the MCPCM particles was 2.5 μm, and the mass concentration of these MCPCM particles was less than or equal to 17.5%. Thus, the flows of interest in this research belong to the class of *disperse two-phase flows* [Brennen (2005)]. Modeling approaches for such flows are generally classified as follows: 1) complete local descriptions or exact formulations; and 2) simplified mathematical models involving different types of averaging procedures and empirical data inputs. When complete local descriptions are used, the governing equations for each phase, along with suitable conditions imposed at the interfaces between the phases, are solved in full detail, to obtain complete descriptions of the velocity and temperature fields. Such models require a tremendous amount of computational resources and are essentially impractical for simulations of most multiphase flows encountered in engineering applications. Since this observation is expected to apply for the foreseeable future, simplified mathematical models remain the sole viable approach for simulations of disperse two-phase flows.

Simplified mathematical models used in practical simulations of dispersed two-phase flows generally belong to three categories. The first one includes *trajectory* or *Lagrangian-Eulerian* models, in which the motion and temperature of the particles are explicitly tracked and calculated using empirical correlations for drag, lift, history or Basset force, added-mass force, and heat transfer. The conveying fluid is modeled via appropriately averaged forms of the governing equations, and the interactions between the constituents are brought in via suitable coupling terms. The second category comprises *two-fluid* or *Eulerian-Eulerian* models, where a set of suitably averaged governing equations is invoked and solved for each of the phases, which are considered as interpenetrating (or superposed) continua. Mass, momentum, and energy exchanges between these two continua are described using empirical correlations or models. Lastly, if the velocity and temperature differences between the disperse and conveying phases are negligibly small, a *homogenous model* can be used. In such an approach, the governing equations are reduced to forms similar to those of the equations that govern single-phase flow and heat transfer, but in which *effective* thermophysical properties pertaining to the homogeneous mixture of the phases are used. Of these three categories of model, the homogeneous model is the most straightforward to implement, and it is also the most cost-effective from a computational standpoint. Some important publications that provide detailed discussions of these models were mentioned in the first paragraph of Section 1.4.5, so they will not be repeated here. It will be demonstrated in the next section that the flows of the MCPCM slurries considered in this work can be treated as homogeneous and modeled as such.

In the proposed 1-D/2-D models of the fluid flow and heat transfer phenomena in the aforementioned closed-loop thermosyphon operating with MCPCM slurries, an axisymmetric two-dimensional homogeneous model is used to describe these phenomena in the vertical heating and cooling sections (details are provided in Section 2.4). In this homogeneous model, the effective thermophysical properties of the MCPCM slurries are prescribed as functions of temperature, MCPCM mass concentration, and state of the PCM, via empirical correlations. The experiments which were undertaken to obtain the data that were needed to formulate the aforementioned empirical correlations for the thermophysical properties of the MCPCM slurries, and these correlations themselves, are presented and discussed in Chapter 3.

One of the key requirements in this research work was the formulation of a suitable model that accounts for the latent heat of fusion (or solidification) of the MCPCM particles when they undergo solid-liquid or liquid-solid phase-change processes in the heating and cooling sections of the closed-loop thermosyphon, respectively. In some of the past studies, this requirement was met by locally solving a solid-liquid phase-change problem (Stefan problem) for spherical particles and including the resulting volumetric rate of heat absorption or release via a source term in the energy equation [Charunyakorn et al. (1991); Zhang and Faghri (1995)]. In other investigations [Ho (2004)], an enthalpy model was used. This model incorporates the latent heat of fusion of the MCPCMs in the definition of the specific enthalpy. In another approach, the solid-liquid phase-change effects of the MCPCM particles are taken into account using an effective specific heat function [Roy and Avanic (2001); Hu and Zhang (2002); Scott (2006)]. This last approach can be formulated quite reliably by basing the effective specific heat on accurate experimental data, and it is also more convenient to implement than the other two approaches mentioned above, so it was adopted in this work.

An effective specific heat function for the MCPCM slurries of interest ($c_{p,s}$) can be determined empirically, using differential scanning calorimetry (DSC) experiments to determine the MCPCM contribution ($c_{p,MCPCM}$), for example. A function that expresses the variation of this effective specific heat with temperature can be designed such that the integration of its increase above the sensible heating value, over the phase-change temperature range, accurately corresponds to the latent heat of fusion. Function shapes that have been used to account for such latent-heat effects include the top-hat (rectangular), left triangle, right triangle, and sine functions. In some early studies, the actual shape of the $c_{p,s}$ function was considered to be relatively inconsequential, as long as the latent-heat value was accounted for correctly. However, Hu and Zhang (2002) have recommended that the $c_{p,s}$ curve should be reproduced as accurately as possible. It should also be noted that when the MCPCM particles are quite small (the mean effective diameter of the MCPCM particles used in this work was 2.5 μm), spatial variations of temperature within the capsule crust and the PCM are negligibly small, even (or especially) during the phase-change process.

In this work, the specific heat of the MCPCMs, $c_{p,MCPCM}$, was measured experimentally by performing differential scanning calorimeter (DSC) investigations, and the data were then curve-fitted as a function of temperature and state (solid or liquid) of the PCM (for both heating and cooling processes). The effective specific heat of the slurries, $c_{p,s}$, which includes contributions from the specific heats of the carrier fluid (distilled water) and MCPCM, was then calculated using the MCPCM mass concentration ϕ as an input. Such an approach was successfully used by Scott (2006) in his numerical simulations of similar MCPCM slurry flows. The experimental investigation which was conducted to determine the effective specific heat of the slurries is fully described in Chapter 3, along with the results.

2.2 Momentum and Thermal Response Times, Stokes Numbers, and Terminal Settling Velocity of the MCPCM particles

In this section, concise derivations of the momentum and thermal response times of the MCPCM particles are presented. These derivations are based on similar derivations performed in the works of Crowe et al. (1998), Fan and Zhu (1998), Crowe (2006), and Scott (2006). It is also shown that the corresponding Stokes numbers, which are the ratios of the response times of the particle to that of the fluid flow, are much smaller than one, thereby demonstrating that it is valid to use a homogeneous model for simulations of the fluid flow and heat transfer phenomena in the closed-loop thermosyphon operated with the MCPCM slurries in this work.

Considering linear motion of a single spherical particle of density ρ_p and diameter d_p, moving at a velocity w_p in a liquid of density ρ_l, dynamic viscosity μ_l, and having a uniform far-field velocity w_l, and assuming that drag is the dominant force on this particle, the following equation can be obtained using Newton's second law:

$$\rho_p \frac{\pi d_p^3}{6}\frac{dw_p}{dt} = C_D \frac{1}{2}\rho_l \left|w_l - w_p\right|\left(w_l - w_p\right)\frac{\pi d_p^2}{4} \tag{2.1}$$

In this equation, C_D is the drag coefficient. If a Reynolds number based on the particle diameter and the relative velocity between the particle and the fluid is introduced in Eq. (2.1), it can be rewritten as follows:

$$\frac{dw_p}{dt} = \frac{18\mu_l}{\rho_p d_p^2} C_D \frac{Re_d}{24}\left(w_l - w_p\right) \quad \text{where} \quad Re_d = \frac{\rho_l d_p \left|w_l - w_p\right|}{\mu_l} \tag{2.2}$$

For a spherical particle in Stokes flow ($Re_d < 1$), the drag coefficient is given by $C_D = 24 / Re_d$ [White (1991)]. Thus, Eq. (2.2) can be recast as follows:

$$\frac{dw_p}{dt} = \frac{1}{\tau_{w_p}}\left(w_l - w_p\right) \quad \text{where} \quad \tau_{w_p} = \frac{\rho_p d_p^2}{18\mu_l} \tag{2.3}$$

In the previous equation, τ_{w_p} denotes the momentum response time of the particle. If the particle is initially at rest and then entrained by the surrounding liquid flowing at a constant velocity w_l, the time-evolution of the particle velocity, w_p, is given by:

$$w_p = w_l\left(1 - e^{-t/\tau_{w_p}}\right) \tag{2.4}$$

Based on this solution, the momentum response time can be interpreted as the time needed for the velocity of the particle to start from zero and reach a value of approximately 63% of the surrounding constant velocity of the liquid.

The momentum Stokes number of the particle, St_{w_p}, is defined as the particle momentum response time divided by a characteristic time scale of the fluid flow. To obtain the upper limit of St_{w_p}, the characteristic time scale of the fluid flow, τ_f, is set equal to its lower limit. In this work, this lower limit of τ_f is taken as the pipe internal diameter, D_i, divided by the maximum fluid velocity, $w_{l,max}$: $\tau_f = D_i / w_{l,max}$ [Crowe et al. (1998), Crowe (2006)]. Thus, the upper limit of St_{w_p} is given by:

$$St_{w_p} = \frac{\tau_{w_p}}{\tau_f} = \frac{\tau_{w_p} w_{l,max}}{D_i} \tag{2.5}$$

When this upper limit of St_{w_p} is much smaller than one, the particle attains the velocity of the surrounding liquid very quickly, and for all practical purposes, the velocity of the particle can be considered to be the same as that of the surrounding fluid.

The *thermal* response time of a spherical particle and its corresponding Stokes number are derived in the context of the following assumptions: 1) the particle behaves as a lumped system (the spatial variation of temperature within it is negligible); 2) it does not undergo mass transfer or chemical reactions with the surrounding fluid; and 3) phase-change processes, if they occur, are entirely contained with the particle (as is the case with the MCPCM particle considered in this work), and the related latent-heat effects can be modeled using an effective specific heat. The following notation is used: the particle diameter is d_p, mass density is ρ_p, specific heat at constant pressure is $c_{p,p}$, instantaneous temperature is T_p, and thermal conductivity is k_p. The particle is surrounded by a liquid that has a uniform far-field temperature, T_l, and the overall heat transfer coefficient on the outer surface of the particle is *h*. In the context of the above-mentioned assumptions and notation, an energy balance on the particle yields:

$$\rho_p \frac{1}{6} \pi d_p^3 c_{p,p} \frac{dT_p}{dt} = h \pi d_p^2 \left(T_l - T_p \right) \tag{2.6}$$

Inserting a Nusselt number, $Nu_d = hd_p / k_l$, in the previous equation, it can be recast as:

$$\frac{dT_p}{dt} = \frac{6 k_l Nu_d}{d_p^2 \rho_p c_{p,p}} \left(T_l - T_p \right) \tag{2.7}$$

In this case, effects of natural convection about the particle are assumed to be negligible. Furthermore, for small values of the momentum Stokes number, the relative velocity between the particle and the liquid is negligibly small, so the particle Reynolds number is essentially zero. For such cases, the value of the Nusselt number approaches $Nu_d = 2$ [Incropera and DeWitt (2002)], and Eq. 2.7 takes on the following form:

$$\frac{dT_p}{dt} = \frac{12k_l}{d_p^2 \rho_p c_{p,p}} \left(T_l - T_p \right) \tag{2.8}$$

This equation can be recast as follows:

$$\frac{dT_p}{dt} = \frac{1}{\tau_{T_p}} \left(T_l - T_p \right) \qquad \text{where} \quad \tau_{T_p} = \frac{d_p^2 \rho_p c_{p,p}}{12k_l} \tag{2.9}$$

In Eq. (2.9), τ_{T_p} denotes the thermal response time of the particle. It corresponds to the time required for the particle-to-liquid temperature difference $(T_l - T_p)$ to decay to approximately 37% of its initial value.

The thermal Stokes number of the particle is defined as its thermal response time divided by a characteristic thermal time scale of the fluid flow. Here again, to obtain the upper limit of the thermal Stokes number, the smallest value of the thermal response time of the flow, τ_f, is chosen. Here, τ_f is again taken as $D_i / w_{l,max}$. This response time also applies to transport by advection (overall fluid motion), and for the MCPCM slurries considered in this work, it is much smaller than the response time of the conduction heat transfer process. The upper limit of the thermal Stokes number of the particle can therefore be expressed as follows:

$$St_{T_p} = \frac{\tau_{T_p}}{\tau_f} = \frac{\tau_{T_p} w_{l,max}}{D_i} \tag{2.10}$$

If the value of St_{T_p} is much smaller than one, then the temperature of the particle very rapidly matches the temperature of the surrounding liquid, and for all practical purposes, these temperatures may be assumed to be locally the same.

The terminal settling velocity of a single spherical particle (relative to the surrounding fluid) can be obtained using the following relation [Maude and Whitmore (1958); Naterer (2003)]:

$$w_{p,set,single} = \sqrt{\frac{4}{3}\frac{d_p}{C_D}\frac{\left(\rho_l - \rho_p\right)}{\rho_l}g} \quad \text{where} \quad C_D = \frac{24}{Re_{d,single}} \tag{2.11}$$

In this equation, the Reynolds number is based on the particle diameter and the settling velocity (relative to the surrounding fluid) of a single particle, as follows: $Re_{d,single} = \rho_l d_p w_{p,set,single} / \mu_l$. The maximum value of $Re_{d,single}$ of the MCPCM particles used in the present work is much smaller than one, thus Stokes flow is assumed to prevail around these particles. Following the work of Maude and Whitmore (1958), a correction to the terminal settling velocity of a single particle is applied, to obtain the terminal setting velocity of particles within a suspension with particle volume concentration φ:

$$w_{p,set} = w_{p,set,single}\left(1-\varphi\right)^{\beta} \tag{2.12}$$

For $Re_{d,single}$ values lower than 1, the parameter β in Eq. (2.12) is approximately equal to 5 [Maude and Whitmore (1958)]. It will be shown that the terminal settling velocity of the MCPCM particles used in this work is much smaller than the average velocities of the slurries in the closed-loop thermosyphon. Thus, the rate of separation or segregation of the MCPCM particles away from the conveying liquid during the operation of the closed-loop thermosyphon was very small, and it was not an issue in the experiments undertaken in this work. The very low particle terminal settling velocity also ensured that loop-wide particle migration did not occur during the fill-up and start-up phases (when the slurry is accelerated from rest) of the experiments with the closed-loop thermosyphon.

In this work, the values of the momentum and thermal response times, the corresponding Stokes numbers, and the terminal settling velocity of the MCPCM particles were computed with the following properties and parameters:

Diameter of MCPCM particles: 0.5 μm $\leq d_p \leq$ 12.5 μm (mean value: 2.5 μm)

MCPCM mass concentration: 7.5% $\leq \phi \leq$ 17.5%

MCPCM volume concentration: 8% $\leq \varphi \leq$ 21%

Mass density of MCPCM particles: 830 kg/m^3 $\leq \rho_{MCPCM} \leq$ 970 kg/m^3

Mass density of liquid water: $\rho_{H_2O} \approx$ 998 kg/m^3

MCPCM effective specific heat: 2000 J/kg°C $\leq c_{p,MCPCM} \leq$ 130,000 J/kg °C

Specific heat of liquid water: $c_{p,H_2O} \approx$ 4190 J/kg °C

Thermal conductivity of liquid water: $k_{H_2O} \approx$ 0.6 W/m °C

Dynamic viscosity of water: 5 x 10^{-4} kg/m s < μ_{H_2O} < 1.5 x 10^{-3} kg/m s

Maximum velocity observed in the closed-loop thermosyphon: $w_{l,max}$ = 0.013 m/s (when it was operated with the MCPCM slurries)

Inside diameter of the closed-loop thermosyphon pipe: D_i = 0.01021 m

For the above-mentioned properties and parameters, the upper limits of the momentum and thermal response times, and their respective Stokes numbers, have the following values: τ_{w_p} = 1.68 x 10^{-5} s, St_{w_p} = 2.14 x 10^{-5}, τ_{T_p} = 2.74 x 10^{-3} s, and St_{T_p} = 3.48 x 10^{-3}. Thus, for all practical purposes, there is no significant local velocity or temperature differences between the MCPCM particles and the surrounding conveying liquid (distilled water), even when the MCPCM undergo phase-change (maximum value of $c_{p,MCPCM}$ = 130,000 J/kg °C, during the freezing process). The terminal settling velocity (with respect to the surrounding liquid) of the largest MCPCM particles (d_p = 12.5 μm) is 1.78 x 10^{-5} m/s (for this case, $Re_{d,single}$ = 7.14 x 10^{-4} << 1). For MCPCM particles having an effective diameter of 2.5 μm (mean value), the terminal settling velocity (with respect to the surrounding liquid) is 7.14 x 10^{-7} m/s (for this case, $Re_{d,single}$ = 5.71 x 10^{-6} << 1). These values of the terminal settling velocity represent the upper-limits, as other effects, such as mutual repulsion forces between the MCPCM particles, diminish these values. It should also be noted that experimental observations of stationary MCPCM slurries having mass concentrations ranging between 7.5% and 17.5% (in these experiments, each slurry was first mixed gently but thoroughly, then filled in identical test tubes, which were supported vertically in a special stand, and then left undisturbed), revealed that no discernable particle segregation occurred over a time-period of 2 days. With these results and observations at hand, the homogenous model was deemed appropriate for simulations of the MCPCM slurries used in this work.

2.3 Overviews of the Closed-Loop Thermosyphon and the Proposed 1-D/2-D Model

The closed-loop thermosyphon used in this investigation is schematically illustrated in Figure 2.1. The following details of this thermosyphon are described and discussed in Chapter 4: the dimensions of its various sections; its design and construction; the related instrumentation; the procedure to determine the overall heat transfer coefficient for calculations of the rates of heat loss to (or gain from) the ambient environment; the procedure to determine the average velocity of the working fluid; and the procedure to run the thermosyphon with distilled water and the MCPCM slurries as the working fluids. Here, to set the stage for the presentation and discussion of the 1-D/2-D model, it is important to note the following main features of the closed-loop thermosyphon illustrated in Figure 2.1: the closed-loop consists of two vertical straight pipes connected together by two semi-circular sections of pipes, of mean bend radius R_{bend} (strictly, each of these sections consists of two 90-degree circular bends, connected by a short straight piece of a T-junction made of the same pipe); all pipes are of circular cross-section, with the same inside radius, r_i, and inside diameter, D_i; the left vertical pipe includes the heating section, which has an active heating length of L_h, and pre- and post-heating sections of lengths $L_{h,pre}$ and $L_{h,post}$, respectively; the right vertical pipe includes the cooling section, which has an active cooling length of L_c, and pre- and post-cooling sections of lengths $L_{c,pre}$ and $L_{c,post}$, respectively.

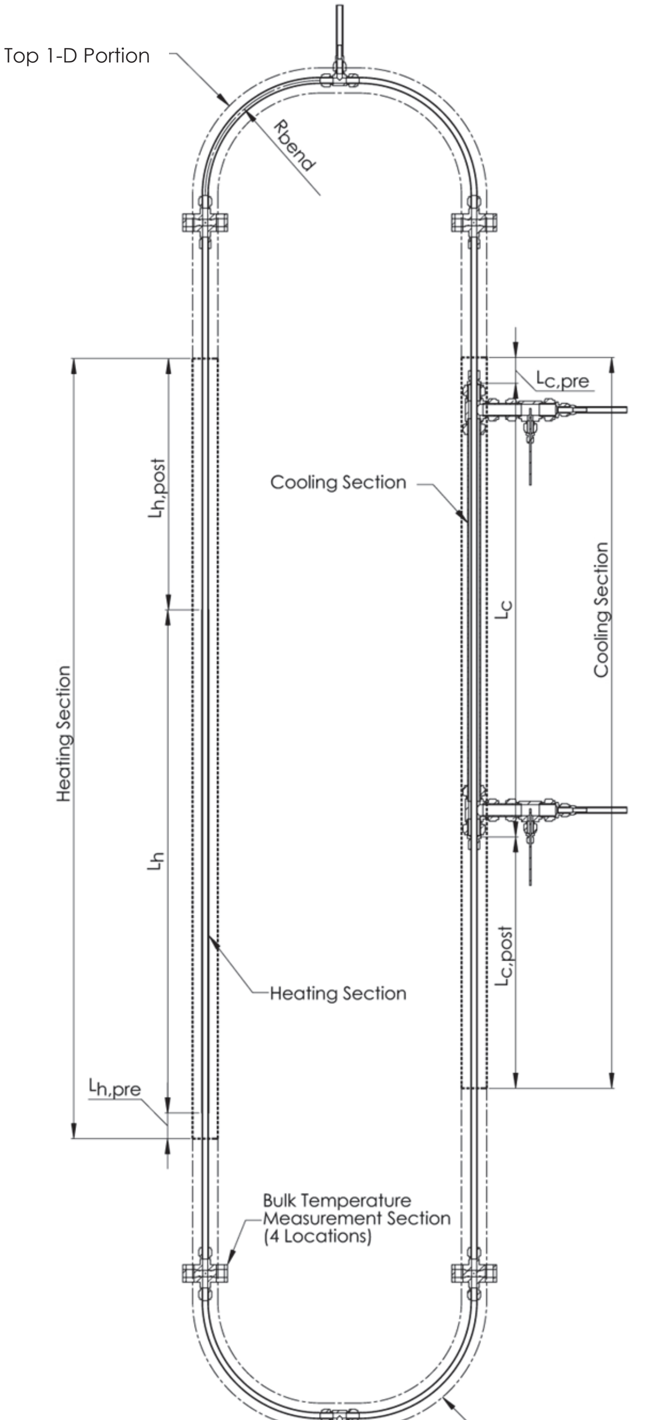

Figure 2.1: Schematic representation of the vertical closed-loop thermosyphon.

The pre- and post-heating lengths ($L_{h,pre}$ and $L_{h,post}$) of the overall heating section were well insulated and not actively heated. They were included in the heating section for the following reasons: 1) the local buoyancy effects in the active heating section (of length L_h) could also influence the flow to some extent upstream of the entrance to this section, but they did not extend over the full length of the pre-heating section (as $L_{h,pre}$ was made sufficiently long), so fully-developed flow conditions (without local buoyancy effects) prevailed at the entrance to the pre-heating section; and 2) the extent of the post-heating section ($L_{h,post}$) was sufficiently long to allow the velocity and temperature profiles leaving it to achieve essentially fully-developed conditions (without local buoyancy effects). Similarly, the pre- and post-cooling lengths ($L_{c,pre}$ and $L_{c,post}$) were not actively cooled, well insulated, and sufficiently long to serve purposes akin to those of the aforementioned pre- and post-heating lengths. These features of the heating and cooling sections allowed convenient formulation of the proposed 1-D/2-D model of the closed-loop thermosyphon, and reliable use of the experimental results as checks on the related numerical predictions. The whole closed-loop thermosyphon was very well insulted on its outer surfaces, to minimize rates of heat loss (or gain) from the ambient environment.

As was mentioned earlier, the closed-loop thermosyphon shown in Figure 2.1 was operated with MCPCM slurries. The experimental investigation and the complementary numerical simulations were conducted with slurries of mass concentration 0% (pure distilled water), 7.5%, 10%, 12.5%, 15%, and 17.5%. The effective thermophysical properties of the MCPCM and the slurries used in this work were briefly described in Chapter 1 and also in the previous section of this chapter. Detailed descriptions of these effective thermophysical properties (including the rheological behavior and properties of the slurries), the special experiments that were undertaken to determine them and their results, the correlations which were fitted to these effective-property data, the various heating (with melting of the PCM) and cooling (with freezing of the PCM) processes, and supercooling effects and the related hysteresis in the effective-property data (which are taken into account in the proposed 1-D/2-D model) are all presented and discussed in Chapter 3.

The proposed 1-D/2-D model of the closed-loop thermosyphon illustrated in Figure 2.1 involves the following features: 1) two-dimensional axisymmetric models of the fluid flow and heat transfer in the vertical heating and cooling sections, including local buoyancy effects; 2) quasi-one-dimensional models of the fluid flow and heat transfer in the remaining portions of the loop; and 3) iterative coupling of the solutions of the aforementioned axisymmetric two-dimensional and quasi-one-dimensional models. In the simulations of the two-dimensional axisymmetric fluid flow and heat transfer in the vertical heating and cooling sections of the closed-loop thermosyphon operating with the MCPCM slurries as the working fluid, homogeneous models are used (the validity of this approach was discussed in the previous section), with suitable empirical correlations for the effective thermophysical properties of the slurries, and appropriate accounting of non-Newtonian behavior and supercooling (related discussions are provided in Chapter 3).

2.4 Axisymmetric, Two-Dimensional, Homogeneous Models of Fluid Flow and Heat Transfer in the Vertical Heating and Cooling Sections

In the closed-loop thermosyphon shown in Figure 2.1, the fluid flow and heat transfer phenomena in the vertical heating and cooling sections are significantly influenced by buoyancy effects. Detailed axisymmetric, two-dimensional, models of these phenomena are presented in this section. Again, when MCPCM slurries are the working fluid in this thermosyphon, a homogeneous model is used (the applicability of this model to the phenomena of interest was discussed in Section 2.2). Schematic illustrations of the vertical heating and cooling sections (both rotated by 90 degrees in the clockwise direction for convenience), along with inserts to show their locations in the closed-loop thermosyphon, are presented in Figs. 2.2 and 2.3, respectively.

To set the stage for the presentations in this section, the following aspects of the complementary experimental investigation of the closed-loop thermosyphon are reiterated in this paragraph. In the heating section, a Teflon-insulated nichrome wire, tightly wound around the outer wall of the pipe, was electrically heated to provide an essentially uniform wall-heat-flux boundary condition over an active heating length of L_h (see Fig. 2.1). In the cooling section, a portion of the pipe of length L_c was maintained at an essentially constant temperature T_{cool}, using a concentric annular heat exchanger and water (as the coolant) supplied from a constant-temperature bath. The outer surfaces of the entire heating and cooling sections of the closed-loop thermosyphon were very well insulated to minimize heat losses to (or gains from) the ambient environment. Full details of the closed-loop thermosyphon, the related instrumentation, and procedures used in the experimental investigation are presented and discussed in Chapter 4.

In the detailed 2-D model of the heating section, pre-heating and post-heating sections of lengths $L_{h,pre}$ and $L_{h,post}$, respectively, were included in the calculation domain (see Fig. 2.2), for reasons that were discussed in the previous section (these pre- and post-heating sections were not actively heated). Similarly, in the detailed 2-D model of the cooling section, pre- and post-cooling sections of lengths $L_{c,pre}$ and $L_{c,post}$, respectively, were included in the calculation domain (see Fig. 2.3), again for reasons that were discussed in the previous section (these pre- and post-cooling sections were not actively cooled). In the remaining portions of the left and right straight vertical sections, laminar fully developed velocity and temperature profiles were assumed to prevail.

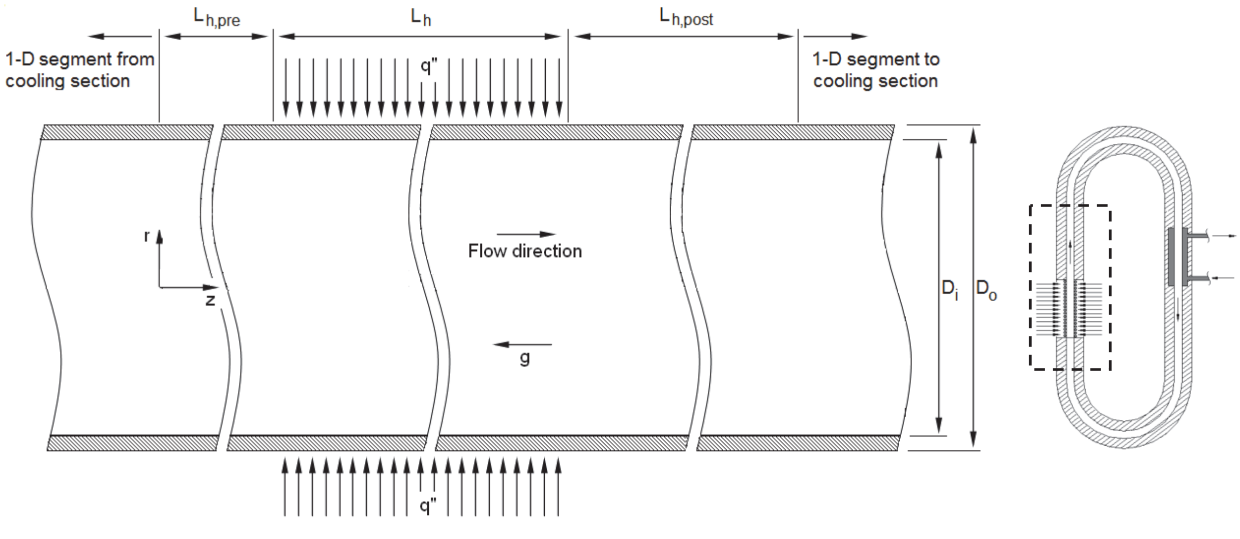

Figure 2.2: Schematic representation of the details of the vertical heating section (rotated 90 degrees clockwise). In the adjoining insert, the location of this section in the closed-loop thermosyphon is indicated by the dotted lines.

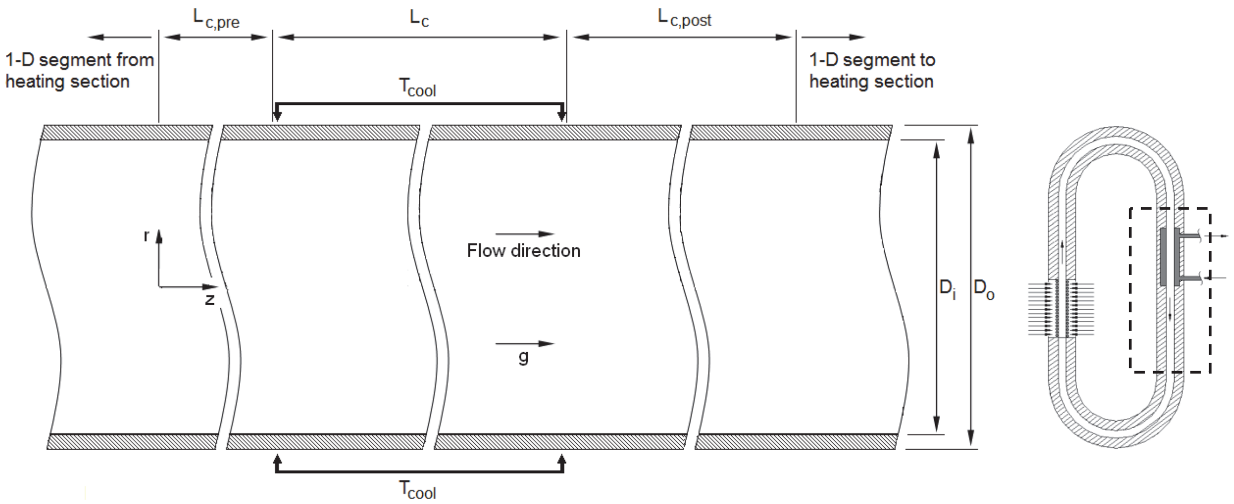

Figure 2.3: Schematic representation of the details of the vertical cooling section (rotated 90 degrees counterclockwise). In the adjoining insert, the location of this section in the closed-loop thermosyphon is indicated by the dotted lines.

The assumptions, governing equations, and boundary conditions used in the proposed mathematical model are presented in the following subsections.

2.4.1 Assumptions

The following assumptions were invoked in the detailed models of the fluid flow and heat transfer phenomena in the vertical heating and cooling sections of the closed-loop thermosyphon.

1. A homogeneous model is applicable when the MCPCM slurries are used as the working fluid (discussions to justify this assumption were presented in Section 2.2).
2. Steady-state, axisymmetric, two-dimensional conditions prevail. In the remaining sections of the closed-loop thermosyphon, fully-developed fluid flow and heat transfer conditions prevail.
3. The prevailing conditions are analogous to those of laminar mixed convection. The validity of this assumption is established in Section 2.8, using a flow regime map provided by Metais and Eckert (1964).

4. Viscous dissipation and the pressure work (Dp/Dt) terms in the energy equation are negligibly small, as the maximum Eckert number was much smaller than one (Ec << 1) in all experiments undertaken in this work.
5. The MCPCM slurries used in this work (values of MCPCM mass concentration in the range $7.5\% \leq \phi \leq 17.5\%$) are characterized by a slight shear-thinning behavior (related details are given Section 3.6). This shear-thinning behaviour can be mathematically described using a power-law model, analogous to the Ostwald and de Waele model [Bird et al. (1987)].
6. The effective thermophysical properties of the MCPCM slurries, such as the density, thermal conductivity, dynamic viscosity, and specific heat, are functions of the local temperature, the MCPCM mass concentration, and the local rate of strain (for the dynamic viscosity only). However, these effective properties are essentially independent of pressure, as the two constituents of the slurries (the MCPCM particles and the distilled water) are essentially incompressible substances in the range of pressures encountered in the closed-loop thermosyphon.
7. The first part of the Boussinesq approximation applies, meaning that the density is considered constant (at a suitably-averaged value, $\rho_{s,ref}$) in all terms of the governing equations, except in the buoyancy terms.
8. The effects of the MCPCM-free layer along the inner surface of the pipe wall are negligible [Cox and Mason (1971), Crowe et al. (1998), Crowe (2006)]. The thickness of this MCPCM-free layer is expected to be of the order of the mean effective diameter of the MCPCM particles (2.5 μm in this work), and this value is much smaller than the inner diameter of the pipe, $D_i = 0.01021$ m. This assumption is supported by the very good agreement observed between the numerical predictions and the experimental results (related details are presented and discussed in Chapter 6).

9. The effective properties of the MCPCM slurries do no drift over time nor are they altered by successive thermal cycling while flowing in the closed-loop thermosyphon.

10. A uniform-heat-flux condition applies at the outer surface ($D = D_o$) of the active heating length L_h (see Fig. 2.2). Most of this imposed heat flux travels radially inwards through the pipe wall and reaches the working fluid. The remaining portion of this heat flux is lost to the environment. These heat losses are assessed in the proposed model using an overall heat transfer coefficient U', as explained later in this section.

11. In the active cooling section (of length L_c, as shown in Fig. 2.3) the inner surface of the tube wall is at the same uniform temperature as the outer surface (T_{cool}), as the radial thermal conduction resistance of the pipe wall is much smaller than the convective resistance of the slurry flow.

12. The heat losses to (or gains from) the ambient environment *per unit length* of the tube can be evaluated using a uniform overall heat transfer coefficient U' [W/m°C], which was determined empirically (see Chapter 4).

13. Melting of the encapsulated PCM is considered to be completed when the temperature of the MCPCM slurry equals 32.5°C. If the slurry leaves the active heating section of the closed-loop thermosyphon at 32.5°C or higher temperature, then during the subsequent cooling processes, the liquid PCM in the MCPCM undergoes supercooling, and lowering of the temperature to a value of 18.1°C is needed in the active cooling section for freezing of the PCM to be initiated. Under these conditions, there is hysteresis in the variation with temperature of the effective density, thermal conductivity, and specific heat of the MCPCM slurry, and they are taken into account in the proposed 1-D/2-D model using suitable empirical correlations (full details are presented in Chapter 3).

14. In the active heating section of the closed-loop thermosyphon, if the temperature of the MCPCM slurry does not exceed 28.0°C, then in the subsequent cooling processes, no supercooling of the liquid PCM occurs. Under these conditions, there is no hysteresis in the variation with temperature of the effective properties of the MCPCM slurries during the heating (with partial melting) and cooling (with freezing) processes in the closed-loop thermosyphon.

15. Segregation or settling of the MCPCM particles does not occur in the closed-loop thermosyphon (over the duration of the experiments and the complementary simulations using the 1-D/2-D model). Consequently, the MCPCM mass concentration remains uniform and constant throughout the closed-loop thermosyphon during each run. Related discussions justifying this assumption were presented in Section 2.2.

16. Axial heat conduction in the pipe wall and in the surrounding insulation layer is considered negligible compared to radial conduction. To put this assumption into context, it is useful to note here that the length of the active heating section is 1.00 m, the length of the active cooling section is 0.902 m, the thickness of the pipe wall is 0.00124 m, and the thickness of the Armaflex insulation is 0.044 m. Also, the thermal conductivities of the stainless steel pipe wall, k_w, and the Armaflex insulation, k_{ins}, are assumed to be essentially constant at the following values in the temperature range of interest: k_w= 14.9 W/m°C and k_{ins}= 0.04 W/m°C. Additional details are given in Chapter 4.

It should be noted that curvature effects and related additional head losses occur in the semicircular (180-degree) pipe bends that join the vertical heating and cooling sections of the closed-loop thermosyphon (see Fig. 2.1). These additional head losses can be taken into account using empirical correlations. In the proposed 1-D/2-D model, these head losses are approximated using a correlation proposed by Gupta and Mishra (1975), which prescribes the relative increase of the local friction factor (with respect to fully-developed flow in a straight pipe). This correlation is applicable to Newtonian fluids and also non-Newtonian fluids whose effective viscosity can be mathematically described using a power-law model.

2.4.2 Governing Equations

The equations of a homogeneous mathematical model that governs the steady, axisymmetric, two-dimensional, laminar fluid flow and heat transfer phenomena in the vertical heating and cooling sections of the closed-loop thermosyphon (see Fig. 2.1) are presented in this subsection. These equations can be presented in a generalized manner that makes them applicable to both the distilled water (a Newtonian fluid) and the MCPCM slurries (which behave as non-Newtonian fluids with shear-thinning behavior that can be mathematically described by a power-law model), with the appropriate expressions for the effective dynamic viscosity and the other effective properties [Hsu and Patankar (1982), Bird et al. (1987), Crowe et al. (1998), Brennen (2005), Crowe (2006)]. Following this approach and invoking the assumptions stated in Subsection 2.4.1, and with respect to the cylindrical coordinate systems shown in Figs. 2.2 and 2.3 (with g_z denoting the component of the gravitational acceleration vector in the positive z direction; and with $P = p - \rho_{s,ref} g_z z$ denoting the reduced pressure), the governing equations can be cast in the following forms:

Continuity:

$$\frac{\partial}{\partial z}\left(\rho_{s,ref} w\right) + \frac{1}{r}\frac{\partial}{\partial r}\left(r \rho_{s,ref} v\right) = 0 \qquad (2.13)$$

z-Momentum:

$$\begin{aligned} \frac{\partial}{\partial z}\left(\rho_{s,ref} ww\right) + \frac{1}{r}\frac{\partial}{\partial r}\left(r \rho_{s,ref} vw\right) = &-\frac{\partial P}{\partial z} + \frac{\partial}{\partial z}\left(\mu_s \frac{\partial w}{\partial z}\right) + \frac{1}{r}\frac{\partial}{\partial r}\left(r \mu_s \frac{\partial w}{\partial r}\right) \\ &+ \left(\rho_s - \rho_{s,ref}\right) g_z + \frac{\partial \mu_s}{\partial z}\frac{\partial w}{\partial z} + \frac{\partial \mu_s}{\partial r}\frac{\partial v}{\partial z} \end{aligned} \qquad (2.14)$$

r-Momentum:

$$\frac{\partial}{\partial z}\left(\rho_{s,ref}wv\right)+\frac{1}{r}\frac{\partial}{\partial r}\left(r\rho_{s,ref}vv\right)=-\frac{\partial P}{\partial r}+\frac{\partial}{\partial z}\left(\mu_s\frac{\partial v}{\partial z}\right)+\frac{1}{r}\frac{\partial}{\partial r}\left(r\mu_s\frac{\partial v}{\partial r}\right)$$
$$-\frac{\mu_s v}{r^2}+\frac{\partial \mu_s}{\partial z}\frac{\partial w}{\partial r}+\frac{\partial \mu_s}{\partial r}\frac{\partial v}{\partial r} \qquad (2.15)$$

Energy :

$$\frac{\partial}{\partial z}\left(\rho_{s,ref}wi_s\right)+\frac{1}{r}\frac{\partial}{\partial r}\left(r\rho_{s,ref}vi_s\right)=\frac{\partial}{\partial z}\left(k_s\frac{\partial T}{\partial z}\right)+\frac{1}{r}\frac{\partial}{\partial r}\left(rk_s\frac{\partial T}{\partial r}\right) \qquad (2.16)$$

In the above-mentioned equations, z and r represent the axial (streamwise) and radial coordinates, respectively; w and v are, respectively, the axial and radial velocity components; p is the static pressure and P is the reduced pressure; i_s is the effective specific enthalpy of the working fluid (slurry or distilled water); and ρ_s, μ_s and k_s are the effective density, effective dynamic viscosity, and effective thermal conductivity of the working fluid (slurry or distilled water), respectively. Again, g_z is the component of the gravitational acceleration vector in the positive z direction. With respect to the coordinate systems shown in Figures 2.2 and 2.3, the value of g_z can be either negative (in the vertical heating section) or positive (in the vertical cooling section); in this work, its magnitude was set equal to $|g_z| = 9.81\,\mathrm{m/s^2}$. Lastly, $\rho_{s,ref}$ represents a suitable reference value of the effective density of the slurry or distilled water, here set equal to the mean effective density of the working fluid in the closed-loop thermosyphon.

The effective dynamic viscosity of the working fluid is prescribed via an effective relative viscosity, η_s, as follows:

$$\eta_s=\frac{\mu_s}{\mu_{H_2O}}=\frac{K[(1/2)D_{ij}:D_{ij}]^{\{(n-1)/2\}}}{\mu_{H_2O}}=m\,\dot{\gamma}^{(n-1)} \quad \text{with}$$
$$m=\frac{K}{\mu_{H_2O}} \quad \text{and} \qquad (2.17)$$
$$\dot{\gamma}=[(1/2)D_{ij}:D_{ij}]^{1/2}=\sqrt{\frac{1}{2}\left[2\left(\frac{\partial v}{\partial z}+\frac{\partial w}{\partial r}\right)^2+4\left(\frac{v}{r}\right)^2+4\left(\frac{\partial v}{\partial r}\right)^2+4\left(\frac{\partial w}{\partial z}\right)^2\right]}$$

In this equation, η_s is the effective relative viscosity of the working fluid (effective dynamic viscosity, μ_s, normalized by the dynamic viscosity of distilled water, μ_{H_2O}, at the same temperature); m is a relative consistency index (consistency index, *K*, divided by μ_{H_2O}); D_{ij} is the rate of strain tensor; $\dot{\gamma}$ represents the magnitude of the rate of strain tensor; and n is the flow behaviour index, the value of which is slightly less than one for the slurries investigated in this work. This shear-thinning power-law behavior has been commonly observed for slurries and suspensions of particles consisting of (or coated with) polymers [Bird et al. (1987); Ferguson and Kembłowski (1991)]. Both m and n are functions of the MCPCM mass concentration, ϕ, of the slurries. For distilled water (ϕ = 0), $m = 1$ and $n = 1$, so the dynamic viscosity is equal to μ_{H_2O}.

Additional details of ρ_s, μ_s and k_s, the experiments that were conducted to determine these effective properties for the MCPCM slurries, and the correlations proposed for these properties are presented and discussed in Chapter 3.

It is preferable to modify the energy equation into a form where the specific enthalpy of the working fluid, i_s, in the advection transport terms is expressed in term of the temperature, and then rearranged, for convenience in the formulation of the numerical method and the corresponding computer simulations. To this end, the effective enthalpy of the working fluid is first expressed as follows:

$$i_s = \int_{T_{ref}}^{T} c_{p,s} dT + i_{s,ref} \tag{2.18}$$

In this equation, $i_{s,ref}$ denotes the effective specific enthalpy of the working fluid at a suitable reference temperature, T_{ref}, and $c_{p,s}$ represents its effective specific heat, which can be obtained using a mass-weighted average (for the slurries), and cast as follows:

$$c_{p,s} = \phi c_{p,MCPCM} + \left(1-\phi\right) c_{p,H_2O} \tag{2.19}$$

In this equation, ϕ is the MCPCM mass concentration of the slurry ($\phi = 0$ for distilled water), $c_{p,MCPCM}$ is the effective specific heat of the MCPCMs, and c_{p,H_2O} is the specific heat of the distilled water. The specific heat of distilled water is prescribed with a curve-fit to reference data found in the literature [Incropera and DeWitt (2002)]. The effective specific heat of the MCPCM, $c_{p,MCPCM}$, was determined by conducting experiments using differential scanning calorimetry (DSC), and the empirical data were then curve-fitted, as functions of temperature, for both the heating and cooling processes (full details are given in Chapter 3). These correlations are substituted into Eq. (2.19) to obtain the effective specific heat of the working fluid, $c_{p,s}$, for a given temperature, MCPCM mass concentration, and PCM state (solid or liquid) during the heating and cooling processes in the closed-loop thermosyphon.

The effective specific heat of the MCPCM slurries varies strongly with temperature during the phase-change processes in the heating and cooling sections. This variation is accounted for in this work by adopting a special procedure proposed by Elkouh and Baliga (1995), and also described in Sinton and Baliga (2003). Following this procedure, the effective specific heat of the working fluid, $c_{p,s}$, is written in the following form:

$$c_{p,s} = c_{p,s,ref}\left[1 + f\left(T\right)\right] \tag{2.20}$$

In this equation, $c_{p,s,ref}$ is the effective specific heat of the working fluid evaluated at a suitable reference temperature, T_{ref}, which is normally located outside the phase-change temperature range for the MCPCM, and evaluated as follows:

$$c_{p,s,ref} = \phi\, c_{p,MCPCM}\Big|_{T_{ref}} + \left(1-\phi\right) c_{p,H_2O}\Big|_{T_{ref}} \tag{2.21}$$

Equation (2.20) is substituted in Eq. (2.18), and the following equation is obtained:

$$\begin{gathered} i_s = c_{p,s,ref}\int_{T_{ref}}^{T}\left[1+f\left(T\right)\right]dT + i_{s,ref} = c_{p,s,ref}\left[\left(T-T_{ref}\right)+F\left(T\right)\right]+i_{s,ref} \\ \text{where } F\left(T\right)=\int_{T_{ref}}^{T} f\left(T\right)dT \end{gathered} \tag{2.22}$$

Full details of the functions $f(T)$ and $F(T)$ for the particular MCPCM used in this work are provided in Chapter 3 and Appendix B. Finally, this expression for the effective enthalpy of the working fluid is introduced into the energy equation, and the following form of this equation is obtained:

$$\begin{aligned}\frac{\partial}{\partial z}\left(\rho_{s,ref} wT\right)+\frac{1}{r}\frac{\partial}{\partial r}\left(r\rho_{s,ref} vT\right)=\frac{\partial}{\partial z}\left(\frac{k_s}{c_{p,s,ref}}\frac{\partial T}{\partial z}\right)+\frac{1}{r}\frac{\partial}{\partial r}\left(r\frac{k_s}{c_{p,s,ref}}\frac{\partial T}{\partial r}\right)\\ -\left[\frac{\partial}{\partial z}\left(\rho_{s,ref} wF(T)\right)+\frac{1}{r}\frac{\partial}{\partial r}\left(r\rho_{s,ref} vF(T)\right)\right]\end{aligned} \tag{2.23}$$

In this form of the energy equation, the temperature is now present in the advection terms and two additional terms appear on the right side. These two additional terms act like a volumetric heat sink or source, and they incorporate the MCPCM phase-change effects. In this form, the energy equation is divided by $c_{p,s,ref}$, mainly for convenience in the numerical solution of this equation (additional details are provided in Chapter 5).

2.4.3 Boundary Conditions

In the vertical heating section shown in Fig. 2.2 (note: $r_i = D_i / 2$), the boundary conditions are the following:

At $z = 0$ and $0 \le r \le r_i$:

$$w = w_{in\ fully\text{-}developed}\ ;\ v = 0;\ T = T_{b,in} \tag{2.24}$$

At $z = \left(L_{h,pre} + L_h + L_{h,post}\right)$ and $0 \le r \le r_i$:

$$\partial w / \partial z = 0\ ;\ \partial v / \partial z = 0\ ;\ \partial T / \partial z = 0 \tag{2.25}$$

At $r = 0$ and $0 \le z \le \left(L_{h,pre} + L_h + L_{h,post}\right)$:

$$\partial w / \partial r = 0\ ;\ v = 0\ ;\ \partial T / \partial r = 0 \tag{2.26}$$

At $r = r_i$ and $0 \le z \le L_{h,pre}$ and $\left(L_{h,pre} + L_h\right) \le z \le \left(L_{h,pre} + L_h + L_{h,post}\right)$:

$$w = 0\,;\; v = 0\,;\; q'_{out} = U'_i\left(T_{r=r_i} - T_\infty\right) \tag{2.27}$$

At $r = r_i$ and $L_{h,pre} < z < \left(L_{h,pre} + L_h\right)$:

$$w = 0\,;\; v = 0\,;\; q'_{in} = 2\pi r_i\left(k_s \partial T / \partial r\right) \tag{2.28}$$

Eq. (2.24) represents the set of inflow boundary conditions in the heating section. The entering temperature of the working fluid (at z = 0) is set equal to the bulk temperature, $T_{b,in}$, exiting the one-dimensional thermosyphon segment preceding the heating section. The fully-developed velocity profile specified at the section inlet (at z = 0) is given by the following analytical solution for a non-Newtonian fluid for which the power-law model given in Eq. (2.17) applies [Bird et al. (1987)] :

$$w_{in\ fully\text{-}developed} = w_{av}\frac{\left(\dfrac{1}{n}+3\right)}{\left(\dfrac{1}{n}+1\right)}\left(1-\left(\frac{r}{r_i}\right)^{\frac{1}{n}+1}\right) \tag{2.29}$$

In this equation, w_{av} is the average velocity of the working fluid in the thermosyphon loop. Its value is iteratively obtained using a loop-wide momentum balance which is given in Section 2.6. It should also be noted here that when distilled water (a Newtonian fluid) is used as the working fluid, n = 1, and the fully-developed velocity profile prescribed in Eq. (2.29) reverts to the well-known Poiseuille parabola.

Eq. (2.25) corresponds to the well-established outflow treatment [Patankar (1980)]. In the numerical simulations conducted in this work, the chosen post-heated pipe length, $L_{h,post}$, was made sufficiently long to allow the redevelopment of the velocity and temperature profiles, thereby ensuring that the outflow treatment was appropriate, and it had negligible effects on the fluid flow and heat transfer in the upstream active heating section. Eq. (2.27) represents the heat losses to (or gains from) the ambient environment along the pre- and post-heating lengths. The value of the overall heat transfer coefficient

$U_i^{'}$ is determined experimentally (see Chapter 4). The subscript *i* denotes that this coefficient is based on the difference between the temperatures of inner surface of the pipe wall and the ambient environment.

In Eq. (2.28), $q_{in}^{'}$ represents the rate of heat transfer per unit length supplied to the working fluid at the inner surface of the pipe wall ($r = r_i$) in the active heating section. Not all of the electrical power input per unit length, q', supplied to the electrical heating wire that was tightly wound around the outer surface of the active heating section, is supplied to the working fluid, as some of it is lost to the ambient environment. Thus, the value of $q_{in}^{'}$ cannot be prescribed *a priori*; rather, it was computed (iteratively, in the numerical solution procedure described in Chapter 5) by assuming one-dimensional radial heat conduction in both the pipe wall and the insulation on its outer surface, and calculating the corresponding heat loss to the environment, $q_{loss}^{'}$, using the following equations:

$$q' = q_{heating,total} / L_h \tag{2.30}$$

$$q_{in}^{'} = q^{'} - q_{loss}^{'} \tag{2.31}$$

$$q_{loss}^{'} = U_o^{'}\left(T_{r=r_o} - T_\infty\right) \tag{2.32}$$

$$T_{r=r_o} = q_{in}^{'}\left[\ln\left(r_o / r_i\right) / 2\pi k_w\right] + T_{r=r_i} \tag{2.33}$$

In Eq. (2.32), $U_o^{'}$ is the overall heat transfer coefficient based on the difference between the temperatures of outer surface of the pipe wall and the ambient environment. The value of $U_o^{'}$ is nearly identical to $U_i^{'}$, but in this work, the radial thermal conduction resistance per unit length of the pipe wall was accounted in the evaluation of $U_o^{'}$ (full details are provided in Chapter 4).

The boundary conditions pertaining to the vertical cooling section can be obtained from Eq. (2.24) to (2.27) by replacing $L_{h,pre}$ by $L_{c,pre}$, L_h by L_c, and $L_{h,post}$ by

$L_{c,post}$. However, in the active cooling section, namely, $L_{c,pre} < z < (L_{c,pre} + L_c)$, the boundary condition is one of prescribed constant temperature, so at $r = r_i$, $T_{r=r_i} = T_{cool}$.

2.5 Quasi-One-Dimensional Models of Fluid Flow and Heat Transfer

In the portions of the closed-loop thermosyphon that join the vertical heating and cooling sections, quasi-one-dimensional (1-D) models of the fluid flow and heat transfer phenomena were used, as the local buoyancy effects are essentially negligible. The upper 1-D portion starts at the exit plane of the post-heating length (see Figs. 2.1 and 2.2), includes the top 180º bend, and ends at the entry plane of the pre-cooling length (see Figs. 2.1 and 2.3). The lower 1-D portion starts at the exit plane of the post-cooling length (see Figs. 2.1 and 2.3), includes the bottom 180º bend, and ends at the entry plane of the pre-heating length (see Figs. 2.1 and 2.2). Even though the outer surfaces of these 1-D portions are well insulated, they do experience some heat exchange with the ambient environment. So the temperature of the working fluid in these 1-D portions changes (albeit slightly). Thus, to enhance the accuracy of the numerical simulations, a segmented approach was adopted in the proposed 1-D models of the fluid flow and heat transfer in these portions. An example of a segment of the upper 180º bend is schematically illustrated in Figure 2.4, along with the related notation used in the formulation of the 1-D models.

The velocity and temperature profiles in the 1-D segments, such as the one shown in Fig. 2.4, are assumed to be fully-developed. An energy balance over the segment of length Δs (see Fig. 2.4) yields the following equation:

$$q_{in,\Delta s} = \dot{m}\left(i_{s,b,exit} - i_{s,b,entry}\right) \tag{2.34}$$

In the previous equation, $q_{in,\Delta s}$ denotes the rate of heat gain over the segment, $\dot{m}$ denotes the mass flow rate of the working fluid in the loop, and $i_{s,b,exit}$ and $i_{s,b,entry}$ denote the effective specific enthalpies of the working fluid at the exit and entry cross-sections of the segment. Using Eq. (2.22) and by introducing the average velocity, w_{av}, the following equations are obtained:

$$
\begin{aligned}
q_{in,\Delta s} &= \rho_{s,ref} w_{av} A_{cs} \left(i_{s,b,exit} - i_{s,b,entry} \right) \\
q_{in,\Delta s} &= \rho_{s,ref} w_{av} A_{cs} c_{p,s,ref} \left(T_{b,exit} - T_{b,entry} + F\left(T_{b,exit}\right) - F\left(T_{b,entry}\right) \right)
\end{aligned} \tag{2.35}
$$

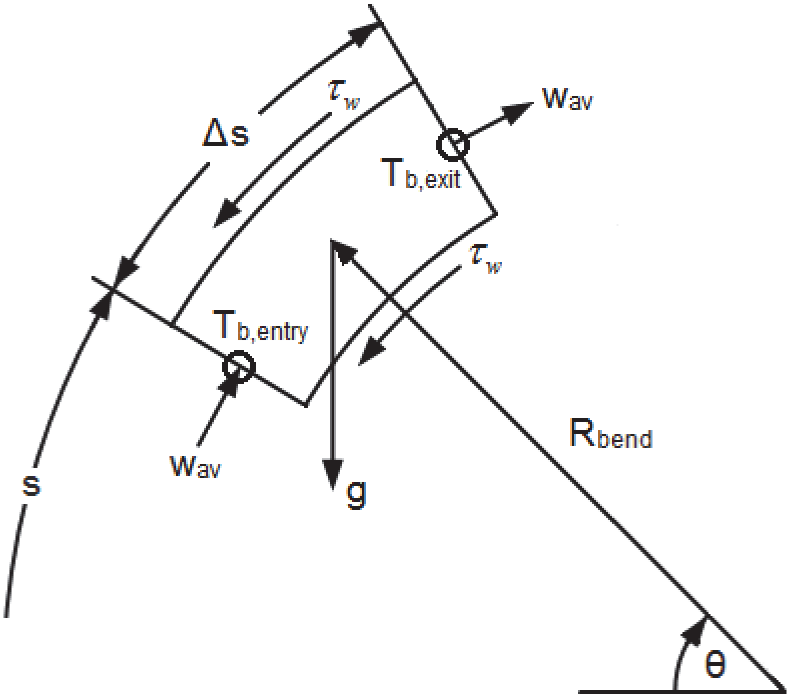

Figure 2.4: Segment of the upper 180º bend of the closed-loop thermosyphon and related notation used in the formulation of the proposed 1-D models.

In each segment, the rate of heat gain from the ambient environment can be calculated using an overall heat transfer coefficient, $U_b^{'}$, *per unit length*. In this work, $U_b^{'}$ was determined empirically (details are presented in Chapter 4). Thus:

$$q_{in,\Delta s} = -U_b^{'} \Delta s \left(\overline{T}_{b,\Delta s} - T_\infty \right) \tag{2.36}$$

In this equation, $\overline{T}_{b,\Delta s}$ represents the average bulk temperature of the working fluid in the segment of Δs, and T_∞ is the temperature of the ambient fluid. Using Eqs. (2.35) and (2.36), the following equation for the bulk temperature at the exit of the segment is obtained:

$$T_{b,exit} = \frac{U_b^{'}\Delta s}{\rho_{s,ref} w_{av} A_{cs} c_{p,s,ref}}\left(T_\infty - \overline{T}_{b,\Delta s}\right) + F\left(T_{b,entry}\right) - F\left(T_{b,exit}\right) + T_{b,entry} \tag{2.37}$$

The right-hand side of Eq. (2.37) contains terms that are dependent on $T_{b,exit}$, namely, $\overline{T}_{b,\Delta s}$ and $F\left(T_{b,exit}\right)$, and these terms are not known *a priori*. In the numerical solution of the governing equations of the proposed 1-D/2-D model (see Chapter 5 for details), an iterative procedure is used to solve for $T_{b,exit}$. The length Δs of the segment is relatively small (compared to the total length of the closed-loop thermosyphon), and the bulk temperature of the fluid does not change much over a segment. Therefore, in each segment, the mean bulk temperature $\overline{T}_{b,\Delta s}$ is evaluated as the arithmetic mean of the entering and exiting bulk temperatures. Once the temperature distributions in the 1-D portions of the closed-loop thermosyphon are calculated, the effective density is evaluated at the nodes located at the entrance and exit planes of each of the segments (see Fig. 2.4), and stored for later use when the overall momentum balance is invoked to solve for w_{av} (as described in the next section).

Using the power-law model for the effective dynamic viscosity of the working fluids considered in this research [see Eq. (2.17)], the shear stress at the inner surface of the pipe wall can be calculated using the following equation:

$$\tau_{wall} = \mu_{s,wall}\dot{\gamma}_{wall} = (\mu_{H_2O} m \dot{\gamma}_{wall}^{n-1})\dot{\gamma}_{wall} = \mu_{H_2O} m \dot{\gamma}_{wall}^{n} \tag{2.38}$$

For fully-developed flow in the 1-D segments of the closed-loop thermosyphon, the following expression for $\dot{\gamma}_{wall}$ can be obtained using Eq. (2.29):

$$\dot{\gamma}_{wall} = \left|\left(\frac{\partial w}{\partial r}\right)_{r=r_i}\right| = \frac{w_{av}}{r_i}\left[\frac{1}{n} + 3\right] \tag{2.39}$$

The Fanning friction factor in the 1-D segments is defined and calculated using the following equations:

$$\begin{aligned} f_{Fanning} &\triangleq \frac{\tau_{wall}}{\frac{1}{2}\rho_{s,ref} w_{av}^2} = \frac{\mu_{H_2O} m \left(\frac{w_{av}}{r_i} \left[\frac{1}{n} + 3 \right] \right)^n}{\frac{1}{2}\rho_{s,ref} w_{av}^2} \\ &= \frac{\mu_{H_2O} m \left(\frac{8 w_{av}}{D_i} \left[\frac{1}{4n} + \frac{3}{4} \right] \right)^n}{\frac{1}{2}\rho_{s,ref} w_{av}^2} \end{aligned} \tag{2.40}$$

A generalized Reynolds number, based on a generalized effective dynamic viscosity, $\mu_{s,gen}$, can be defined as follows [Chhabra and Richardson (1999)]:

$$\begin{aligned} Re_{D_i,gen} &\triangleq \frac{\rho_{s,ref} w_{av} D_i}{\mu_{s,gen}} \\ \mu_{s,gen} &= \mu_{H_2O} m \left(\frac{8 w_{av}}{D_i} \right)^{n-1} \left(\frac{1}{4n} + \frac{3}{4} \right)^n \end{aligned} \tag{2.41}$$

By combining Eqs. (2.40)-(2.41), the following convenient relation is obtained [Metzner and Reed (1955), Chhabra and Richardson (1999)]:

$$f_{Fanning} = \frac{16}{Re_{D_i,gen}} \tag{2.42}$$

It should be noted that when distilled water is used as the working fluid in the closed-loop thermosyphon, $n = 1$, $m = 1$, and $\mu_{s,gen}$ reduces to μ_{H_2O}, and the definition of $Re_{D_i,gen}$ becomes equivalent to the classical definition used for Newtonian fluids. The generalized effective dynamic viscosity $\mu_{s,gen}$ can also be used to define additional dimensionless parameters pertaining to non-Newtonian fluids in the problems considered in this work, such as Prandtl and Grashof numbers (see Section 2.8).

For the 1-D segments located in the pipe bends, a correction was applied to the calculated values of $f_{Fanning}$ in order to take into account the related additional head losses associated. This was done using an empirical correlation proposed by Gupta and Mishra (1975), which prescribes the relative increase of the friction factor with respect to the value pertaining to fully-developed flow in a straight pipe, and is applicable to flows of Newtonian fluids and also non-Newtonian fluids for which the effective dynamic viscosity can be prescribed using the power-law behavior given in Eq. (2.17). This correlation is expressed as a function of a generalized Dean number, De_{gen}, as follows:

$$\begin{aligned} &\frac{f_{Fanning,curved}}{f_{Fanning,straight}} = 1 + 0.026\left(De_{gen}\right)^{0.675} \\ &\text{with} \quad De_{gen} = Re_{D_i,gen}\left(r_i / R_{bend}\right)^{0.5} \end{aligned} \tag{2.43}$$

In this equation, r_i denotes the inner radius of the pipe, and R_{bend} is the radius of each of the two 180-degree semicircular bends of the closed-loop thermosyphon.

2.6 Overall Momentum Balance

To determine an overall average velocity of the working fluid in the closed-loop thermosyphon, an overall momentum balance was used. This momentum balance is obtained by first writing a momentum balance for an elemental control volume, shown in Fig. 2.5 along with a schematic of the full closed-loop thermosyphon, and then integrating it over the full closed-loop. The angle θ in Figure 2.5 denotes the orientation of the control volume with respect to the horizontal, and *s* is the axial coordinate around the closed-loop.

By using a momentum balance on the elemental control volume and then performing a contour integration along the coordinate *s* around the closed-loop (see Fig. 2.5), the following result is obtained [Bernier and Baliga (1992b)]:

$$\oint \tau_w 2\pi r_i ds = -\oint g\rho_s \cos\theta \pi r_i^2 ds \tag{2.44}$$

This equation can be interpreted as follows: in steady-state operation, the net buoyancy force in the thermosyphon is equal to and opposed by the cumulative force of the viscous shear stresses acting along the inner pipe surface. The contributions of the static pressure and momentum advection terms to the contour integral are zero, as the starting and ending limits of the integral coincide (the velocity profiles and the pressure distribution are the same over the starting and ending cross-sections). It should also be noted that in this equation, g is the magnitude of the gravitational acceleration.

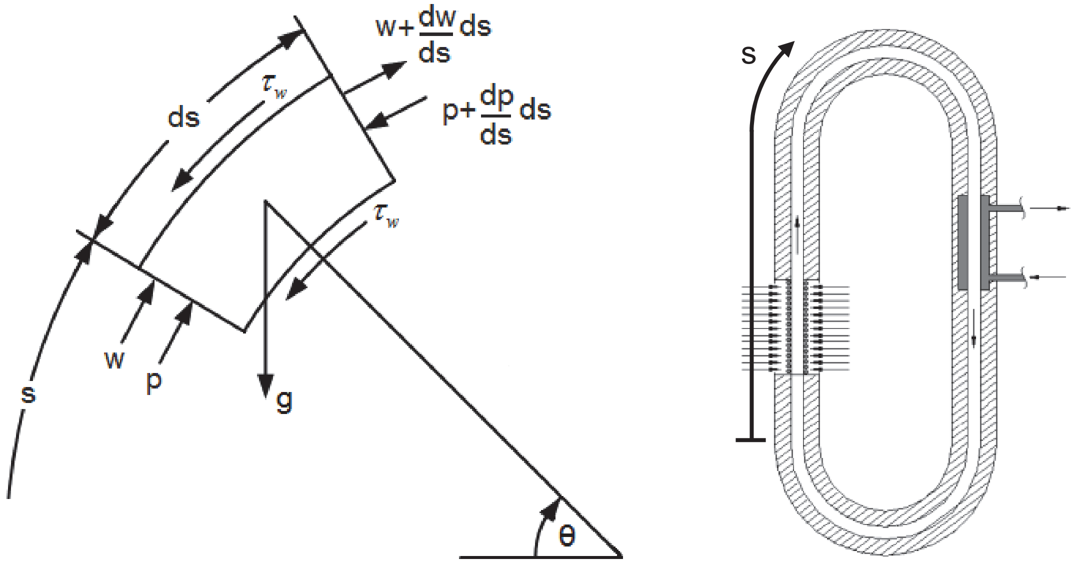

Figure 2.5: Elemental control volume used in the derivation of the overall momentum balance equation, and the axial coordinate *s* shown on a schematic of the closed-loop thermosyphon.

Eq. (2.44) can be rewritten as follows using the Fanning friction factor, $f_{Fanning}$, defined in Eq. (2.40), but using an overall average velocity of the working fluid in the loop:

$$w_{av}^2 \oint f_{Fanning} ds = -\frac{r_i}{\rho_{s,ref}} g \oint \rho_s \cos\theta ds \tag{2.45}$$

The overall average velocity, w_{av}, can thus be calculated using the following equation:

$$w_{av} = \sqrt{\frac{-\frac{r_i}{\rho_{s,ref}} g \oint \rho_s \cos\theta ds}{\oint f_{Fanning} ds}} \tag{2.46}$$

In the proposed 1-D/2-D model, after solving the fluid flow and heat transfer problems in all sections of the closed-loop thermosyphon, the values of the local Fanning friction factor, $f_{Fanning}$, and the effective density, ρ_s, are calculated along the full closed-loop and then stored. These stored values of $f_{Fanning}$ and ρ_s are used to evaluate the contour integrals in Eq. (2.46) (numerically). It should also be noted that the result of the contour integration in the numerator of Eq. (2.46) is negative, given the nomenclature shown in Fig. 2.5 and the thermosyphon geometry being considered. Thus, Eq. (2.46) does not yield an imaginary number.

The numerical methods which were used to solve the governing equations of the proposed 1-D/2-D model, and also the procedure which was used to iteratively couple solutions of the 2-D and 1-D models presented in Sections and 2.5 and 2.6, are presented and discussed in Chapter 5.

2.7 Definition of a Modified Bulk Temperature

In mathematical descriptions and solutions of single-phase convective heat transfer problems in ducts, the following well-established definition of the bulk temperature is commonly used [Eckert and Drake (1972), Incropera and DeWitt (2002)]:

$$T_{b,std} = \frac{\int_{A_{c.s.}} \rho w c_p T dA_{c.s.}}{\int_{A_{c.s.}} \rho w c_p dA_{c.s.}} \tag{2.47}$$

This definition of the bulk temperature is useful for local and overall energy balances when the specific heat, c_p, of the working fluid is constant or assumed constant at a suitable average value. However, this standard definition of the bulk temperature is not adequate if c_p changes significantly with temperature, as is the case with the effective specific heat of the MCPCM slurries when the encapsulated PCM undergoes phase change. The inadequacy arises because of the following difficulties: i) the numerator of the expression on the right-hand side of Eq. (2.47) does not strictly represent the rate of transport of enthalpy across the duct cross-section of interest, as the specific enthalpy must now be evaluated using Eq. (2.18); and ii) the evaluation of the integrals over the duct cross-section, in both the numerator and denominator on the right-hand side of Eq. (2.47), requires a knowledge of the temperature distribution over the same cross-section of the duct, details which are rarely, if ever, measured or available to the experimentalist.

Scott (2006), who worked with the same MCPCM as that used in this work, proposed a new definition of the bulk temperature, $T_{b,modified}$, which circumvents the limitations of the abovementioned standard definition. For convenience, this modified bulk temperature is simply referred to as bulk temperature in the remainder of this thesis, thus $T_b = T_{b,modified}$. This new bulk temperature is defined using an effective bulk specific enthalpy, $i_{s,b}$, as follows:

$$i_{s,b} = \frac{\int_{A_{c.s.}} \rho w i_s dA_{c.s.}}{\int_{A_{c.s.}} \rho w dA_{c.s.}} = \frac{\int_{A_{c.s.}} \rho w i_s dA_{c.s.}}{\dot{m}} \tag{2.48}$$

$$i_{s,b} = \int_{T_{ref}}^{T_b} c_{p,s} dT + i_{s,ref} \tag{2.49}$$

Eq. (2.49) provides a relationship between the bulk temperature T_b (upper limit of the integral on the right-hand side) and the effective bulk enthalpy of the slurry, $i_{s,b}$, which is evaluated using Eq. (2.48). This new definition of the bulk temperature can be appropriately used for overall or local steady-state energy balances. For example, the net rate of heat transfer over a section of the pipe bounded by axial positions z_1 and z_2 is given by:

$$i_{s,b,2} - i_{s,b,1} = \int_{T_{b,1}}^{T_{b,2}} c_{p,s} dT \tag{2.50}$$

$$q_{in,net,z_1 \le z \le z_2} = \dot{m}\left(i_{s,b,2} - i_{s,b,1}\right) \tag{2.51}$$

Therefore, if $\dot{m}$, $T_{b,1}$, $T_{b,2}$ and $c_{p,s}$ (as a function of temperature) are known or specified, $q_{in,net,z_1 \le z \le z_2}$ can be calculated using Eqs. (2.50) and (2.51). Conversely, if $\dot{m}$, $T_{b,1}$, $q_{in,net,z_1 \le z \le z_2}$ and $c_{p,s}$ are known, $i_{s,b,2}$ can be computed using Eq. (2.51), and then $T_{b,2}$ can be obtained using Eq. (2.50). Lastly, for cases in which c_p is constant, the bulk temperature definition proposed by Scott (2006) becomes identical to the standard bulk temperature definition of Eq. (2.47), as expected.

To obtain the value of T_b corresponding to a value of $i_{s,b}$ and an available function for the variation of $c_{p,s}$ with temperature, it is necessary to solve Eq. (2.49). This task is not straightforward for the MCPCM slurries considered in the present work, as the relationship between $c_{p,s}$ and T is a complicated nonlinear function, due to the phase-change effects of the encapsulated PCM. Since $i_{s,b}$ is a monotonically increasing function of T_b, an iterative scheme similar to a binary search algorithm [Press et al. (1992)] was implemented and used to determine the value of T_b associated with $i_{s,b}$. This search algorithm iteratively searches for T_b associated with $i_{s,b}$ by progressively narrowing upper and lower bounds of T_b which enclose the value of $i_{s,b}$ of interest. Ultimately, both bounds essentially merge towards the desired (correct) value of T_b, and the process is halted when a specified tolerance criterion is met. In this work, this tolerance criterion was specified as follows:

$$\varepsilon = \max\left\{\left|T_{b,upper\,bound} - T_b\right|, \left|T_b - T_{b,lower\,bound}\right|\right\} / T_{b,abs} \tag{2.52}$$

This criterion was considered satisfied when the value of ε was less than 10^{-10}. It should also be noted that the criterion shown in Eq. (2.52) is divided by the latest value of T_b expressed in Kelvin ($T_{b,abs}$), so as to maintain the applicability of the criterion if temperature values less than or equal to 0°C are encountered (although this was not the case in the present work). Additional details of this procedure can be found in the works of Scott (2006) and Scott, Lamoureux, and Baliga (2010).

2.8 Determination of Flow Regime

As was mentioned earlier in Subsection 2.4.1, laminar mixed convection was assumed in the closed-loop thermosyphon investigated in this work. This assumption is justified in this section with the use of a flow regime map provided by Metais and Eckert (1964). This map, shown in Fig. 2.6, shows the bounds of forced, mixed, and free (natural) convection regimes, and also the related laminar, transitional, and turbulent regimes. This flow regime map applies to both *aiding flow*, where the mean flow and buoyancy force are in the same direction, and *opposing flow* configurations, for which the aforementioned directions are opposite to one another. The abbreviations UWT and UHF, respectively, indicate data pertaining to the uniform wall temperature and uniform wall heat flux. Lastly, the dimensionless parameters used in this flow regime map are the Reynolds, Prandtl, and Grashof numbers, defined as follows [Metais and Eckert (1964) and Aung (1987)]:

$$Re = \frac{\rho w_{av} D_i}{\mu}; \quad Pr = \frac{\mu c_p}{k}; \quad Gr = \frac{g\beta\left(\overline{T}_w - \overline{T}_b\right) D_i^3}{\left(\mu / \rho\right)^2} \tag{2.53}$$

In the definition of the Grashof number, β is the thermal volumetric expansion coefficient, and $\overline{T}_w$ and $\overline{T}_b$, respectively, denote the suitably averaged values of the pipe-wall temperature and the bulk temperature of the fluid [Aung (1987)].

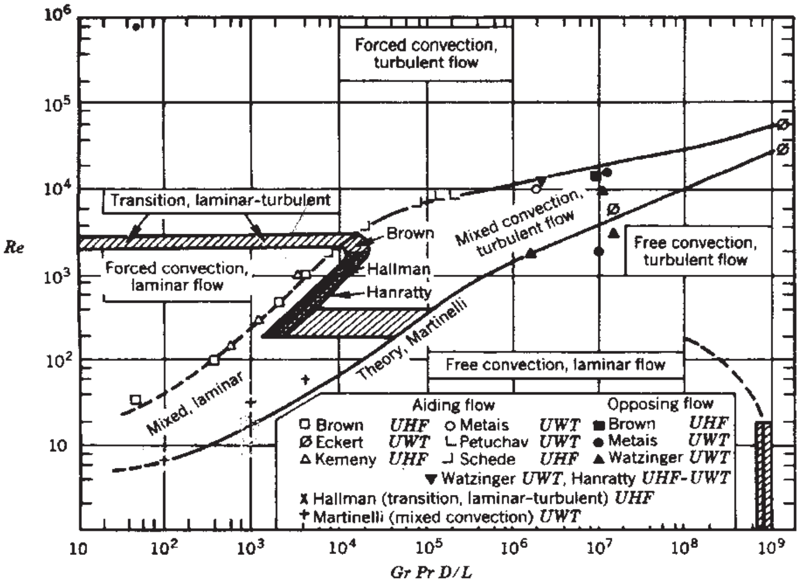

Figure 2.6: Flow regime map for natural, mixed and forced convection in vertical pipes [taken from the work of Metais and Eckert (1964)].

In this work, the buoyancy forces in the vertical heating and cooling sections act in the same direction as the mean flow (thus, the *aiding flow* configuration prevails in both these sections). Also, the flow regime map shown in Fig. 2.6 pertains to single-phase heat transfer, and it is presumed here that the laminar-to-turbulent transition regions remain essentially unaltered for homogeneous slurries having moderate MCPCM mass concentration. It should be noted, however, that for the MCPCM slurries, it is expected that the laminar-to-turbulent transition would occur at higher *Re* or *Gr* values, due to potential turbulence dampening effects of the MCPCM particles [Inaba et al. (2004)]. Therefore, Fig. 2.6 is used to show that the slurry flows studied in this work are located well in the laminar regime of the map.

The Reynolds, Prandtl, and Grashof number values shown below were evaluated using suitable average values of the effective properties over any particular heat-exchange section of interest. The maximum values of *Re*, *Pr*, *Gr*, and $GrPr(D_i/L)$, with $L = L_h$ or L_c, prevailing in the closed-loop thermosyphon apparatus during the experiments were the following for distilled water ($\phi = 0\%$):

$$5 \le Pr \le 6.2;\;\; Re \le 200;\;\; Gr \le 3.1\text{x}10^4;\;\; GrPr\left(D_i / L\right) \le 1960 \tag{2.54}$$

The values of *Re* and $GrPr(D_i/L)$ were found to be maximized when $\phi = 0\%$ (distilled water). For non-Newtonian fluids characterized by a power-law behavior, modified definitions of *Re* , *Gr*, and *Pr* are conventionally used. These modified dimensionless parameters are referred to as being *generalized* and they are based on a suitable reference value of the generalized dynamic viscosity $\mu_{s,gen}$ defined in Eq. (2.41). These *generalized* parameters are denoted as Re_{gen} , Gr_{gen}, and Pr_{gen}, and obtained by replacing μ in the original definitions given in Eq. (2.53) by $\mu_{s,gen}$. These parameters become equivalent to the original definitions when the flow behavior index *n* is set equal to unity (for a Newtonian fluid), as expected. Although the flow regime map of Metais and Eckert (1964) pertains to Newtonian fluids, it was used with the following maximum values of Re_{gen}, Pr_{gen}, Gr_{gen} and $Gr_{gen}Pr_{gen}(D_i/L)$ that prevailed in the experiments performed with MCPCM slurries ($7.5\% \le \phi \le 17.5\%$):

$$68 \le Pr_{gen} \le 320; \;\; Re_{gen} \le 8.0; \;\; Gr_{gen} \le 940; \;\; Gr_{gen} Pr_{gen}\left(D_i / L\right) \le 935 \qquad (2.55)$$

The flow regime map of Metais and Eckert (1964) is strictly applicable for $10^{-2} \le Pr(D_i/L) \le 1$. It should be noted that for the highest MCPCM mass concentration used in this work (17.5%), the value of $Pr_{gen}\left(D_i / L\right)$ exceeded unity. However, the highest values of $Gr_{gen}Pr_{gen}\left(D_i / L\right)$ were observed for the lowest MCPCM mass concentrations, thus the flow regime map was considered applicable in this work.

Use of Fig. 2.6 with the maximum values of the parameters values in Eqs. (2.54) and (2.55) shows that the flows of distilled water and also the MCPCM slurries in the vertical heating and cooling sections of the closed-loop thermosyphon were laminar, and they do not undergo transition to the turbulent regime. This flow regime map also indicates that laminar-mixed convection prevailed in these sections. This finding also indicates that there is a need for detailed two-dimensional axisymmetric simulations of the flow and heat transfer in the vertical heating and cooling sections, as the local buoyancy forces could significantly influence the velocity and temperature profiles in these sections. Finally, it was concluded that the flows in the other sections of the closed-loop thermosyphon were also laminar, as the corresponding buoyancy effects were negligibly small (or absent, for all practical purposes), and the related values of Reynolds number were well below the transition limit of $Re \approx 2300$ for Newtonian fluids or $Re_{gen} \approx 2100$ for non-Newtonian power-law fluids [Chhabra and Richardson (1999)].

3. Thermophysical Properties

As was shown in Chapter 2, it is valid to use a homogeneous model to mathematically describe the flow and heat transfer inside the closed-loop thermosyphon operated in this work with slurries of a microencapsulated phase-change material (MCPCM) suspended in distilled water. In this homogeneous model, several characteristics and effective thermophysical properties of the MCPCM slurries are needed as inputs. In this chapter, the experimental apparatus, procedures, and/or correlations that were used for determining and/or prescribing the following characteristics and thermophysical properties of the MCPCM slurries in the temperature range 5°C to 55°C are described: 1) mass concentration of the MCPCM in the slurries; 2) shape and effective diameter of the MCPCM particles; 3) effective densities of the slurries and the MCPCM; 4) effective thermal conductivity of the slurries and the MCPCM; 5) effective specific heat, latent heats of melting and solidification, phase-change behavior, and melting and freezing temperature ranges of the MCPCM; and 6) rheological behavior and effective dynamic viscosity of the MCPCM slurries.

3.1 Mass Concentration of the MCPCM in the Slurries

The MCPCM particles used in this work were manufactured by Outlast Ventures Inc., based in Boulder, Colorado. They were supplied in the form of a high concentration paste, composed of the MCPCM particles in a proportion of 50.2% by total mass, the remainder being mostly water and minute traces from the encapsulation process. This paste has the appearance of a viscous, white, and opaque liquid, similar to a thick paint. The slurries were prepared by adding distilled water to this MCPCM paste, in amounts needed to obtain the desired value of the MCPCM mass concentration, and then mixing these ingredients gently, but thoroughly.

The final mass concentration of MCPCM particles in distilled water can be calculated with the following equation:

$$\phi = \frac{0.502 m_{MCPCM\ paste}}{m_{MCPCM\ paste} + m_{H_2O}} \tag{3.1}$$

In this equation, ϕ is the mass concentration of the MCPCM particles, $m_{MCPCM\ paste}$ denotes the mass of the MCPCM paste (which has an MCPCM mass concentration of 50.2%), and m_{H_2O} represents the mass of distilled water added to the MCPCM paste to form the slurry.

3.2 Shape and Effective Diameter of the MCPCM particles

As was mentioned earlier, the MCPCM particles used in this work were the same as those used by Scott (2006). He took photomicrographs of dilute slurries, and used them to characterize the shape of the MCPCM particles and determine their effective diameters. One such photomicrograph is shown in Fig. 3.1. From a visual inspection of Fig. 3.1, it can be seen that the two-dimensional projections of the MCPCM particle are not perfectly circular. Hence, it was deduced that the MCPCM particles are not perfectly spherical in shape, and an effective diameter (defined as the diameter of a circle of area equal to the area of the two-dimensional projection of the particle), rather than a diameter, was used to characterize their size.

Scott (2006) first measured the effective diameter of the MCPCM particles by making numerous manual measurements of their two-dimensional projections on the photomicrographs, using a ruler and appropriate scaling. Using such measurements on a total 296 MCPCM particles, he obtained the following results: a mean effective diameter of 2.5 μm; smallest and largest effective diameters of 1.0 μm and 12.5 μm, respectively; and a standard deviation of 1.0 μm. Scott (2006) then used digital image-processing software (*Image*, from the National Institutes of Health, in Bethesda, Maryland, U.S.A.) to analyze the photomicrographs and determine the mean effective diameter of the MCPCM particles. Using this technique on photomicrographs of 206 MCPCM particles, he obtained a mean effective diameter of 2.84 μm. A personal communication from *Outlast Ventures Inc*. stated that the mean effective diameter of the MCPCM particles was 2.5 μm, and 99% of the particles had an effective diameter of less than 12.5 μm. On the basis of this information and the aforementioned data obtained from the photomicrographs, it was assumed that the MCPCM particles were essentially spherical in shape, with mean and maximum effective diameters of 2.5 μm and 12.5 μm, respectively.

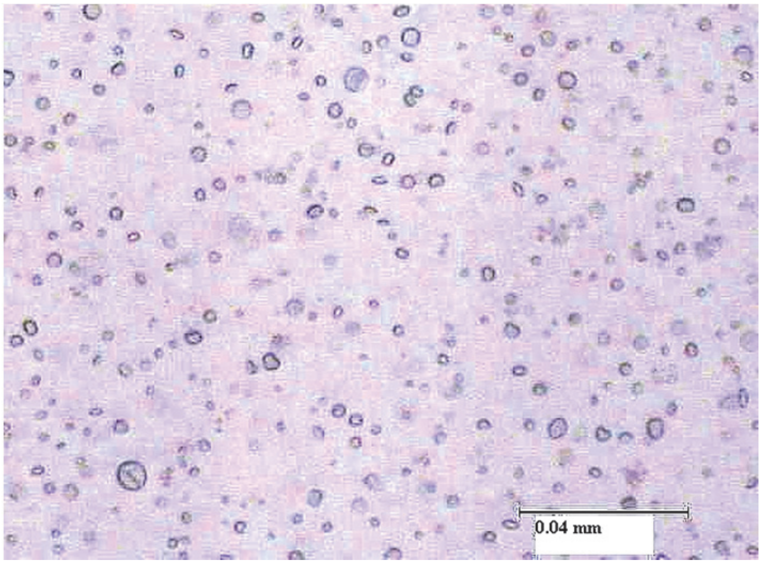

Figure 3.1: Photomicrograph of a dilute MCPCM suspension [from Scott, Lamoureux, Baliga (2010)].

3.3 Effective Density of the Slurries and the MCPCM

The effective density of the MCPCM slurries was measured using a glass hydrometer: *Ertco* hydrometer, having a density range of 950.0 kg/m^3 to 1000.0 kg/m^3, and a scale divided into increments of 0.5 kg/m^3. In each experiment, this hydrometer was inserted into a slurry sample, which was contained in a graduated cylinder sufficiently long to allow for the hydrometer displacements. This graduated cylinder was positioned in another cylinder assembly, and distilled water at a controlled temperature (supplied from a constant-temperature bath, *Neslab* RTE 211) was circulated between them, to control the temperature of the slurry sample. The temperature of the slurry sample was measured with the probe of a *Hewlett-Packard* 2804A quartz thermometer (± 0.01°C accuracy), inserted through the top insulating lid of the outer cylinder. The apparatus (specially designed, constructed, and used in this work) and also the constant-temperature bath can be seen in the photograph given in Fig. 3.2.

Figure 3.2: Photograph of the effective density measurement apparatus and the constant-temperature bath.

As can be seen in Fig. 3.2, the exterior of the outer cylinder of the density measurement apparatus was well insulated. A small observation window was cut out from the insulation on the outer surface of the cylinder, to allow convenient readings of the hydrometer scale. Distilled water from the constant-temperature bath was pumped in via an insulated hose connected to the bottom of the outer cylinder, made to flow through the annular space between the outer cylinder and the graduated inner cylinder (which contained the slurry sample), and then returned back to the constant-temperature bath. This set-up ensured that no significant spatial variations of temperature were present in the slurry sample during the density measurements: the temporal temperature fluctuations were less than ± 0.05°C, once the steady-state condition was reached. A few minutes before each density measurement, the slurry sample was manually stirred (using a specially-designed ring-shaped stirrer) to further reduce any spatial variations of temperature and make sure the settling of the MCPCM particles did not occur (even if this phenomena was not observed in any of the experiments).

Using the above-mentioned apparatus and procedure, the density measurements were performed for values of the slurry temperature from 5°C to 55°C, in increments of approximately 2°C, and two different values of the MCPCM mass concentration, 12.00% and 15.00%. For each slurry temperature and MCPCM mass concentration (ϕ), the effective density of the slurry, ρ_s, was obtained using the above-mentioned apparatus and procedure, and the effective density of the MCPCM particles, ρ_{MCPCM}, was calculated, using accurate and well-established values of the density of the distilled water, ρ_{H_2O}, and the following equation (derived using the requirement that the total volume of the slurry is equal to the sum of the volumes of the distilled water and MCPCM particles):

$$\frac{1}{\rho_s} = \frac{\phi}{\rho_{MCPCM}} + \frac{(1-\phi)}{\rho_{H_2O}} \tag{3.2}$$

It should be noted here that the hydrometer used in these experiments was originally calibrated to measure the density of liquid samples at a temperature of 15°C. Thus, to obtain accurate values of the sample density at temperatures that differ from 15°C, it was essential to apply a correction that accounted for the thermal expansion or contraction of the hydrometer bulb. This correction (which has a value of zero at 15°C) was determined by measuring the density of distilled water, comparing the results to the corresponding reference values reported in the *NBS/NRC Steam Tables* [Haar et al. (1984)], and using a least-squares procedure to fit a linear function to the differences between the corresponding measured and reference values. The final corrected density values were obtained using the following equation:

$$\rho_{corrected} = \rho_{measured} - 0.04935(T-15) \tag{3.3}$$

In this equation, T is the sample temperature expressed in °C. The uncorrected measurements and the corrected values of the density of distilled water are shown in Fig. 3.3, along with the reference values reported in the *NBC/NRC Steam Tables*. As can be seen from these results, the corrected values of the density of distilled water are in excellent agreement with the reference data of Haar et al. (1984): in quantitative terms, the maximum absolute difference between the corrected and the reference density values was 0.49 kg/m^3, a value essentially equal to the stated measurement accuracy of the *Ertco* hydrometer ($\pm$ 0.5 kg/m^3) used in these experiments.

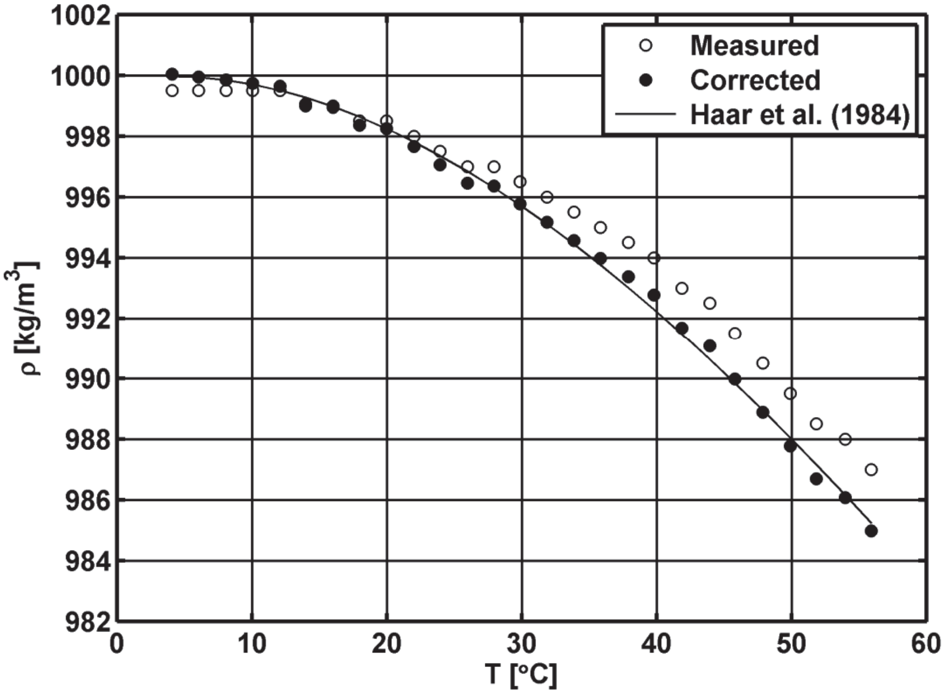

Figure 3.3: Measured, corrected, and reference values of the density of distilled water.

The above-described apparatus and procedures were used to obtain the density of the MCPCM slurries, of MCPCM mass concentrations of 12.00% and 15.00%, during both monotonic heating (including PCM melting) and monotonic cooling (including PCM freezing) processes. For each MCPCM concentration, the slurry density measurements during the monotonic heating process were started at 5°C, and then obtained at successive increments of 2°C (except for initial and final increments of 5°C), all the way to a slurry temperature of 55°C; and by reversing this procedure after the maximum slurry temperature of 55°C was achieved during the heating process, the slurry density measurements during the cooling process were obtained (thus, the encapsulated PCM was in a fully liquid state before the cooling process was initiated). The results yielded by these experiments are shown in Fig. 3.4, along with the reference density values of distilled water [Haar et al. (1984)] for comparison purposes.

As can be seen from the results presented in Fig. 3.4, the effective density of the slurries at any given temperature diminishes with an increase in the mass concentration of the MCPCM. This is to be expected, as the effective density of the MCPCM particles is less than that of distilled water. During the monotonic heating process, a sharp decrease of the effective slurry density occurs between 26°C and 29°C, a temperature range over which most of the PCM melting takes place. During the monotonic cooling process, a sudden increase of the effective slurry density occurs around 19°C, a temperature value which roughly corresponds to the initiation of the PCM solidification when supercooling is required. Consequently, when monotonic heating of the slurries is carried all the way to full melting of the PCM and then the cooling process is initiated, due to the supercooling that is needed to initiated the PCM freezing, there is a hysteresis in the variation of the effective density with temperature: the values corresponding to the monotonic heating and cooling processes differ between 19°C and 30°C, approximately. Outside this temperature range, the effective density of the slurry during the heating and cooling processes is essentially the same, for a fixed MCPCM mass concentration.

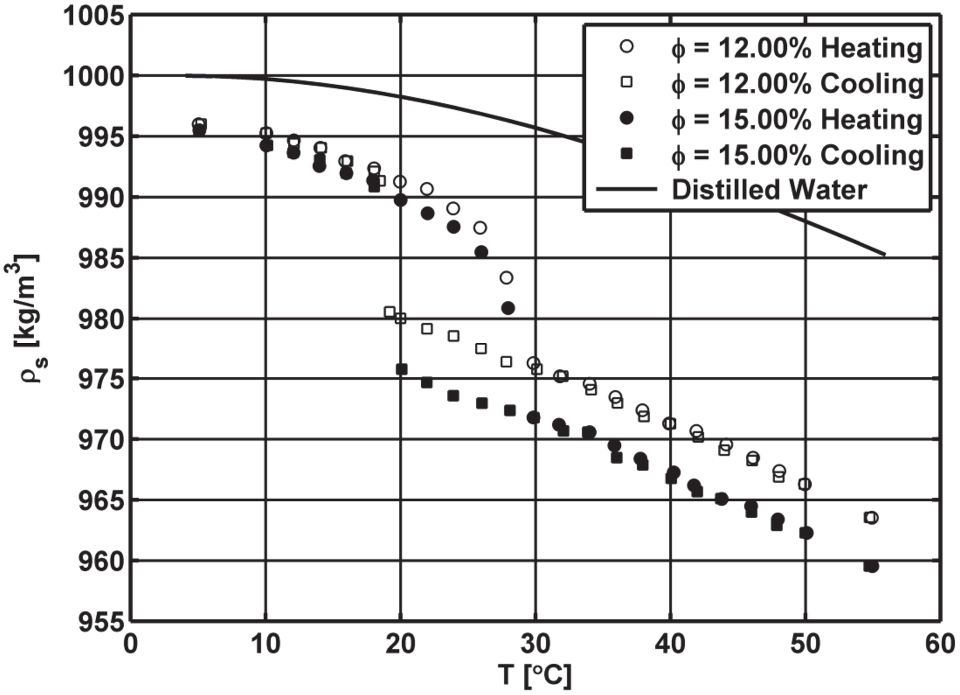

Figure 3.4: Variation of the effective density of MCPCM slurries with temperature during monotonic heating and cooling processes (with cooling initiated after full melting of the PCM), for MCPCM mass concentrations of 12% and 15%.

With the values of the effective density of the slurries, ρ_s, at hand, it was possible to calculate the effective density of the MCPCM particles, ρ_{MCPCM}, using the reference values of the density of distilled water density, ρ_{H_2O}, and Eq. (3.2). These calculated values of ρ_{MCPCM}, obtained with the values of ρ_s for the slurries of 12.00% and 15.00% MCPCM mass concentrations, are plotted in Fig. 3.5 as a function of temperature, for both the monotonic heating and cooling processes.

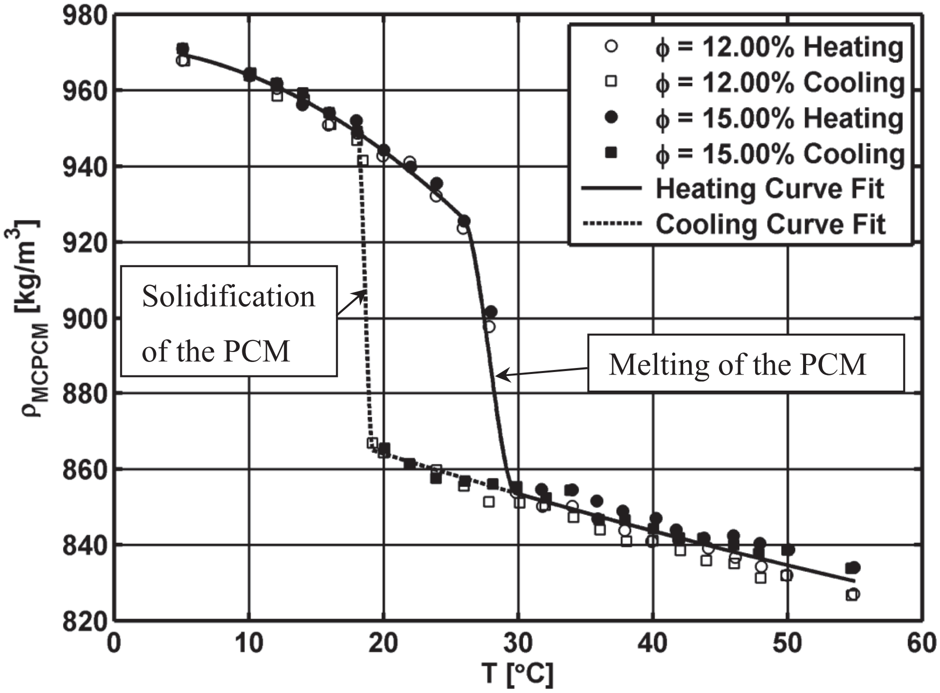

Figure 3.5: Effective density of MCPCM particles with respect to temperature and curve fits for the heating and cooling processes.

As is shown by the results presented in Fig. 3.5, the agreement between the values of ρ_{MCPCM} calculated with the ρ_s values for the slurries of 12% and 15% MCPCM mass concentrations is very good. The sudden decrease and increase in the values of ρ_{MCPCM} corresponding to the melting and freezing temperature ranges of the encapsulated PCM is again observed, along with the hysteresis effect caused by the supercooling requirement. A three-region polynomial function was fitted to the ρ_{MCPCM} data for both the monotonic heating and cooling processes. The resulting curve fits are the following:

Monotonic heating process:

$$\begin{aligned}
&\text{For } 5\,^{\circ}\text{C} \le T \le 25.9\,^{\circ}\text{C:}\\
&\rho_{MCPCM} = -6.157\text{x}10^{-2}T^2 - 1.564\text{x}10^{-1}T + 9.717\text{x}10^2\\
&\text{For } 25.9\,^{\circ}\text{C} < T \le 29.85\,^{\circ}\text{C:}\\
&\rho_{MCPCM} = 2.083T^3 - 1.739\text{x}10^2T^2 + 4.812\text{x}10^3T - 4.3256\text{x}10^4\\
&\text{For } 29.85\,^{\circ}\text{C} < T \le 55\,^{\circ}\text{C:}\\
&\rho_{MCPCM} = 3.977\text{x}10^{-3}T^2 - 1.258T + 8.876\text{x}10^2
\end{aligned} \tag{3.4}$$

Monotonic cooling process (initiated after full melting of the PCM):

$$\begin{aligned}
&\text{For } 5\,^{\circ}\text{C} \le T \le 18.05\,^{\circ}\text{C:}\\
&\rho_{MCPCM} = -6.157\text{x}10^{-2}T^2 - 1.564\text{x}10^{-1}T + 9.717\text{x}10^2\\
&\text{For } 18.05\,^{\circ}\text{C} < T \le 19.21\,^{\circ}\text{C:}\\
&\rho_{MCPCM} = 1.049\text{x}10^2T^3 - 5.868\text{x}10^3T^2 + 1.092\text{x}10^5T - 6.7582\text{x}10^5\\
&\text{For } 19.21^{\circ}\text{C} < T \le 55\,^{\circ}\text{C:}\\
&\rho_{MCPCM} = 3.977\text{x}10^{-3}T^2 - 1.258T + 8.876\text{x}10^2
\end{aligned} \tag{3.5}$$

In these equations, T is in °C and ρ_{MCPCM} is in kg/m^3. It is worth noting that the effective density values prescribed by the above-mentioned polynomial functions for the monotonic heating and cooling processes are identical outside the temperature range for which a hysteresis effect is present: that is, below $18.05\,^{\circ}\text{C}$ and above $29.85\,^{\circ}\text{C}$ in this case (these temperature values were based on differential scanning calorimetry data presented later in this chapter). This is an expected result, as the values of the effective density of the MCPCM outside the hysteresis region should not differ for the heating and cooling processes.

In the 1-D/2-D model proposed in Chapter 2 for the simulations of the fluid flow and heat transfer phenomena in the thermosyphon (see Figure 2.1) operating with the above-mentioned MCPCM slurries, the effective density of the MCPCM is prescribed as follows: 1) if the MCPCM in the slurry enters the heating section in the fully frozen (solid) state and leaves it in the fully melted (liquid) state with temperatures exceeding 32.5 °C, then supercooling is needed to freeze the MCPCM in the cooling section, and Eqs. (3.4)-(3.5) are employed in the detailed CVFEM simulations in the heating and cooling sections, respectively; and 2) if the MCPCM in the slurry enters the heating section in the fully frozen (solid) state and leaves it only in a partially melted (part solid and part liquid) state with all temperatures below 28°C, then supercooling is not needed to freeze the MCPCM in the cooling section (no hysteresis is involved), so Eq. (3.4) is employed in the detailed CVFEM simulations in both the heating and cooling sections. Lastly, it should be noted that in the numerical simulations of the closed-loop thermosyphon operating with the slurries, the effective density of the MCPCM slurry, ρ_s, is computed by using Eq. (3.2), with the values of ρ_{H_2O} calculated using curve fits to the available reference data (see Appendix A) and the values of ρ_{MCPCM} computed using Eqs. (3.4)-(3.5), as needed (in accordance with the discussions given earlier in this paragraph).

3.4 Effective Thermal Conductivity of the Slurries and the MCPCM

As was mentioned earlier, Scott (2006) worked with the same MCPCM particles as those used in this work. As a part of his investigations, he conducted experiments to determine the effective thermal conductivity of MCPCM slurries during a monotonic heating process that started with the PCM in the fully solid phase, proceeded through the PCM melting temperature range, and ended with the PCM in the fully liquid state. In this work, the effective thermal conductivity data obtained by Scott (2006) was adapted to a monotonic cooling process that started with the PCM in the fully liquid state and ended with the PCM in the fully solid state, after going undergoing supercooling.

Scott (2006) designed and constructed an apparatus analogous to a parallel-plate thermal conductivity cell to obtain the above-mentioned effective thermal conductivity data. He first validated his experimental setup by measuring the thermal conductivity of distilled water and then comparing his results with reference data found in the literature. He then measured the effective thermal conductivity of the MCPCM slurries, k_s, for three different values of the MCPCM mass concentration: 5.33%, 10.15% and 15.25%. Using this data in Eq. (1.1), which is adapted from the work of Maxwell (1954), Scott

(2006) calculated the effective thermal conductivity of MCPCM particles. This equation is repeated below convenience:

$$\frac{k_s}{k_{H_2O}} = \frac{2k_{H_2O} + k_{MCPCM} + 2\varphi\left(k_{MCPCM} - k_{H_2O}\right)}{2k_{H_2O} + k_{MCPCM} - \varphi\left(k_{MCPCM} - k_{H_2O}\right)} \tag{3.6}$$

In Eq. (3.6), φ denotes the volume concentration of the MCPCM particles. The relation between the MCPCM mass concentration ϕ and its volume concentration φ is given by:

$$\varphi = \phi\left(\frac{\rho_s}{\rho_{MCPCM}}\right) \tag{3.7}$$

After processing his results, Scott (2006) observed that the value of k_{MCPCM} primarily depended on the state of the PCM, as follows:

$$\begin{aligned} k_{MCPCM,solid} &= 0.171\,\text{W/m°C} \\ k_{MCPCM,liquid} &= 0.097\,\text{W/m°C} \end{aligned} \tag{3.8}$$

These values were found to be essentially constant over the temperature ranges investigated for the solid and liquid states of the PCM. In the calculation of k_{MCPCM}, Scott (2006) assumed that the change of phase of the PCM occurs about a single temperature value, even though the melting and freezing phenomena take place over a temperature range. Such a treatment was found to provide satisfactory accuracy in the numerical investigations [Scott (2006); Scott, Lamoureux, Baliga (2010)]. Therefore, it was also adopted in this work, as follows:

Monotonic heating process:

$$\begin{aligned} &\text{For } 5\,^{\circ}\text{C} \le T \le 28.64\,^{\circ}\text{C:} \\ &k_{MCPCM} = 0.171\,\text{W/m°C} \\ &\text{For } 28.64\,^{\circ}\text{C} < T \le 55\,^{\circ}\text{C:} \\ &k_{MCPCM} = 0.097\,\text{W/m°C} \end{aligned} \tag{3.9}$$

Monotonic cooling process (initiated after full melting of the PCM):

$$\begin{aligned}&\text{For } 5\,^{\circ}\text{C} \le T \le 18.06\,^{\circ}\text{C:}\\&k_{MCPCM} = 0.171\,\text{W/m°C}\\&\text{For } 18.06\,^{\circ}\text{C} < T \le 55\,^{\circ}\text{C:}\\&k_{MCPCM} = 0.097\,\text{W/m°C}\end{aligned} \tag{3.10}$$

In Eq. (3.9), the change from the solid-phase to the liquid-phase values of k_{MCPCM} is assumed to occur at 28.64°C, a value which corresponds roughly with the end of the melting-temperature range of the PCM (this value was determined in differential scanning calorimetry studies, which are described in the next subsection). In Eq. (3.10), which corresponds to a monotonic cooling process that includes supercooling, the change from the liquid-phase to the solid-phase values of k_{MCPCM} is prescribed at 18.06°C, the temperature at which the solidification process is initiated when supercooling of the PCM is necessary. The effective thermal conductivity of the slurry, k_s, can be computed with Eq. (3.6) once the values of φ, k_{MCPCM}, and k_{H_2O} (see Appendix A) have been evaluated. The predicted values of k_s for the monotonic heating process are compared with the data of Scott (2006) for three different MCPCM mass concentrations in Fig. 3.6. The thermal conductivity values of distilled water are also shown in Fig. 3.6, for comparison purposes. The maximum relative difference between the predicted values of k_s and the experimental data of Scott (2006) was less than 2.5%. This level of agreement was judged satisfactory for the present work.

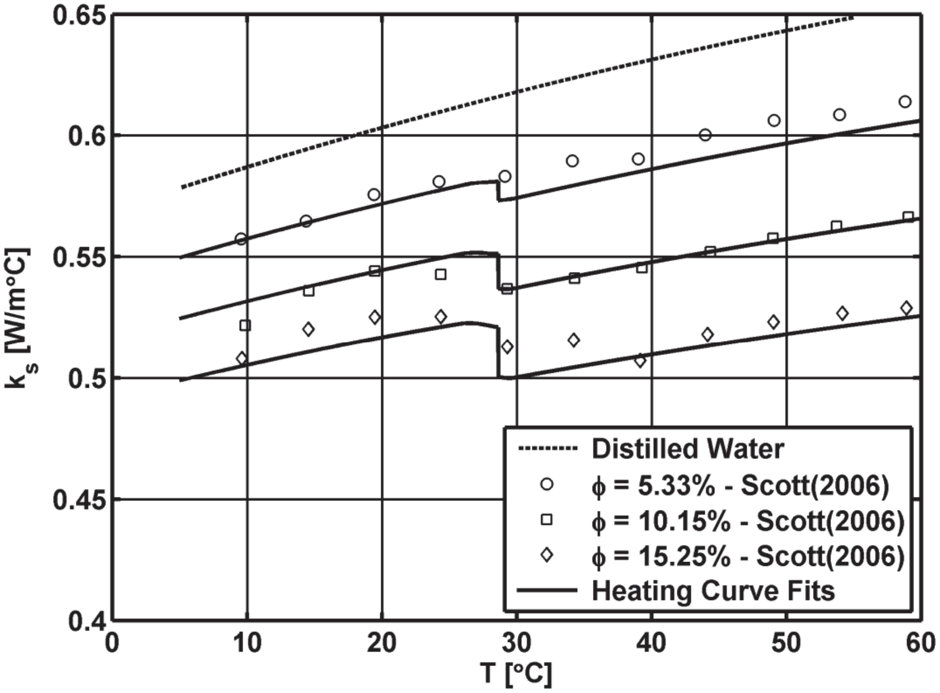

Figure 3.6: Effective thermal conductivity data of Scott (2006) for slurries of three different MCPCM mass concentrations, corresponding predictions obtained with Eq. (3.6) for the monotonic heating process, and reference data for distilled water.

Scott (2006) assumed that micro-convection effects, which could result in an increase of the effective thermal conductivity of the slurry, were negligible in his work. In some previous studies of forced convection heat transfer with MCPCM slurries [Zhang and Faghri (1995), Charunyakorn et al. (1991)], the increase of k_s due to micro-convection effects has been expressed as a function of a particle Péclet number, defined as $Pe_p = |\left(dw/dr \right)| \, d_p^2 / \left(k_l / \rho_l c_{P,l} \right)$. Scott (2006) calculated the maximum value of this particle Péclet number encountered in his mixed-convection experiments with the MCPCM slurries, and concluded that for all practical purposes, the effects of micro-convection on the effective thermal conductivity were negligibly small. The maximum velocity gradients observed in this work are even smaller in magnitude than those encountered in the work of Scott (2006). Thus in this work too, it was assumed that the micro-convection effects were negligibly small.

3.5 Effective Specific Heat, Latent Heats of Melting and Solidification, Phase-Change Behavior, and Melting and Freezing Temperature Ranges of the MCPCM

A differential scanning calorimeter (DSC) was used to determine the effective specific heat, the latent heats of melting and solidification, the phase-change behavior, and the melting and freezing temperature ranges of the MCPCM. These experiments were conducted with a Q100 DSC manufactured by *TA Instruments*. This instrument allows a wide range of temperature ramping rates (starting as low as 0.2°C/min) in both the positive and negative directions. This DSC was operated in the so-called standard (non-modulated) mode, as this setting was found to be more reliable when the phase-change phenomena were present. The Q100 DSC and the cooling system that was used in this work can be seen in the photograph given in Fig. 3.7.

Figure 3.7: Differential scanning calorimeter (*TA Instruments* Q100) and cooling system.

The DSC studies were performed with slurries having relatively high MCPCM mass concentrations, to better capture the contribution of the MCPCM particles to the effective specific heat of the slurries. The values of the MCPCM mass concentration of the slurries that were used in these studies are the following: 19.99%, 29.91% and 50.2% (pure MCPCM paste). In each case, a small amount of the slurry was introduced into the sample pans, which were then hermetically sealed with crimped lids. The mass of the slurry samples was measured with a *Sartorius* CP225D digital scale (capacity of 220g, accuracy of ± 0.02mg) which was fitted with a draft shield. The mass of the slurry samples ranged between 12.37mg to 17.67mg, and the mass of the sample pans varied between 55.56mg and 55.87mg.

First, the DSC and the procedures used in the studies were validated by measuring the specific heat of distilled water and comparing the results to reference data found in the literature. In this validation experiment, the specific heat of the distilled water sample was measured using temperature ramping rates of 0.2°C/min, 1.0°C/min and 2.0°C/min and the following procedure:

1. Stabilize sample temperature at 1°C.
2. Increase the sample temperature at the chosen ramping rate until it reaches 60°C.
3. Stabilize the sample temperature at 60°C.
4. Decrease the sample temperature at the chosen sampling rate until it reaches 1°C.

The maximum observed discrepancy between the measured and reference values of the specific heat of distilled water was less than 1.5%, and the average discrepancy between these values was less than 1%, for all three temperature ramping rates (0.2°C/min, 1.0°C/min and 2.0°C/min), between 5°C and 55°C (the temperature range of interest in this work). This level of precision was deemed satisfactory for the main DSC experiments performed with the MCPCM slurries.

The main DSC experiments were then conducted with MCPCM slurries having mass concentrations of 19.99%, 29.91% and 50.2% (pure MCPCM paste), with temperature ramping rates of 0.2°C/min, 1.0°C/min and 2.0°C/min. The four-step procedure presented above for the preliminary DSC experiments with distilled water was also followed during the DSC experiments with the MCPCM slurries, with a sole exception: for the ramping rate of 0.2°C/min, the maximum sample temperature was limited to 40°C, instead of 60°C. This restriction was invoked to ensure that the experiments performed at this ramping rate could be completed within reasonable overall time limits. Also, the experiments conducted with this lowest temperature ramping rate (0.2°C/min) were mainly aimed at measuring the shape of the effective specific heat curve over the phase-change temperature range of the MCPCM particles. The 1°C to 40°C temperature range of these experiments comfortably encompasses the phase-change effects of the MCPCM particles for both the heating and cooling processes. The data yielded by the DSC experiments performed with the higher ramping rates of 1.0°C/min and 2.0°C/min were judged to be more accurate outside the phase-change temperature range, and they were therefore used to model the effective MCPCM specific heat curve in the sensible heating and cooling regions (additional details on the curve-fitting approach are presented later in this subsection).

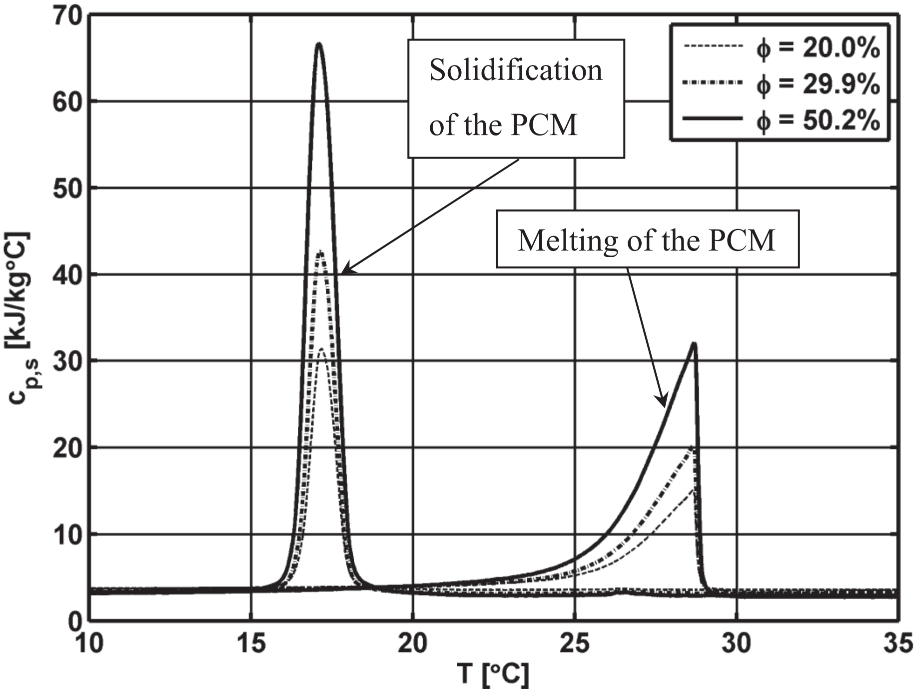

Figure 3.8: DSC measurements of the effective specific heat of slurries having MCPCM mass concentrations of 19.99%, 29.91% and 50.2% (ramping rate: 0.2°C/min).

The effective specific heats, $c_{p,s}$, of slurries having mass concentrations of 19.99%, 29.91% and 50.2% are plotted as functions of temperature in Fig. 3.8, for a temperature ramping rate of 0.2°C/min. As was expected, the melting and solidification peaks increase in magnitude as the MCPCM mass concentration increases. Also, the results show that supercooling is necessary to initiate the freezing when the cooling process is initiated after full melting of the PCM.

Using the values of the measured effective specific heat of a slurry, $c_{p,s}$, of a particular MCPCM mass concentration and the reference specific heat of distilled water, c_{p,H_2O}, as discussed in Appendix A, the value of the effective specific heat of the MCPCM particles, $c_{p,MCPCM}$, can be computed using the relation described in Eq. (2.19), and repeated below for convenience:

$$c_{p,s} = \phi c_{p,MCPCM} + \left(1-\phi\right) c_{p,H_2O} \tag{3.11}$$

The values of $c_{p,MCPCM}$ which were computed with $c_{p,s}$ values of a slurry having an MCPCM mass concentration of 50.2% are shown in Fig. 3.9, for the three different temperature ramping rates used in the DSC experiments. These results show that the higher temperature ramping rates smear the melting and solidification peaks, spreading them over a wider temperature range. Therefore, the lowest ramping rate (0.2°C/min) was chosen to obtain the shape of the effective specific heat curve ($c_{p,MCPCM}$ vs. T) in the phase-change regions. Data measured with this lowest ramping rate was also used to determine the PCM melting and freezing temperature ranges, and the corresponding latent heats of melting and solidification. However, the higher ramping rates were used to obtain the effective specific heat curve ($c_{p,MCPCM}$ vs. T) in the sensible heating and cooling regions, as they yield more accurate results when phase-change phenomena are absent.

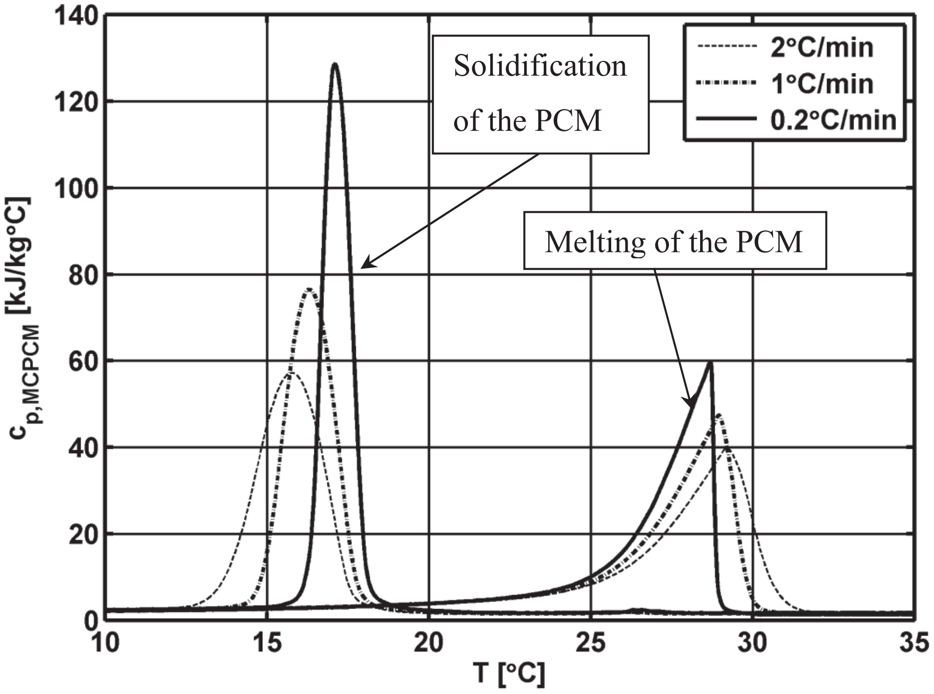

Figure 3.9: Effective specific heat of the MCPCM particles calculated with DSC data obtained with ramping rates of 0.2°C/min, 1.0°C/min and 2.0°C/min, and MCPCM mass concentration of 50.2%.

Quantitative results obtained from the DSC experiments on the MCPCM slurries are summarized in Table 3.1. In this table, the following notation is used: $T_{melting\ onset}$ denotes the temperature at which melting of the PCM starts; $T_{melting\ main\ range}$ is the temperature range over which melting of the PCM mainly occurs; $T_{max\ PMNSCNH}$ is the limiting temperature at which if a heating process is halted with the PCM in a partially melted state and a cooling process is initiated, then freezing of the PCM can be achieved with no supercooling and there is no hysteresis (in that the variations of the effective thermophysical properties of the MCPCM slurries with temperature during this heating process also apply during the subsequent cooling process, provided the maximum temperature does not exceed $T_{max\ PMNSCNH}$); $T_{melting\ completed}$ denotes the temperature at which melting of the PCM is completed; $T_{freezing\ SC\ onset}$ and $T_{freezing\ SC\ end}$ represent the temperatures at which freezing of the supercooled PCM starts and ends, respectively; and the latent heats of melting and freezing (when supercooling is required) of the MCPCM particles are denoted as $\lambda_{melting,MCPCM}$ and $\lambda_{freezing,MCPCM}$, respectively.

Table 3.1: Phase-change characteristics of the MCPCM.

$T_{melting\ onset}$	20.0°C
$T_{melting\ main\ range}$	25.8°C $\leq T \leq$ 28.6°C
$T_{max\ PMNSCNH}$	28.0°C
$T_{melting\ completed}$	32.5°C
$T_{freezing\ SC\ onset}$	18.06°C
$T_{freezing\ SC\ end}$	15.0°C
$\lambda_{melting,MCPCM}$	129.5 kJ/kg
$\lambda_{freezing,MCPCM}$	134.0 kJ/kg

The values of $T_{max\ PMNSCNH}$ and $T_{melting\ completed}$ were determined by performing the abovementioned four-step DSC experiment with a ramping rate of 1.0°C/min, trying different values of the melting temperature limit in the range 27.0°C to 33.0°C, with differences of 0.5°C between these trial values. In each of these tests, the measured effective specific heat curve of the subsequent cooling process was inspected and compared with its heating counterpart: for maximum heating temperatures less than or equal to 28°C, the measured effective specific heat curve during cooling was essentially identical to that obtained during heating, and there was no evidence of supercooling or hysteresis; this phase-change behavior is referred to as the partial-melting-no-supercooling-no-hysteresis (or PMNSCNH) process, as was discussed above. When the slurry temperature reached or exceeded 32.5°C during the heating process, full melting of the PCM was achieved, and during the subsequent cooling process, supercooling to a temperature of 18.06°C was required to initiate freezing of the encapsulated PCM: this phase-change process is referred to as the full-melting-supercooling-with-freezing-and-hysteresis (or FMSCWFH) process, as it involves full melting, freezing with supercooling, and hysteresis in the variation of the effective thermophysical properties of the MCPCM slurries with temperature; for such cases, it is necessary to use different sets of effective-property correlations for the heating and cooling processes. It was also found in these DSC experiments that if the increase in the slurry temperature during the heating process is halted between 28.0°C and 32.5°C, and then the cooling process is started, part of the liquid PCM solidifies in the melting-temperature range, but to achieve full solidification, the temperature of the remaining (supercooled) liquid PCM must be lowered to a value equal to or below 18°C (this supercooled freezing is indicated by a second freezing peak in the DSC measurements). For this special case, the effective specific heat of the MCPCM particles becomes additionally dependent on the maximum temperature reached during the melting process. This special case was not investigated in the main experiments involving the closed-loop thermosyphon operated with the MCPCM slurries, nor was it investigated in the corresponding numerical simulations undertaken in this work. Rather, in these main experiments and numerical simulations, only the above-mentioned FMSCWFH and PMNSCNH processes were investigated.

Another heating and cooling process of interest involves the following sub-processes: an initial heating process to temperatures beyond $T_{melting\ completed}$ (= 32.5°C), so that full melting of the PCM is achieved; and then a cyclical cooling and heating process that does not involve any temperature below $T_{freezing\ SC\ onset}$ (= 18.06°C), so the PCM remains in a liquid phase throughout. This process, which is referred to as full-melting-no-supercooled-freezing-no-hysteresis (FMNSCFNH), was not used in the main closed-loop thermosyphon experiments, as it does not involve any latent-heat effects during the cyclical heating and cooling process (started after the initial heating process). However, this process was used in a series of special closed-loop thermosyphon experiments which were undertaken as part of a hybrid technique for determining the rheological properties of the MCPCM slurries. Additional details of this hybrid technique are provided in Section 3.6, and details of the aforementioned special closed-loop thermosyphon experiments are provided in Appendix C.

The latent heat of melting and freezing of the MCPCM particles, $\lambda_{melting,MCPCM}$ and $\lambda_{freezing,MCPCM}$, were determined to be 129.5 kJ/kg and 134.0 kJ/kg, respectively. The latent heat of freezing is slightly higher than the latent heat of melting because the value of the effective MCPCM specific heat $c_{p,MCPCM}$ during sensible heating or cooling (no phase change) with the PCM in the liquid state is slightly lower than that when it is in the solid state. Since the difference between the values of specific enthalpy of the MCPCM evaluated at two different temperatures outside the phase-change temperature range (15.0°C to 32.5°C) must be identical regardless of whether the phase-change process involves melting or freezing, the value of the latent heat during the freezing process must be slightly larger than its value during the melting process, to compensate for the relatively lower specific heat of the liquid PCM over the sensible cooling region (32.5°C to 18.06°C). With the values of $\lambda_{melting,MCPCM}$ and $\lambda_{freezing,MCPCM}$ at hand, the latent heat of melting and freezing of a slurry of mass concentration ϕ can be calculated using the following relations:

$$\begin{aligned} \lambda_{melting,s} &= \lambda_{melting,MCPCM} \cdot \phi \\ \lambda_{freezing,s} &= \lambda_{freezing,MCPCM} \cdot \phi \end{aligned} \tag{3.12}$$

Polynomial functions were fitted (using a non-linear least-squares procedure) to the MCPCM effective specific heat data for both the heating and cooling processes. For the heating process, the following seven-region polynomial curve fits are proposed:

$$
\begin{aligned}
&\text{For } 5\ {}^{\text{o}}\text{C} \le T \le 20\ {}^{\text{o}}\text{C}: \\
&c_{p,MCPCM} = 2.442\text{x}10^{-6}\left(T-5\right)^5 - 6.210\text{x}10^{-5}\left(T-5\right)^4 \\
&\qquad +8.517\text{x}10^{-4}\left(T-5\right)^3 - 1.982\text{x}10^{-3}\left(T-5\right)^2 \\
&\qquad +4.451\text{x}10^{-2}\left(T-5\right) + 2.016 \\
&\text{For } 20\ {}^{\text{o}}\text{C} < T \le 27\ {}^{\text{o}}\text{C}: \\
&c_{p,MCPCM} = 2.726\text{x}10^{-3}\left(T-20\right)^5 - 1.925\text{x}10^{-2}\left(T-20\right)^4 \\
&\qquad +6.910\text{x}10^{-2}\left(T-20\right)^3 - 4.970\text{x}10^{-2}\left(T-20\right)^2 \\
&\qquad +4.556\text{x}10^{-1}\left(T-20\right) + 3.823 \\
&\text{For } 27\ {}^{\text{o}}\text{C} < T \le 28.66\ {}^{\text{o}}\text{C}: \\
&c_{p,MCPCM} = 1.037\left(T-27\right)^2 + 1.740\text{x}10^1\left(T-27\right) + 27.87 \\
&\text{For } 28.66\ {}^{\text{o}}\text{C} < T \le 28.72\ {}^{\text{o}}\text{C}: \\
&c_{p,MCPCM} = -4.164\text{x}10^2\left(T-28.66\right)^2 + 2.582\text{x}10^1\left(T-28.66\right) \\
&\qquad +59.60 \\
&\text{For } 28.72\ {}^{\text{o}}\text{C} < T \le 28.9\ {}^{\text{o}}\text{C}: \\
&c_{p,MCPCM} = -2.951\text{x}10^2\left(T-28.72\right) + 59.65 \\
&\text{For } 28.9\ {}^{\text{o}}\text{C} < T \le 29.1\ {}^{\text{o}}\text{C}: \\
&c_{p,MCPCM} = 3.079\text{x}10^2\left(T-28.9\right)^4 - 4.791\text{x}10^2\left(T-28.9\right)^3 \\
&\qquad +2.741\text{x}10^2\left(T-28.9\right)^2 - 6.245\text{x}10^1\left(T-28.9\right) \\
&\qquad +6.533 \\
&\text{For } 29.1\ {}^{\text{o}}\text{C} < T \le 55\ {}^{\text{o}}\text{C}: \\
&c_{p,MCPCM} = 1.620\text{x}10^{-3}\left(T-29.1\right) + 1.668
\end{aligned}
\tag{3.13}
$$

In this equation, $c_{p,MCPCM}$ is in kJ/kg°C and T is in °C. These seven-region polynomial curve fits were necessary to accurately model the values of $c_{p,MCPCM}$ during the melting process. The resulting $c_{p,MCPCM}$ functions are smooth and continuous over the transition points between the different regions. The following desirable property should also be noted: the latent heat of melting computed with the polynomial fits given in Eq. (3.13) for $c_{p,MCPCM}$ is essentially equal to the value measured with the DSC.

The curve-fitting approach described above was also applied to the data pertaining to the cooling (freezing) process, and the following seven-region polynomial curve fits are proposed:

$$
\begin{aligned}
&\text{For } 5\,^{\mathrm{o}}\mathrm{C} \le T \le 15\,^{\mathrm{o}}\mathrm{C}:\\
&c_{p,MCPCM} = 2.442\text{x}10^{-6}\left(T-5\right)^5 - 6.210\text{x}10^{-5}\left(T-5\right)^4\\
&\qquad +8.517\text{x}10^{-4}\left(T-5\right)^3 - 1.982\text{x}10^{-3}\left(T-5\right)^2\\
&\qquad +4.451\text{x}10^{-2}\left(T-5\right) + 2.016\\
&\text{For } 15^{\mathrm{o}}\,\mathrm{C} < T \le 16.35\,^{\mathrm{o}}\mathrm{C}:\\
&c_{p,MCPCM} = 1.609\text{x}10^{1}\left(T-15\right)^5 - 3.072\text{x}10^{1}\left(T-15\right)^4\\
&\qquad +2.053\text{x}10^{1}\left(T-15\right)^3 - 3.719\left(T-15\right)^2\\
&\qquad +6.414\text{x}10^{-1}\left(T-15\right) + 2.738\\
&\text{For } 16.35\,^{\mathrm{o}}\mathrm{C} < T \le 16.9\,^{\mathrm{o}}\mathrm{C}:\\
&c_{p,MCPCM} = -4.900\text{x}10^{2}\left(T-16.35\right)^3 + 4.763\text{x}10^{2}\left(T-16.35\right)^2\\
&\qquad +5.861\text{x}10^{1}\left(T-16.35\right) + 17.41\\
&\text{For } 16.9\,^{\mathrm{o}}\mathrm{C} < T \le 17.3\,^{\mathrm{o}}\mathrm{C}:\\
&c_{p,MCPCM} = 1.612\text{x}10^{2}\left(T-16.9\right)^4 + 3.276\text{x}10^{2}\left(T-16.9\right)^3\\
&\qquad -5.434\text{x}10^{2}\left(T-16.9\right)^2 + 1.752\text{x}10^{2}\left(T-16.9\right)\\
&\qquad +1.122\text{x}10^{2}\\
&\text{For } 17.3\,^{\mathrm{o}}\mathrm{C} < T \le 18.0\,^{\mathrm{o}}\mathrm{C}:\\
&c_{p,MCPCM} = 2.665\text{x}10^{2}\left(T-17.3\right)^3 - 2.863\text{x}10^{2}\left(T-17.3\right)^2\\
&\qquad -7.699\text{x}10^{1}\left(T-17.3\right) + 1.204\text{x}10^{2}\\
&\text{For } 18.0\,^{\mathrm{o}}\mathrm{C} < T \le 18.7\,^{\mathrm{o}}\mathrm{C}:\\
&c_{p,MCPCM} = 1.746\text{x}10^{2}\left(T-18.0\right)^4 - 3.327\text{x}10^{2}\left(T-18.0\right)^3\\
&\qquad +2.405\text{x}10^{2}\left(T-18.0\right)^2 - 8.807\text{x}10^{1}\left(T-18.0\right)\\
&\qquad +17.62\\
&\text{For } 18.7\,^{\mathrm{o}}\mathrm{C} < T \le 55\,^{\mathrm{o}}\mathrm{C}:\\
&c_{p,MCPCM} = 1.620\text{x}10^{-3}\left(T-18.7\right) + 1.651
\end{aligned}
\tag{3.14}
$$

In this equation, $c_{p,MCPCM}$ is expressed in kJ/kg°C and T in °C. Again, these seven-region polynomial curve fits were necessary to obtain accurate and smooth functions over the complete temperature range of interest. As was stated above, the difference between the values of specific enthalpy of the MCPCM evaluated at two different temperatures located outside the phase-change temperature range must be identical for both the heating and cooling processes. To meet this requirement, it was necessary to apply a very slightly correction to the magnitude of the freezing peak: this minor correction consisted of increasing the area under the freezing peak by 0.047%, a modification which barely altered the modeled $c_{p,MCPCM}$ cooling curve. The polynomial curve fits for the variations of $c_{p,MCPCM}$ with temperature during the heating and cooling (with supercooling) processes are depicted in Fig. 3.10, along with the measured values for comparison purposes. As can be seen from these results, the predicted and measured values of the effective specific heat of the MCPCM are essentially indistinguishable.

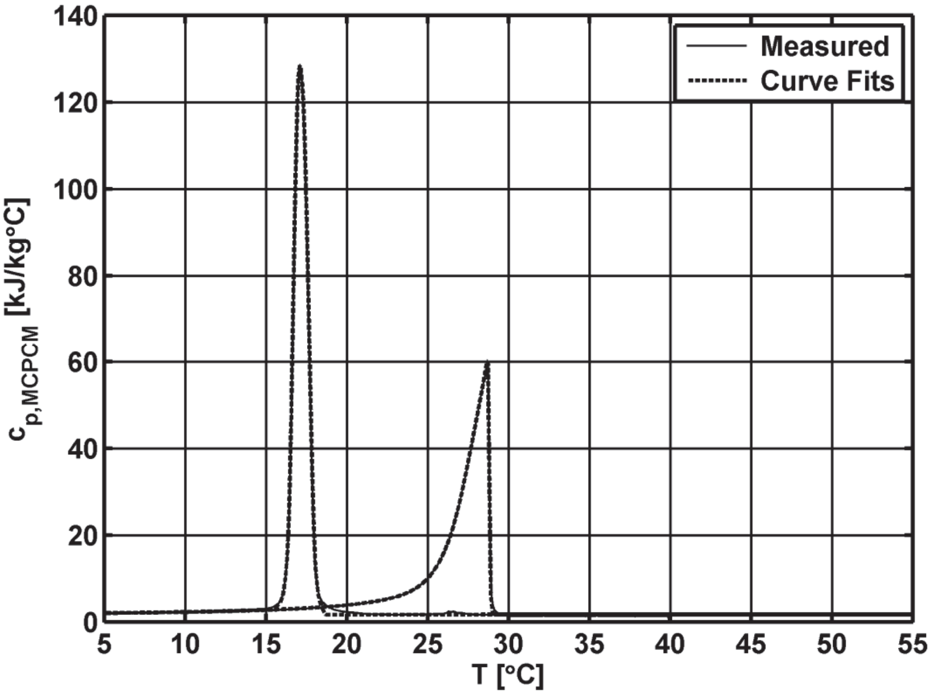

Figure 3.10: Comparison between predicted and measured values of the MCPCM effective specific heat during heating and freezing (with supercooling) processes.

3.6 Rheological Behavior and Effective Dynamic Viscosity of the MCPCM Slurries

As was mentioned in earlier parts of this thesis, the MCPCM used in this work was the same as that used by Scott (2006). He had assumed that the MCPCM slurries behaved as essentially Newtonian fluids for MCPCM mass concentrations of less than or equal to 20%. However, preliminary experiments performed in this work with a cone-and-plate rheometer (*TA Instruments* AR 2000 rheometer) revealed that the MCPCM slurries have a slight shear thinning, non-Newtonian behavior.

In the above-mentioned preliminary experiments performed with the cone-and-plate rheometer, a small quantity of MCPCM slurry was first dropped on a flat plate having a diameter of 40mm and a solid cone was then vertically lowered into position, as shown schematically in Fig. 3.11. The angle between the cone and flat plate was of 2° (this angle is exaggerated in Fig. 3.11). During these experiments, the temperatures of the chamber of this rheometer and the sample were maintained constant at 25°C. The rate of strain, which is essentially constant in the whole sample due to the cone-and-plate geometry, was varied from approximately 3 to 3000s^{-1}, in logarithmic increments (factors of 10). Slurry samples with MCPCM mass concentrations of 12.5%, 15% and 20% were analyzed.

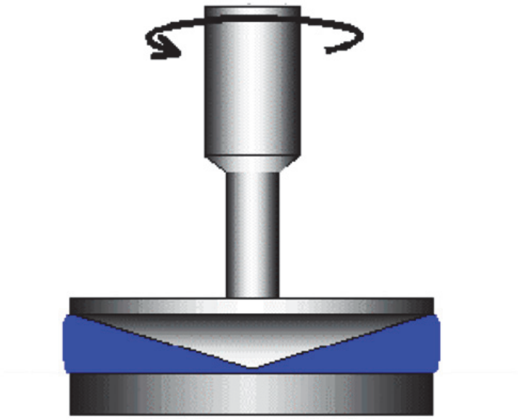

Figure 3.11: Schematic of the cone and plate rheometer geometry (adapted from the *TA Instruments* AR 2000 operator's manual).

These preliminary studies revealed that the MCPCM slurries investigated in this work essentially obey a power-law behavior, analogous to the Ostwald and de Waele model. Thus, the apparent or effective dynamic viscosity of the slurries could be expressed in the following form [Bird et al. (1987)]:

$$\eta_s = \frac{\mu_s}{\mu_{H_2O}} = m\,\dot{\gamma}^{n-1} \tag{3.15}$$

In this equation, η_s is the effective relative viscosity of the slurry (effective dynamic viscosity of the slurry, μ_s, normalized by the dynamic viscosity of distilled water, μ_{H_2O}, at the same temperature); m is a relative consistency index (with respect to distilled water); $\dot{\gamma}$ represents the magnitude of the local rate of strain; and n is the flow behaviour index, the value of which is slightly less than one for the slurries investigated in this work. This shear-thinning power-law behavior has been commonly observed for slurries and suspensions of particles consisting of (or coated with) polymers [Bird et al. (1987); Ferguson and Kembłowski (1991)]. Both m and n are functions of the MCPCM mass concentration, ϕ, of the slurries. The results obtained in these preliminary experiments showed that the value of m increases with the MCPCM mass concentration, and the flow behaviour index, n, starts at values very close to one for low values of the MCPCM concentration, and then decreases gradually as this concentration is increased.

Unfortunately, the values of m and n could not be definitively determined with the above-mentioned rheometer (and, in this work, it was the only rheometer available) for two reasons. First, the agreement between the effective dynamic viscosity data (for the slurries) measured with this rheometer and glass capillary-tube viscometers were less than desirable (for corresponding rates of strain). At relatively high rates of strain ($>300\text{s}^{-1}$) the effective dynamic viscosity measured with the rheometer was in all cases considerably higher than the values obtained with glass capillary-tube viscometers at corresponding rates of strain. As the calibration of the rheometer was done with single-phase viscosity standards, it is probable the aforementioned undesirable results were caused by the migration of the MCPCM particles in the slurries towards the outer portion of the cone-and-plate geometry due to prolonged effects of the centrifugal forces at the higher angular speeds of the cone which are associated with the higher rates of strain. Such a displacement of the MCPCM particles towards the outer portion of the cone-and-plate geometry would increase the local MCPCM particle concentration in the corresponding regions and consequently augment the apparent viscosity that is related the torque measured by the rheometer (the contribution of the viscous shear stress along the outer portion of the cone to the measured torque is greater than that of this stress near the center, because of the longer moment arm). Second, the results provided by the rheometer where found to be unreliable (not repeatable) for relatively low rates of strain (<300 s^{-1}), because the torque exerted by the slurries undergoing the corresponding low levels of viscous shear was very small (at or below the lower limit of the rheometer) and difficult to measure accurately. This limitation could not be circumvented, as the highest rates of strain present in the experimental investigation of the thermosyphon operated with the MCPCM slurries were an order of magnitude lower than the aforementioned value of 300 s^{-1}. Nevertheless, the above-mentioned preliminary experiments with the rheometer were useful in revealing the power-law shear-thinning behaviour of the MCPCM slurries studied in this work. It is also worth mentioning that the observed shear-thinning behaviour could not have been caused by the aforementioned particle migration phenomena, as the measured effective dynamic viscosity decreased with increases in the rates of strain (and corresponding increases in the angular velocity of the cone).

As was mentioned in Chapter 2, the governing equations presented in Section 2.4.2 could be used to model the flow of both Newtonian and non-Newtonian fluids, with appropriate expressions for the effective dynamic viscosity. It was also assumed that the effective dynamic viscosity of the MCPCM slurries could be accurately modeled by the power-law relation given in Eq. (3.15), over the full range of the rates of strain encountered in the thermosyphon experiments. However, it should be noted that for such a power-law model, the predicted effective dynamic viscosity approaches infinity as the rate of strain is reduced to zero, whereas the value of the actual effective dynamic viscosity of the slurries remains finite throughout. This is because the actual effective dynamic viscosity undergoes a transition from a power-law behavior to a constant-value region (for a specified fixed temperature) as the rate of strain is decreased. This transition region generally occurs at very small values of the rate of strain, typically of the order of $10^{-2}s^{-1}$ to $10^{-1}s^{-1}$ [Bird et al. (1987), Ferguson and Kembłowski (1991)], and this transition region for the slurries of interest could not be determined with the instruments available in this work. However, since the rates of strain encountered in the thermosyphon experiments were generally two to three orders of magnitude higher than the aforementioned typical transition values, the power-law model was expected to accurately predict the effective dynamic viscosity of the MCPCM slurries in these experiments. Lastly, very good agreement was obtained between the numerical predictions and the results of the main experiments (these results will be presented in Chapter 6), thereby indicating that the adopted power-law model was accurate in the present context.

The effective *relative* viscosity of the slurries, η_s, given by Eq. (3.15), was assumed to be essentially independent of temperature, over the temperature range encountered in the thermosyphon experiments (5°C to 55°C) This behavior of η_s has been observed in past rheological studies of suspensions [Vand (1945)] and MCPCM slurries [Goel et al. (1994), Inaba et al. (2004)], and it was also confirmed by Scott (2006), albeit in the context of the assumption that the MCPCM slurries behaved as a Newtonian fluid in his experiments. When using Eq. (3.15), the value of the dynamic viscosity of distilled water, μ_{H_2O}, was determined using a curve-fit to reference data found in the literature [Incropera and DeWitt (2002)]: this curve fit is presented in Appendix A. In this context, it should be noted that the temperature dependence of the effective dynamic viscosity of the MCPCM slurries is taken into account by the variation of μ_{H_2O} with temperature.

To prescribe the effective dynamic viscosity of the MCPCM slurries via Eq. (3.15), it is necessary to provide relationships that give m and n as functions of the MCPCM mass concentration of the slurries. A special investigation was undertaken to determine these relationships. The first step in this investigation consisted of performing measurements of the effective kinematic viscosity of the slurries using Cannon-Ubbelohde glass capillary-tube viscometers. A schematic illustration of a Cannon-Ubbelohde glass capillary-tube viscometer is shown in Fig. 3.12. A distinguishing (and very useful) feature of these instruments is that their viscometer constant is essentially independent of temperature. Hence, it was not necessary to correct the measurements of the effective kinematic viscosity for temperature conditions that did not correspond to the temperature at which the viscometers were calibrated. Four different Cannon-Ubbelohde glass capillary-tube viscometers were used to account for the wide range of values of the effective kinematic viscosity displayed by the MCPCM slurries employed in this work. The characteristics of these four viscometers are listed in Table 3.2.

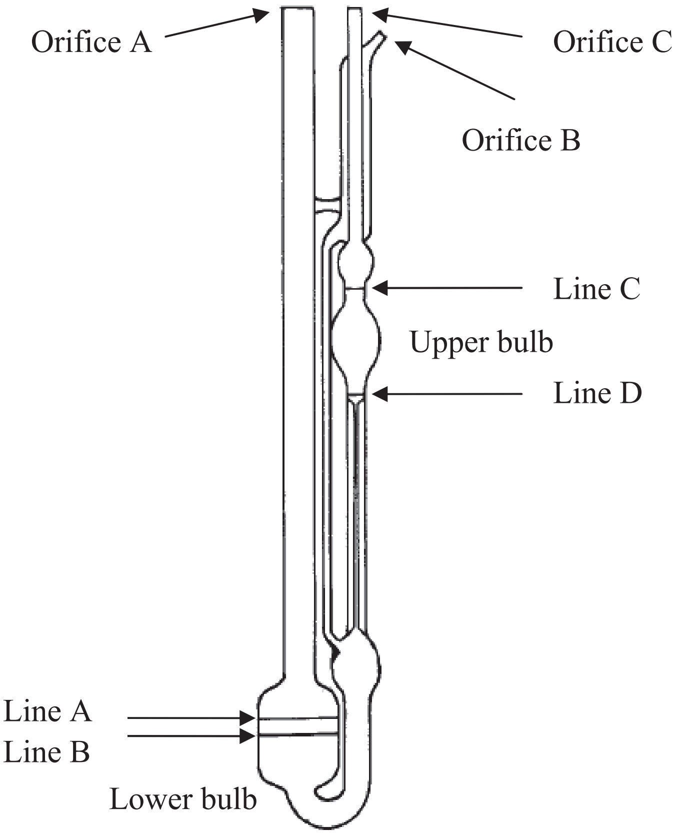

Figure 3.12: Schematic of a Cannon-Ubbelohde glass capillary-tube viscometer.

Table 3.2: Characteristics of the Cannon-Ubbelohde glass capillary-tube viscometers used for measuring the effective kinematic viscosity in this work.

Viscometer / Manufacturer	Range	Capillary diameter	Upper bulb volume
Size 50 / Koehler Instrument Co.	0.8-4 mm^2/s	0.44 mm	3.0 mL
Size 100 / Ever Ready Thermometer Co.	3-15 mm^2/s	0.63 mm	3.0 mL
Size 150 / Cannon Instrument Co.	7-35 mm^2/s	0.78 mm	3.0 mL
Size 200 / Technical Glass Products Inc.	20-100 mm^2/s	0.99 mm	3.0 mL

The measurements of the effective kinematic viscosity were performed at room temperature. The viscometers were supported vertically in these experiments, using a specially designed and constructed holder. The room temperature was monitored with a calibrated thermocouple probe (details of the thermocouples, their calibration, and the data acquisition system used in this work are presented in Chapter 4). Prior to any particular series of measurements, the slurry sample and the viscometer were allowed sufficient time to reach thermal equilibrium with the surrounding air. After this equilibrium was reached, the slurry sample was fed into the lower bulb of the viscometer (see Fig. 3.12) through orifice A, until the liquid-level reached a position between lines A and B. Then, orifice B was sealed using a finger, and a suction bulb fitted to orifice C was used to draw the fluid into the upper bulb until the liquid-level was located above line C. Orifice B was subsequently opened, but the suction bulb was used to keep the slurry sample suspended in the capillary tube and the upper bulb. Finally, the suction bulb was removed from orifice C, and the slurry sample was allowed to flow through the capillary tube. The effective kinematic viscosity of the slurry, υ_s, was then obtained by multiplying the viscometer constant with the time required for the meniscus of the slurry sample to drop from line C to line D (again, see Fig. 3.12 for details). The effective dynamic viscosity of the slurry, μ_s, was then obtained by multiplying υ_s with the effective density of the slurry density, ρ_s, evaluated at the same temperature and the corresponding MCPCM mass concentration, using Eq. (3.4) (the encapsulated PCM was in solid state during these experiments). Lastly, the effective relative viscosity of the slurry, η_s, was obtained by dividing the calculated value of μ_s with the dynamic viscosity of water evaluated at the same temperature.

Before undertaking measurements of the effective kinematic viscosity of the slurries, the glass capillary-tube viscometers and the above-mentioned experimental procedure were benchmarked by making measurements of the kinematic viscosity of distilled water. The size 50 and 100 viscometers (see Table 3.2) were used in these initial experiments. The results obtained showed that the largest discrepancy between measured values of the kinematic viscosity of distilled water and the reference data found in the literature was less than 0.7%, and this level of precision was considered acceptable.

Following the completion of the above-mentioned bench-marking experiments, measurements of the effective kinematic viscosity of the slurries were performed for MCPCM mass concentrations of 7.47%, 10.00%, 12.49%, 14.95%, and 17.50%. Two (minimum) or three viscometers were used for each of these values of the MCPCM concentration, depending on the effective kinematic viscosity of the samples and the measurement range of the available viscometers. For each slurry and viscometer combination, measurements were performed at least three times to establish the reproducibility of the results. The results revealed that for a fixed value of MCPCM mass concentration in the above-mentioned range, the values of effective kinematic viscosity obtained with different viscometers differed slightly. This observation confirmed that the slurries are characterized by a slight non-Newtonian behavior, as the rates of strain prevailing in the capillary tube of the different viscometers are different (for a given MCPCM concentration). This observation also showed that to obtain the actual values of the effective kinematic viscosity, it was necessary to apply a correction to the values yielded by viscometer measurements, as the stipulated constant for each of the above-mentioned viscometers applies strictly only to measurements for Newtonian liquids. Furthermore, since the rate of strain and the corresponding effective kinematic viscosity of the slurry now vary radially inside the capillary tube, the commonly used and convenient practice of assessing their values at the inside surface the capillary tube [Ferguson and Kembłowski (1991)] was adopted to relate the kinematic viscosity to a corresponding rate of strain. The procedure for the evaluation of these quantities at the inside surface of the capillary tube is described next.

The values of kinematic viscosity and the corresponding rate of strain at the inside surface of the capillary tube (which will be referred to as the wall of the capillary tube from this point on, for convenience) are first evaluated without applying any correction, as if they pertain to a Newtonian liquid (and denoted as $\upsilon_{wall,Newtonian}$ and $\dot{\gamma}_{wall,Newtonian}$), as follows:

$$\begin{aligned} \upsilon_{wall,Newtonian} &= C_{visc} t \\ \dot{\gamma}_{wall,Newtonian} &= \frac{32\dot{Q}}{\pi D_{cap}^3} = \frac{32\left(Vol/t\right)}{\pi D_{cap}^3} \end{aligned} \tag{3.16}$$

In this equation, C_{visc} denotes the prescribed viscometer constant, t represents the measured time interval during the experiment, D_{cap} is the diameter of the capillary tube,

$\dot{Q}$ is the time-mean value of the volume flow rate through the capillary tube, and *Vol* represents the volume of the upper bulb bounded by lines C and D depicted in Fig. 3.12. A correction is first applied to $\dot{\gamma}_{wall,Newtonian}$, to account for the alteration of the classical Poiseuille parabola for the velocity profile (for a fully-developed Newtonian fluid flow in a capillary tube) by the non-Newtonian nature of the liquid, and obtain the actual value, $\dot{\gamma}_{wall}$. For a power-law behavior of the liquid, such as the one presented in Eq. (3.15), the actual rate of strain at the wall is obtained as follows [Ferguson and Kembłowski (1991)]:

$$\dot{\gamma}_{wall} = \left(\frac{3n+1}{4n} \right) \dot{\gamma}_{wall,Newtonian} \tag{3.17}$$

In Eq. (3.17), n is the flow behavior index. If $n = 1$, the fluid is Newtonian and the correction factor is equal to unity, as expected.

Next, a correction is applied to the kinematic viscosity measurement. The average wall shear stress for a Newtonian fluid flowing inside the capillary tube of a given viscometer is given by the following equation:

$$\tau_{wall,Newtonian} = \mu_{wall,Newtonian} \dot{\gamma}_{wall,Newtonian} = \rho \left(C_{visc} t \right) \dot{\gamma}_{wall,Newtonian} \tag{3.18}$$

The expression for $\dot{\gamma}_{wall,Newtonian}$ given in Eq. (3.16) is now introduced in Eq. (3.18), to obtain the following result:

$$\tau_{wall,Newtonian} = \rho C_{visc} \frac{32 Vol}{\pi D_{cap}^{3}} \tag{3.19}$$

Eq. (3.19) shows that the shear stress prevailing on the wall of the vertical capillary tube depends solely on the density of the liquid being tested and the viscometer geometry (assuming fully-developed flow prevails over the majority of the capillary-tube length and the effects associated with the acceleration of the liquid are essentially negligible). This wall shear stress in a specific viscometer would be essentially the same for Newtonian and non-Newtonian liquids of the same density. Thus, $\tau_{wall,Newtonian}$ is equivalent to τ_{wall} for a non-Newtonian liquid of the same density, and the value of υ_{wall} for a non-Newtonian liquid can be evaluated as follows:

$$\upsilon_{wall} = \frac{\mu_{wall}}{\rho} = \frac{\tau_{wall}}{\rho \dot{\gamma}_{wall}} = \frac{\rho \left(C_{visc} t \right) \dot{\gamma}_{wall,Newtonian}}{\rho \dot{\gamma}_{wall}} = \left(C_{visc} t \right) \frac{\dot{\gamma}_{wall,Newtonian}}{\dot{\gamma}_{wall}} \tag{3.20}$$

Using the expression for $\upsilon_{wall,Newtonian}$ given in Eq. (3.16) and the correction for the wall rate of strain given in Eq. (3.17), the effective kinematic viscosity for a non-Newtonian liquid can be obtained by correcting $\upsilon_{wall,Newtonian}$ as follows [Leblanc et al. (1998)]:

$$\upsilon_{wall} = \upsilon_{wall,Newtonian} \left(\frac{4n}{3n+1} \right) \tag{3.21}$$

To apply the corrections specified in Eqs. (3.17) and (3.21), the flow behavior index of the slurry sample, *n*, must be known. A well-known approach to determining the value of *n* consists of obtaining kinematic viscosity measurements for the same slurry, but at different rates of strain, using multiple capillary-tube viscometers (normally five or more). Another approach is to use a specially-built capillary-tube apparatus which allows control of the wall shear stress (and strain rate). The data obtained using one or the other of these approaches are then curve-fitted with a power-law relation, and the value of *n* is determined, which then allows the evaluation of m. Unfortunately, in this work, the maximum number of glass capillary-tube viscometers available for such measurements on any given slurry was limited to only two for some concentrations. Furthermore, though the rates of strain associated with the kinematic viscosity measurements with the two viscometers in such cases were different, they were of the same order of magnitude: thus, the results yielded by curve-fitting data obtained with these two viscometers lacked accuracy, especially when the shear-thinning behavior was only slight, as was the case for the MCPCM slurries used in this work.

To overcome the above-mentioned difficulty, a hybrid technique was designed and implemented to determine the values of m and *n*, for the values of MCPCM mass concentration used in this work. This technique involves a combination of raw data from measurements with the glass capillary-tube viscometers, measurements from closed-loop thermosyphon experiments specially undertaken in this context (and quite different from the main closed-loop thermosyphon experiments), and numerical simulations of the flows of the MCPCM slurries in these special thermosyphon experiments (using a modified version of the 1-D/2-D model described in Chapter 2).

The first step of this hybrid technique is to provide the raw data obtained from the glass capillary-tube viscometers (in the form of uncorrected effective relative viscosity data) and the corresponding uncorrected rates of strain at the wall as inputs to a modified version of the 1-D/2-D thermosyphon model described in Chapter 2. These uncorrected effective relative viscosity data are plotted with respect to their corresponding uncorrected rates of strain in Fig. 3.13. As seen from the uncorrected results in this figure, the relative viscosity at a given rate of strain increases with MCPCM mass concentration. The shear-thinning (non-Newtonian) behavior of the slurries becomes increasingly apparent at higher particle concentrations.

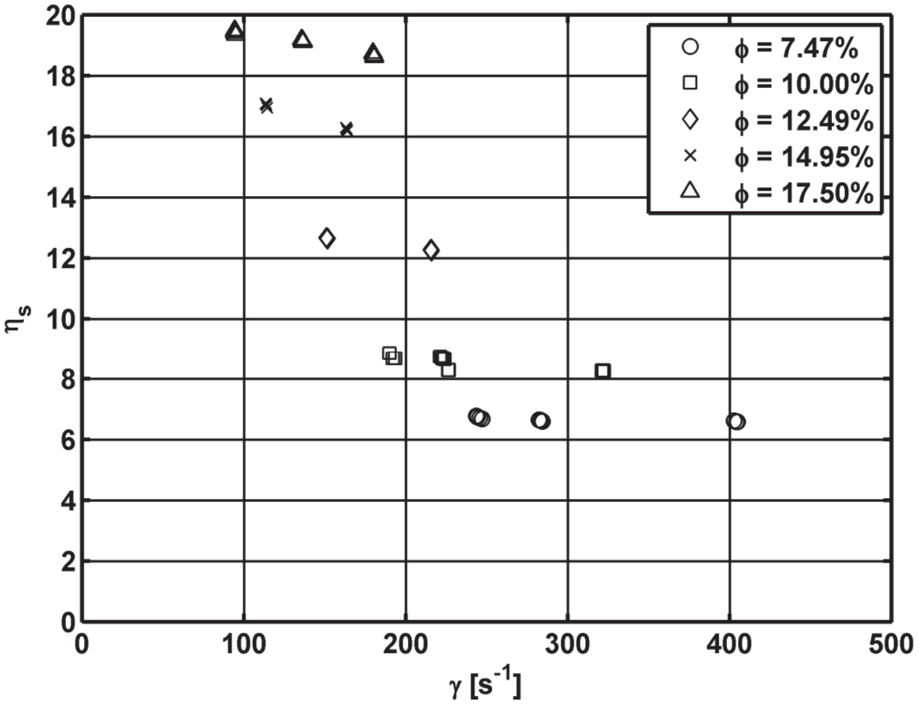

Figure 3.13: Variation of the effective relative viscosity of the slurries with the corresponding rates of strain (data not corrected for non-Newtonian behavior).

For each value of the MCPCM mass concentration, with the uncorrected data shown in Fig. 3.13 as inputs, a modified version of the 1-D/2-D model of the thermosyphon was used, in conjunction with results obtained from the aforementioned series of special closed-loop thermosyphon experiments, to iteratively solve for the corresponding values of m and n. The special closed-loop thermosyphons experiments used in this technique involved the full-melting-no-supercooled-freezing-no-hysteresis (FMNSCFNH) process discussed earlier in Section 3.5. Additional details of these special experiments are provided in Appendix C.

In this modified version of the proposed 1-D/2-D thermosyphon model, the average velocity w_{av} is not solved for iteratively; rather, the experimentally measured value of w_{av} is provided as an input (along with the aforementioned uncorrected data depicted in Fig. 3.13), and the values of m and n are determined. The procedure is summarized below:

1. Specify the value of w_{av} measured in an experiment performed with the thermosyphon apparatus operating with a slurry of a given MCPCM mass concentration, ϕ. Also provide the corresponding experimental parameters, such as the total heating power, the cooling water temperature, and the room temperature.

2. Propose $n = 1$ (Newtonian behavior) as an initial guess value of n, and provide the uncorrected effective relative viscosity data (pertaining to the given mass concentration, ϕ) and the corresponding uncorrected rates of strain as additional inputs to the 1-D/2-D thermosyphon model.

3. If necessary (for $n \neq 1$), apply the corrections specified in Eqs. (3.17)-(3.21) to the uncorrected relative viscosity data and the corresponding uncorrected rates of strain.

4. With the latest available value of n, and the *corrected* values of η_s and $\dot{\gamma}$, perform a least-square regression curve fit to obtain the value of m associated with the mass concentration of the slurry.

5. Using the specified value of w_{av}, solve the detailed 2-D axisymmetric flow and heat transfer problems in the vertical heating and cooling sections, and also the 1-D problems in the remaining portions of the closed-loop thermosyphon. Using these numerical solutions, calculate the cumulative viscous shear force acting on the inside surface of the pipe.

6. Using the overall momentum balance [Eq. (2.46)], compute the cumulative viscous shear force acting along the inner pipe surface that would yield the prescribed value of w_{av}. Compare this value of cumulative viscous shear force with that computed in Step 5, and correct the latest available value of the flow behavior index *n* as follows: i) decrease its value if a higher values of viscous wall shear stress are needed to attain the value of w_{av}, or ii) increase its value if the opposite case is encountered.

7. Monitor convergence until all specified criteria are met (the main criterion used in this procedure was $\{\left|n_{new} - n_{old}\right| / n_{old}\} \leq 10^{-6}$). Return to step 3 and repeat this procedure until convergence is attained.

This iterative procedure was used for each of the previously mentioned MCPCM mass concentrations to determine the values of m and *n*, with inputs from the above-mentioned special thermosyphon experiments conducted with the MCPCM slurries operating in the full-melting-no-supercooled-freezing-no-hysteresis (FMNSCFNH) process (again, details of these special thermosyphon experiments for all five MCPCM mass concentrations used in this work are provided in Appendix C). The proposed hybrid technique for determining the rheological properties of the MCPCM slurries was inspired by a procedure employed by Nir and Acrivos (1974) to deduce the effective dynamic viscosity of slurries at near-zero rates of strain using inputs from an investigation of natural convection in an enclosure.

The values of *n* yielded by the proposed hybrid technique were used to obtain the following curve-fit relation for predicting the value of *n* as a function of MCPCM mass concentration, ϕ:

$$n = -1.132\text{x}10^3\phi^4 + 3.979\text{x}10^2\phi^3 - 4.068\text{x}10^1\phi^2 + 1 \quad (3.22)$$

The mean relative difference between the values of n yielded by the proposed hybrid technique and the values obtained with Eq. (3.22) is 2.0% over the range of MCPCM mass concentrations investigated; and the maximum discrepancy, observed at ϕ = 17.50%, is 5.3%. Considering the nature of this rheological investigation, this precision was deemed acceptable for the present work. It is worth noting that the value of n predicted by Eq. (3.22) for an MCPCM mass concentration of zero (distilled water) is unity, the value corresponding to the behavior of a Newtonian fluid. Also, the slope of n at ϕ = 0, $dn/d\phi|_{\phi=0}$, is equal to zero, as the addition of MCPCM particles in minute concentrations (< 1%) in distilled water is not expected to induce a significant shear thinning behavior. Lastly, the accuracy of the relation proposed in Eq. (3.22) is expected to be best for MCPCM mass concentrations in the range $7.5\% \le \phi \le 17.5\%$, the range of ϕ over which the effective dynamic viscosity investigations were conducted. This range also corresponds to the MCPCM mass concentrations of the slurries that were used in the main experiments performed with the thermosyphon apparatus.

The corresponding values of m yielded by the proposed hybrid technique for each of the MCPCM mass concentrations of interest are shown in Fig. 3.14, along with the proposed curve-fit relation. This relation for predicting the value of m as a function of the MCPCM mass concentration, ϕ, is the following:

$$m = 1.297\text{x}10^3\phi^3 + 7.451\text{x}10^2\phi^2 + 7.044\text{x}10^1\phi + 1 \quad (3.23)$$

In Eq. (3.23), the units of m are seconds to the power n-1 [s^{n-1}]. The value of m predicted by the proposed curve-fit relation at ϕ = 0 is equal to unity, which is the appropriate value for distilled water. The mean and maximum relative differences between the values of m yielded by the proposed hybrid technique and the values obtained with Eq. (3.23) are 1.5% and 3.5%, respectively. It is worth noting that the proposed curve fits for n and m do not depend on the state (solid or liquid PCM) of the MCPCM particles, as the PCM remains encapsulated at all times, and effects of the associated volume changes of the MCPCM particles (the relative change of the effective particle diameter, due to the change of phase of the PCM, was less that 5%) on these rheological parameters were negligibly small.

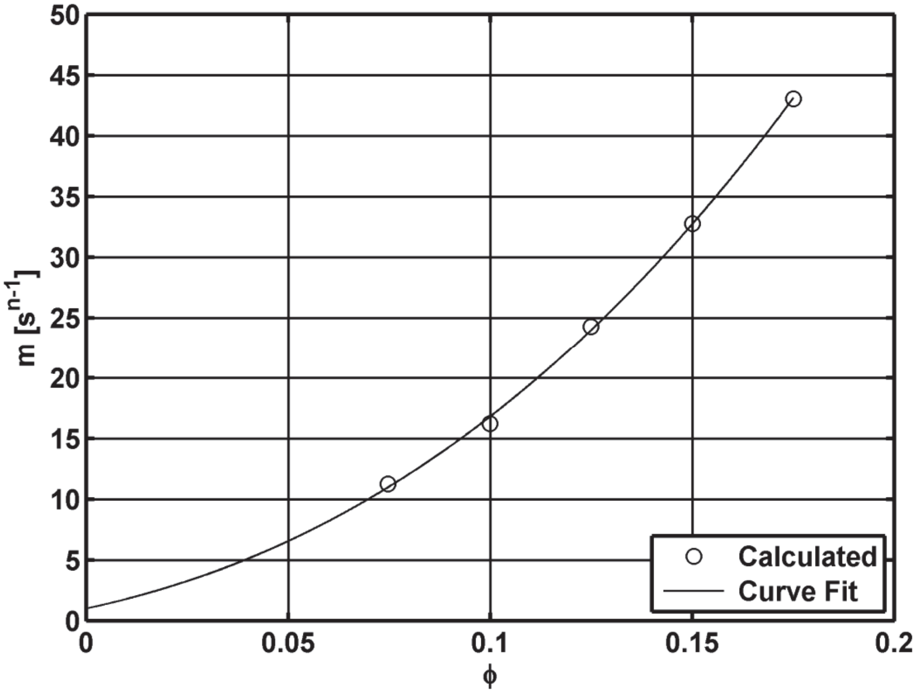

Figure 3.14: Values of the relative consistency index *m* yielded by the proposed hybrid technique, as a function of MCPCM mass concentration.

Lastly, the magnitude of the local rate of strain, $\dot{\gamma}$, which is used in Eq. (3.15) for the calculation of the local effective dynamic viscosity of the slurry, is related to the radial gradient of the axial velocity for one-dimensional shear flows, such as the fully-developed flows of the MCPCM slurries in the glass capillary-tube viscometers used in this work. For multidimensional flows of so-called generalized Newtonian fluids, $\dot{\gamma}$ is taken to be the magnitude of the rate-of-strain tensor [Bird et al. (1987)]. Therefore, for the two-dimensional axisymmetric flows of the MCPCM slurries in the vertical heating and cooling sections of the closed-loop thermosyphon investigated in this work, the value of $\dot{\gamma}$ was obtained using the following equation [Bird et al. (1987)]:

$$\dot{\gamma} = \sqrt{\frac{1}{2}\left[2\left(\frac{\partial v}{\partial z}+\frac{\partial w}{\partial r}\right)^2 + 4\left(\frac{v}{r}\right)^2 + 4\left(\frac{\partial v}{\partial r}\right)^2 + 4\left(\frac{\partial w}{\partial z}\right)^2\right]} \tag{3.24}$$

In conclusion, it is noted that the proposed correlations for the effective thermophysical properties of the MCPCM particles and slurries are concisely presented in Appendix B, for convenience.

4. Thermosyphon Apparatus and Experimental Procedures

As was mentioned in Chapter 1, the work presented this thesis mainly involved complementary computational and experimental investigations of steady, laminar, fluid flow and heat transfer in a vertical closed-loop thermosyphon operating with slurries of a microencapsulated phase-change material (MCPCM) suspended in distilled water. In the experimental part of this work, the closed-loop thermosyphon was designed, constructed, assembled, instrumented, insulated, and used. Details of the MCPCM and the slurries, and also experiments that were conducted to determine their effective properties, were presented in Chapter 3. In this chapter, an overview of the closed-loop thermosyphon is provided in the first section. In subsequent sections, details of the various components of the thermosyphon, supporting components and instrumentation, and various experimental procedures that were employed in this work are presented and discussed.

4.1 Overview of the Closed-Loop Thermosyphon

The bare (uninsulated) closed-loop thermosyphon and its dimensions are schematically illustrated in Fig. 4.1. It was made of two vertical straight pipes connected together by two vertical 180-degree bends made of the same pipe, each of which consisted of two 90-degree circular bends of the same mean radius, R_{bend}, connected together (at one of their ends) by two opposite fittings of a T-junction. All these pipes were of circular cross-section, with the same inside and outside diameters. The left vertical pipe included the heating section, which had an active heating length of L_h. Over this active heating length, a Teflon-insulated nichrome wire, tightly (and closely) wound around the outer wall of the pipe, was electrically heated to provide an essentially uniform wall-heat-flux boundary condition. The right vertical pipe included the cooling section, which had an active cooling length of L_c. This active cooling length was maintained at an essentially constant temperature, T_{cool}, using a concentric annular heat exchanger and distilled water (as the coolant) supplied from a constant-temperature bath.

To accommodate the thermal expansion (and contraction) of the working fluid during the operation of the closed-loop thermosyphon, an expansion chamber was located at the top of the loop. A filling/draining valve and port were incorporated at the bottom of the loop. Four bulk-temperature measurement sections, each with a calibrated sheathed thermocouple probe inserted through a suitable port, were located at the extremities of the left and right vertical pipes.

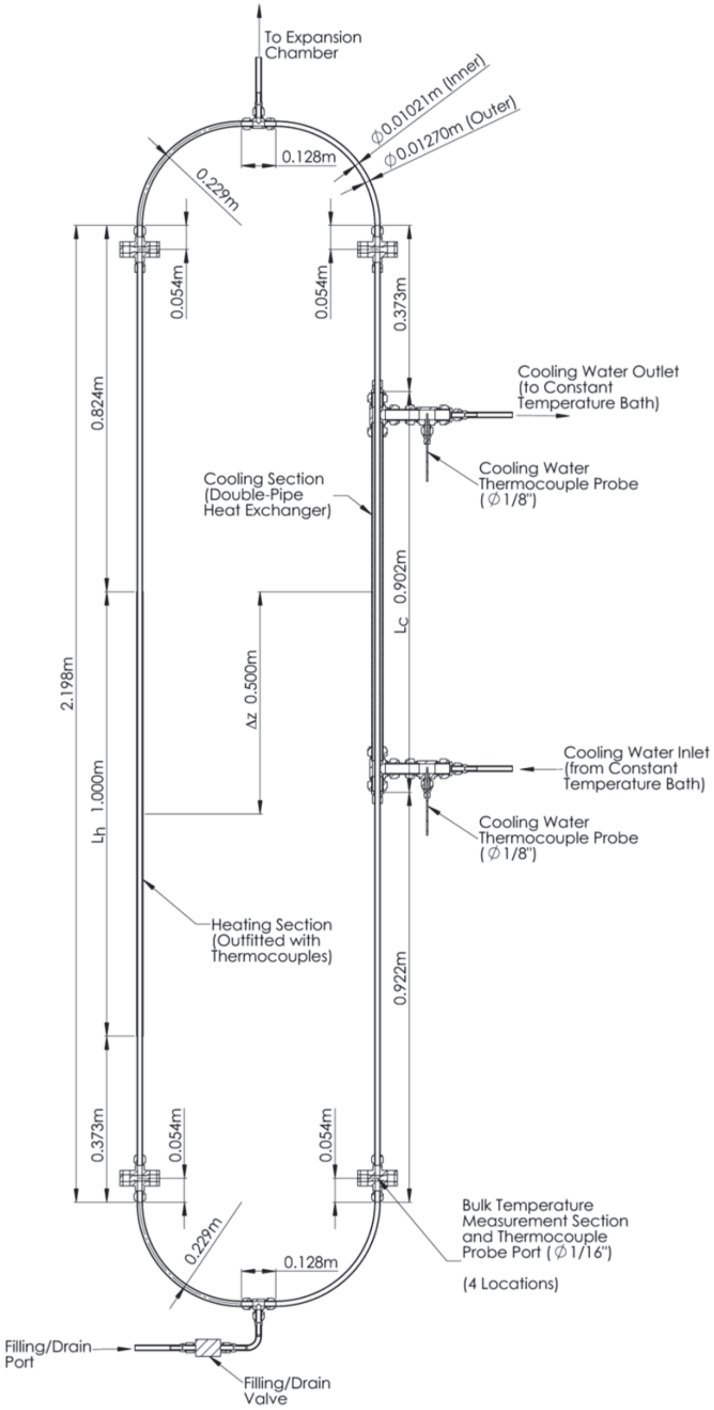

Figure 4.1: Schematic illustration of the bare (uninsulated) closed-loop thermosyphon and its dimensions.

The dimensions of the closed-loop thermosyphon apparatus were determined on the basis on the following considerations: the objectives of this work, as stated in Chapter 1; the space available for this work in the Heat Transfer Laboratory of the Department of Mechanical Engineering at McGill University; the machining facilities, instrumentation, and materials that were either available or accessible for this work; the overall budget for this work; the results of numerous computer simulations based on a preliminary version of the 1-D/2-D model and the numerical solution methods presented in Chapters 2 and 5, respectively; and an assessment of the aforementioned results using the flow regime map of Metais and Eckert (1964), in a manner akin to that discussed in Section 2.8.

The majority of the fluid-flow circuit of the closed-loop thermosyphon was made of stainless steel tubes (316 SS) and *Swagelok* compression fittings. The inner and outer diameters of these stainless steels tubes were 10.21 mm and 12.70 mm, respectively. The left and right vertical pipes (see Fig. 4.1) were each 2.198 m long. The active heating length of the left vertical pipe was $L_h = 1.000$ m, and the active cooling length of the right vertical pipe was $L_c = 0.902$ m. Each of the four 90-degree pipe bends had the same mean radius, $R_{bend} = 0.229$ m. Each of the top and bottom 180-degree bends was constructed by joining two of the aforementioned 90-degree bends with a 0.128 m long horizontal tube segment of a T-junction. The total length of the fluid-flow circuit, based on the centerline of the tubing, was 6.088 m. A minimum of 0.5 liters of working fluid was required for proper operation of the closed-loop thermosyphon.

The center of the active heating portion of the left vertical leg of the closed-loop thermosyphon was positioned at a distance $\Delta z = 0.500$ m below the center of the active cooling portion of its right vertical leg (see Fig. 4.1). For a given power input to the active heating section and a given temperature of the active cooling section, the geometrical parameter, Δz, governs the overall buoyancy force that drives the flow of the working fluid in the closed-loop thermosyphon; and an increase in the value of Δz results in an increase of the average velocity of this working fluid.

The overall set-up for the experiments with the closed-loop thermosyphon included the following supporting components and instrumentation: a DC power supply for the insulated nichrome electrical heating wire wrapped around the active heating section; a digital multimeter to measure the electrical current supplied to this heating wire; 40 calibrated thermocouples for measuring temperatures along the outer surface of the active heating section; a constant-temperature bath for providing cooling water to the concentric annular heat exchanger that surrounds the active cooling section; two calibrated sheathed thermocouple probes positioned near the inlet and outlet of this annular heat exchanger, for measuring the cooling-water temperature at these locations; two calibrated thermocouples located adjacent to the centers of the top and bottom 180-degree bends, for measuring the temperature of the room air at these locations; a data acquisition system interfaced with a personal computer for monitoring and recording the thermocouples outputs and other experimental data; a diaphragm pump, connected to the filling port, to fill the apparatus with the working fluid (distilled water or MCPCM slurries; this port was also used to drain the working fluid after the completion of each series of experimental runs); and a layer of *Armaflex* insulation added over the outer surface of the closed-loop thermosyphon, to minimize heat loses to (or gains from) the ambient environment. The closed-loop thermosyphon was supported and maintained in the vertical position using wood brackets which were mounted on an aluminum-and-wood frame. A photograph of this closed-loop thermosyphon apparatus at an intermediate stage of its construction, with the *Armaflex* insulation installed only on the active heating section and the rest of the sections bare (uninsulated), is shown in Fig. 4.2.

The results of the main experiments conducted with this closed-loop thermosyphon were used to check those obtained by numerically solving the 1-D/2-D model proposed in Chapter 2. These results and comparisons are presented and discussed in Chapter 6. This thermosyphon was also used to run some special experiments which were used to establish the rheological properties of the MCPCM slurries. These special experiments, the corresponding results, and their use to establish the rheological properties of the MCPCM slurries were discussed in Chapter 3.

Additional details of the active heating, active cooling, and bulk-temperature measurement sections are presented in Sections 4.2, 4.3 and 4.4, respectively. The top and bottom 180-degree bends, the expansion chamber, the filling/draining valve and port, the diaphragm pump, and the constant-temperature bath are discussed in Section 4.5. Details of the supporting components and instrumentation are presented in Section 4.6. The experimental procedures for preparing the MCPCM slurries, filling (and draining) the working fluids, and running the main experiments are summarized in Section 4.7. The auxiliary experiment and procedure which were used for determining the overall heat transfer coefficients needed in the calculations of the heat losses to (or gains from) the ambient environment are described in Section 4.8. The technique that was used to determine the mass flow rate and average velocity of the working fluid, its experimental validation, and assessment of the related uncertainties are presented in Section 4.9.

Figure 4.2: Photograph of the closed-loop thermosyphon at an intermediate stage of its construction.

4.2 Active Heating Section

As was mentioned earlier, the active heating section of the closed-loop thermosyphon consisted of a 1.000 m long portion of its left vertical leg, which was a stainless steel tube having inner and outer diameters of 10.21 mm (0.402”) and 12.70 mm (0.5”), respectively, and a total length of 2.032 m, as illustrated schematically in Fig. 4.1. Two *Swagelok* stainless steel ANSI flange adapters, each having a nominal outer diameter (of the flange) of 82.55 mm (3.5”) and bore diameter of 10.41 mm (almost identical to the inner diameter of the stainless steel tube) were fastened to the two ends of this 2.032 m long stainless steel tubing, using compression fittings. The inner surface of this tube-and-flanges combination was smooth, uninterrupted (for all practical purposes), and essentially constant in diameter, except for a minute increase in diameter (less than 2%) inside the flange adapters.

A total of 40 calibrated Type-E thermocouples (30 AWG) were attached to the outer surface of the stainless steel tube of the active heating section. The beads of these thermocouples (suitably insulated) were positioned at the centers of 25 mm (± 0.5mm) axial (lengthwise) intervals along the tube, with the first thermocouple positioned 12.5 mm downstream of the start of the active heating section, in accordance with the following equation:

$$z_{thermocouple} = 25 \times \left(N_{thermocouple} - 1 \right) + 12.5 \tag{4.1}$$

In this equation, $z_{thermocouple}$ represents the axial location (in mm) of thermocouple number $N_{thermocouple}$. The beads of these thermocouples were attached in a helical pattern, with the azimuthal (theta) positions of successive thermocouples differing by 90°±5°: thus, along any straight line parallel to the longitudinal axis of the active heating section, the spacing between any two adjacent thermocouples was 4 x 25 mm (= 100 mm). The fabrication and calibration of these thermocouples (and also the other thermocouples used in the experimental investigation) are discussed in Section 4.6.

A Teflon-coated nichrome heating wire (22 AWG wire; 0.3 mm thickness of Teflon coating) was tightly (and closely) wound around the outer surface of the stainless steel tube of the active heating section. Electrical power input (from a DC power supply) to this nichrome wire coil was used to obtain an essentially uniform heat flux on the outer surface of the stainless steel tube. The Teflon coating ensured that there was no direct electrical contact between the nichrome wire and the outer surface of the stainless steel tube. This Teflon-coated nichrome wire was wound on top of the beads and short portions (of roughly 25 mm length) of each of the aforementioned 40 thermocouples, using a specially designed and constructed jig and procedure (details given later in this section).

Prior to the attachment of the beads of the above-mentioned 40 thermocouples and winding of the Teflon-coated nichrome wire, a thin layer of a high-thermal-conductivity paste (*Omegatherm* 201, thermal conductivity of 2.31 W/m°C) was applied on the outer surface of the active heating portion of the stainless steel tube. This paste was used to reduce the thermal contact resistance between the nichrome wire, and also the thermocouples beads, and the outer surface of the stainless steel tube of the active heating section. Once the nichrome wire was tightly (and closely) wound around the stainless steel tubing, and also the beads and short (roughly 12.5 mm long) portions of each of the 40 thermocouples, the outer surface of this assembly was wrapped with thin Teflon sheets, to contain any excess high-thermal-conductivity paste and provide a clean outer surface that could be conveniently handled during the final assembly of the closed-loop thermosyphon. After the wrapping of these thin Teflon sheets, two 6.35 mm (1/4”) thick and 3.5”x3.5” square blocks of Teflon, each with a 12.70 mm diameter central hole (which matches the outer diameter of the stainless steel tube), were secured at the extremities of the coil of nichrome wire. Electrical bus-bar terminals were attached to each of these Teflon blocks, and the extremities of the nichrome wire were fastened to these terminals. Larger-gauge insulated copper wires (of per-unit-length electrical resistance much lower than that of the nichrome wire) were used to connect these terminals to the main DC power supply unit.

A specially designed and constructed jig was used to wind the Teflon-coated nichrome wire on the outer surface of the active heating portion of the left vertical stainless steel tube. A photograph of this jig is shown in Fig. 4.3. The stainless steel tube was held in place horizontally near its end by two supports. A movable middle support, seen in the bottom-right portion of Fig. 4.3, was also used to prevent the stainless steel tube from bending during the winding of the Teflon-coated nichrome heating wire. A crank and a cross-shaped frame were temporarily fastened to one end of the stainless steel tube. The crank was used to rotate the tube; and this crank could also be locked in place to maintain the tube at a desired angular position. A spool of the Teflon-coated nichrome wire was supported on a solid steel rod whose longitudinal axis was maintained parallel to the axis of the stainless steel tube of the active heating section (as can be seen in Fig. 4.3).

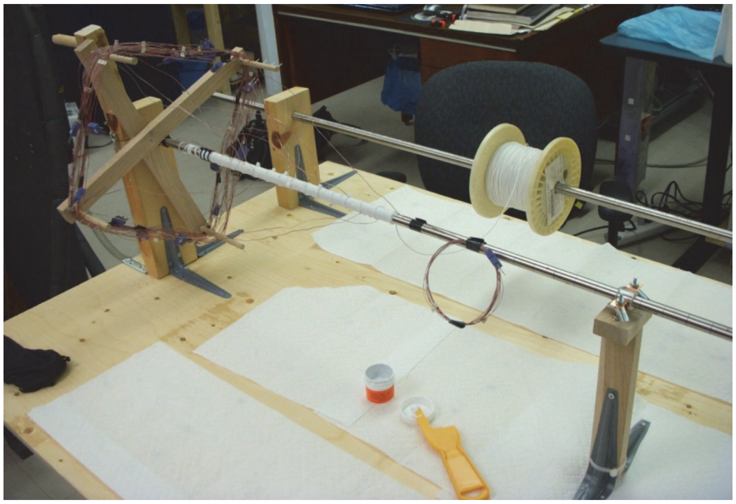

Figure 4.3: Photograph of the jig that was used to wind the Teflon-coated nichrome wire on the outer surface of the stainless steel tube of the active heating section.

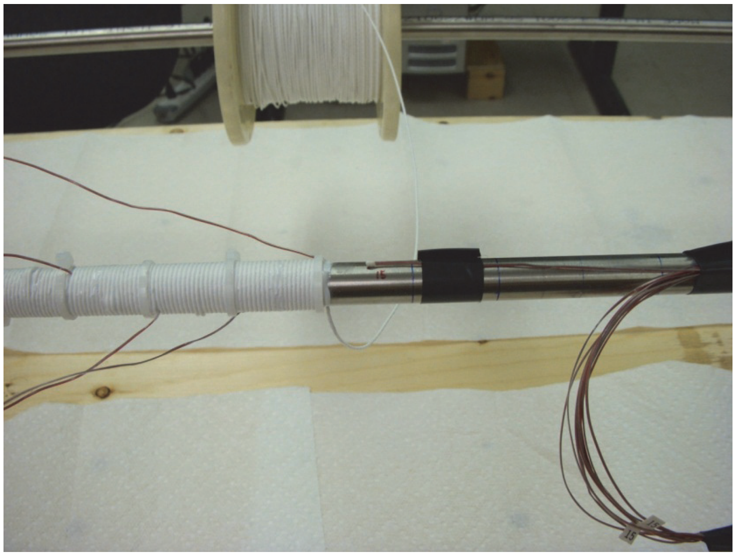

Figure 4.4: Photograph of the active heating section during attachment of the calibrated thermocouples and winding of the nichrome heating wire on its outer surface.

The bead of each of the 40 calibrated thermocouples was made from *Omega* TT-E-30 Teflon-insulated thermocouple wire. The beads were covered with a thin layer of electrically nonconductive epoxy, Omegatherm 101, and were attached (sequentially) to the active heating portion of the left vertical stainless steel tube in the following manner: 1) the thermocouple bead was properly located on the outer surface of the stainless steel tube at the longitudinal center of a 25 mm long sector, in accordance with Eq. (4.1) and the helical pattern discussed earlier in this section; 2) the thermocouple was secured in place temporarily using electrical tape, about 15 mm behind the bead, as can be seen in Fig. 4.4; 3) the 25 mm long tube sector and the thermocouple bead were covered with a high-thermal-conductivity paste (Omegatherm 201); 4) the Teflon-coated nichrome wire was wound tightly and closely around this 25 mm long portion of tube, over the thermocouple bead and wire; 5) a tie-wrap was used to temporarily hold the coiled nichrome wire in place; 6) the electrical tape holding the thermocouple lead wire on the outer surface of the tube was removed; and 7) the thermocouple lead wire was bent away from the outer surface of the tube and secured to the cross-frame fixed at one end of the tube (see Fig. 4.3). This procedure was repeated sequentially until the beads of all 40 thermocouples were attached and the winding of the Teflon-coated nichrome wire was completed.

The above-mentioned procedure for attaching the beads of the thermocouples and winding the Teflon-coated nichrome wire on the outer surface of the active heating section was performed by two persons: the first turned the crank slowly and locked it in place when needed; and the second attached the thermocouples, applied the high-thermal-conductivity paste, and ensured that the Teflon-coated nichrome wire was wound tightly and closely, but without any overlap. Once this procedure was completed, the previously mentioned tie-wraps were successively removed, and thin Teflon sheets were wrapped around the outer surface of the nichrome wire coil and fastened with new tie-wraps. A close-up photograph of a portion of the final assembled active heating section is provided in Fig. 4.5. After the completion of this procedure, the previously mentioned square Teflon blocks and electrical bus bars were installed at the two ends of the nichrome wire coil, and the *Swagelok* ANSI flange adapters were secured at the extremities of the left vertical stainless steel tube.

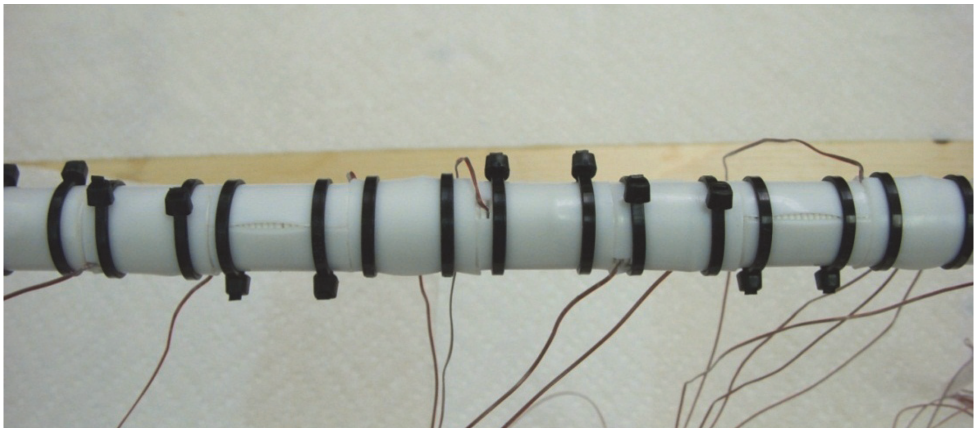

Figure 4.5: Close-up photograph of a portion of the assembled active heating section.

Next, the total electrical resistance of the nichrome wire coil was measured at the laboratory room temperature (approximately 22°C): 119.85 ± 0.1 ohms (this value does not include the resistance of the high-conductivity copper lead wires that were used to connect the nichrome wire coil to the DC power supply). Once finalized, the assembled active heating section was insulated with two layers of *Armaflex* foam pipe insulation (having a thermal conductivity of approximately 0.04 W/m°C). The outer diameter of this insulation was equal to 100 mm (≈4”). After full assembly and insulation of the active heating section, the left leg of the closed-loop thermosyphon was mounted vertically on wooden brackets which were fastened on an aluminum and wood frame (see Fig. 4.2).

4.3 Active Cooling Section

The active cooling section of the closed-loop thermosyphon spanned a 0.902 m long segment of its right vertical leg, which was a stainless steel tube having inner and outer diameters of 10.21 mm (0.402”) and 12.70 mm (0.5”), respectively, and a total length of 2.032 m, as illustrated schematically in Fig. 4.1. This active cooling section was maintained at an essentially constant temperature, T_{cool}, using a concentric annular heat exchanger and water (as the coolant) supplied from a constant-temperature bath at a mass flow rate that was much higher than that of the working fluid circulating inside the closed-loop thermosyphon (for all cases considered in this study). The outer tube of this concentric annular heat exchanger was also made of stainless steel: it was 0.760 m long, its outer diameter was 25.4 mm (1”), and it had *Swagelok* compression fittings on each end.

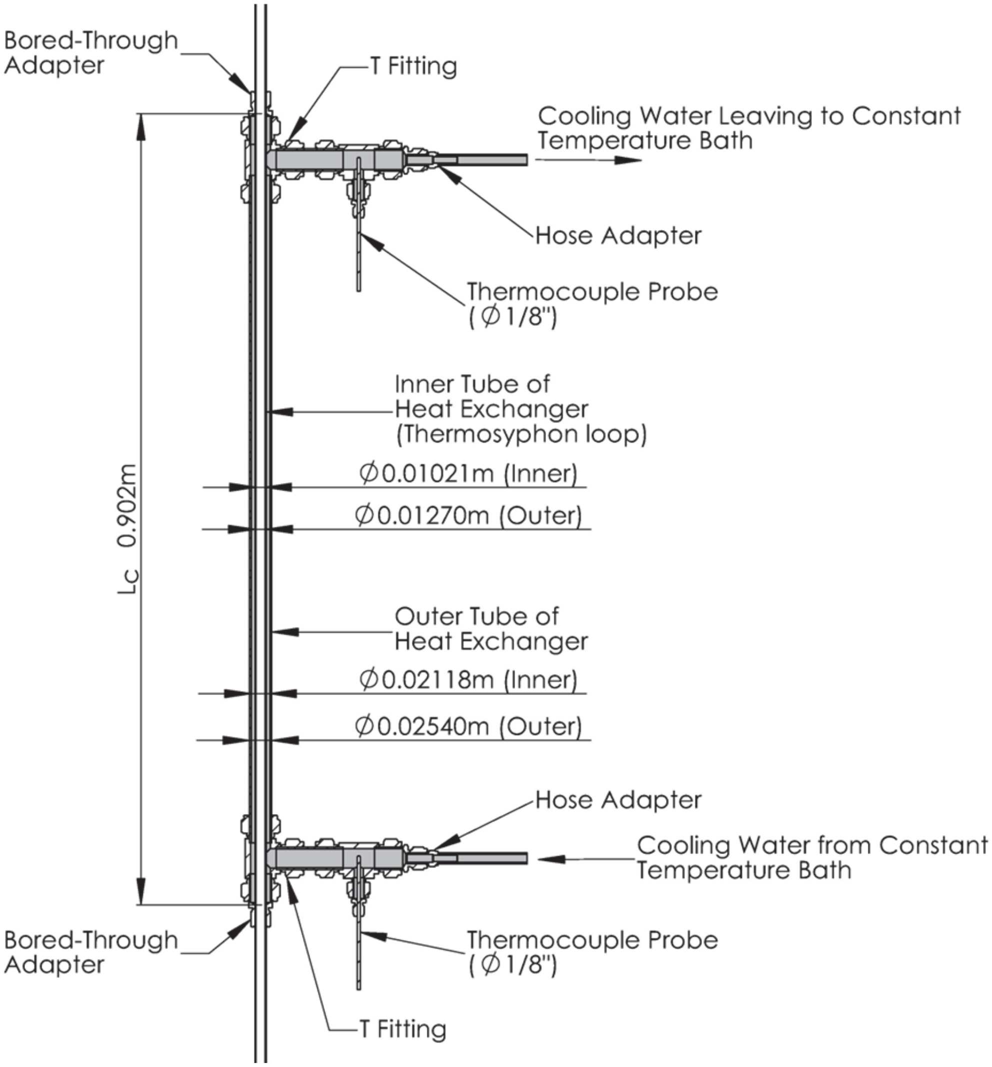

Figure 4.6: Schematic illustration of the cooling section, its components, and key dimensions (*Armaflex* insulation not shown).

A schematic illustration of the active cooling section, along with its various components and key dimensions, is shown in Fig. 4.6 (*Armaflex* insulation is not shown in this figure). The grey area in this figure represents the flow path of the cooling water. In this active cooling section, the working fluid flowed downwards in the smaller tube, and the cooling water flowed in the opposite direction (counter flow), from the bottom inlet port to the top outlet port of the annular region. Two 1/8” diameter sheathed thermocouple probes, which were previously calibrated in accordance with the procedure described in Section 4.6, were inserted through adapter fittings into the cooling water flow, near the inlet and outlet ports. These sheathed thermocouple probes were used to measure the inlet and outlet temperatures of the cooling water, and the mass flow rate of this cooling water was adjusted to ensure that it was high enough to make the difference between the aforementioned temperatures negligibly small: in this work, the maximum observed increase in the cooling-water temperature over the whole active cooling section was less than 0.1°C. In the corresponding numerical simulations, the arithmetic mean of the inlet and outlet temperatures of the cooling water was assumed to be the constant wall temperature, T_{cool}, in the active cooling section. In this context, it should be noted that the thermal resistance associated with radial heat conduction through the stainless steel wall of the inner tube was approximately two orders of magnitude smaller than the thermal resistance of convection heat transfer on the inner surface of this tube (see Section 4.8).

It should be noted that active cooling section was made sufficiently long (0.902 m) to ensure complete freezing of the MCPCM particles with easily achievable cooling-water temperatures, even when supercooling of the PCM was required. In the experiments with the MCPCM slurries, a cooling-water temperature of approximately 13.0°C was sufficient to lower the exit temperature of the MCPCM slurries to below 15.0°C, and hence fully freeze the MCPCM particles.

The assembly of the active cooling section on the right vertical leg of the closed-loop thermosyphon was done in the following manner. The two sheathed thermocouple probes, the two hose adapters (that served as the cooling water inlet and outlet ports), and the corresponding two T-shaped compression fittings (see Fig. 4.6) were assembled first. The outer tube of the annular heat exchanger was attached at its two ends to two additional T-shaped compression fittings. These two T-shaped compression fittings were then mated to the two previously-assembled T-shaped compression fittings (the ones to which the sheathed thermocouple probes and the hose adapters were attached), using short tube junctions (as illustrated schematically in Fig. 4.6). The tube that formed the right vertical leg of the closed-loop thermosyphon was then introduced concentrically into the outer tube assembly, through the bored-through adapters (which were also compression fittings) of the T-junctions, and these compression fittings were then tightened to seal and secure the annular heat exchanger at the desired vertical position (on the right leg). These *Swagelok* T-junctions with the compression fittings allowed a design which ensured that the inner surface of the thermosyphon loop remained smooth, uninterrupted, and essentially unaltered in diameter (except for a minute change in diameter caused by the constriction of the ferules of the compression fitting when they were tightened). Lastly, two *Swagelok* stainless steel ANSI flange adapters, identical to those used on the left vertical leg, were fastened the ends of the stainless steel tube that formed the right vertical leg of the closed-loop thermosyphon.

The right vertical leg of the closed-loop thermosyphon, with the fully-assembled annular heat exchanger of the active cooling section fitted on it, was mounted vertically with wooden brackets fastened to an aluminum and wood frame (see Fig. 4.2). Once mounted, the outer surface of entire right vertical leg of the closed-loop thermosyphon, including the active cooling section, was insulated with two layers of *Armaflex* foam pipe insulation. The outer diameter of this insulation was again essentially equal to 100 mm (≈ 4”). The inlet and outlet ports of the annular heat exchanger of the active cooling section were connected to a constant-temperature water bath (*NESLAB* RTE 221) using flexible *Tygon* tubes having inner and outer diameters of 3/8” and 1/2”, respectively. These Tygon tubes were secured on the barbed hose adapters with stainless steel hose clamps and then insulated with a 12.7 mm (1/2”) thick layer of *Armaflex* insulation.

4.4 Bulk-Temperature Measurement Sections

As is shown in Fig. 4.1, four bulk-temperature measurement sections were used in the closed-loop thermosyphon, and they were located at the junctions of its left and right vertical legs with the top and bottom 180° bends. The working-fluid bulk temperatures measured at the bottom and top of the left vertical leg of the thermosyphon are designated as $T_{b,in,heating}$ and $T_{b,out,heating}$, respectively; and those at the top and bottom of the right vertical leg of the thermosyphon are denoted as $T_{b,in,cooling}$ and $T_{b,out,cooling}$, respectively. A schematic illustration of the components of a bulk-temperature measurement section and also some of its dimensions are shown in Fig. 4.7.

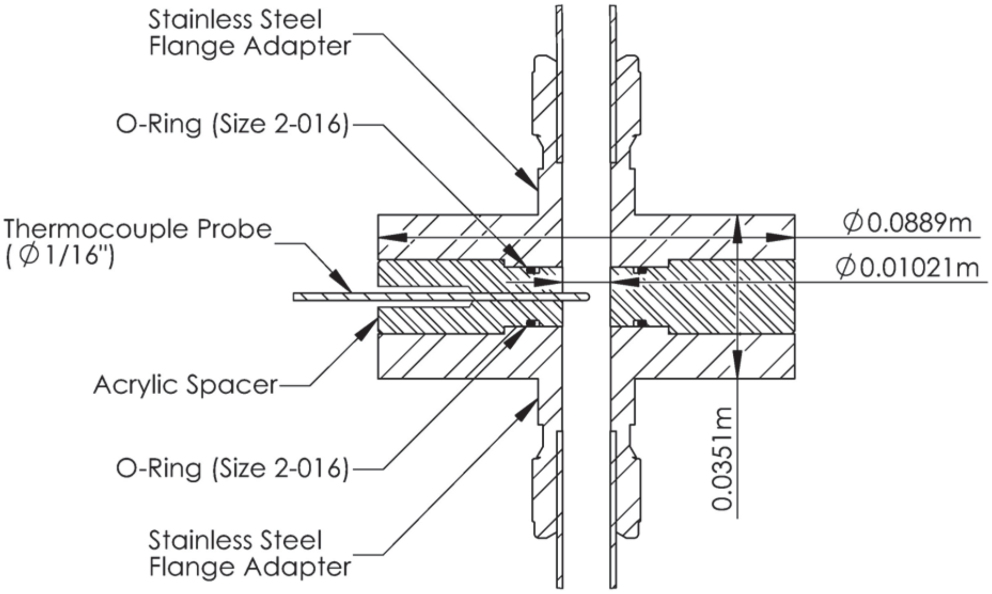

Figure 4.7: Schematic of the components of a bulk-temperature measurement section and some of its dimensions (*Armaflex* insulation not shown).

A calibrated sheathed thermocouple probe (with a 6” long and 1/16” diameter stainless steel sheath) was inserted in each bulk-temperature measurement section, through a lateral hole in the acrylic spacer (see Fig. 4.7). The diameter of this lateral hole over about one-half of its length adjacent to the central orifice of the acrylic spacer was just a tiny bit larger than the diameter of the sheathed thermocouple probe, allowing a slip fit of the latter; and over its other half-length, it had a slightly larger diameter (1/8”). The sheathed thermocouple probe was positioned such that its tip coincided with the longitudinal axis of the central orifice of the acrylic spacer orifice, which was a part of the flow passage of the closed-loop thermosyphon.

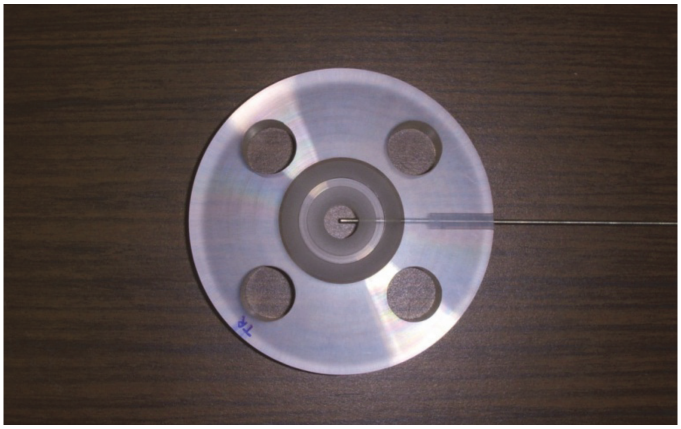

Figure 4.8: Photograph of an acrylic spacer and a sheathed thermocouple probe of a bulk-temperature measurement section.

A photograph of the acrylic spacer with the sheathed thermocouple probe inserted in it is presented in Fig. 4.8. Once this thermocouple probe was inserted and properly positioned inside the lateral hole in the acrylic spacer, a *GE* waterproof silicon sealant was introduced in the larger-diameter portion of the lateral hole, to seal the thermocouple probe in place and prevent leakage of the working fluid out of the closed-loop thermosyphon.

As was mentioned earlier, the four bulk-temperature measurement sections were fitted in between the flanged Swagelok fittings at the extremities of the left and right vertical legs of the closed-loop thermosyphon. Thus, these bulk-temperature measurement sections were located well upstream of the pre-heating and pre-cooling lengths and well downstream of the post-heating and post-cooling lengths of the left and right vertical legs of the closed-loop thermosyphon, respectively, as can be seen in Fig. 2.1 Therefore, inside the central orifice of each of these four bulk-temperature measurement sections, the cross-sectional variation of the working-fluid temperature was negligibly small (as was also confirmed by the numerical simulations, presented and discussed in Chapter 6). Consequently, the temperature measurement yielded by the tip of the sheathed thermocouple probe in each of these sections could be assumed equal to the bulk temperature at that particular location. The maximum uncertainty in the temperature measurements obtained with the calibrated sheathed thermocouple probes was less that ±0.085°C (the calibration of these and other thermocouples is discussed in Section 4.6).

The outer diameter of each acrylic spacer was equal to the diameter of the solid rod from which it was machined (so no machining of the outer surface of the solid rod was required), and the inner surface of the orifice at the center of the acrylic spacer was polished after it was machined, to restore its transparency in the radial direction. These radially transparent curved portions of the acrylic spacers allowed visual inspections of the working fluid and the closed-loop thermosyphon flow circuit at the locations of the thermocouple-measurement sections when desired (for example, during filling, draining, and cleaning operations). Two O-ring grooves (for size 2-016 O-rings) were machined on the two flat surfaces of each acrylic spacer. Each bulk-temperature measurement section was integrated into the closed-loop thermosyphon flow circuit by sandwiching the acrylic spacer (after proper installation of the sheathed thermocouple probe) in between the surfaces of the two adjoining *Swagelok* ANSI flanged compression fittings installed on the ends of the neighboring sections (of either the left or right vertical legs, and the corresponding top or bottom semicircular tubes). Four sets of stainless steel hexagonal-socket-head machine screw (1/2-20, 3”-long), washers, and corresponding nuts were used to hold together each combination of two flanges and the sandwiched acrylic spacer, after insertion of two O-rings (size 2-016) in the aforementioned grooves machined in the two flat mating faces of the acrylic spacer. After assembly of the closed-loop thermosyphon, each bulk-temperature measurement sections was insulated with a one-inch thick layer of *Armaflex* insulation, in a manner that allowed convenient removal and reinstallation of this insulation if visual observations (through the radially transparent curved surfaces of the acrylic spacers) of the working fluid or the flow circuit were desired.

As was discussed in Chapter 2, when the working fluid temperature is uniform over any particular cross-section of the flow circuit within the closed-loop thermosyphon, the modified bulk temperature becomes equal to this uniform temperature [Scott (2006); Scott, Lamoureux and Baliga (2010)]. It should also be noted that the blockages of the flow path caused by the flow-immersed portions of the sheathed thermocouple probes were relatively minor and localized: thus, the viscous and form drag forces on these flow-immersed portions of the probes were very small compared to the viscous shear force prevailing over the complete inner surface of the closed-loop thermosyphon, and the effects of these minor blockages on the overall momentum balance (which was discussed in Chapter 2) could be considered negligible.

4.5 Top and Bottom Tube Bends, Expansion Chamber, Diaphragm Pump, and Constant-Temperature Bath

Details of the top and bottom 180° tube bends, expansion chamber, diaphragm pump, and constant-temperature bath are presented in this section.

4.5.1 Top and Bottom Tube Bends

The top and bottom 180° tube bends in the closed-loop thermosyphon flow circuit were each comprised of two 90° stainless steel tube bends, each with a curvature radius of 0.229 m (based on the centerline of the tube) and joined together (at one of their ends) by two opposite compression-fittings of a *Swagelok* stainless steel T-junction (see Fig. 4.1). The tube bending was performed by *Cintube Ltd*. in Montreal, and special care was taken to ensure that the circular cross-section of the tube remained unaltered, for all practical purposes. Once two of the aforementioned 90° bent tubes were joined together (at one of their ends) by the two opposite fittings of the T-junction, two *Swagelok* stainless steel ANSI flange adapters, identical to those attached to the extremities of the vertical legs of the thermosyphon, were attached to their remaining ends (see Fig. 4.1). The resulting flow paths inside the assembled top and bottom 180° tube bends were smooth and essentially free of any surface discontinuities and inner diameter variations, with the exception of the small opening (10.41 mm in diameter) within each of the two T-junctions, one leading to the port connected to the expansion chamber attached to the top 180° tube bend and the other connected to the filling/draining valve on the bottom 180° tube bend. These two relatively small openings had essentially negligible effects on the overall momentum balance along the flow path inside the closed-loop thermosyphon.

The third leg of the T-junction on the bottom 180° tube bend was connected to a barbed hose adapter, which was connected to one end of a plastic ball valve using a short segment of a *Tygon* tube. This ball valve was opened during the filling and draining operations, and it was kept closed during the thermosyphon experiments. The other end of the ball valve was connected to the female end of a quick-disconnect coupling. During the filling operation, the outlet of a diaphragm pump was connected to this quick-disconnect coupling using *Tygon* tubing, and the ball valve was kept open to allow the working fluid to be pumped into the apparatus. When draining of the apparatus was desired, this ball valve was opened, and the working fluid was collected in a plastic container for possible reuse (additional details of these procedures are presented in Section 4.7).

The third leg of the T-junction on the top 180° tube bend was connected to an expansion chamber, using a short segment of *Tygon* tubing and a quick-disconnect coupling. Details of this expansion chamber are given in the next subsection.

Prior to their connection with the vertical legs (and the bulk-temperature measurement sections) of the closed-loop thermosyphon, the top and bottom 180° tube bends were insulated with two layers of *Armaflex* insulation. The outer diameter of the outermost layer of this insulation was about 100 mm (≈ 4”), matching the insulation on the vertical legs of the closed-loop thermosyphon.

4.5.2 Expansion Chamber

The purpose of the expansion chamber was to accommodate the thermal expansion or contraction of the working fluid circulating in the closed-loop thermosyphon. It ensured that the flow circuit of the thermosyphon remained filled with the working fluid at all times, and there was no spilling of the working fluid out of the apparatus. A photograph of the expansion chamber is shown in Fig. 4.9. It was composed of a 170 mm long transparent tube of 19.05 mm (3/4”) in inner diameter, connected at its two ends to straight barbed hose adapters (3/4” ID to 3/8” ID). The volume of the expansion chamber was roughly 0.05 liters, a value which corresponds to approximately 10% of the total volume of the flow circuit of the closed-loop thermosyphon. The lower port of the expansion chamber was connected to the top 180° tube bend of the thermosyphon, and its top port was exposed to the ambient environment (atmospheric pressure) in the laboratory (via a *Tygon* tube routed downwards, to minimize evaporation and contamination of the working fluid).

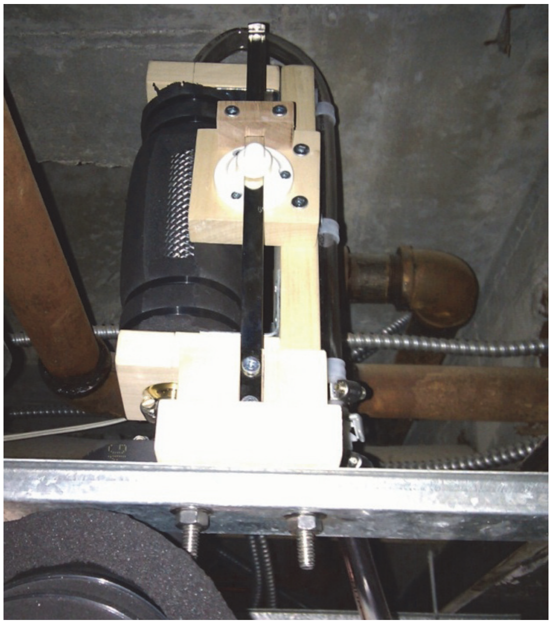

Figure 4.9: Photograph of the expansion chamber.

The transparent tube of the expansion chamber was insulated with a 25.4 mm (1”) thick layer of *Armaflex* insulation and fixed inside a wooden frame which was mounted on the ceiling of the laboratory, in alignment with the apparatus. A small observation window was cut out along the length of this insulation to allow visual inspections of the working fluid level during the filling procedure and also during the operation of the thermosyphon. Prior to any experimental run, the closed-loop thermosyphon was filled until the level of the working fluid reached the mid-position (or half-height) of the transparent tube of the expansion chamber.

4.5.3 Diaphragm Pump

In this work, the working fluid was introduced (filled) in the thermosyphon apparatus using a diaphragm pump: *Masterflex* PTFE diaphragm pump (model 7090-42) attached to a *Masterflex* L/S variable-speed drive. A picture of the diaphragm pump, its variable-speed drive, and Teflon and stainless steel fittings is presented in Fig. 4.10. The main characteristics this diaphragm pump and its variable-speed drive are the following: maximum flow rate of 800 mL/min; maximum drive speed of 600 RPM; maximum pressure of 3.5 bars above atmosphere; and total volume of the pump diaphragm chamber of 16 mL. This pump was selected for this work because the earlier work of Scott (2006) had demonstrated that it did not damage the MCPCM particles in the slurries.

Figure 4.10: Photographs of the diaphragm pump and its variable-speed drive (on the left), and the dampening chamber (on the right).

The diaphragm pump was principally used to fill the working fluid (either distilled water or MCPCM slurries) in the closed-loop thermosyphon. During the filling procedure, the working fluid was drawn from a plastic container using a suitable length of *Tygon* tubing connected to the pump inlet, and it was filled in the thermosyphon from the bottom to the top, using another *Tygon* tube that connected the outlet port of the pump to the ball valve (opened) located at the bottom of the apparatus. The filling procedure was performed at the lowest speed of the pump drive, to prevent unnecessary churning of the working fluid and avoid the formation of air bubbles. This filling procedure also ensured that there were no regions of trapped air (or “dead zones”) in the flow circuit of the closed-loop thermosyphon.

The diaphragm pump was also used in auxiliary experiments that were conducted to 1) determine the overall heat transfer coefficients used for calculating the heat losses to (or gains from) the environment (see Section 4.8), and 2) validate a technique for determining the mass flow rate of working fluid in the closed-loop thermosyphon (see Section 4.9). In both of these auxiliary experiments, the diaphragm pump was used to continuously feed distilled water to the left vertical leg of the thermosyphon, set up in an open-configuration (details provided in Sections 4.8 and 4.9);

and to attenuate the flow pulsations caused by the diaphragm pump, the distilled water was fed to the aforementioned set-up of the left vertical leg via a dampening chamber with a volume of approximately 1.2L (see Fig. 4.10). This dampening chamber was designed and constructed by Scott (2006). It provided essentially smooth and continuous flow of the working fluid at its exit port during these auxiliary experiments.

It should also be noted that with a diaphragm pump, such as the one used in this work, and also all other positive displacement pumps, it is essentially to include a properly-selected pressure relief valve in the flow circuit. Such a valve prevents the increase of pressure in the flow circuit beyond a preset limit by opening a venting port, and thus protects the positive displacement pump (and other flow-circuit components) from getting damaged and, more importantly, ensures the safety of persons who are using or happen to be in the vicinity of the pump and the equipment to which it is connected. In this work, a pressure relief valve (*Swagelok* RL3S4) was connected to the copper tube attached to the top of the dampening chamber (see Fig. 4.10), when the diaphragm pump was used in above-mentioned auxiliary experiments.

4.5.4 Constant-Temperature Bath

In the main closed-loop thermosyphon experiments, a *NESLAB* RTE-221 constant-temperature bath was used to supply the cooling water to the annular heat exchanger of the active cooling section (described in Section 4.3). A photograph of this constant-temperature bath is given in Fig. 4.11. The characteristics of this constant-temperature bath are the following: temperature stability of ±0.01°C; maximum cooling capacity of 500 W; bath volume of 20.5L; and a maximum pumping capacity of 15 liters per minute. The inlet and outlet ports of the bath were connected to those of the active cooling section using suitable lengths of a *Tygon* tube (3/8” ID and 1/2” OD) wrapped with *Armaflex* insulation. As was mentioned previously, the mass flow rate of the cooling water was maintained at a significantly higher value than that of working fluid inside the closed-loop thermosyphon in all of the main closed-loop thermosyphon experiments, which ensured that the tube-wall temperature in the active cooling section was maintained at an essentially constant value. When full solidification of the MCPCM particles in the slurries was desired, the constant-temperature bath was set to maintain the distilled water at 13°C. With this setting, the bulk temperature of the slurry at the exit plane of the active cooling section was always less than 15°C, ensuring full solidification of the MCPCM particles, even for cases in which subcooling of the PCM was required.

Figure 4.11: Photograph of the *NESLAB* RTE-221 constant-temperature bath.

The *NESLAB* RTE-221 constant-temperature bath was also used in auxiliary experiments for calibrating thermocouples (see Section 4.6), determining overall heat transfer coefficients (see Section 4.8), and validating the technique for determining the mass flow rate of the working fluid in the thermosyphon experiments (see Section 4.9).

4.6 Supporting Components, Instrumentation, and Calibration of Thermocouples

Details of the following supporting components and instrumentation are presented first in this section: DC power supplies, multimeter, data acquisition system, and an overheat-safeguard system. Then, details of the thermocouples used in this work and the procedure that was used to calibrate them are presented.

4.6.1 DC Power Supplies, Multimeter, Data Acquisition, and Overheat-Safeguard

A *Sorensen* model DCR 300-3B DC power supply was used in the main thermosyphon experiments, to power the nichrome wire of the active heating section. A photograph of this power supply is given Fig. 4.12. This power supply is capable of supplying voltages ranging between 0 to 300V, and a maximum current of 3A.

Figure 4.12: Photograph of the main DC power supply.

A *Hewlett-Packard* 3478A multimeter was used to measure the electrical current passing through the nichrome wire of the active heating section. The voltage difference across this nichrome wire was measured using the voltmeter of the data acquisition unit (*Hewlett-Packard* 3497A; details presented later in this subsection). The multimeter and the data acquisition unit were hooked up to a personal computer via two-way HP-IB interfaces, enabling essentially real-time data acquisition and control. The measured voltage difference across the nichrome wire and the corresponding electrical current were multiplied to obtain the electrical power input to the active heating section. In the current-measurement mode, the resolution of the HP3478A multimeter is ± 0.01mA and the uncertainty is ± 1mA. The uncertainty of the voltmeter in the HP3497A data acquisition unit is ± 3μV. Using these values in the uncertainty analysis of Kline and McClintock (1953), the accuracy of the power input data was determined to be better than ±0.14% of the values used in this work.

The data acquisition unit (HP3497A), the HP3478A multimeter, a secondary DC power supply, and a safety relay used in an overheating prevention circuit are shown in the photograph given in Fig. 4.13.

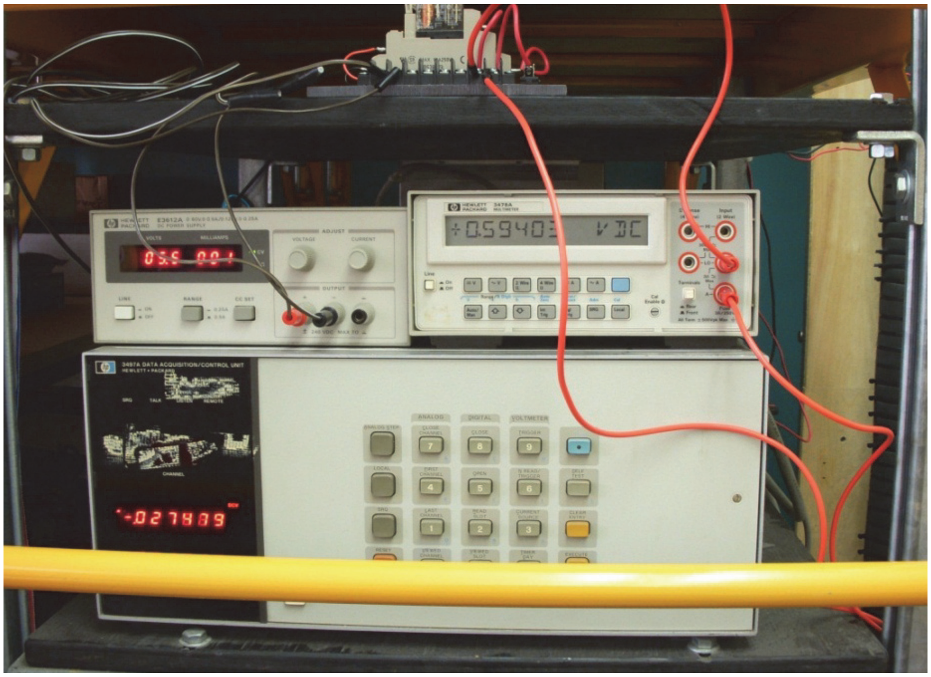

Figure 4.13: Photograph of the data acquisition unit (bottom), multimeter (middle right), secondary DC power supply (middle left), and safety relay (top).

The data acquisition unit (HP3497A) was equipped with three 20-channel multiplexer cards, each with internal hardware compensation enabled for Type-E (chromel-constantan) thermocouples. The lead wires of the thermocouples (and sheathed thermocouple probes) were connected to the terminals of these multiplexer cards, and the corresponding voltage outputs were sequentially measured, on demand, using the voltmeter integrated in the data acquisition unit. These voltage measurements were transmitted to a personal computer, using the aforementioned HP-IB interfaces, and stored in ASCII format in specially designated files. A schematic illustration of the data acquisition and other electrical circuits are presented in Fig. 4.14.

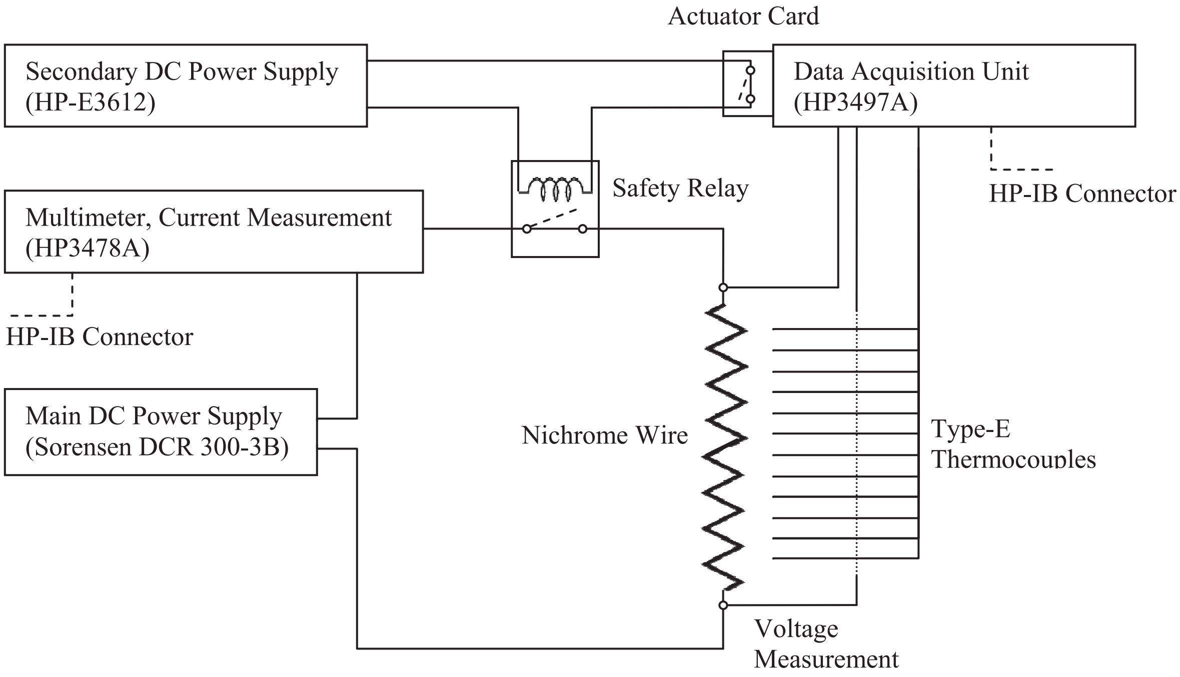

Figure 4.14: Schematic of the data acquisition and other electrical circuits.

The data acquisition and control tasks were managed by a program run on the personal computer. This program was specially designed for these tasks and written using the *Agilent* VEE-OneLab software. It was used to acquire and record the voltage outputs of the thermocouples and sheathed thermocouple probes, and also the nichrome-wire voltage difference and the current supplied by the main power supply. The measured thermocouple voltages outputs were converted to temperatures using calibration polynomials (details given in the next subsection). The electrical power input to the active heating section was calculated, essentially in real time, with the latest sampled nichrome-wire voltage drop and current. During the main closed-loop thermosyphon experiments, the aforementioned data were sampled every 10 seconds. Once processed by the program, the experimental data were progressively added to an ASCII file, along with the corresponding time and date stamps. It should also be noted that a visual interface, which was designed to allow convenient user inputs and data monitoring, was incorporated in the data acquisition program. A screen-capture picture of this visual interface is shown in Fig. 4.15.

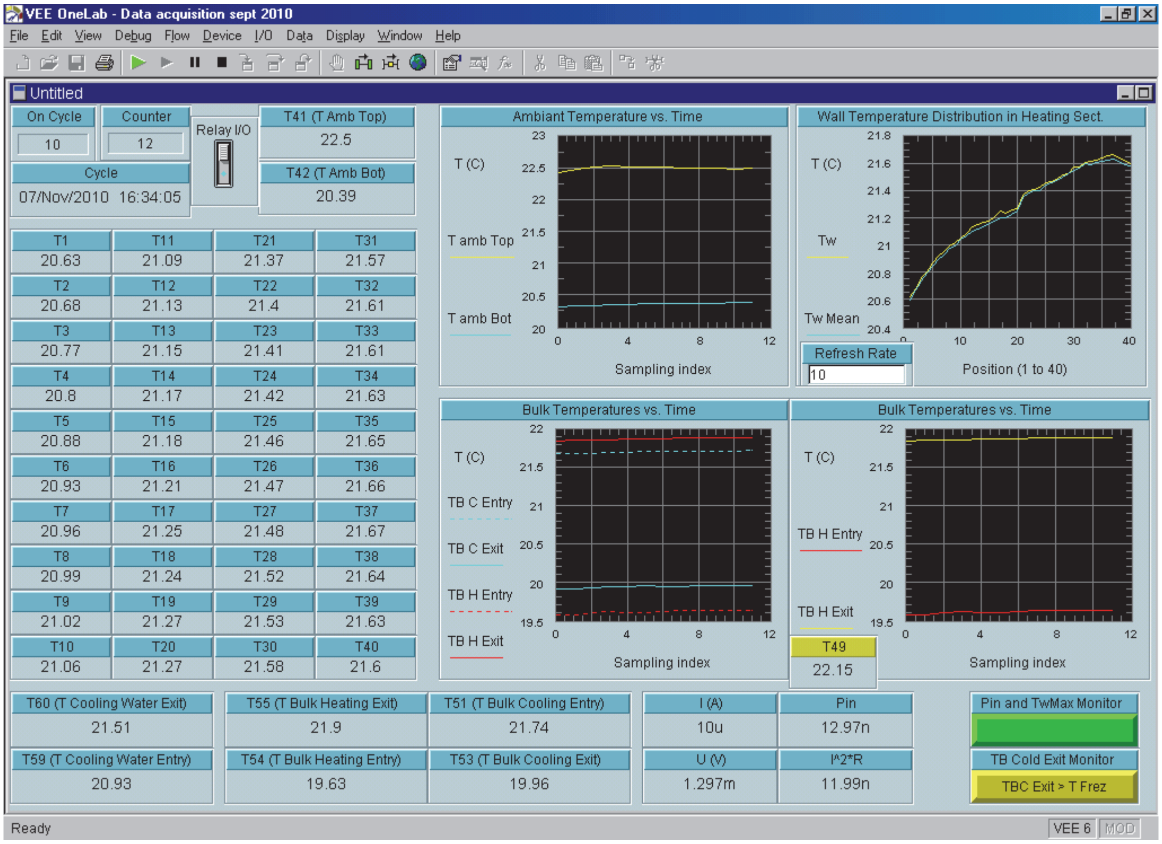

On Cycle: 10

Counter: 12

Cycle: 07/Nov/2010 16:34:05

T41 (T Amb Top): 22.5

T42 (T Amb Bot): 20.39

T1	20.63	T11	21.09	T21	21.37	T31	21.57
T2	20.68	T12	21.13	T22	21.4	T32	21.61
T3	20.77	T13	21.15	T23	21.41	T33	21.61
T4	20.8	T14	21.17	T24	21.42	T34	21.63
T5	20.88	T15	21.18	T25	21.46	T35	21.65
T6	20.93	T16	21.21	T26	21.47	T36	21.66
T7	20.96	T17	21.25	T27	21.48	T37	21.67
T8	20.99	T18	21.24	T28	21.52	T38	21.64
T9	21.02	T19	21.27	T29	21.53	T39	21.63
T10	21.06	T20	21.27	T30	21.58	T40	21.6

Refresh Rate: 10

T49: 22.15

T60 (T Cooling Water Exit): 21.51

T59 (T Cooling Water Entry): 20.93

T55 (T Bulk Heating Exit): 21.9

T54 (T Bulk Heating Entry): 19.63

T51 (T Bulk Cooling Entry): 21.74

T53 (T Bulk Cooling Exit): 19.96

I (A): 10u

U (V): 1.297m

Pin: 12.97n

I^2*R: 11.99n

Pin and TwMax Monitor

TB Cold Exit Monitor: TBC Exit > T Frez

Figure 4.15: Screen-capture picture of the visual interface of the data acquisition program.

In addition to data displays and monitoring graphics, the visual interface included indicators which warned the user if the bulk temperature exiting the vertical legs of the closed-loop thermosyphon did not respect predefined limits. For example, an indicator was activated if the bulk temperature of the MCPCM slurries in the exit plane of the right vertical leg (which housed the active cooling section; see Fig. 4.1) was greater than 15ºC, the value at which the solidification of the PCM was considered to be completed. Similarly, if complete melting of the MCPCM particles in the slurries was desired, a warning was issued if the bulk temperature in the exit section of the left vertical leg (which housed the active heating section; see Fig. 4.1) was less than 32.5ºC, the value at which melting of the PCM was considered to be complete.

The visual interface of the data acquisition and control program also included a virtual switch through which the electrical power input to the active heating section could be interrupted using an electromechanical DC relay, which was part of an overheat-prevention safeguard system (see Fig. 4.14). This relay was connected to a relatively low voltage (approximately 5.5 V) secondary DC power supply (HP-E3612A, see Figs. 4.13 and 4.14): when it was powered, the relay was closed and it completed the power-supply circuit to the nichrome wire of the active heating section. If the monitored thermocouples indicated a maximum wall temperature in the active heating section greater than a user-defined safety threshold (in this case, 55ºC), then the electrical power input to the relay was interrupted, using an actuator card inserted in the data acquisition unit: this action caused the mechanical switch inside the relay to open; and the opening of the relay turned off the DC power supply to the nichrome wire of the active heating section.

4.6.2 Thermocouples and Calibration Procedure

In this work, 48 thermocouples were fabricated in-house from 9 m long segments of Teflon insulated 30 AWG Type-E (chromel-constantan) wire (*Omega* TT-30-E) as follows: the insulation was stripped from both ends of each of these wire segments; a thermocouple bead was then formed at one of the ends of each wire segment, using a spark-welding apparatus; the stripped wires at the other end were attached to a male connector plug (*Omega*, Type-E mini-connector); the beads of these thermocouples were then covered with a thin layer of a two-part high-thermal-conductivity epoxy (*Omega* Omegabond 101). After fabrication, these thermocouples were calibrated using a procedure discussed later in this section. Of these 48 calibrated thermocouples, 40 were installed along the exterior wall of the tube of the active heating section (using the procedure discussed previously in Section 4.2), two were used in regions adjacent to top and bottom 180-degree tube bends for monitoring the ambient air temperature in the laboratory at these locations, and the remaining six were kept as spares. In addition to these fabricated thermocouples, a total of 12 prefabricated stainless steel sheathed Type-E thermocouple probes, eight with 1/16" diameter and four with 1/8" diameter sheaths, each sheath of 6" length, were purchased (from *Omega*) and connected to compatible thermocouple extension wire segments (of suitable length) and male mini-connectors. All of these sheathed thermocouple probes were also calibrated (procedure given later in this section). Four of the calibrated 1/16" diameter sheathed thermocouple probes were used in the bulk-temperature measurement sections (as was described in Section 4.4), one was employed for various other temperature measurements, and three were kept as spares. Two of the calibrated 1/8” diameter sheathed thermocouple probes were used for measuring the cooling-water temperature near the inlet and exit ports of the annular heat exchanger of the active cooling section (as was described in section 4.3), and the remaining two were kept as spares.

The male mini-connectors of the above-mentioned in-house-fabricated thermocouples and prefabricated sheathed thermocouple probes were connected to female mini-connectors that were housed in a connector-box. This connector box was designed to house 60 female mini-connectors, which were individually attached to (one end) of 60 segments (each 3 m long) of Type-E thermocouple extension wire. The other ends of these 60 segments of thermocouple extension wire were connected to the terminals of three 20-channel multiplexer cards, each with hardware-compensation for Type-E thermocouples. These multiplexer cards were then inserted in the data acquisition unit (HP3497A). As was mentioned earlier, a voltmeter integrated in the data acquisition unit was used to sequentially measure the output voltages of the above-mentioned thermocouples (resolution of ±1μV and uncertainty of ±3μV). All thermocouple voltages measured by the data acquisition unit were sent to and recorded on a personal computer via an HP-IB interface.

The 48 in-house-fabricated thermocouples and the 12 prefabricated sheathed thermocouple probes were calibrated prior to their use. This calibration was performed for temperatures ranging between 2ºC to 60ºC, in intervals of 2ºC. For performing this calibration, a quartz thermometer (*Hewlett-Packard* 2804A) was used to obtain the reference temperature measurements. The uncertainty in the temperatures measured by this quartz thermometer was ±0.005ºC between 0ºC to 95ºC, as was established in a calibration of this instrument against a platinum resistance thermometer (a primary standard), at the Physics Division of the National Research Council, in Ottawa.

The objective of the procedure that was used to calibrate the aforementioned thermocouples was to record their voltage outputs and the corresponding temperatures, as indicated by the quartz thermometer, over the full range of interest (2ºC to 60ºC), in intervals of 2ºC, and then curve-fit this data using suitable polynomial functions. This thermocouple calibration procedure is summarized below:

1. Insert and secure the beads of the in-house-fabricated thermocouples, the tips of the prefabricated sheathed thermocouple probes, and the sensor of the quartz thermometer into blind holes drilled into a cylindrical copper block (diameter of 75 mm and a height of 50 mm). During the calibration, this copper block ensured that the sensor of the quartz thermometer and the beads/tips of the thermocouples were exposed to essentially the same temperature (to within less than ± 0.02ºC).

2. Submerge the above-mentioned copper block with the inserted (and secured) beads/tips of the thermocouples in a constant-temperature bath (in this work, *NESLAB* RTE-221) filled with distilled water, and fitted with a special insulating lid that closed the opening of the bath, but allowed the passage of the lead wires of the thermocouples and the stainless steel support shaft of the quartz-thermometer sensor. Set the bath temperature to 2ºC, the lowest temperature of the calibration range. Connect the male mini-connectors on the thermocouples lead wires to the female mini-connectors inserted in the above-mentioned connector box (the thermocouple extension wires from this connector box were previously connected to the data acquisition and control system), and also hook up the quartz thermometer to the personal computer using the HP-IB interface. Turn on all electronic equipment (data acquisition and control system, quartz thermometer, and the personal computer) and let them warm up for at least two hours.

3. Monitor the voltage outputs of the thermocouples and the temperature indicated by the quartz thermometer, and wait until this data demonstrates that steady-state conditions have been reached. In this work, steady-state conditions were considered to be attained when the temperature measured by the quartz thermometer did not fluctuate by more than ± 0.01ºC over at least a 15-minute period.

4. Once steady-state conditions are reached, record the voltage outputs of the thermocouples and the temperature indicated by the quartz thermometer, use the data acquisition and control system to sample these data at least 300 times over a period of approximately 30 minutes. In this work, these tasks were accomplished using a special computer program that was designed and written using the *Agilent* VEE-OneLab software.

5. Increase the bath temperature by approximately 2ºC, and return to Step 3. Repeat these steps until the aforementioned temperature range (2ºC to 60ºC) has been covered.

The data yielded by the above-mentioned calibration procedure were curve-fitted with using third- or fourth-order polynomial functions that related the output voltage of each thermocouple to the corresponding value of temperature indicated by the quartz thermometer. These polynomial functions have the following generic form:

$$T_{measured} = a_n V^n + a_{n-1} V^{n-1} + ... + a_1 V^1 + a_0 \tag{4.2}$$

In this equation, $T_{measured}$ is the temperature sensed by the bead or tip of the thermocouple in ºC (taken to be equal to the temperature indicated by the quartz thermometer), a_n are the polynomial coefficients, and V denotes the voltage output of the thermocouple in mV.

For most of the thermocouples used in this work, third-order polynomials were found to provide the best fit to the calibration data. However, for three of the prefabricated sheathed thermocouple probes, a fourth-order polynomial function was found to provide the best fit to the calibration data. The coefficients of the polynomial functions fitted to the calibration data for each of the thermocouples used in this work are presented in Appendix D, along with information on the location of these thermocouples in the experimental apparatus.

The average discrepancy between the temperatures predicted by the above-mentioned curve-fitted calibration polynomials (for specified voltage outputs of the thermocouples) and the corresponding (actual) temperature values indicated by the quartz thermometer was ±0.015°C for the in-house-fabricated thermocouples and ±0.029°C for the prefabricated sheathed thermocouple probes, and the corresponding maximum values of these discrepancies were ±0.042°C and ±0.074°C, respectively. As was mentioned earlier, the accuracy of the voltmeter integrated in the data acquisition unit was ±3μV. By applying the uncertainty analysis of Kline and McClintock (1953) to these data, the maximum uncertainty in the temperatures measured using the above-mentioned calibrated in-house-fabricated thermocouples and the prefabricated sheathed thermocouple probes were determined to be ±0.063°C and ±0.085°C, respectively.

4.7 Experimental Procedures

The procedures for preparing the MCPCM slurries, filling the working fluid in the thermosyphon, running the main thermosyphon experiments, and draining the working fluid from the thermosyphon after the completion of any particular series of experiments are described in this section.

4.7.1 Preparation of the MCPCM Slurries

The MCPCM slurries used in the main closed-loop thermosyphon experiments were prepared in quantities of approximately 1.2 liters and stored in 2L *Nalgene* plastic containers. For relatively large quantities of the slurries, a beam balance (*Ohaus* series 700 triple beam balance), having a capacity of 2610g and an accuracy of ± 0.1g, was used for the mass measurements. For the preparation and storage of smaller MCPCM slurry samples, an *Acculab* VI-350 digital scale, having a capacity of 350g and accuracy of ± 0.01g if calibrated before each use (as was done in this work), and 60 mL *Nalgene* plastic containers were used. The procedure that was used to prepare these slurries is described below:

1. Measure and record the mass of a clean and empty plastic container ($m_{container}$). For an MCPCM slurry of desired mass concentration, ϕ, and total mass, m_{total}, compute and record the ideal mass of the MCPCM paste (consisting of 50.2% MCPCM by mass; and the rest essentially water) as follows: $m_{MCPCM\ paste} = m_{total}\phi / 0.502$.

2. Place the empty container on the weighing pan of the beam balance (or the digital scale) and carefully add MCPCM paste into it (in small amounts) until the added mass is essentially equal to the ideal value of $m_{MCPCM\ paste}$. Determine the actual total mass of the plastic container with the added MCPCM paste, deduce the actual mass of MCPCM paste added, and record this value. With the actual value of $m_{MCPCM\ paste}$ and the desired MCPCM mass concentration, ϕ, compute the ideal mass of distilled water, m_{H_2O}, which must to be added to the plastic container to form the desired slurry.

3. Add the distilled water in small amounts to the plastic container (containing the previously added MCPCM paste) until the added mass is essentially equal to the ideal value of m_{H_2O}. To achieve high precision in this water-addition process, add the last few grams of water in very small amounts using a glass dropper. Measure the total mass of the plastic container with the added MCPCM paste and distilled water, and deduce the actual value of the added distilled water mass, m_{H_2O}. Record this value, and then using the previously ascertained value of $m_{MCPCM\ paste}$, compute the actual MCPCM mass concentration, ϕ, of the slurry, using Eq. (3.1).

4. Screw the lid of the plastic container in place, and shake the container until the slurry appears homogenous and no portions of the MCPCM paste remain stuck on the container walls. Place a label on the container, indicating the date of production and the actual MCPCM mass concentration of the slurry.

4.7.2 Filling Working Fluid in the Closed-Loop Thermosyphon

The procedure that was used for filling the working fluid (distilled water or MCPCM slurries) in the closed-loop thermosyphon is presented below:

1. If distilled water is to be used as the working fluid, then first boil it in an almost-full 1L beaker for about 30 minutes, to expel as much of the dissolved air as possible, prior to use in the main experiments. After this boiling

process, seal the top surface of the beaker with a plastic film to limit exposure of the boiled water to ambient air. Allow the boiled distilled water to cool down to room temperature prior to filling it in the closed-loop thermosyphon.

If an MCPCM slurry is to be used as the working fluid, then gently stir it in its container for at least five minutes, avoiding excessive churning, to expel as much of the dissolved air as possible (the boiling procedure that is suitable for degassing distilled water cannot be used with the MCPCM slurries, at it would permanently damage the MCPCM particles). Allow the stirred slurry to stand still for about five minutes, to let any air bubble within the slurry to reach its surface and get expelled, before filling it (the slurry) in the closed-loop thermosyphon.

2. Place the beaker (filled with the boiled and cooled distilled water) or container (filled with the gently-stirred MCPCM slurry) and the diaphragm pump near the bottom filling/draining port of the closed-loop thermosyphon. Connect one end of a *Tygon* tube to the inlet port of the pump and insert its other end into the distilled water in the beaker or the MCPCM slurry in the plastic container. Connect the outlet of the pump to the filling/draining port of the closed-loop thermosyphon, using another *Tygon* tube, and then open the ball valve connected to the filling/draining port.
3. Turn on the drive unit of the diaphragm pump, and slowly increase its speed to a low setting (2 on its full scale of 10). Visually check if the working fluid is being drawn from the beaker or container through the *Tygon* tube and pushed into the closed-loop thermosyphon, and also check the flow rate to ensure that it is low.
4. When approximately 0.5L of working fluid has been drawn from the beaker or container and filled in the closed-loop thermosyphon, inspect the working-fluid level through the observation window of the expansion chamber. When the lower part of the meniscus of the working fluid reaches the half-height

position of the expansion-chamber tube, shut off the drive unit of the diaphragm pump (the working fluid will remain in place in the closed-loop thermosyphon, as there is a PTFE non-return valve installed on the outlet port of the pump). Close the ball valve attached to the filling/draining port of the closed-loop thermosyphon, and then disconnect the diaphragm pump from this apparatus.

5. If an MCPCM slurry is being used as the working fluid, clean the diaphragm pump by circulating water through it, until no traces of MCPCM particles are observed exiting through its outlet port.

4.7.3 Performing the Main Experiments with the Closed-Loop Thermosyphon

The following procedure was used for performing the main experiments with the closed-loop thermosyphon (after it was filled with the desired working fluid):

1. Turn on the personal computer, the data acquisition unit, the multimeter, the main and secondary power supplies, and the constant-temperature bath. Ensure that the electrical power input to the nichrome wire coil of the active heat section is set to zero, and adjust the settings of the constant-temperature bath to obtain the desired cooling-water temperature. Allow at least two hours for these instruments and equipment to warm up.
2. Activate the data acquisition program and initiate recording of the experimental data (with a sampling period of 10 seconds). Adjust the settings of the main power supply to the nichrome wire coil of the active heating section to the desired level. Monitor the cooling-water temperature and adjust the constant-temperature bath settings, if needed.
3. Wait for the thermosyphon apparatus to reach a steady-state condition. Check if the bulk temperatures of the working fluid exiting the vertical heating and cooling legs of the closed-loop thermosyphon are within the desired limits. If not, adjust the heating power input and/or the cooling-water

temperature, as needed, and wait again for the thermosyphon apparatus to reach a steady-state condition.

4. When the desired steady-state operation of the thermosyphon apparatus is attained, use the data acquisition program to obtain all measurements and save them in a new ASCII file. Using the aforementioned sampling rate of 10 seconds, acquire a minimum of 200 data sets.
5. Once the data acquisition and recording tasks are completed, rename the saved ASCII file and place it in an appropriate folder, as needed. If an additional experimental run is to be performed with the currently loaded working fluid, reset the data acquisition program and return to Step 2.

4.7.4 Draining the Working Fluid and Cleaning the Closed-Loop Thermosyphon

Following the completion of any particular series of experimental runs, the working fluid was drained out of the closed-loop thermosyphon by simply opening the ball valve connected to the filling/draining port at the bottom of this apparatus (see Fig. 4.1).

If the working fluid was distilled water, it was drained into a beaker and then disposed off. Then the aforementioned ball valve attached to the filling/draining port was maintained open and filtered air, supplied by a small compressor, was passed through the thermosyphon (from the top port of the expansion chamber and out of the bottom filling/draining port) to accelerate the drying process.

If an MCPCM slurry was used as the working fluid, it was recuperated in its original container (containing the same slurry, of identical mass concentration) for possible later use. The apparatus was then cleaned by circulating tap water from the bottom draining/filling port to the top port of the expansion chamber and vice-versa. In this cleaning operation, the top port of the expansion chamber was connected to a hose that could be used to drain or supplying the cleaning water, as needed. After the closed-loop thermosyphon was throughly cleaned using tap water in this manner (no visible signs of the MCPCM slurry exited with this cleaning water), this apparatus was filled with distilled water for a final cleaning, and then this distilled water was fully drained and discarded. Then the aforementioned ball valve attached to the filling/draining port was maintained open and filtered air, supplied by a small compressor, was passed through the thermosyphon (from the top port of the expansion chamber and out of the bottom filling/draining port) to accelerate the drying process.

4.8 Determination of Overall Heat Transfer Coefficients

In the mathematical models proposed in Chapter 2, three different overall heat transfer coefficients, $U_i^{'}$, $U_o^{'}$, $U_b^{'}$ (defined on a per-unit-length basis, rather than per-unit-area, in Eqs. (2.27), (2.32), and (2.36), respectively) were introduced for calculations of rates of heat loss to (or gain from) the ambient air in the laboratory from (or to) the following portions of the closed-loop thermosyphon, respectively: 1) the inner surface of the pre- and post-heated lengths of the vertical heating section, $l_{h,pre}$ and $l_{h,post}$, respectively (see Fig. 2.1); 2) the outer surface of the nichrome wire coil in the active heating section, of length l_h (see Fig. 2.1); and 3) the working fluid in the parts of the closed-loop thermosyphon <u>other than</u> the vertical heating ($l_{h,pre}$ + l_h + $l_{h,post}$) and cooling ($l_{c,pre}$ + l_c + $l_{c,post}$) sections. The overall heat transfer coefficient denoted as $U_i^{'}$ was also used to calculate the rate of heat gain from the ambient air in the laboratory to the inner surface of the pre- and post-cooled lengths of the vertical cooling section, $l_{c,pre}$ and $l_{c,post}$, respectively (see Fig. 2.1), using an equation akin to Eq. (2.27).

In this section, the experiments which were undertaken to determine the overall heat transfer coefficient denoted as $U_b^{'}$ are described first. After that, the estimations of $U_i^{'}$ and $U_o^{'}$, using the experimentally determined value of $U_b^{'}$, are presented.

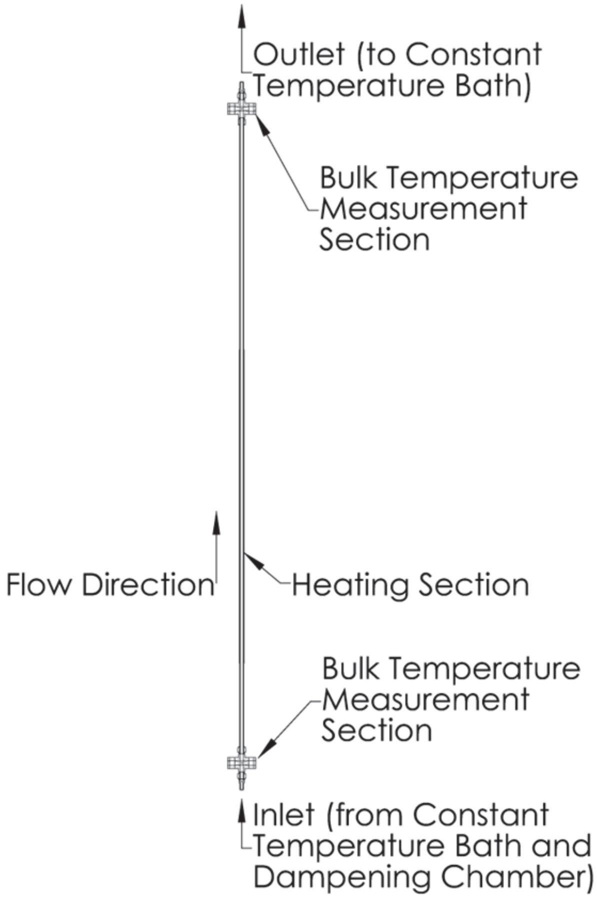

Figure 4.16 Open-configuration set-up of the vertical left leg of the thermosyphon (shown here without *Armaflex* insulation) used for determining overall heat transfer coefficients.

In the experiments which were undertaken to determine the value of $U_b^{'}$, only the left vertical leg of the closed-loop thermosyphon apparatus was used, in an open configuration, without supplying electrical power to the nichrome wire coil of the active heating section. This open-configuration set-up, without the *Armaflex* insulation, is schematically illustrated in Fig. 4.16. The diaphragm pump was used to draw distilled water (at various constant time-mean mass flow rates) from the constant-temperature bath at temperatures higher than that of the ambient air temperature in the laboratory, force this distilled water first through a well-insulated dampening chamber (which attenuated the pulsations of the flow exiting the diaphragm pump), then through the aforementioned open-configuration set-up of the left vertical leg of the thermosyphon (see Fig. 4.16), and finally back to the constant-temperature bath. The bulk-temperature measurement sections located at the top and bottom of the set-up shown in Fig. 4.16 were used to measure the corresponding temperatures of the distilled water. The mass flow rate of this distilled water through the set-up illustrated in Fig. 4.16 was determined by diverting it to a beaker of known mass (pre-weighed) for a suitable sampling time (approximately two minutes; precise value measured using a chronometer), measuring the mass of the water collected in this beaker, and then dividing this mass by the sampling time.

The overall heat transfer coefficient, $U_b^{'}$, was determined using the following procedure.

1. Turn on the constant-temperature bath, the data acquisition and control system, and the personal computer, at least two hour prior to the experimental measurements. Clean the beaker, weigh it using a digital scale, and record its mass.

2. Adjust the constant-temperature bath to the desired setting (in this experiment, values of 40°C, 45°C or 50°C were used).

3. Activate the diaphragm pump, and fill the dampening chamber partially, by opening a purge-valve located on its top surface and shutting off a valve at its exit port. Once this is done, open the exit port of the dampening chamber and shut off its purge valve, and allow the distilled water to flow through the set-up illustrated in Fig. 4.16, and back to the constant-temperature bath. Set the diaphragm pump drive speed at a setting the yields the desired mass flow rate of the distilled water. Wait until a steady-state condition is reached.

4. Activate the data acquisition program, and start recording the temperatures indicated by the bulk-temperature measurements sections located at the entrance and exit planes of the left vertical leg of the thermosyphon (see Fig. 4.16), with a sampling period of 10 seconds. Divert the distilled water to the pre-weighed beaker for approximately two minutes, and use a chronometer to precisely record this time. Measure the mass of the water collected in this beaker. Then divide this mass by the precisely-recorded sampling time to

obtain the mass flow rate of the distilled water, $\dot{m}_{H_2O}$. Stop the recording of the inlet and outlet bulk temperatures, and calculate and save their time-mean values, $T_{b,in}$ and $T_{b,out}$, respectively.

5. Repeat Steps 2-4, until all desired distilled-water flow rates and constant-temperature bath settings are covered.

An energy balance performed on the distilled water flowing through the apparatus illustrated in Fig. 4.16 yields the following equation:

$$q_{loss} = \dot{m}_{H_2O} c_{p,H_2O} \left(T_{b,in} - T_{b,out} \right) \tag{4.3}$$

Using the experimental values of $\dot{m}_{H_2O}$, $T_{b,in}$, and $T_{b,out}$, and the value of c_{p,H_2O} at the arithmetic-mean value of $T_{b,in}$ and $T_{b,out}$ (see Appendix A for curve-fits to the property data of distilled water) in Eq. (4.3), calculate the corresponding values of q_{loss}. This rate of heat loss can also be expressed in terms of the overall heat transfer coefficient, $U_b^{'}$, and the log-mean value of the bulk-to-environment temperature differences, as follows:

$$q_{loss} = U_b^{'} L_{heat\,loss} (T_b - T_\infty)_{LMTD} \tag{4.4}$$

The log-mean bulk-to-environment temperature difference in this equation is given by the following expression:

$$(T_b - T_\infty)_{LMTD} = \frac{\left(T_{b,in} - T_\infty \right) - \left(T_{b,out} - T_\infty \right)}{\ln \left(\dfrac{\left(T_{b,in} - T_\infty \right)}{\left(T_{b,out} - T_\infty \right)} \right)} \tag{4.5}$$

In this equation, T_∞ is the ambient air temperature in the laboratory: for each set of measured $\dot{m}_{H_2O}$ and $T_{b,in}$, it was taken as the arithmetic mean of the corresponding air temperatures (time-mean) recorded by two thermocouples, located adjacent to the centers of the top and bottom bends of the closed-loop thermosyphon set-up. The length $L_{heat\,loss}$

was taken as the distance between the central planes of the inlet and outlet bulk-temperature measurement sections (see Fig. 4.16), namely, 2.089m.

This experiment was performed six times: for three different settings of the constant-temperature bath, 40°C, 45°C and 50°C, and two different settings of the drive unit of the diaphragm pump. The results obtained are shown in Table 4.1.

Table 4.1: Results of the experiments conducted to determine $U_b^{'}$.

Run	$\dot{m}_{H_2O}$ [kg/s]	$T_{b,in}$ [°C]	$T_{b,out}$ [°C]	c_{p,H_2O} [J/kg°C]	T_∞ [°C]	$U_b^{'}$ [W/m°C]
1	0.001203	36.89	36.14	4177.9	25.59	0.1650
2	0.001343	41.09	40.15	4178.6	24.76	0.1605
3	0.001179	44.62	43.31	4179.5	25.21	0.1650
4	0.001795	37.59	36.96	4178.0	24.42	0.1749
5	0.002372	42.73	42.07	4179.1	24.47	0.1741
6	0.001742	45.93	44.99	4180.0	25.07	0.1603

The arithmetic mean of the $U_b^{'}$ values reported in Table 4.1 is 0.1666 W/m°C: the average and maximum absolute relative differences between the reported values and this arithmetic-mean value are 3.1% and 5.0%, respectively; these values are well within the maximum uncertainties in the reported values of $U_b^{'}$, estimated using the analysis of Kline and McClintock (1953), which ranged from 9.2% (Run 3) and 19.2% (Run 4). The values of $\dot{m}_{H_2O}$ in Runs 1, 2, and 3 are representative of the mass flow rates of the distilled water, and two to three times higher than the mass flow rates of the MCPCM slurries, in the main closed-loop thermosyphon experiments undertaken in this work. However, the values of $U_b^{'}$ are largely determined by the value of the radial conductance (per unit length) of the *Armaflex* insulation; and the influence of the convection heat transfer coefficients on the inside surface of the tube (with both distilled water and MCPCM slurries as the working fluid) on the corresponding values of $U_b^{'}$ are negligibly small (as is shown in the next paragraph). In the light of these observations, it was assumed that $U_b^'$ = 0.1666 W/m°C (which is its aforementioned arithmetic mean value).

With $U_b^'$ = 0.1666 W/m°C, the total thermal resistance per unit length of the portions of the closed-loop thermosyphon other than the heating and cooling sections (of lengths $L_{h,pre} + L_h + L_{h,post}$ and $L_{c,pre} + L_c + L_{c,post}$, respectively) was calculated as follows: $R_{th,total}^' = 1/U_b^'$ = 6.002 °C-m/W. Taking the thermal conductivity of stainless steel (SS 316) at 25°C as k_{ss} = 14.64 W/m°C, the contribution of radial heat conduction through the stainless steel pipe (with D_i = 10.21 mm and D_o = 12.70 mm, respectively) to $R_{th,total}^'$ is $R_{th,ss\,pipe}^'$ = $[\ln(D_o / D_i)/(2\pi k_{ss})]$ = 0.002372 °C-m/W. The contribution to $R_{th,total}^'$ of fully-developed laminar forced convection inside the closed-loop thermosyphon, with distilled water as the working fluid (average thermal conductivity of k_{H_2O} = 0.61 W/ m°C, which corresponds to its value for water a 25°C) and the Nusselt number taken as $Nu_{forced\,conv}$= $(h_{forced\,conv} D_i / k_{H_2O})$ = 4.364 (applicable to a thermal boundary condition of uniform wall heat flux), can be approximated as $R_{th,forced\,conv}^'$= $1/(\pi D_i h_{forced\,conv})$ = 0.1194 °C-m/W; and $R_{th,forced\,conv}^'$ is expected have similar values with the MCPCM slurries as the working fluid, as the maximum increase of the Nusselt number value due to the related non-Newtonian effects is less than 2.1% for the values of *n* considered in this work [Chhabra and Richardson (1999)]. Using the above-mentioned values of $R_{th,total}^'$, $R_{th,ss\,pipe}^'$, and $R_{th,forced\,conv}^'$, the values of $U_i^'$ and $U_o^'$ were estimated and set to the following values: $U_i^'$ = $[R_{th,total}^' - R_{th,forced\,conv}^']^{-1}$ = 0.17001 W/m°C; and $U_o^'$ = $[R_{th,total}^' - R_{th,forced\,conv}^' - R_{th,ss\,pipe}^']^{-1}$ = 0.17008 W/m°C. As was expected, these results show that $U_i^' \approx U_o^'$. They also confirm that the values of $U_b^'$ are primarily determined by the value of the radial conductance (per unit length) of the *Armaflex* insulation. The uncertainties in the values of $U_i^'$ and $U_o^'$ are similar to those in the values of $U_b^'$.

4.9 Determination of Mass Flow Rate and Average Velocity of Working Fluid in the Closed-Loop Thermosyphon

The technique that was employed to determine the mass flow rate of the working fluid in the closed-loop thermosyphon, its experimental validation, the assessment of the related uncertainty, and an equation to calculate the average velocity of the working fluid in the closed-loop thermosyphon are presented this section. In this work, commonly-used techniques for measuring flow rates [Tavoularis (2005); Holman (2011)] could not be used for the following reasons: the magnitude of the fluid velocities in the closed-loop thermosyphon were very low (representative results are presented in Chapter 6); the MCPCM slurries were essentially opaque (at the concentrations considered) and electrically nonconductive (so optical and some other non-invasive techniques were inapplicable); and additional flow restrictions or alterations caused by invasive techniques were not acceptable, especially with the MCPCM slurries as the working fluid. Thus, the mass flow rate, $\dot{m}$, of the working fluid (distilled water or MCPCM slurries) was determined indirectly, by performing a steady-state energy balance over the left vertical leg of the thermosyphon (see Fig. 4.1), as follows:

$$\dot{m} = \frac{q_{heating,total} - \left(q_{loss,L_{h,pre,exp}} + q_{loss,L_h} + q_{loss,L_{h,post,exp}}\right)}{i_{s,b,in} - i_{s,b,out}} \tag{4.6}$$

In Eq. (4.6), $q_{heating,total}$ is the measured total electrical power input to the nichrome wire coil; $q_{loss,L_{h,pre,exp}}$, q_{loss,L_h} and $q_{loss,L_{h,post,exp}}$ denote the rates of heat loss to the ambient air in the laboratory occurring over the corresponding portions of the left vertical leg of the thermosyphon; and $i_{s,b,in}$ and $i_{s,b,out}$ represent the effective bulk enthalpies of the working fluid corresponding to the measured bulk temperatures $T_{b,in,heating}$ and $T_{b,out,heating}$, respectively. The experimental pre- and post-heating lengths are denoted as $L_{h,pre,exp}$ and $L_{h,post,exp}$ (they are not the same as $L_{h,pre}$ and $L_{h,post}$ used in the mathematical models described in Chapter 2). Here, $L_{h,pre,exp}$ denotes the distance from the bottom thermocouple-measurement section to the bottom of the nichrome wire coil; and $L_{h,post,exp}$

denotes the distance from the top of the nichrome wire coil to the top bulk-temperature measurement section. Their values were the following: $L_{h,pre,exp}$ = 0.319 m and $L_{h,post,exp}$ = 0.770 m. The values of $i_{s,b,in}$ and $i_{s,b,out}$ were evaluated using Eq. (2.22) and the corresponding values of the measured bulk temperatures, $T_{b,in,heating}$ and $T_{b,out,heating}$, respectively. With the appropriate value of the MCPCM mass concentration, ϕ, as an input, the expression presented in Eq. (4.6) is valid when either an MCPCM slurry or distilled water is used as the working fluid (ϕ was set to zero for distilled water).

The value of $q_{loss,L_{h,pre,exp}}$ was evaluated by assuming that $T_{b,in,heating}$ remained essentially unchanged over $L_{h,pre,exp}$:

$$q_{loss,L_{h,pre,exp}} = U_b^{'} L_{h,pre,exp}\left(T_{b,in,heating} - T_\infty\right) \tag{4.7}$$

Similarly, the value of $q_{loss,L_{h,post,exp}}$ was evaluated by assuming that $T_{b,out,heating}$ remained essentially unchanged over $L_{h,post,exp}$:

$$q_{loss,L_{h,post,exp}} = U_b^{'} L_{h,post,exp}\left(T_{b,out,heating} - T_\infty\right) \tag{4.8}$$

An iterative procedure could have been used to determine log-mean values of $\left(T_{b,in,heating} - T_\infty\right)$ and $\left(T_{b,out,heating} - T_\infty\right)$ in Eqs. (4.7) and (4.8), but the aforementioned assumptions yielded results of essentially similar accuracy. Lastly, the rate of heat loss over the active heating section of total length L_h (see Fig. 4.1) was evaluated by summing the corresponding rates of heat loss over the tube segments (each of 25mm length) associated with each of the 40 thermocouples attached to the outer surface of the tube wall in this section, as follows:

$$q_{loss,L_h} = \sum_{N=1}^{40} U_o^{'} L_{segment}\left(T_{r=r_o,N} - T_\infty\right) \tag{4.9}$$

In this equation, $L_{segment}$ is equal to 0.025m and $T_{r=r_o,N}$ denotes the temperature of the outer surface of the tube wall measured by thermocouple *N*.

The proposed technique for determining the mass flow rate of the working fluid in the closed-loop thermosyphon was validated by undertaking an auxiliary experiment with distilled water. In this auxiliary experiment, an open-configuration set-up of the vertical left leg of the thermosyphon, identical to the one illustrated schematically in Fig. 4.16 and described in the previous section, was used. Distilled water was fed through this open-configuration set-up at various essentially constant values of the mass flow rate, using the diaphragm pump and the dampening chamber (as described in the previous section), and the constant-temperature bath to maintain the inlet temperature of the water essentially constant (at approximately 21°C). In this auxiliary experiment, electrical power input was provided to the nichrome wire coil of the active heating section on the vertical left leg (at several appropriate constant values), and the aforementioned technique was used to determine the mass flow rate of the distilled water. The values of the mass flow rate yielded by this technique were then checked against those obtained directly, as follows: diverting the distilled water to a pre-weighed beaker for approximately two minutes, using a chronometer to precisely record this time, measuring the mass of the water collected in the beaker, and then dividing this mass by the precisely-recorded sampling time. The maximum absolute uncertainty in the values of the mass flow rate obtained with the direct (beaker and chronometer) technique, which were considered in this validation exercise as the benchmark results, was evaluated as 1.2% (of the values measured), using the method of Kline and McClintock (1953). A summary of this validation procedure is given below:

1. Turn on the constant-temperature bath, the data acquisition and control system, the main DC power supply (set to zero volts at this stage), and the personal computer, at least two hour prior to the experimental measurements. Clean the beaker, weigh it using a digital scale, and record its mass. Set the constant temperature bath at the desired temperature, in this case 20°C (with this setting, due to the rate of heat gained from the ambient air in the laboratory, the temperature of the distilled water entering the apparatus shown in Fig. 4.16 was about 21°C).

2. Activate the diaphragm pump, and fill the dampening chamber partially, by opening a purge-valve located on its top surface and shutting off a valve at its exit port. Once this is done, open the exit port of the dampening chamber and shut off its purge valve, and allow the distilled water to flow through the set-up illustrated in Fig. 4.16, and back to the constant-temperature bath.

3. Set the speed of diaphragm pump drive to a value that yields the desired mass flow rate of the distilled water. Set the electrical power input to the nichrome wire coil of the active heating section to the desired value. Wait until a steady-state condition is reached.

4. Activate the data acquisition program, and start recording the temperatures indicated by the bulk-temperature measurement sections located at the entrance and exit planes of the left leg of the thermosyphon (see Fig. 4.16), the temperatures indicated by the 40 thermocouples attached to the outer surface of the active heat section, and the values of electrical power input to the nichrome wire coil, with a sampling period of 10 seconds. Divert the distilled water to the pre-weighed beaker for approximately two minutes, and use a chronometer to precisely record this time. Measure the mass of the water collected in this beaker. Then divide this mass by the precisely-recorded sampling time to obtain the mass flow rate of the distilled water yielded by this direct method, $\dot{m}_{H_2O,direct}$. Stop the recording of the aforementioned experimental data, and calculate and save the time-mean values of $T_{b,in,heating}$, $T_{b,out,heating}$, $T_{r=r_o,N(N=1,2,...,40)}$, and $q_{heating,total}$. Determine the mass flow rate of the distilled water using the proposed technique, $\dot{m}_{H_2O,\,proposed\,technique}$.

5. Repeat Steps 3 and 4 until all desired values of the distilled-water mass flow rate and electrical power input are covered.

Sixteen different runs of this auxiliary experiment were performed: four different values of the electrical power input; and for each of these, four different speeds of the drive of the diaphragm pump (yielding four different values of the distilled-water mass flow rate). The results are presented in Table 4.2.

Table 4.2: Results of auxiliary experiments undertaken to validate the proposed technique for determining the mass flow rate of the working fluid in the closed-loop thermosyphon.

Run	$q_{heating,total}$ [W]	$T_{b,in}$ [°C]	$T_{b,out}$ [°C]	T_∞ [°C]	$\dot{m}_{H_2O,\,proposed\,technique}$ [kg/s]	$\dot{m}_{H_2O,direct}$ [kg/s]	Difference [%]
1	5.002	21.78	25.53	22.92	$2.855\text{x}10^{-4}$	$3.018\text{x}10^{-4}$	-5.4%
2	9.991	21.55	28.51	22.59	$2.956\text{x}10^{-4}$	$2.841\text{x}10^{-4}$	4.0%
3	20.07	21.34	35.59	22.17	$2.836\text{x}10^{-4}$	$2.974\text{x}10^{-4}$	-4.6%
4	30.07	21.36	41.25	22.30	$3.081\text{x}10^{-4}$	$3.140\text{x}10^{-4}$	-1.9%
5	5.028	21.43	23.73	23.30	$5.294\text{x}10^{-4}$	$5.282\text{x}10^{-4}$	0.2%
6	10.00	21.52	25.79	23.69	$5.392\text{x}10^{-4}$	$5.281\text{x}10^{-4}$	2.1%
7	20.03	21.66	29.92	23.87	$5.399\text{x}10^{-4}$	$5.394\text{x}10^{-4}$	0.1%
8	40.07	21.23	37.64	22.80	$5.319\text{x}10^{-4}$	$5.440\text{x}10^{-4}$	-2.2%
9	5.006	21.23	23.15	24.00	$6.837\text{x}10^{-4}$	$7.130\text{x}10^{-4}$	-4.1%
10	10.06	21.07	24.52	23.62	$6.941\text{x}10^{-4}$	$7.207\text{x}10^{-4}$	-3.7%
11	20.04	21.11	27.64	23.48	$6.992\text{x}10^{-4}$	$7.189\text{x}10^{-4}$	-2.7%
12	40.25	20.97	33.42	22.85	$7.221\text{x}10^{-4}$	$7.348\text{x}10^{-4}$	-1.7%
13	5.101	20.72	22.31	22.54	$7.963\text{x}10^{-4}$	$8.243\text{x}10^{-4}$	-3.4%
14	10.06	20.72	23.56	22.55	$8.304\text{x}10^{-4}$	$8.415\text{x}10^{-4}$	-1.3%
15	19.96	20.75	26.40	22.71	$8.078\text{x}10^{-4}$	$8.301\text{x}10^{-4}$	-2.7%
16	40.04	20.75	31.79	22.68	$8.170\text{x}10^{-4}$	$8.335\text{x}10^{-4}$	-2.0%

Using the results presented in Table 4.2, the average and maximum values of the absolute relative difference between corresponding values of $\dot{m}_{H_2O,\,proposed\,technique}$ and $\dot{m}_{H_2O,direct}$ (which were taken as the benchmark values) were calculated as 2.6% and 5.4%, respectively. The highest value of this relative difference (-5.4%) was observed for the lowest value of $q_{heating,total}$ and one of the lowest values of the mass flow rate, when the total rate of heat loss to the ambient air in the laboratory takes on a value that is a relative high portion of $q_{heating,total}$. The values of $q_{heating,total}$ and $\dot{m}$ in Table 4.2 are representative of the values in the main experiments conducted with the closed-loop thermosyphon operated with either distilled water or MCPCM slurries as the working fluid, except for some cases in which the value of $q_{heating,total}$ was higher than 40W (the maximum value used in this auxiliary experiment). However, for values of $q_{heating,total}$ greater than 40W, the uncertainties in the values of $\dot{m}$ determined using the proposed technique are lower than the aforementioned uncertainties, as the rates of heat loss to the ambient air in the laboratory (the main source of the uncertainty) are lower relative to $q_{heating,total}$.

The aforementioned auxiliary experiment for validating the proposed technique for determining the mass flow rate of the working fluid was undertaken only with distilled water, mainly for convenience. It should be noted in this context that the aforementioned results and the corresponding differences (here treated as measures of uncertainty) with respect to results obtained with the direct measurement technique are expected to also apply quite well to cases in which the MCPCM slurries are the working fluid: this is because the sources of uncertainty in the evaluation of $\dot{m}$ using the experimentally obtained inputs to Eq. (4.6) remain essentially the same, with the sole exception of the uncertainty related to the effective specific heat, $c_{p,MCPCM}$, of the MCPCM slurries (required for calculating the effective specific enthalpies of the slurries, as was shown in Chapter 2); the uncertainty in the experimentally determined values of values of $c_{p,MCPCM}$ were ± 1%, which is only a bit higher than the corresponding uncertainty in the values of c_{p,H_2O} determined using curve-fits to the corresponding data in the published literature (Appendix A).

After calculating the mass flow rate of the working fluid, $\dot{m}$, the average velocity of the working fluid was evaluated using the following equation:

$$w_{av} = \frac{\dot{m}}{\rho_{s,ref} A_{c-s}} \tag{4.10}$$

In this equation, A_{c-s} is the cross-sectional area of the flow passage through the pipe; and $\rho_{s,ref}$ is a reference effective mass density of the working fluid, having a value representative of the mean value of ρ_s in the thermosyphon (see Chapters 2). A similar technique for determining the mass flow rate of the working fluid and then calculating its average velocity was used by Bernier and Baliga (1992b) for a closed-loop thermosyphon operating with pure distilled water, and it was found to yield accurate results.

4.10 Closing Remarks

The closed-loop thermosyphon apparatus, the supporting components and instrumentation, and the related experimental procedures were described in the earlier sections of this chapter. The results of the main experiments performed with the closed-loop thermosyphon are presented in Chapter 6, along with the results of the corresponding numerical simulations. Details of the complete set of experimental runs and the related data obtained from them are listed in Appendix E. Lastly, a photograph of the closed-loop thermosyphon covered with the *Armaflex* insulation is presented below in Fig. 4.17.

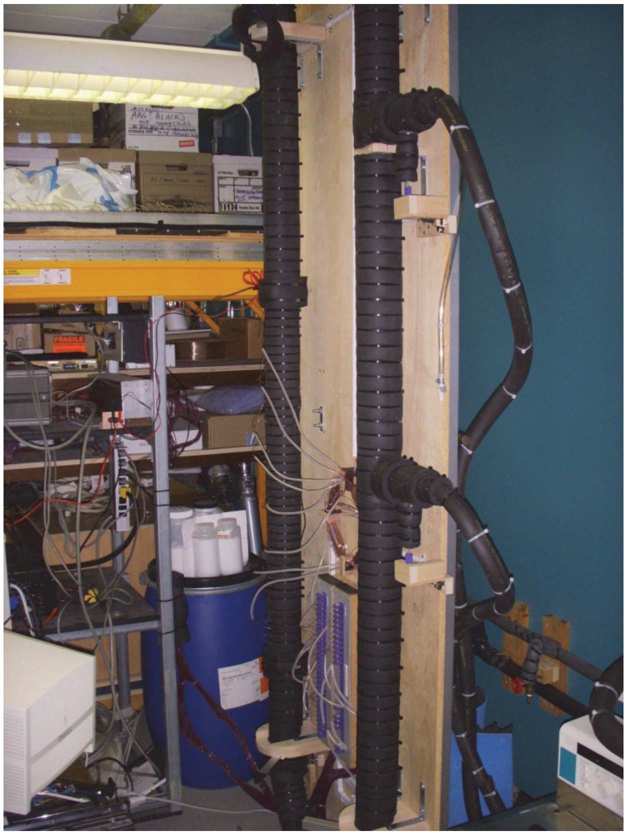

Figure 4.17: Photograph of the closed-loop thermosyphon covered with *Armaflex* insulation.

5. Numerical Methods and Solution Procedures

The numerical methods and the procedures used for solving the 1-D/2-D model of the problems of interest in this work (see Chapter 2) are presented in this chapter. A control-volume finite element method (CVFEM) was specially formulated, implemented, tested, and then used to solve the two-dimensional axisymmetric (2-D) models of the steady fluid flow and heat transfer phenomena in the vertical heating and cooling sections of the closed-loop thermosyphon (see Figures 2.1 and 4.1). The formulation of this CVFEM, which incorporates several novel aspects that improve the performance of some previously published CVFEMs [Baliga and Patankar (1980, 1983), Prakash and Patankar (1985), Masson et al. (1994), Saabas and Baliga (1994)], is described in Section 5.1. The proposed CVFEM and its implementation (computer code) were validated by solving several test problems. Two of these test problems and the results are presented in Section 5.2. The details of segmented quasi-one dimensional (1-D) models of the fluid flow and heat transfer in the rest of the closed-loop thermosyphon (that is, the portions other than the vertical heating and cooling sections) were presented in Chapter 2, Section 2.5, so only a brief overview of the salient aspects of these segmented 1-D models are presented in Section 5.3. The numerical evaluation of the overall momentum balance (see description in Section 2.6) is presented in Section 5.4. Lastly, the overall solution procedure that was used to iteratively solve the discretized equations of the 1-D/2-D model of the closed-loop thermosyphon is described in Section 5.5.

5.1 Control-Volume Finite Element Method for Steady Two-Dimensional Axisymmetric Fluid Flow and Heat Transfer

This control-volume finite element method (CVFEM) was formulated by amalgamating and extending ideas and concepts proposed by Baliga and Patankar (1980, 1983), Prakash and Patankar (1985), Schneider and Raw (1986), Masson et al. (1994), Saabas and Baliga (1994), and Baliga and Atabaki (2006). As was mentioned above, the formulation of this CVFEM incorporates several novel aspects that improve the performance of some previously published CVFEMs [Baliga and Patankar (1980, 1983), Prakash and Patankar (1985), Schneider and Raw (1986), Masson et al. (1994), Saabas and Baliga (1994), and Baliga (1997)]. These improvements mainly pertain to the discretized pressure equation and the boundary treatments. They were published in a journal article by the author of this thesis and his supervisor [Lamoureux and Baliga (2011), in *Numerical Heat Transfer, Part B: Fundamentals*], in the context of steady, incompressible, planar two-dimensional fluid flow and heat transfer problems, solved with reference to a Cartesian coordinate system. However, the key ideas of the improvements proposed in Lamoureux and Baliga [2011] also apply to CVFEMs formulated for the solution of two-dimensional axisymmetric and three-dimensional, steady and unsteady, incompressible fluid flow and heat transfer problems. In this work, these ideas were adapted and incorporated in the formulation of the proposed CVFEM for the solution of steady, incompressible, two-dimensional axisymmetric fluid flow and heat transfer problems. This CVFEM is presented in this section, with special attention to the details of the improved formulations of the discretized pressure equation and boundary treatments, and only concise descriptions of the other discretized equations and the overall solution procedure, as they are available in the works of Masson et al. (1994) and Baliga and Atabaki (2006). This presentation, which is largely borrowed from that in Lamoureux and Baliga (2011), is done in a relatively general manner, as the proposed CVFEM (which is one of the main contributions of this thesis) could be used to solve a wide variety of two-dimensional axisymmetric fluid flow and heat transfer problems.

5.1.1 Synopsis of Background and Context

CVFEMs are formulated by amalgamating and extending concepts that are native to finite-volume methods (FVMs) and finite element methods (FEMs), as has been discussed in the earlier works of Patankar (1980), Baliga and Patankar (1980, 1983), Prakash and Patankar (1985), Schneider and Raw (1986), Masson et al. (1994), Masson and Baliga (1998), Saabas and Baliga (1994), Costa et al. (1995), Baliga (1997), Tran et al. (2006), and Baliga and Atabaki (2006). These methods could be regarded as FEMs based on the subdomain-type (or control-volume-based) method of weighted residuals [Finlayson (1972)], and they could also be thought of as element-based vertex-centered FVMs [Baliga (1997), Zienkiewicz and Taylor (2000b)]. Thus, though the proposed improved formulations of the discretized pressure equation and boundary treatments apply specifically to CVFEMs, some of their key ideas may also be relevant and beneficial to other element-based vertex-centered and cell-centered FVMs [Acharya et al (2007), Ferziger and Perić (2002), Murthy et al. (2006)].

As was first pointed out in the now classical works of Harlow and Welch (1965) and Patankar and Spalding (1972), and later discussed in books by Patankar (1980) and Ferziger and Perić (2002), for example, in the formulation of numerical methods for the solution of primitive-variables-based mathematical models of incompressible fluid flow, special care and procedures are needed to avoid physically unrealistic oscillations in the pressure and velocity fields. Examples of such special procedures include the following: staggered or mutually displaced grids for the pressure and the velocity components; unequal-order formulations, in which a relatively coarser grid and a lower-order interpolation are used for pressure than those for the velocity components and other dependent variables; and the so-called momentum-interpolation scheme in the context of co-located formulations.

Staggered schemes are generally not well suited for implementation on body-fitted curvilinear (orthogonal and nonorthogonal) and unstructured grids. Unequal-order formulations are afflicted by the following disadvantages [Baliga (1997)]: (1) the need to use two sets of control volumes or elements makes the specification and calculation of geometric information unwieldy; (2) mass conservation is satisfied on the relatively coarser grid for pressure, but it is not necessarily satisfied over the finer grid for velocity components and other dependent variables; and (3) accurate solutions of fluid-flow problems involving high Reynolds numbers or large pressure gradients necessitate the use of fine pressure grids, which then implicitly require excessively fine grids for the velocity components and other dependent variables. Thus, the methods of choice in computational fluid dynamics today typically employ primitive-variables-based, co-located, equal-order formulations that invoke the momentum-interpolation scheme, especially when unstructured grids are used [Ferziger and Perić (2002), Baliga and Atabaki (2006), Murthy et al. (2006), Acharya et al. (2007)].

As is discussed in Lamoureux and Baliga (2011), despite the research and improvements reported in many published works on co-located equal-order CVFEMs, many of these method suffer from relatively slow convergence (and sometimes divergence), and also produce physically unrealistic features in the distributions of the calculated pressure in the vicinity of the domain boundaries, when used for the solution of incompressible fluid flow problems with specified velocity and inflow/outflow boundary conditions. In this section, the improvements proposed by Lamoureux and Baliga (2011) to some specific aspects of the formulations of the discretized pressure equation and boundary treatments, which were identified as the main sources of the aforementioned difficulties, are adapted and presented in the context of the proposed CVFEM for the solution of steady two-dimensional axisymmetric fluid flow and heat transfer problems. These improvements maintain the strength of the links (or coefficients) that connect nodal values of pressure in the discretized equations associated with grid points on or immediately adjacent to the calculation-domain boundaries with specified velocity and inflow/outflow conditions, and help in keeping the coefficient matrix of these equations diagonally dominant.

A brief presentation of the general form of the equations that govern the steady, two-dimensional axisymmetric, incompressible fluid flow and heat transfer problems considered in this work is provided in the next subsection. The details of the proposed improved formulations of the discretized pressure equation and boundary treatments are presented in the subsequent subsections, along with concise descriptions of the other aspects of the overall formulation of the CVFEM.

5.1.2 General Form of the Governing Equations

The equations that govern the steady, two-dimensional axisymmetric, incompressible fluid flow and heat transfer problems of interest can be cast in the following general form [Patankar (1980)]:

$$\frac{\partial}{\partial z}\left(\rho w\Phi\right)+\frac{1}{r}\frac{\partial}{\partial r}\left(r\rho v\Phi\right)=\frac{\partial}{\partial z}\left(\Gamma_{\Phi}\frac{\partial\Phi}{\partial z}\right)+\frac{1}{r}\frac{\partial}{\partial r}\left(r\Gamma_{\Phi}\frac{\partial\Phi}{\partial r}\right)+S_{\Phi} \tag{5.1}$$

In this equation, ρ denotes the density of the fluid, Φ is a general specific (per unit mass) scalar dependent variable, and Γ_{Φ} and S_{Φ} are the corresponding diffusion coefficient and volumetric source term, respectively. It should be noted that Eq. (5.1) can be specialized to the continuity, *z*-momentum, *r*-momentum, and energy equations presented in Chapter 2, Eqs. (2.13), (2.14), (2.15) and (2.23), respectively, by assigning appropriate meanings to Φ, Γ_{Φ}, and S_{Φ}. These specializations are listed in Table 5.1.

Table 5.1: Specializations of the general governing equation for modeling steady, two-dimensional axisymmetric, incompressible fluid flow and heat transfer problems in the vertical heating and cooling sections of the closed-loop thermosyphon.

	Φ	Γ_{Φ}	S_{Φ}
Continuity equation	1	0	0
z-momentum equation	w	μ_s	$-\frac{\partial P}{\partial z}+\left(\rho_s-\rho_{s,ref}\right)g_z+\frac{\partial \mu_s}{\partial z}\frac{\partial w}{\partial z}+\frac{\partial \mu_s}{\partial r}\frac{\partial v}{\partial z}$
r-momentum equation	v	μ_s	$-\frac{\partial P}{\partial r}-\frac{\mu_s v}{r^2}+\frac{\partial \mu_s}{\partial z}\frac{\partial w}{\partial r}+\frac{\partial \mu_s}{\partial r}\frac{\partial v}{\partial r}$
Energy equation	T	$\frac{k_s}{c_{p,s,ref}}$	$-\left[\frac{\partial}{\partial z}\left(\rho_{s,ref}wF\left(T\right)\right)+\frac{1}{r}\frac{\partial}{\partial r}\left(r\rho_{s,ref}vF\left(T\right)\right)\right]$

With respect to the specializations given in Table 5.1, and following the discussions provided earlier in Chapter 2, Subsection 2.4.2, it should be noted that the dependent variables are the following: the *z*- and *r*-direction velocity components, *w* and *v*, respectively; the reduced pressure, *P*; and the temperature, *T*. The component of the gravitational acceleration in the positive *z* direction is denoted by g_z. The effective properties of the MCPCM slurries are evaluated using the correlations and expressions given and discussed in Chapter 3 (see also Appendix B). Correlations for the evaluation of the thermophysical properties of distilled water are provided in Appendix A. Lastly, when the proposed CVFEM is used to solve other steady, two-dimensional axisymmetric, incompressible fluid flow and heat transfer problems, such as the two test problems presented later in this chapter, the values of Φ, Γ_{Φ} and S_{Φ} are adapted appropriately (the specializations used for the two test problems are presented in Section 5.2).

5.1.3 Domain Discretization

An unstructured-grid discretization of a sample irregular-shaped, two-dimensional axisymmetric calculation domain is schematically shown in Fig. 5.1 (longitudinal cross-section view). First, the longitudinal cross-section of the calculation domain is discretized into three-node triangular elements: in Fig. 5.1, the solid lines and black dots show the edges and nodes (vertices) of such elements, respectively. The centroid of each triangular element is then joined to the midpoints of its sides, as shown by the dashed lines in Fig. 5.1, thereby dividing each triangular element into three equal areas (regardless of the shape of the triangular element). Collectively, these areas form non-overlapping contiguous polygonal cross-sections of toroidal-shaped control volumes, each associated with a node in the finite-element mesh. The cross-sections of two such control volumes are depicted by the hashed regions in Fig. 5.1, and the associated details are shown in Figs. 5.2 (a) and (b). In co-located CVFEMs, all dependent variables of interest are stored at the same nodes. The full azimuthal extent of the axisymmetric calculation domain ($0 \le \theta \le 2\pi$ radians) is taken into account in the implementation of the CVFEM.

Schematic illustrations of the two-dimensional axisymmetric calculation domains of interest in this work, namely, the vertical heating and cooling sections (including the lengths of their pre- and post-heating, and pre- and posting-cooling, sections), were presented in Chapter 2 (see Figs. 2.1, 2.2, and 2.4). Their longitudinal cross-sections are rectangular regions defined by the following coordinate ranges: $0 \le z \le L_{total}$ and $0 \le r \le r_i$ (where L_{total} is the total length of the heating or cooling sections, including the lengths of the pre- and post-heating or pre- and post-cooling sections, and $r_i = D_i / 2$). Grids having an orthogonal line-by-line node arrangement were used for the solution of the steady, two-dimensional, incompressible fluid flow and heat transfer problems in these domains (details of these grids are presented in Chapter 6). However, the formulation of the proposed CVFEM was done in a general manner, which allowed it to be used for the solution of problems involving regular or irregular-shaped calculation domains; and this general formulation is presented in this section.

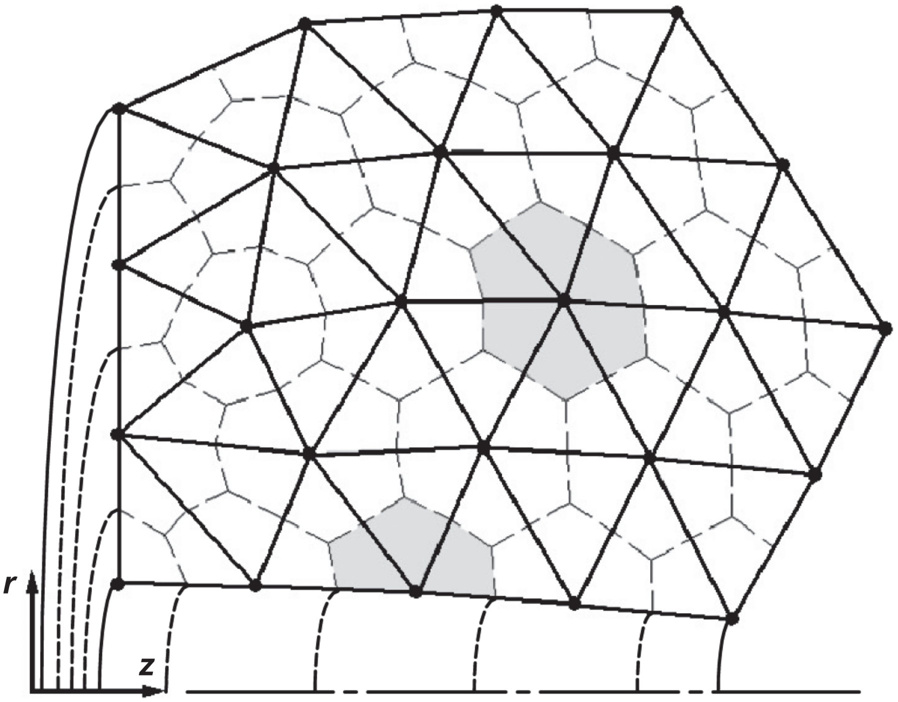

Figure 5.1: An unstructured-grid discretization of an irregular-shaped two-dimensional axisymmetric calculation domain (longitudinal cross-section view).

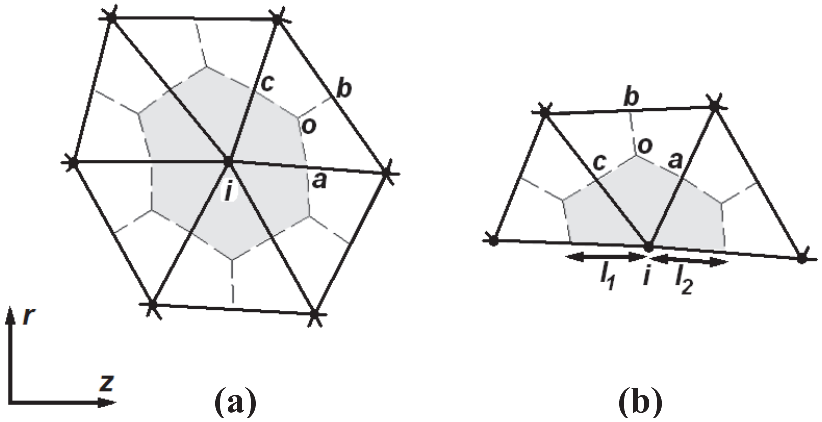

(a) (b)

Figure 5.2: Cross-sectional views of elements and a control volume, and related nomenclature, associated with (a) an internal node and (b) a boundary node.

5.1.4 Integral Conservation Equation for Φ

Let $\vec{J}$ denote the combined diffusion and advection fluxes of the general, specific (per unit mass), scalar dependent variable, Φ. Then these combined fluxes can be expressed as $\vec{J} = (-\Gamma_\Phi \partial\Phi / \partial z + \rho w \Phi)\vec{i} + (-\Gamma_\Phi \partial\Phi / \partial r + \rho v \Phi)\vec{j}$. In this expression, $\vec{i}$ and $\vec{j}$ are unit vectors in the positive z and r coordinate directions, respectively. The integral form of the conservation equation for Φ applied to a control volume associated with the node *i* shown in Figs. 5.2 (a) and (b) can be expressed as follows:

$$\begin{aligned}&\left(\int_a^o \vec{J}\cdot\vec{n}\,2\pi r ds + \int_o^c \vec{J}\cdot\vec{n}\,2\pi r ds - \int_{iaoc} S_\Phi dV\right)\\ &+\left(\text{similar contributions from other elements associated with node i}\right)\\ &+\left(\text{contributions from boundary conditions, if applicable}\right) = 0\end{aligned} \tag{5.2}$$

In this equation, dV is the differential volume, ds is the differential length along the face of the control volume in its longitudinal cross-section, and $\vec{n}$ is a unit vector normal to ds and pointing outwards with respect to the control volume associated with node *i*.

5.1.5 Interpolation Functions

The discretized equations are algebraic approximations to integral conservation equations akin to Eq. (5.2). To derive these equations, appropriate interpolation functions must specified for the diffusion coefficients (Γ_Φ), density (ρ), source terms (S_Φ), and the dependent variables (Φ). In earlier published works on CVFEMs, for example, Baliga and Patankar (1980) and Masson et al. (1994), nodal values of Γ_Φ were stored and interpolated linearly in each element. With that interpolation scheme, however, it is not possible to ensure that algebraic approximations to the diffusion transport terms in Eq. (5.2) contribute positively to the coefficients in the discretized equations. In this work, therefore, in each triangular element, the value of Γ_Φ at the centroid is assumed to prevail over the corresponding element. Even with this interpolation of Γ_Φ, special restrictions are needed to ensure positive contributions from the algebraic approximations of the diffusions transport terms to the discretized equations. These restrictions are elaborated later in this section. With regard to the interpolation of ρ, in each triangular element, the value at the centroid is assumed to prevail over the corresponding element. The source term, S_Φ, is first linearized, if necessary, and expressed as follows [Patankar (1980)]: $S_\Phi = G^{S_\Phi} + E^{S_\Phi}\Phi$. In each element, the nodal values of G^{S_Φ} and E^{S_Φ} are assumed to prevail over the corresponding portions of the control volumes associated with these nodes and contained within the element under consideration.

In the calculation of mass flow rates across the control-volume faces, the mass-conserving velocity components in the z and r directions are denoted by w^m and v^m, respectively, and interpolated using a special momentum-interpolation scheme that prevents spurious pressure and velocity oscillations. This momentum-interpolation scheme is based on ideas borrowed from the works of Rhie and Chow (1983) and Prakash and Patankar (1985). Details of this scheme are given after the presentation of the discretized momentum equations. In the derivation of algebraic approximations to the gradients of the reduced pressure that appear in the momentum equations and the aforementioned momentum-interpolation scheme, the reduced pressure, P, is interpolated linearly within each element.

In the derivation of algebraic approximations to the surface integrals of diffusion fluxes in Eq. (5.2), the gradients of the dependent variable inside each triangular element are approximated using linear interpolation functions. Full details of these interpolation functions can be found in Baliga and Patankar (1980) and Baliga and Atabaki (2006). It should be noted that with the linear interpolation of Φ and the aforementioned piecewise-constant (centroidal-value prevailing) interpolation of Γ_Φ within each element, to ensure that the algebraic approximations of the diffusion transport terms in Eq. (5.2) contribute positively to the coefficients in the discretized equations, every triangular element in the longitudinal cross-section of the calculation domain must be an acute-angle triangle (that is, each vertex angle must be $\leq \pi/2$ radians). Venditti (1998) has presented a proof of this sufficient condition for two-dimensional planar problems.

For the derivation of algebraic approximations to the advection transport terms in equation Eq. (5.2), Baliga and Patankar (1980) proposed a flow-oriented upwind scheme (FLO) for the interpolation of Φ in each element. In this scheme, which is constructed by borrowing ideas from the works of Spalding (1972) and Raithby (1976), Φ is assumed to vary exponentially in the direction of an element-average mass-conserving velocity vector and linearly in the direction normal to this vector. When an element-based Peclet number, Pe_{Δ}, approaches zero, this function becomes fully linear. Full details of this scheme and related references can be found in Baliga and Patankar (1980), Baliga (1997), and Baliga and Atabaki (2006).

In problems that involve acute-angle triangular elements and relatively modest values of Pe_{Δ}, the FLO scheme performs well. However, when large gradients of the dependent variable occur within an element in a direction normal to the element-average velocity vector, or when obtuse-angle triangular elements are used in problems with large values of Pe_{Δ}, the FLO scheme can lead to undesirable negative contributions of the advection transport terms to the coefficients in the discretized equations. Masson et al. (1994) have proposed a mass-weighted skew upwind scheme (MAW) that overcomes this difficulty. However, this MAW scheme, which is an adaptation of the positive-coefficient schemes of Schneider and Raw (1986) and Saabas and Baliga (1994), is only first-order accurate. Recently, Tran et al. (2006) have proposed a second-order accurate extension of this MAW scheme, but their scheme is not bounded (allows negative coefficients), as has been discussed by Costa et al. (2007). The formulation of a uniformly second-order accurate and bounded Φ interpolation scheme for the algebraic approximation of the advection transport terms in CVFEMs is a topic that requires further work, and it is outside the scope of this thesis. In this work, the grids used were composed of acute-angle triangular elements and the values of Pe_{Δ} were relatively small in the problems of interest: thus, the FLO scheme was used and it performed well.

5.1.6 Discretized equations for Φ

The discretized equations for the specific (per unit mass) general scalar dependent variable, Φ, are obtained by first deriving algebraic approximations to the element contributions and the boundary contributions in Eq. (5.2), using the interpolation functions discussed previously, and then assembling these contributions appropriately [Baliga and Atabaki (2006)]. The algebraic approximation to the total (diffusion, advection, and source terms) contribution of a given element, composed of nodes 1, 2, and 3, to Eq. (5.2) for a node i = 1 can be expressed compactly as follows:

$$\left(\int_a^o \vec{J}\cdot\vec{n}\,2\pi r ds + \int_o^c \vec{J}\cdot\vec{n}\,2\pi r ds - \int_{iaoc} S_\Phi dV\right) = C_1^{\Phi,1}\Phi_1 + C_1^{\Phi,2}\Phi_2 + C_1^{\Phi,3}\Phi_3 + D_1^\Phi \tag{5.3}$$

When similar algebraic approximations to the contributions of all elements associated with the node i in Figs. 5.2 (a) and (b) are derived and appropriately assembled, the resulting approximation of Eq. (5.2) can be cast in the following general form:

$$\begin{aligned}[(a_i^\Phi)_{element\ contributions}]\Phi_i = \sum_{nb,i}[(a_{nb,i}^\Phi)_{element\ contributions}]\Phi_{nb,i} + (b_i^\Phi)_{element\ contributions} \\ + (\Re_{total,i,in}^\Phi)_{if\ applicable}\end{aligned} \tag{5.4}$$

In this equation, $(\Re_{total,i,in}^\Phi)_{if\ applicable}$ denotes the total (diffusion + advection) rate of transport of Φ across the boundary of the calculation domain into the control volume associated with node i, if applicable. If node i is an internal node of the computational mesh (that is, it does not lie on the boundary of the calculation domain), then $(\Re_{total,i,in}^\Phi)_{if\ applicable}$ = 0, and the assembled element contributions yield the complete discretized equation for Φ associated with this node.

For both internal and boundary nodes, the final discretized equation for Φ can be expressed as follows:

$$a_i^\Phi \Phi_i = \sum_{nb,i} a_{nb,i}^\Phi \Phi_{nb,i} + b_i^\Phi \tag{5.5}$$

The coefficient a_i^Φ in this equation is related to the neighbor-point coefficients, $a_{nb,i}^\Phi$, by the following equation:

$$\begin{aligned}a_i^\Phi = \sum_{nb,i} a_{nb,i}^\Phi - \sum_{elements\ assc.\ with\ i} (E_i^{S_\Phi} V_{iaoc})_{element} \\ + [\text{algebraic approx. to net mass flow rate out of CV}_i]\end{aligned} \tag{5.6}$$

When the CVFEM solution is fully converged (to within the specified tolerance), the algebraic approximation to the net mass flow rate out of the control volume associated with node *i* in Eq. (5.6) is zero for the steady-state problems of interest. During the iterative solution of the discretized equations, however, the algebraic approximation to the net mass flow rate out of the control volume associated with node *i* could be negative (instead of its fully converged value of zero): in such situations, if a_i^{Φ} is computed by either suitable assembly of the associated element and boundary (when applicable) contributions or using equation Eq. (5.6), then the corresponding discretized equation would not be diagonally dominant; and that, in turn, could slow down convergence or lead to divergence of iterative solution procedures [Patankar (1980)]. To avoid this potential difficulty, it is recommended that the neighbor coefficients, $a_{nb,i}^{\Phi}$, be computed first, by assembling the associated element and boundary (when applicable) contributions, and then the following equation be used to calculate a_i^{Φ}:

$$a_i^{\Phi} = \sum_{nb,i} a_{nb,i}^{\Phi} - \sum_{elements\ assc.\ with\ i} (E_i^{S_\Phi} V_{iaoc})_{element} \tag{5.7}$$

5.1.7 Discretized Momentum Equations

The integral momentum conservation equations are similar to the integral conservation equation for Φ presented earlier, except for the presence of integrals of the pressure gradients, along with other momentum source terms. For a node $i = 1$, such as that shown in Figs. 5.2 (a) and (b), the contributions of the integrals of the pressure gradients in the *z*- and *r*-momentum equations over the portion of the control volume contained within an element associated with this node are approximated as follows:

$$\int_{1aoc} \left(-\frac{\partial P}{\partial z} \right) dV = -\left(\frac{\partial P}{\partial z} \right)_{\Delta} V_{1aoc} \ ; \ \int_{1aoc} \left(-\frac{\partial P}{\partial r} \right) dV = -\left(\frac{\partial P}{\partial r} \right)_{\Delta} V_{1aoc} \tag{5.8}$$

As the reduced pressure, *P*, is interpolated linearly in each element, the pressure gradients $(\partial P / \partial z)_{\Delta}$ and $(\partial P / \partial r)_{\Delta}$ are uniform within the element, and each is related linearly to the values of *P* at the three nodes of the element. The discretized momentum equations for node i are obtained by assembling the contributions of the associated elements appropriately, and they can be cast in the following forms:

$$\begin{aligned}[(a_i^w)_{element\ contributions}]w_i = \sum_{nb,i}[(a_{nb,i}^w)_{element\ contributions}]w_{nb,i} + (b_i^w)_{element\ contributions} \\ -\left(\overline{\partial P/\partial z}\right)_{V_i} V_i + (\Re_{total,i,in}^w)_{if\ applicable}\end{aligned} \tag{5.9}$$

$$\begin{aligned}[(a_i^v)_{element\ contributions}]v_i = \sum_{nb,i}[(a_{nb,i}^v)_{element\ contributions}]v_{nb,i} + (b_i^v)_{element\ contributions} \\ -\left(\overline{\partial P/\partial r}\right)_{V_i} V_i + (\Re_{total,i,in}^v)_{if\ applicable}\end{aligned} \tag{5.10}$$

In this equation, $(\Re_{total,i,in}^w)_{if\ applicable}$ and $(\Re_{total,i,in}^v)_{if\ applicable}$ denote the total (diffusion + advection) rate of transport of *z*- and *r*-direction components of momentum, respectively, across the boundary of the calculation domain into the control volume associated with node *i*, if applicable. The terms $\left(\overline{\partial P/\partial z}\right)_{V_i}$ and $\left(\overline{\partial P/\partial r}\right)_{V_i}$ denote volume-averaged values of the corresponding reduced-pressure gradients over V_i, which is the total volume of the control volume associated with node *i*. Here too, if node *i* is an internal node of the computational mesh, then $(\Re_{total,i,in}^w)_{if\ applicable}$ = 0 and $(\Re_{total,i,in}^v)_{if\ applicable}$ = 0, and the assembled element contributions yield the complete discretized equation for *w* and *v* associated with this node. For both internal and boundary nodes, the final discretized equations for w_i and v_i can be expressed as follows:

$$a_i^w u_i = \sum_{nb,i} a_{nb,i}^w w_{nb,i} + b_i^w - \left(\overline{\partial P/\partial z}\right)_{V_i} V_i \tag{5.11}$$

$$a_i^v v_i = \sum_{nb,i} a_{nb,i}^v v_{nb,i} + b_i^v - \left(\overline{\partial P/\partial r}\right)_{V_i} V_i \tag{5.12}$$

The coefficients a_i^w and a_i^v in these equation are related to the corresponding neighbor coefficients, $a_{nb,i}^w$ and $a_{nb,i}^v$, respectively, by equations akin to Eq. (5.6). However, for reasons already mentioned in connection with Eq. (5.6), it is recommended that the neighbor coefficients $a_{nb,i}^w$ and $a_{nb,i}^v$ be computed first, by assembling the associated element and boundary (when applicable) contributions, and then the following equations be used to calculate a_i^w and a_i^v:

$$a_i^w = \sum_{nb,i} a_{nb,i}^w - \sum_{elements\ assc.\ with\ i} (E_i^{S_w} V_{iaoc})_{element} \tag{5.13}$$

$$a_i^v = \sum_{nb,i} a_{nb,i}^v - \sum_{elements\ assc.\ with\ i} (E_i^{S_v} V_{iaoc})_{element} \tag{5.14}$$

5.1.8 Momentum-Interpolation Scheme and Mass-Conserving Velocity Components

The momentum interpolation scheme used in this work is based on ideas first proposed by Rhie and Chow (1983) and Prakash and Patankar (1985). The first step in the formulation of this scheme is the recasting of the discretized momentum equations at each node *i* in the following forms:

$$\begin{gathered} w_i = \hat{w}_i + d_i^w \left[-\left(\overline{\partial P / \partial z} \right)_{V_i} \right] \; ; \; v_i = \hat{v}_i + d_i^v \left[-\left(\overline{\partial P / \partial r} \right)_{V_i} \right] \\ \hat{w}_i = \frac{\sum_{nb,i} a_{nb,i}^w w_{nb,i} + b_i^w}{a_i^w} \; ; \; \hat{v}_i = \frac{\sum_{nb,i} a_{nb,i}^v v_{nb,i} + b_i^v}{a_i^v} \\ d_i^w = \frac{V_i}{a_i^w} \; ; \; d_i^v = \frac{V_i}{a_i^v} \end{gathered} \tag{5.15}$$

Next, in each element, the mass-conserving velocity components, w^m and v^m, are defined and calculated at any point within the element using the following adaptation of the momentum interpolation scheme:

$$w^m = \hat{w}_{\text{lin.int.}} + \left(d^w \right)_o \left[-\left(\frac{\partial P}{\partial z} \right)_\Delta \right] \; ; \; v^m = \hat{v}_{\text{lin.int.}} + \left(d^v \right)_o \left[-\left(\frac{\partial P}{\partial r} \right)_\Delta \right] \tag{5.16}$$

In this equation, $\hat{w}_{\text{lin.int.}}$ and $\hat{v}_{\text{lin.int.}}$ indicate linear interpolation of the nodal values of $\hat{w}_i$ and $\hat{v}_i$, respectively, to the point of interest within the element. The centroidal values, $\left(d^w \right)_o$ and $\left(d^v \right)_o$, are equal to one-third of the sums of the corresponding three nodal values of d_i^w and d_i^v, respectively, and they are assumed to prevail in the element. As was mentioned earlier, the reduced pressure, *P*, is interpolated linearly in each element, so the reduced-pressure gradients $(\partial P/\partial z)_{\Delta}$ and $(\partial P/\partial r)_{\Delta}$ are uniform within the element, and each is related linearly to the values of P at the three nodes of the element [Baliga and Atabaki (2006)].

In some of the earlier publications on CVFEMs, for example, Masson et al. (1994) and Saabas and Baliga (1994), the recommended procedure in the aforementioned momentum-interpolation scheme was a linear interpolation of the nodal values of d_i^w and d_i^v in each element (in addition to linear interpolation of the nodal values of $\hat{w}_i$ and $\hat{v}_i$ within the element). However, with that procedure, it is possible to generate negative coefficients in the discretized pressure equation. The reason for this can be understood if the discretized pressure equation is interpreted as a discretized Poisson equation, with d^w and d^v playing a role akin to that of a diffusion coefficient: in this context, if the linear interpolation of P is combined with linear interpolation of d^w and d^v with each element, then positive coefficients in the discretized pressure equations are not guaranteed, as is discussed in the works Venditti (1998) and Venditti and Baliga (1998). Therefore, in this work, linear interpolation of P and the aforementioned piecewise-constant interpolation of d^w and d^v (centroidal values $\left(d^w\right)_o$ and $\left(d^v\right)_o$ prevailing) within each element are recommended, with the complementary recommendation that every element be an acute-angle triangle. However, it should be noted that even with these recommendations, if d_i^w and d_i^v are not the same within each element (as would be the case if $E_i^{S_w}$ and $E_i^{S_v}$ are not the same within each element), then positive coefficients are not guaranteed in the discretized pressure equations.

5.1.9 Discretized Equations for Pressure

These equations are algebraic approximations to the integral mass conservation equations, derived using the mass-conserving velocity components and the momentum-interpolation scheme described in the previous section. The integral mass conservation equation applied to the control volume associated with node *i* in Figs. 5.2 (a) and (b) is expressed as follows:

$$\begin{aligned}&\int_a^o \rho\vec{v}^m\cdot\vec{n}\,2\pi r ds+\int_o^c \rho\vec{v}^m\cdot\vec{n}\,2\pi r ds\\&+\left(\text{similar contributions from other elements associated with node i}\right)\\&+\left(\text{contributions from inflow and/or outflow B.C., if applicable}\right)=0\end{aligned}\tag{5.17}$$

The algebraic approximation to the contribution of an element composed of nodes 1, 2, and 3 to the previous equation for a node i = 1 can be expressed in terms of the corresponding nodal values of pressure and cast in the following form:

$$\int_a^o \rho\vec{v}^m\cdot\vec{n}\,2\pi r ds+\int_o^c \rho\vec{v}^m\cdot\vec{n}\,2\pi r ds=C_1^{P,1}P_1+C_1^{P,2}P_2+C_1^{P,3}P_3+D_1^P\tag{5.18}$$

When similar algebraic approximations to the contributions of all elements associated with the node i in Figs. 5.2 (a) and (b) are derived and appropriately assembled, the resulting approximation of Eq. (5.17) can be cast in the following general form:

$$\begin{aligned}[(a_i^P)_{element\ contributions}]P_i=&\sum_{nb,i}[(a_{nb,i}^P)_{element\ contributions}]P_{nb,i}\\&+(b_i^P)_{element\ contributions}+(\Re_{mass,i,in})_{if\ applicable}\end{aligned}\tag{5.19}$$

In this equation, the coefficients $(a_{nb,i}^P)_{element\ contributions}$ and $(a_i^P)_{element\ contributions}$ depend on the values of d^w and d^v, and $(b_i^P)_{element\ contributions}$ depends on the values of $\hat{w}$ and $\hat{v}$, at the node i and its neighbor nodes. $(\Re_{mass,i,in})_{if\ applicable}$ denotes the rate of transport of mass across the boundary of the calculation domain into the control volume associated with node i, if applicable. The algebraic approximation of $\Re_{mass,i,in}$ is calculated using linear interpolation of the latest available values of ρ, w, and v (either specified or calculated) at nodes on inflow and outflow boundaries, rather than the values of w^m and v^m which are used to compute the mass flow rate across control-volume faces within the elements. If node i is an internal node of the computational mesh, then $(\Re_{mass,i,in})_{if\ applicable}$ = 0, and the assembled element contributions yield the complete discretized equation for P associated with this node. For both internal and boundary nodes, the final discretized equation for P can be expressed as follows:

$$a_i^P P_i = \sum_{nb,i} a_{nb,i}^P P_{nb,i} + b_i^P \tag{5.20}$$

The coefficient a_i^P in this equation is related to the neighbor-point coefficients, $a_{nb,i}^P$, by the following equation:

$$a_i^P = \sum_{nb,i} a_{nb,i}^P \tag{5.21}$$

5.1.10 Boundary Treatments

Fixed (nonmoving) domain boundaries that coincide with impermeable solid walls, symmetry surfaces, and inflow and outflow regions are considered in this work. The following five commonly encountered boundary conditions and their treatments are discussed below: no normal fluid flow and specified value of the dependent variable; no normal fluid flow and specified normal diffusion flux of the dependent variable into the calculation domain; no normal fluid flow and specified external convection transfer coefficient and reference value of dependent variable; inflow with specified value of dependent variable; and outflow.

No normal fluid flow and specified value of the dependent variable

For any node i on such boundaries, with respect to the discretized equation for Φ_i, the values of the coefficients and constant that are obtained by assembling the contributions of the associated elements are first stored (for later use):

$$\begin{aligned} &(a_{nb,i}^{\Phi})_{stored} = (a_{nb,i}^{\Phi})_{element\ contributions} \ ; \ (b_i^{\Phi})_{stored} = (b_i^{\Phi})_{element\ contributions} \\ &(a_i^{\Phi})_{stored} = \sum_{nb,i} (a_{nb,i}^{\Phi})_{element\ contributions} - \sum_{elements\ assc.\ with\ i} (E_i^{S_\Phi} V_{iaoc})_{element} \end{aligned} \tag{5.22}$$

Then the coefficients and constant in the discretized equation for Φ_i at this boundary node are assigned the following values:

$$a_i^{\Phi} = 1 \ ; \ a_{nb,i}^{\Phi} = 0 \ ; \ b_i^{\Phi} = \Phi_{specified} \tag{5.23}$$

As there is no normal fluid flow, the rate of advection transport into the control volume associated with node *i* across the boundary under consideration is zero. Thus, after the completion of all discretized equations and computation of the unknown values of Φ, and also the satisfaction of the discretized continuity equation for the control volume associated with the aforementioned node *i*, the rate of diffusion transport into this control volume across the faces that lie on the domain boundary, $\Re^{\Phi}_{D,i,in,calc}$, can be computed using the aforementioned stored coefficients and the following equation:

$$\Re^{\Phi}_{D,i,in,calc} = (a^{\Phi}_{i})_{stored}\,\Phi_{i} - \sum_{nb,i}(a^{\Phi}_{nb,i})_{stored}\,\Phi_{nb,i} - (b^{\Phi}_{i})_{stored} \tag{5.24}$$

With respect to the velocity components w_i and v_i at such boundary nodes, the treatment represented by Eqs. (5.22) and (5.23) is suitably adapted and applied. Then, using suitable boundary treatments at other nodes (as needed) and the latest available values of the reduced pressure, *P*, the discretized equations for all unknown values of w_i and v_i are completed and solved (sequentially), and the calculated values of these velocity components at outflow boundaries (if they exist) are corrected to ensure overall mass conservation (using a procedure described later in this subsection). Following that, the rates of diffusion (viscous) transport of the corresponding components of momentum across the domain boundary into the control volume associated with node *i*, $\Re^{w}_{D,i,in,calc}$ and $\Re^{v}_{D,i,in,calc}$, are computed using the stored coefficients as follows:

$$\begin{aligned}\Re^{w}_{D,i,in,calc} &= (a^{w}_{i})_{stored}\,w_{i} - \sum_{nb,i}(a^{w}_{nb,i})_{stored}\,w_{nb,i} \\ &\quad -\{(b^{w}_{i})_{stored} - \left(\overline{\partial P/\partial z}\right)_{V_i} V_i\}\end{aligned} \tag{5.25}$$

$$\begin{aligned}\Re^{v}_{D,i,in,calc} &= (a^{v}_{i})_{stored}\,v_{i} - \sum_{nb,i}(a^{v}_{nb,i})_{stored}\,v_{nb,i} \\ &\quad -\{(b^{v}_{i})_{stored} - \left(\overline{\partial P/\partial r}\right)_{V_i} V_i\}\end{aligned} \tag{5.26}$$

The values of $\Re^{w}_{D,i,in,calc}$ and $\Re^{v}_{D,i,in,calc}$ yielded by the two equations above are used in the computations of the values of $\hat{w}_i$ and $\hat{v}_i$ at a node *i* on such boundaries, along with the computations of d_i^w and d_i^v, using the following equations:

$$\begin{aligned}
\hat{w}_i &= \frac{\sum_{nb,i} (a^w_{nb,i})_{stored} w_{nb,i} + (b^w_i)_{stored} + \Re^w_{D,i,in,calc}}{(a^w_i)_{stored}} \\
\hat{v}_i &= \frac{\sum_{nb,i} (a^v_{nb,i})_{stored} v_{nb,i} + (b^v_i)_{stored} + \Re^v_{D,i,in,calc}}{(a^v_i)_{stored}} \\
d^w_i &= \frac{V_i}{(a^w_i)_{stored}} \; ; \; d^v_i = \frac{V_i}{(a^v_i)_{stored}}
\end{aligned} \tag{5.27}$$

In some of the earlier publications on CVFEMs, for example, Masson et al. (1994), Saabas and Baliga (1994), and Baliga (1997), the following procedure is prescribed at such boundaries: $\hat{w}_i = w_{specified}$, $\hat{v}_i = v_{specified}$, $d_i^w = 0$, and $d_i^v = 0$. This boundary treatment is not incorrect, as the correct pressure field is obtained when the overall iterative solution procedure converges. However, because d_i^w and d_i^v are assigned the value of zero, it diminishes the strength of the coefficients in the discretized pressure equations associated with the nodes on and immediately adjacent to such boundaries, leading to relatively slow convergence (or even divergence) of the overall iterative solution procedure. The relations given in Eq. (5.27) and the related treatments for the computations of $\hat{w}_i$, $\hat{v}_i$, d_i^w, and d_i^v at a node *i* on boundaries with specified values of *w* and *v* and no normal fluid flow ensure that the strengths of the coefficients in the discretized pressure equations for this node and its neighbors are maintained.

No normal fluid flow and specified normal diffusion flux into domain

On such boundaries, the normal component of the diffusion flux of Φ into the calculation domain, $J^{\Phi}_{D,n,in}$, is prescribed with respect to each element edge on the boundary and the two nodes associated with this edge. Therefore, with respect to the left- and right-element edges associated with the boundary node *i* in Fig. 5.2 (b), for which the half-link lengths are l_1 and l_2, respectively, the corresponding values of the normal diffusion flux of Φ into the calculation domain are $(J^{\Phi}_{D,n,in})_{l_1}$ and $(J^{\Phi}_{D,n,in})_{l_2}$, and $\Re^{\Phi}_{D,i,in}$ is approximated as follows:

$$\begin{aligned}\Re^{\Phi}_{D,i,in} &= \int_{l_1} J_{D,n,in} 2\pi r ds + \int_{l_2} J_{D,n,in} 2\pi r ds \\ &\simeq (J^{\phi}_{D,n,in})_{l_1} 2\pi r_{1,mid} l_1 + (J^{\phi}_{D,n,in})_{l_2} 2\pi r_{2,mid} l_2\end{aligned} \tag{5.28}$$

In this equation, $r_{1,mid}$ and $r_{2,mid}$ represent the values of the radial coordinate at the midpoints of the half-links of lengths l_1 and l_2. The approximation given in Eq. (5.28) is appropriate if the values of $(J^{\Phi}_{D,n,in})_{l_1}$ and $(J^{\Phi}_{D,n,in})_{l_2}$ are considered constant over the lengths of their respective half-links.

As there is no normal fluid flow across the boundary under consideration, the corresponding rate of advection transport into the control volume associated with node *i* is zero. Thus, $\Re^{\Phi}_{total,i,in}$ = $\Re^{\Phi}_{D,i,in}$, and the coefficients and constant in the discretized equation for Φ at the boundary node *i* are obtained as follows:

$$\begin{aligned}&a^{\Phi}_{nb,i} = (a^{\Phi}_{nb,i})_{element\ contributions} \;\; ; \;\; b^{\Phi}_{i} = (b^{\Phi}_{i})_{element\ contributions} + \Re^{\Phi}_{D,i,in} \\ &a^{\Phi}_{i} = \sum_{nb,i} a^{\Phi}_{nb,i} - \sum_{elements\ assc.\ with\ i} (E^{S_\Phi}_{i} V_{iaoc})_{element}\end{aligned} \tag{5.29}$$

With respect to the velocity components *w* and *v* at such boundary nodes, the diffusion (viscous) fluxes (or shear stresses) that transport the corresponding components of momentum into the domain are specified, and the discretized equations are completed using suitable adaptations of Eqs. (5.28) and (5.29). Following that, using suitable boundary treatments at other nodes (as needed) and the latest available values of the reduced pressure *P*, the discretized equations for all unknown values of w_i and v_i are completed and solved (sequentially), and the calculated values of these velocity components at outflow boundaries (if they exist) are corrected (also sequentially) to ensure overall mass conservation (using a procedure described later in this subsection). Then, the values of $\hat{w}_i$, $\hat{v}_i$, d^w_i, and d^v_i at the node *i* on such boundaries are computed using the expressions given in Eq. (5.15).

No normal fluid flow and specified external convection transfer coefficient and reference value of dependent variable

For such boundaries, the normal component of the diffusion flux of Φ into the calculation domain, $J^{\Phi}_{D,n,in}$, is a function of an external convection transfer coefficient, h^{Φ}, and a reference value of the dependent variable, Φ_{ref}, which are both prescribed at the two nodes associated with an element-edge on the domain boundary (and their values are assumed to prevail over their neighboring half-links). Therefore, with respect to the left- and right-element edges associated with the boundary node *i* in Fig. 5.2 (b), $\Re^{\Phi}_{D,i,in}$ is approximated as follows:

$$\begin{aligned}\Re^{\Phi}_{D,i,in} &= \int_{l_1} J_{D,n,in} 2\pi r ds + \int_{l_2} J_{D,n,in} 2\pi r ds \\ &= \int_{l_1} h^{\Phi}\left(\Phi_{ref} - \Phi_i\right) 2\pi r ds + \int_{l_2} h^{\Phi}\left(\Phi_{ref} - \Phi_i\right) 2\pi r ds \\ &\simeq \left[h^{\Phi}\left(\Phi_{ref} - \Phi_i\right)\right]_{l_1} 2\pi r_{1,mid} l_1 + \left[h^{\Phi}\left(\Phi_{ref} - \Phi_i\right)\right]_{l_2} 2\pi r_{2,mid} l_2\end{aligned} \tag{5.30}$$

In the approximation given in Eq. (5.30), the value of the normal diffusion flux of Φ into the calculation domain, $h^{\Phi}\left(\Phi_{ref} - \Phi_i\right)$, is considered constant over the length of each half-links. Again, since there is no normal fluid flow across the boundary under consideration, the corresponding rate of advection transport into the control volume associated with node *i* is zero and thus, $\Re^{\Phi}_{total,i,in} = \Re^{\Phi}_{D,i,in}$. The coefficients and constant in the discretized equation for Φ at the boundary node *i* are obtained as follows:

$$\begin{aligned}a^{\Phi}_{nb,i} &= (a^{\Phi}_{nb,i})_{element\ contributions} \\ b^{\Phi}_i &= (b^{\Phi}_i)_{element\ contributions} + \left[h^{\Phi}\Phi_{ref}\right]_{l_1} 2\pi r_{1,mid} l_1 + \left[h^{\Phi}\Phi_{ref}\right]_{l_2} 2\pi r_{2,mid} l_2 \\ a^{\Phi}_i &= \sum_{nb,i} a^{\Phi}_{nb,i} - \sum_{elements\ assc.\ with\ i} (E^{S_\Phi}_i V_{iaoc})_{element} \\ &\quad + \left[h^{\Phi}\right]_{l_1} 2\pi r_{1,mid} l_1 + \left[h^{\Phi}\right]_{l_2} 2\pi r_{2,mid} l_2\end{aligned} \tag{5.31}$$

The completion of the discretized equations of the velocity components *w* and *v* at the boundary nodes are performed with suitable adaptations of Eqs. (5.30) and (5.31).

Again, the discretized equations for all unknown values of w_i and v_i are completed using suitable boundary treatments at other nodes, if needed, and the latest available values of the reduced pressure, *P*, and then solved. The calculated values of these velocity components at outflow boundaries (if these are present) are corrected to ensure overall mass conservation. Lastly, the values of $\hat{w}_i$, $\hat{v}_i$, d_i^w, and d_i^v at the node *i* on such boundaries are computed using the expressions given in Eq. (5.15).

Inflow with specified value of dependent variable

With respect to the discretized equation for Φ at a node *i* on such boundaries, the values of the neighbor coefficients and constant that are obtained by assembling the contributions of the associated elements are first stored (for later use):

$$\begin{aligned}&(a_{nb,\,i}^{\Phi})_{stored} = (a_{nb,\,i}^{\Phi})_{element\ contributions} \ ; \ (b_i^{\Phi})_{stored} = (b_i^{\Phi})_{element\ contributions}\\&(a_i^{\Phi})_{stored} = \sum_{nb,i}(a_{nb,i}^{\Phi})_{element\ contributions} - \sum_{elements\ assc.\ with\ i}(E_i^{S_\Phi} V_{iaoc})_{element}\end{aligned} \qquad (5.32)$$

Then the coefficients and constant in the discretized equation for Φ at this boundary node are assigned the following values:

$$a_i^{\Phi} = 1 \ ; \ a_{nb,\,i}^{\Phi} = 0 \ ; \ b_i^{\Phi} = \Phi_{specified} \qquad (5.33)$$

After the completion of all discretized equations and computation of the unknown values of Φ, and satisfaction of the discretized continuity equation for the control volume associated with aforementioned boundary node *i*, the rates of advection and diffusion transport of Φ into the control volume associated with this node *i* across the faces that lie on the domain boundary are computed as follows. First, with respect to the notation illustrated in Fig. 5.2 (b), the mass flow rate into the control volume across the boundary under consideration, $\Re_{mass,i,in}$, is calculated using linear interpolation of the specified values of *w*, *v*, and fluid density (ρ) at node *i* and the adjacent boundary nodes on the associated left and right element edges. Then the rate of advection transport of Φ into the control volume across the boundary under consideration, $\Re_{advec,i,in}^{\Phi}$, is calculated by assuming that the specified value of Φ_i prevails over the portions l_1 and l_2 of the boundary edges of the associated elements, illustrated in Fig. 5.2 (b):

$$\Re^{\Phi}_{advec,i,in} = \Re_{mass,i,in}\Phi_i \tag{5.34}$$

The above-mentioned procedure for calculating $\Re^{\Phi}_{advec,i,in}$ at a node *i* lying on an inflow boundary is consistent with the procedure that is used to calculate rates of advection transport across control-volume faces along boundary edges of elements associated with nodes lying on outflow boundaries (described next). It is also second-order accurate when the nodes are uniformly distributed on the inflow boundaries under consideration. In practice, when a non-uniform grid may be required to ensure cost-effective computations, the distribution of nodes along the inflow boundaries can be done using a geometric expansion (or contraction) scheme for the distances between the nodes, with a geometric factor relatively close to one, to ensure that the aforementioned procedure for calculating $\Re^{\Phi}_{advec,i,in}$ is almost second-order accurate. More elaborate schemes that ensure second- or higher-order accuracy in the computation of $\Re^{\Phi}_{advec,i,in}$ even with non-uniform grids, for example piecewise linear interpolation or Simpson's rule integration, can be implemented at inflow and outflow boundaries. However, with such higher-order schemes, it is not possible to ensure that the coefficients in the discretized equations for Φ at outflow boundary nodes remain positive: which, in turn, could lead to slow convergence or divergence of iterative schemes for the solution of the discretized equations (due to lack of diagonal dominance of these equations) and (or) physically unrealistic oscillations in the computed solutions. To avoid such potential difficulties, the procedure represented by Eq. (5.34) is recommended in this revised formulation for the calculation of $\Re^{\Phi}_{advec,i,in}$ at nodes on inflow boundaries.

After the completion of the above-mentioned procedure for the calculation of $\Re^{\Phi}_{advec,i,in}$ at a node *i* lying on the inflow boundary under consideration, the rate of diffusion transport into the associated control volume across its faces that lie on the domain boundary, $\Re^{\Phi}_{D,i,in,calc}$, is computed using the aforementioned stored coefficients and the following equation:

$$\begin{aligned}\Re^{\Phi}_{D,i,in,calc} &= \Re^{\Phi}_{total,i,in,calc} - \Re^{\Phi}_{advec,i,in} \\ &= (a_i^{\Phi})_{stored}\Phi_i - \sum_{nb,i}(a^{\Phi}_{nb,i})_{stored}\Phi_{nb,i} - (b_i^{\Phi})_{stored}\end{aligned} \tag{5.35}$$

With respect to the velocity components w_i and v_i at an inflow boundary-node *i*, the treatment represented by Eqs. (5.32) and (5.33) is suitably adapted and applied. Then, using appropriate boundary treatments at other nodes (as needed) and the latest available values of the reduced pressure, *P*, the discretized equations for all unknown values of w_i and v_i are completed and solved (sequentially), and the calculated values of these velocity components at outflow boundaries are corrected (again, sequentially) to ensure overall mass conservation. Following that, the rates of advection transport of the corresponding components of momentum across the domain boundary into the control volume associated with the inflow boundary-node *i*, $\Re^{w}_{advec,i,in,calc}$ and $\Re^{v}_{advec,i,in,calc}$, are computed using suitable adaptations of Eq. (5.34). Then the rates of diffusion (viscous) transport of the corresponding components of momentum across the domain boundary into the control volume associated with the inflow boundary-node *i*, $\Re^{w}_{D,i,in,calc}$ and $\Re^{v}_{D,i,in,calc}$, are computed using the stored coefficients as follows:

$$\begin{aligned}\Re^{w}_{D,i,in,calc} &= \Re^{w}_{total,i,in,calc} - \Re^{w}_{advec,i,in,calc} \\ &= (a_i^{w})_{stored} w_i - \sum_{nb,i}(a^{w}_{nb,i})_{stored} w_{nb,i} - \{(b_i^{w})_{stored} - \left(\overline{\partial P/\partial z}\right)_{V_i} V_i\}\end{aligned} \tag{5.36}$$

$$\begin{aligned}\Re^{v}_{D,i,in,calc} &= \Re^{v}_{total,i,in,calc} - \Re^{v}_{advec,i,in,calc} \\ &= (a_i^{v})_{stored} v_i - \sum_{nb,i}(a^{v}_{nb,i})_{stored} v_{nb,i} - \{(b_i^{v})_{stored} - \left(\overline{\partial P/\partial r}\right)_{V_i} V_i\}\end{aligned} \tag{5.37}$$

The values of $\Re^{w}_{D,i,in,calc}$ and $\Re^{v}_{D,i,in,calc}$ yielded by Eqs. (5.36) and (5.37) are used in the computations of the values of $\hat{w}_i$ and $\hat{v}_i$ at a node *i* on such inflow boundaries, along with the computations of d_i^w and d_i^v, using the following equations:

$$\hat{w}_i = \frac{\sum_{nb,i} (a_{nb,i}^w)_{stored} \, w_{nb,i} + (b_i^w)_{stored} + \Re_{D,i,in,calc}^w}{(a_i^u)_{stored}}$$

$$\hat{v}_i = \frac{\sum_{nb,i} (a_{nb,i}^v)_{stored} \, v_{nb,i} + (b_i^v)_{stored} + \Re_{D,i,in,calc}^v}{(a_i^v)_{stored}} \qquad (5.38)$$

$$d_i^w = \frac{V_i}{(a_i^w)_{stored}} \;\; ; \;\; d_i^v = \frac{V_i}{(a_i^v)_{stored}}$$

Again, in some of the earlier publications on CVFEMs, the following procedure is prescribed at such boundaries: $\hat{w}_i = w_{specified}$, $\hat{v}_i = v_{specified}$, $d_i^w = 0$, and $d_i^v = 0$. However, here too, assigning the values of zero to d_i^w and d_i^v diminishes the strength of the coefficients in the discretized pressure equations associated with the nodes on and immediately adjacent to such boundaries, leading to relatively slow convergence (or even divergence) of the overall iterative solution procedure. In contrast, the above-mentioned revised treatment ensures that the strengths of the coefficients in the discretized pressure equations for this node and its neighbors are maintained.

Outflow

On outflow boundaries, following well-established practice [Patankar (1980)], the normal component of the diffusion flux of Φ out of the calculation domain, $J_{D,n,out}^{\Phi}$, is assumed to be negligibly small with respect to the corresponding advection flux, $J_{advec,n,out}^{\Phi}$. Thus, at a node *i* on an outflow boundary, it is assumed that $\Re_{D,i,out}^{\Phi} = 0$. With respect to the notation given in Fig. 5.2 (b), the mass flow rate out of the control volume across the boundary under consideration, $\Re_{mass,i,out}$, is calculated using linear interpolation of the latest available values of *w*, *v*, and fluid density (ρ) at the node *i* and the adjacent boundary nodes on the associated left and right element edges. Then, the rate of advection transport of Φ out of a given control volume across the boundary under consideration, $\Re_{advec,i,out}^{\Phi}$, is calculated by assuming that the specified value of Φ_i prevails over the portions l_1 and l_2 of the boundary edges of the associated elements, an example of which is shown in Fig. 5.2 (b):

$$\Re^{\Phi}_{advec,i,out} = \Re_{mass,i,out} \Phi_i \tag{5.39}$$

The above-mentioned procedure for calculating $\Re^{\Phi}_{advec,i,out}$ at a node i lying on an outflow boundary ensures that it does not contribute negatively to the coefficients in the associated discretized equation. This procedure is also second-order accurate when the nodes are uniformly distributed on the outflow boundaries under consideration. Again, if a non-uniform grid is required to ensure cost-effective computations, the distribution of nodes along the outflow boundaries can be done using a geometric expansion (or contraction) scheme for the distances between the nodes, with a geometric factor relatively close to one, to ensure that the aforementioned procedure for calculating $\Re^{\Phi}_{advec,i,out}$ is almost second-order accurate. More elaborate schemes that ensure second- or higher-order accuracy in the computation of $\Re^{\Phi}_{advec,i,out}$ even with non-uniform grids are not implemented here for reasons akin to those stated earlier, in the paragraph immediately after Eq. (5.34).

With $\Re^{\Phi}_{D,i,out} = 0$, $\Re^{\Phi}_{advec,i,out}$ is calculated using the procedure described above, and assuming that the continuity equation is satisfied for the control volume associated with the node i lying on an outflow boundary, the coefficients and constant in the discretized equation for Φ at this boundary node are obtained as follows:

$$\begin{aligned} &a^{\Phi}_{nb,\,i} = (a^{\Phi}_{nb,\,i})_{element\ contributions} \quad ; \; b^{\Phi}_i = (b^{\Phi}_i)_{element\ contributions} \\ &a^{\Phi}_i = \sum_{nb,i} a^{\Phi}_{nb,i} - \sum_{elements\ assc\ with\ i} (E^{S_\Phi}_i V_{iaoc})_{element} \end{aligned} \tag{5.40}$$

With respect to each of the velocity components w and v at outflow boundary nodes, the diffusion (viscous) fluxes (or shear stresses) that transport the corresponding components of momentum out of the domain are assumed to be negligible compared to the respective advection fluxes, and the coefficients and constant in the respective discretized equations are computed using suitable adaptations of Eq. (5.40), and then stored (for later calculations of $\hat{w}_i$ and d^w_i, or $\hat{v}_i$ and d^v_i, at the node i on outflow boundaries). Following that, using other boundary treatments (as needed) and the latest available nodal values of the reduced pressure, P, the discretized equations for all unknown nodal values of *w* (or *v*) are completed and solved (note that *w* and *v* are solved not simultaneously, but sequentially). Then the calculated values $w_{i,calc,ouflow}$ (or $v_{i,calc,outflow}$) at all nodes *i* on outflow boundaries are corrected to ensure overall mass conservation over the calculation domain. To make these corrections, first, with respect to the notation shown in Fig. 5.2 (b), the rates of mass flow into and out of the domain, $\Re_{mass,i,in}$ and $\Re_{mass,i,calc,out}$, lying on inflow and outflow boundaries, respectively, are calculated using piecewise-linear interpolation of $w_{i,specified,inflow}$, $v_{i,specified,inflow}$, $w_{i,calc,ouflow}$ (or $v_{i,calc,outflow}$) and the latest available values of $v_{i,outflow}$ (or $w_{i,outflow}$) and ρ_i at the boundary-node *i* and the adjacent boundary nodes on the associated left- and right-element edges. After that, the corresponding total rates of mass flow into and out of the calculation domain, $\Re_{mass,total,in}$ and $\Re_{mass,total,calc,out}$, respectively, are calculated as follows:

$$\begin{aligned} \Re_{mass,total,in} &= \sum_{inflow\,boundary\,nodes} \Re_{mass,i,in} \\ \Re_{mass,total,calc,out} &= \sum_{outflow\,boundary\,nodes} \Re_{mass,i,calc,out} \end{aligned} \tag{5.41}$$

Finally, the values of $w_{i,calc,ouflow}$ (or $v_{i,calc,outflow}$) at all nodes on outflow boundaries are corrected using the following equations:

$$\begin{aligned} Fac_{corr} &= \frac{\Re_{mass,total,in}}{\Re_{mass,total,calc,out}} \\ u_{i,ouflow} &= Fac_{corr}\, u_{i,calc,outflow} \text{ (or } v_{i,ouflow} = Fac_{corr}\, v_{i,calc,outflow}) \end{aligned} \tag{5.42}$$

It should be noted that when the overall solution is fully converged (to within the specified tolerances), the correction factor, Fac_{corr}, would be essentially equal to unity.

After the calculation of all unknown nodal values of *w* (or *v*) and the correction of the calculated values of this velocity component at nodes on outflow boundaries (using the above-mentioned procedure), the nodal values of $\hat{w}_i$ and d_i^w (or $\hat{v}_i$ and d_i^v) are computed using the expressions given in the following equations:

$$\hat{w}_i = \frac{\sum_{nb,i} a^w_{nb,i} w_{nb,i} + b^w_i}{a^w_i} \ \text{(or } \hat{v}_i = \frac{\sum_{nb,i} a^v_{nb,i} v_{nb,i} + b^v_i}{a^v_i}\text{)}$$
$$d^w_i = \frac{V_i}{a^w_i} \ \text{(or } d^v_i = \frac{V_i}{a^v_i}\text{)} \qquad (5.43)$$

5.1.11 Fixing of Pressure at a Chosen Node

In incompressible fluid flow and heat transfer problems, the density of the fluid is not dependent on the pressure. Furthermore, the dynamic viscosity, thermal conductivity, and specific heat at constant pressure of the fluid are usually only very weakly dependent on pressure, so they can be assumed to be essentially independent with respect to it. Thus, as discussed by Patankar (1980), only differences between the nodal values of pressure (or reduced pressure in this formulation), rather than the absolute values of pressure at the nodes, influence the fluid flow. Therefore, for the incompressible fluid flow problems of interest, the value of the reduced pressure was specified (fixed) at only one suitable node in the calculation domain, and this value was assigned the convenient value of zero. This treatment was implemented by overwriting the coefficients in the discretized equation for pressure at the chosen node *i* as follows:

$$a^P_i = 1 \ ; \ a^P_{nb,\,i} = 0 \ ; \ b^\Phi_i = P_{specified} = 0 \qquad (5.44)$$

5.1.12 Solution of the Discretized Equations

For the solution of the nonlinear, coupled sets of discretized equations for *w*, *v*, *P*, and any other dependent variable of interest, Φ, an adaptation of the sequential iterative variable adjustment (SIVA) procedure proposed by Saabas and Baliga (1994) is recommended. The steps in this procedure are summarized below.

1. Provide specified or guess values of the velocity components, reduced pressure, and all other dependent variables of interest: w = w^*, v = v^*, P = P^*, and Φ = Φ^*. Set $d^w = 0$, $d^v = 0$, $\hat{w} = w^*$, $\hat{v} = v^*$, $w^m = w^*$, and $v^m = v^*$ at all nodes.

2. If needed, update the nodal values of the effective thermophysical properties using the latest values of the dependent variables.

3. Compute coefficients in the discretized z-momentum equations; do not add reduced-pressure-gradient contributions, and do not under-relax these equations at this stage; and store the center-point coefficients (a_i^w) and the constant terms (b_i^w).

4. Add the reduced-pressure-gradient contributions to the discretized z-momentum equations; implement the boundary treatments; under-relax; and solve these discretized equations. Correct the calculated values of w at all nodes on outflow boundaries, if applicable, to ensure overall mass conservation. Update the boundary conditions associated with w, if needed.

5. Calculate $\hat{w}$ and d^w at all nodes in the calculation domain, using the non-under-relaxed center-point coefficients and the constant terms stored in Step 3, and the related equations and procedures described in Subsections 5.1.8 and 5.1.10.

6. Compute coefficients in the discretized r-momentum equations; do not add reduced-pressure-gradient contributions, and do not under-relax these equations at this stage; and store the center-point coefficients (a_i^v) and the constant terms (b_i^v).

7. Add the reduced-pressure-gradient contributions to the discretized r-momentum equations; implement the boundary treatments; under-relax; and solve these discretized equations. Correct the calculated values of v at all nodes on outflow boundaries, if applicable, to ensure overall mass conservation. Update the boundary conditions associated with v, if needed.

8. Calculate $\hat{v}$ and d^v at all nodes in the calculation domain, using the non-under-relaxed center-point coefficients and the constant terms stored in Step 6, and the related equations and procedures described in Subsections 5.1.8 and 5.1.10.

9. Calculate coefficients in the discretized equations for reduced-pressure; do not under-relax; tie the value of reduced pressure at a suitably chosen node to a specified value, using Eq. (5.44); and solve these discretized equations to obtain the newly calculated pressure field, P_{nc}.

10. Use the newly calculated reduced-pressure field, P_{nc}, and the latest available values of $\hat{w}$, d^w, $\hat{v}$, and d^v for calculating the mass-conserving velocity components, w^m and v^m, using Eq. (5.16).

11. Update the reduced-pressure field as follows: $P = \alpha_P P_{nc} + (1-\alpha_P) P^*$, where P^* is the previously available reduced-pressure field (either guessed or computed in the previous iteration of this procedure), and α_P is the under-relaxation factor for the reduced-pressure.

12. Calculate coefficients, suitably under-relax, and sequentially solve the discretized equations for all other dependent variables (Φ). Update the boundary conditions associated with each dependent variable Φ, if needed.

13. Check if user-specified convergence criteria are satisfied. If they are, store the nodal values of w, v, P, Φ, $\hat{w}$, $\hat{v}$, d^w, d^v, w^m, and v^m; compute and store all other desired results; and stop computation. If convergence criteria are not yet satisfied, go to the next step.

14. With the latest available nodal values of w, v, P, Φ, $\hat{w}$, $\hat{v}$, d^w, d^v, w^m, and v^m as the new guess values, return to Step 2, and repeat Steps 2 to 13.

The following implicit scheme proposed by Patankar (1980) is recommended for under-relaxing the discretized equations for all dependent variables, except reduced pressure (for which the discretized equations are not under-relaxed):

$$\left(\frac{a_i^{\Phi}}{\alpha_{\Phi}}\right)\Phi_i = \sum_{nb} a_{nb}^{\Phi}\Phi_{nb} + b_i^{\Phi} + \left(\frac{1-\alpha_{\Phi}}{\alpha_{\Phi}}\right)a_i^{\Phi}\Phi_i^{*} \tag{5.45}$$

In this equation, α_{Φ} is the under-relaxation factor for Φ and Φ_i^{*} is its latest available value. For the problems considered in this work (namely, numerical prediction of the fluid flow and heat transfer phenomena in the vertical heating and cooling sections), the values of α_w and α_v were set equal to 0.5. The value of the under-relaxation factor, α_P, which is employed for updating the reduced pressure field using the procedure summarized in Step 11 of the SIVA procedure, ranged between 0.5 and 0.75. When solving for the temperature field, the prescribed value of α_T ranged between 0.5 and 0.75. Essentially identical values of α_{Φ} were used in the solution of the two test problems presented later in this Chapter.

The following convergence criteria were used in the CVFEM simulations of the fluid flow and heat transfer in the vertical heating and cooling sections: for all dependent variables, the maximum value of the absolute residues of the discretized equations, normalized with respect to an appropriate reference transport rate, was less than 10^{-8}; and the values of other user-defined criteria, such as the values of absolute relative differences between mass flow rates over the inflow and outflow boundaries, and the normalized residue of an energy balance performed over the full boundary of the calculation domain, were all less than 10^{-6}. For the test problems presented in the next section, these criteria also included the absolute relative changes in selected overall results (such as a Nusselt number or a dimensionless flow development length) between successive iterations.

In the Steps 4, 7, 9, and 12 of the above-mentioned SIVA procedure, decoupled and linearized sets of discretized equations for the dependent variables, w, v, P_{nc}, and Φ are solved sequentially. As was mentioned earlier, the proposed CVFEM was formulated and implemented for use with both structured and unstructured grids; and in each of the aforementioned steps, iterative solution methods, such as the conjugate-gradient method and the bi-conjugate-gradient method (stabilized), were used to solve the set of decoupled and linearized discretized equations. The simulations were conducted on multi-core personal computers. To take advantage of the multi-core feature of these computers in lowering overall solution times, the aforementioned iterative solvers and several other routines of the CVFEM were specially coded to facilitate efficient parallel processing.

5.1.13 Evaluation of the Effective Thermophysical Properties of the MCPCM Slurries and the Thermal Boundary Condition in the Active Heating Section

As was mentioned in Chapter 2, the first part of the Boussinesq approximation was invoked, meaning that the effective slurry density was considered constant (= $\rho_{s,ref}$) in all terms of the governing equations, except the buoyancy terms. Hence, in the evaluation of the contributions of the advection terms of the governing equations to the discretized momentum and energy equations, a suitable reference value of the effective density of the MCPCM slurries (and also the distilled water, when it is the working fluid), $\rho_{s,ref}$, was required. The value of $\rho_{s,ref}$ was updated at the beginning of each loop-wide iteration of the procedure that was used to solve 1-D/2-D model of the thermosyphon (this iterative procedure is presented in Section 5.5). This reference value of the effective density was evaluated at a mean-temperature of the working fluid, approximated in this work as the arithmetic mean of the bulk temperatures at the exits of the left and right vertical legs of the closed-loop thermosyphon, $T_{b,out,heating}$ and $T_{b,out,cooling}$ (as can be seen in Figs. 2.1 and 4.1, these locations correspond to bulk-temperature measurement sections in the experimental set-up); thereby, consistency was ensured with the experimental procedure that was used to determine the mass flow rate and then the average velocity in the closed-loop thermosyphon (see Chapter 4, Section 4.9). The effective density of the working fluid, which appears in the buoyancy term of the z-momentum equation (see Eq. (2.14) in Chapter 2 and also the corresponding specialization of the general equation given in Table 5.1), was evaluated at every node in Step 2 of the overall iterative solution procedure of the proposed CVFEM (see Subsection 5.1.12).

The values of the local rate of strain, $\dot{\gamma}$, were first evaluated and stored in each element, using linear interpolation functions and Eq. (3.24). Then, volume-averaged values of $\dot{\gamma}$ were obtained for each control volume and stored at the associated node. These nodal values of $\dot{\gamma}$ were then employed (along with the nodal values of temperature and mass concentration of the slurry) to evaluate the nodal values of the effective dynamic viscosity of the slurry, μ_s. Similarly, the values of the slurry volume concentration (which is not constant), φ, were evaluated and stored at each node (using Eq. 3.7), and then used to evaluate the corresponding nodal values of the effective thermal conductivity of the slurry, k_s. These nodal values of μ_s and k_s were then invoked in the CVFEM, in accordance with the treatments presented in the preceding subsections.

With respect to the *z*- and *r*-momentum equations, the terms which account for the spatial variations of the effective dynamic viscosity of the working fluid (see the source terms given Table 5.1) were first evaluated and stored in each element, using linear interpolation functions, and then these values were volume-averaged over each control volume and stored at the associated node (these volume-averaged nodal values were used in the CVFEM). Lastly, with respect to the energy equation, the terms which account for the spatial variations of the effective specific heat of the slurry (see source terms given in Table 5.1) were evaluated as follows: first, the values of $F(T)$ (details of this function are provided in Appendix B) were evaluated at each node in the finite element mesh; then, the contribution of these source terms to the discretized energy equations were evaluated using the same algebraic approximations as those that were used for discretization of the advection transport terms in the energy equation, written in terms of the temperature, *T*, using the FLO scheme of Baliga and Patankar (1980). This treatment was preferred to discretization based on simple linear interpolation function within each element, to ensure consistency with the discretization of the advection terms in the energy equation (written in terms of *T*): since both the advection terms and the source terms, containing $F(T)$, in the energy equation written in terms of the temperature, *T*, originate from the advection of the effective specific enthalpy (see the corresponding descriptions Chapter 2, Subsection 2.4.2), the aforementioned consistent treatment was preferred, as it ensured conservation of energy over the control volumes and, collectively, over the complete calculation domain.

The thermal boundary condition in the active heat section, $l_{h,pre} < z < \left(l_{h,pre} + l_h\right)$ as shown schematically in Fig. 2.1, was discussed in Chapter 2 and is given in Eq. (2.28). Of the total electrical power input per unit length to this section ($q' = q_{heating,total} / l_h$), the portion that is transmitted to the working fluid ($q^{'}_{in} = q^{'} - q^{'}_{loss}$) is not known a priori, as the calculation of rate of heat loss from the outer surface of the tube (insulated with the *Armaflex* insulation) to the ambient air, $q^{'}_{loss} = U^{'}_{o}\left(T_{r=r_o} - T_{\infty}\right)$, requires a knowledge of the unknown temperature distribution along the outer surface of the tube wall, $T_{r=r_o}$. Thus, based on the specified values of $q' = q_{heating,total} / l_h$, T_{∞}, and $U^{'}_{o}$, this boundary condition was imposed by incorporating the following updating procedure in the overall 2-D CVFEM solution procedure (presented in Subsection 5.1.12): 1) start the overall solution procedure by setting $q^{'}_{loss} = 0$ and $q^{'}_{in} = q^{'}$, in Step 1 of the overall CVFEM solution procedure; 2) execute Steps 2-12 of the overall CVFEM solution procedure and obtain the temperature on the inner surface of the tube, $T_{r=r_i}$; 3) at the end of Step 12 of the overall CVFEM solution procedure, calculate the temperature of the outer surface of the tube using Eq. (2.33), and update the value of $q^{'}_{loss}$, using eq. (2.32); and 4) go to Step 13 of the overall CVFEM solution procedure, and then repeat this overall procedure until user-specified convergence criteria (discussed in Subsection 5.1.12) are satisfied.

5.2 Application of the Proposed CVFEM to Test Problems

The proposed CVFEM was validated by applying it to several test problems, two of which are presented and discussed in this section. The solutions are compared to corresponding numerical results available in the published literature. The two test problems are the following:

1. Test Problem 1: Steady, two-dimensional axisymmetric, laminar natural convection in a vertical cylindrical enclosure, with variable fluid viscosity.

2. Test Problem 2: Steady, developing, two-dimension axisymmetric, laminar, incompressible fluid flow in a straight pipe of circular cross-section.

5.2.1 Test Problem 1

Problem Statement

This test problem involves steady, two-dimensional axisymmetric, laminar natural convection in a vertical cylindrical enclosure, with variable dynamic viscosity of the fluid. A schematic illustration of this problem is depicted in Fig. 5.3. The top and bottom surfaces of the cylindrical enclosure are maintained at constant temperature T_C and T_H, respectively, with $T_H > T_C$. The curved vertical surface of the cylindrical enclosure is considered to be perfectly insulated (adiabatic).

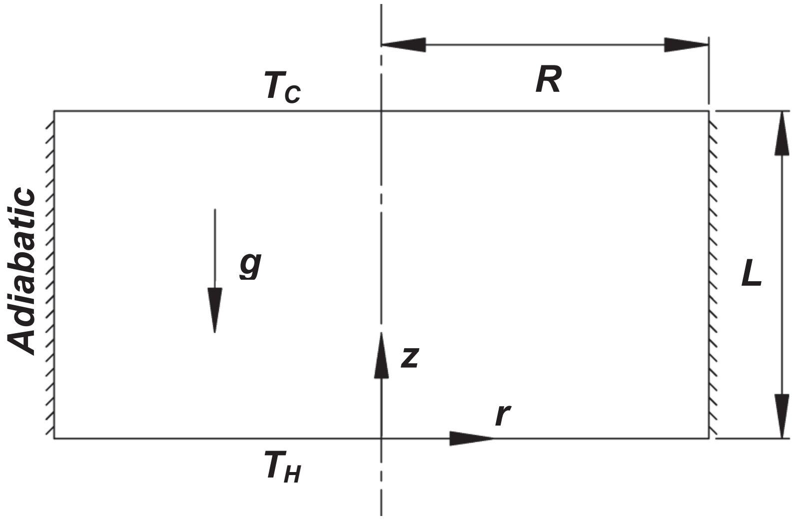

Figure 5.3: Schematic illustration of Test Problem 1.

In this problem, the first part of the Boussinesq approximation is invoked: thus, the density is considered constant (= ρ_0) in all terms of the governing equations, except the buoyancy term in the *z*-momentum equation, where it is prescribed as follows:

$$\rho = \rho_0 \left[1 - \beta \left(T - T_0 \right) \right] \tag{5.46}$$

In this equation, ρ is the density of the fluid, β is the thermal volumetric expansion coefficient, T is the temperature, and ρ_0 is the value of the fluid density at a specified reference temperature, T_0. The specific heat and the thermal conductivity of the fluid are considered to be constant. For purposes of comparison with the work of Liang et al. (1969), the dynamic viscosity of the fluid is prescribed using the following relation:

$$\mu = \mu_0 \left(1 + \eta \left(\frac{T - T_C}{T_H - T_C} \right) \right) \tag{5.47}$$

In this equation, μ denotes the dynamic viscosity, μ_0 is its reference value, and η is a specified parameter.

The specializations of the general governing equation for this test problem are given in Table 5.2.

Table 5.2: Specializations of the general governing equation for the simulations pertaining to Test Problem 1.

	Φ	Γ_Φ	S_Φ
Continuity equation	1	0	0
z-momentum equation	w	μ	$-\frac{\partial P}{\partial z} + \beta g \left(T - T_0 \right) + \frac{\partial \mu}{\partial z}\frac{\partial w}{\partial z} + \frac{\partial \mu}{\partial r}\frac{\partial v}{\partial z}$
r-momentum equation	v	μ	$-\frac{\partial P}{\partial r} - \frac{\mu v}{r^2} + \frac{\partial \mu}{\partial z}\frac{\partial w}{\partial r} + \frac{\partial \mu}{\partial r}\frac{\partial v}{\partial r}$
Energy equation	T	$\frac{k}{c_p}$	0

The boundary conditions for this problem are given below, with respect to the cylindrical coordinate system shown in Fig. 5.3.

At $z = 0$ and $0 \le r \le R$:

$$w = 0;\ v = 0;\ T = T_H \tag{5.48}$$

At $z = L$ and $0 \le r \le R$:

$$w = 0;\ v = 0;\ T = T_C \tag{5.49}$$

At $r = 0$ and $0 \le z \le L$:

$$\partial w / \partial r = 0;\ v = 0;\ \partial T / \partial r = 0 \tag{5.50}$$

At $r = R$ and $0 \le z \le L$:

$$w = 0;\ v = 0;\ \partial T / \partial r = 0 \tag{5.51}$$

The dimensionless parameters associated with this problem are the cavity radius-to-height ratio (*R/L*), the Prandtl number (*Pr*), and the Grashof number (*Gr*). The last two parameters are defined as follows:

$$Pr = \frac{\mu_0 c_p}{k} \qquad Gr = \frac{\beta g \left(T_H - T_C\right) L^3}{\left(\mu_0 / \rho_0\right)^2} \qquad \text{Eq. (5.52)}$$

For comparison purposes with the work of Liang et al. (1969), results were obtained for *R/L* = 1, *Gr* = 2, *Pr* = 2500 and η = -0.2.

Grids and Procedure for Obtaining Extrapolated Grid-Independent Results

A grid with an orthogonal line-by-line arrangement of the nodes was used for the solution of this test problem. The node distribution was uniform and the inter-node spacing in the z-direction was identical to that in the r-direction.

A pattern-preserving grid-refinement procedure was used to obtain extrapolated grid-independent results. In this procedure, each triangular element was divided into smaller elements of the same shape, using uniformly-spaced straight lines parallel to each of the three sides and a grid-refinement factor, defined as the ratio of the length of an element edge in the grid under consideration to the length of the corresponding element in the aforementioned coarsest grid (thus the grid-refinement factor for the coarsest grid is equal to one). The results were obtained with four different grids, having grid-refinement factors of 1 (21x21 nodes, the baseline grid), 1/2 (41x41 nodes), 1/4 (81x81 nodes), and

1/8 (161x161 nodes). Essentially grid-independent results, in this case an average Nusselt number, were obtained using the results yielded by the four aforementioned grids in conjunction with an extension of the extrapolation technique proposed by Richardson (1910). Results yielded by the grids with grid-refinement factors of 1/2 and 1/4, and 1/4 and 1/8, were extrapolated using this procedure (assuming second-order accuracy of the proposed CVFEM) to obtain values representative of infinitely-fine grids. The absolute relative difference between these two extrapolated results was less than 0.0014%: in this sense, the extrapolated value obtained using the results yielded by the two finest grids, the ones with grid-refinement factors of 1/4 and 1/8, was considered to be essentially grid-independent and is reported here as such.

Results

As was stated earlier, to allow a comparison with the results of Liang et al. (1969), the simulations were performed for the following values of the aforementioned parameters: $Gr = 2$, $Pr = 2500$ and $\eta = -0.2$. For these parameter values, two steady-state solutions exist: one with upflow along the axis of the cylindrical enclosure and another one with downflow. The desired flow direction was attained by appropriately defining the initial (guess) temperature field in the center of the enclosure. The average Nusselt number is defined as follows for this problem:

$$Nu_{av} = \frac{h_{av} L}{k} = \frac{\left(q_{total} / A_{surface}\right)}{\left(T_H - T_C\right)} \frac{L}{k} \tag{5.53}$$

In this equation, q_{total} is the total rate of heat transfer from the bottom (hot) surface to the top (cold) surface; $A_{surface}$ denotes the area of the top and bottom faces ($A_{surface} = \pi R^2$); and k is the thermal conductivity of the fluid.

The values of the average Nusselt number yielded by the four above-mentioned grids are listed in Table 5.3 along with the extrapolated grid-independent value (extrapolated using results yielded by the two finest grids) and the results of Liang et al. (1969). The grid-independent (extrapolated) results obtained by Scott (2006), using a co-located, two-dimensional axisymmetric, finite volume method (FVM), akin to the two-dimensional planar Cartesian FVM described in Baliga and Atabaki (2006), and a similar grid-refinement procedure are also included in this table for comparison purposes.

Table 5.3: Values of the average Nusselt number for Test Problem 1.

Grid	$Nu_{av}\left(Upflow\right)$	$Nu_{av}\left(Downflow\right)$
21x21	1.77085	1.76864
41x41	1.78395	1.78195
81x81	1.78744	1.78552
161x161	1.78833	1.78643
Extrapolated	1.78863	1.78673
Scott (2006)	1.78864	1.78678
Liang et al. (1969)	1.767	1.761

The largest absolute discrepancy between the extrapolated grid-independent results obtained with the proposed CVFEM and the results of Liang et al. (1969) is 1.4%. This agreement is good, considering that Liang et al. (1969) used a non-conservative finite difference method and a relatively coarse grid consisting of 19x19 nodes in the radial and axial directions. The largest absolute discrepancy between extrapolated grid-independent results and the results of Scott (2006) is 0.0028%, which is excellent. The value of the average Nusselt number for the upflow case is slightly higher than that associated with the downflow case, by 0.11%. Similar results were obtained by Liang et al. (1969) who noticed a 0.34% difference between the values of the Nusselt number for these two cases. Lastly, the results obtained with the coarsest grid (21x21 nodes) differ by less than 1.0% from the corresponding grid-independent values. Thus, for this problem, the proposed CVFEM produced accurate results even with relatively coarse grids.

5.2.2 Test Problem 2

Problem Statement

This test problem involves steady, developing, two-dimensional axisymmetric, laminar, incompressible fluid flow in a straight pipe of circular cross-section. In this problem, the thermophysical properties of the working fluid are considered to be constant.

The inside radius of the pipe is denoted as $R = D/2$, where D represents the inside diameter. The total length of the pipe is denoted as L. The specializations of the general governing equation for this test problem are given in Table 5.4.

Table 5.4: Specialization of the general governing equation for the simulations pertaining to Test Problem 2.

	Φ	Γ_Φ	S_Φ
Continuity equation	1	0	0
z-momentum equation	w	μ	$-\frac{\partial P}{\partial z}$
r-momentum equation	v	μ	$-\frac{\partial P}{\partial r}-\frac{\mu v}{r^2}$

The boundary conditions for this test problem are given below, with respect to a cylindrical coordinate system with the origin anchored to the center of the inlet plane of the pipe, and with the z coordinate axis aligned with the longitudinal axis of the pipe and pointing in the direction of the main flow.

At $z = 0$ and $0 \le r \le R$:

$$w = w_{avg} = \dot{m} / \left(\rho\left(\pi D^2 / 4\right)\right);\ v = 0 \tag{5.54}$$

At $z = L$ and $0 \le r \le R$ (outflow-boundary treatment)

$$\partial w / \partial z = 0;\ \partial v / \partial z = 0 \tag{5.55}$$

At $r = 0$ and $0 \le z \le L$:

$$\partial w / \partial r = 0;\ v = 0 \tag{5.56}$$

At $r = R$ and $0 \le z \le L$:

$$w = 0;\ v = 0 \tag{5.57}$$

In this problem, the velocity at the inlet plane of the pipe is uniform (and equal to w_{avg}), and the flow is allowed to develop over the length of the calculation domain.

The dimensionless parameter associated with this problem is the Reynolds number which is defined below, along with the dimensionless coordinates and velocities:

$$\begin{aligned} &Re_D = \frac{\rho w_{avg} D}{\mu}; \quad z^* = z / D; \quad r^* = r / D \\ &w^* = w / w_{avg} \qquad v^* = v / w_{avg} \end{aligned} \tag{5.58}$$

In order to allow a comparison with the work of Friedmann et al. (1968) and Masson (1993), results were obtained for Re_D = 40. These results consist of maximum and centerline dimensionless velocities at five axial locations and the dimensionless flow development length.

Grids and Procedure for Obtaining Extrapolated Grid-Independent Results

Spatially uniform grids with orthogonal line-by-line arrangement of the nodes were used in the solution of this test problem. The total length of the calculation domain was chosen such that it was equal to 2.5 times the hydrodynamic development length predicted by the Langhaar expression $(z_{fully-developed} / D) = 0.06 Re_D$ [White (1998)], to ensure that fully-developed conditions prevail at the exit of the calculation domain.

The pattern-preserving grid-refinement procedure and extrapolation technique for obtaining grid-independent solutions in Test Problem 1 were also used in this test problem. Four grids having grid-refinement factors of 1 (241x41 nodes, the baseline grid), 1/2 (481x81 nodes), 1/3 (721x121 nodes), and 1/4 (961x161 nodes) were used in this investigation. Grid-independent results for a dimensionless hydrodynamic development length and dimensionless maximum and centerline velocities at five different axial positions in the pipe were obtained using the results yielded by the aforementioned four grids and extrapolation technique. Results yielded by the grids with grid-refinement factors of 1/2 and 1/3, and 1/3 and 1/4, were extrapolated to values representative of infinitely fine grids. The absolute relative differences between the two set of extrapolated results were all less than 0.13%: thus the extrapolated values obtained with the results yielded by the grids with grid-refinement factors of 1/3 and 1/4 were considered to be essentially grid-independent and are reported here as such.

Results

The following results are presented: in Table 5.5, values of the maximum dimensionless axial velocity over the pipe cross-section, $w^*_{\max} = w_{max} / w_{avg}$, at five different values of the dimensionless axial coordinate $z^+ = z / \left(D \cdot Re_D \right)$; in Table 5.6, values of the dimensionless centerline velocity, $w^*_{centerline} = w_{centerline} / w_{avg}$, at five different values of the dimensionless axial coordinate $z^+ = z / \left(D \cdot Re_D \right)$; and in Table 5.7, values of the dimensionless hydrodynamic development length, defined as $z^+_{fully-developed} = z^+ \Big|_{w^*_{centerline} = 0.99\, w^*_{max\ fully-developed}}$, with $z^+ = z / \left(D \cdot Re_D \right)$. The results yielded by the four above-mentioned grids are listed in these tables, along with their grid-independent values (obtained by extrapolating the results yielded by the two finest grids) and the results of Friedmann et al. (1968). The results obtained by Masson (1993) with a two-dimensional axisymmetric CVFEM and non-uniform grids of 111x61 nodes are also included in these tables.

Table 5.5: Maximum dimensionless axial velocities $w^*_{\max}$ at five different z^+ values.

Grid	z^+				
	0.003125	0.0625	0.009375	0.0125	0.015625
241x41	1.20787	1.31046	1.40420	1.49665	1.58700
481x81	1.21459	1.31322	1.40520	1.49609	1.58515
721x121	1.21664	1.31371	1.40514	1.49565	1.58443
961x161	1.21754	1.31387	1.40503	1.49538	1.58405
Extrapolated	1.21871	1.31406	1.40489	1.49505	1.58358
Friedmann et al. (1968)	1.2189	1.3138	1.4046	1.4947	1.5833
Masson (1993)	1.219	1.313	1.404	1.495	1.583

Table 5.6: Dimensionless centerline axial velocities $w^*_{\text{centerline}}$ at five different z^+ values.

Grid	z^+				
	0.003125	0.0625	0.009375	0.0125	0.015625
241x41	1.07250	1.19354	1.34047	1.47583	1.58619
481x81	1.06015	1.18306	1.33266	1.47048	1.58265
721x121	1.05610	1.17967	1.33015	1.46875	1.58148
961x161	1.05409	1.17801	1.32893	1.46791	1.58092
Extrapolated	1.05151	1.17587	1.32737	1.46684	1.58020
Friedmann et al. (1968)	1.0484	1.1738	1.3263	1.4664	1.5799
Masson (1993)	1.048	1.173	1.325	1.465	1.579

Table 5.7: Dimensionless hydrodynamic development length obtained for $\text{Re}_D = 40$.

Grid	$z^+_{fully-developed} = z^+\big\|_{w^*_{centerline}=0.99\,w^*_{max\ fully-developed}}$
241x41	0.060502
481x81	0.060719
721x121	0.060773
961x161	0.060795
Extrapolated	0.060825
Friedmann et al. (1968)	0.061
Masson (1993)	0.0615

The agreement between the grid-independent values of $w^*_{\max}$ and $w^*_{centerline}$ and those obtained by Friedmann et al. (1968) and Masson (1993) is excellent: the largest absolute difference between the extrapolated values of these results and the corresponding values reported by Friedmann et al. (1968) is 0.3%, for all z^+ locations; and the maximum absolute difference between the extrapolated values of these results and the corresponding values reported by Masson (1993) is also 0.3%, for all z^+ locations. The agreement between the extrapolated value of $z^+_{fully-developed}$ and those reported by Friedmann at al. (1968) and Masson (1993) is very good: the absolute relative differences between the extrapolated value of $z^{+}_{fully-developed}$ and those reported by Friedmann et al. (1968) and Masson (1993) are 0.29% and 1.1%, respectively.

5.2.3 Summary Remarks

The results obtained for the two test problems presented in the previous two subsections and their successful comparisons with corresponding numerical results in the published literature demonstrate the validity of the proposed CVFEM. The improved treatments of the discretized pressure equation and the boundary conditions incorporated in this CVFEM were also successfully validated by solving planar two-dimensional test problems, in a Cartesian coordinate system: the results of these test problems are available in Lamoureux and Baliga (2011). Lastly, the proposed CVFEM was also validated, along with the proposed 1-D/2-D model of the closed-loop thermosyphon, by performing simulations with distilled water as the working fluid and comparing the results with the corresponding baseline results obtained in the experimental portion of this work: these results and comparisons are presented and discussed in Chapter 6.

5.3 Overview of the Segmented Quasi-One-Dimensional Model

As was mentioned in Chapter 2, in the portions of the closed-loop thermosyphon that join the vertical heating and cooling sections, segmented quasi-one-dimensional (1-D) models of the fluid flow and heat transfer phenomena were used, as the local effects of buoyancy are essentially negligible on the shape of the velocity profile of the working fluid, so it is essentially fully-developed in these portions of the thermosyphon. The top (upper) 1-D portion starts at the exit plane of the post-heating length, includes the top 180º bend, and ends at the entry plane of the pre-cooling length (see Figs. 2.1 and 2.3). The bottom (lower) 1-D portion starts at the exit plane of the post-cooling length, includes the bottom 180º bend, and ends at the entry plane of the pre-heating length (see Figs. 2.1 and 2.2). Even though the outer surfaces of these 1-D portions were well insulated, they experienced some heat interactions with the ambient environment. So the temperature of the working fluid in these portions changed (albeit slightly). Thus, to enhance the accuracy of the numerical simulations, a segmented approach was adopted in the proposed 1-D models of the fluid flow and heat transfer in these portions of the closed-loop thermosyphon. In this approach, the aforementioned 1-D portions of the thermosyphon were discretized into segments of length Δs. Balances of mass, momentum, and energy were then imposed on each of these segments to derive equations that govern the bulk temperatures at the inlet and exit plane of the segment, and the corresponding value of the shear stress and Fanning friction factor on the inner surface of the pipe wall. A schematic illustration of a segment of the upper 180º bend was given in Figure 2.4, along with the related notation used in the formulation of the 1-D models, and it is repeated below in Fig. 5.4, for convenience.

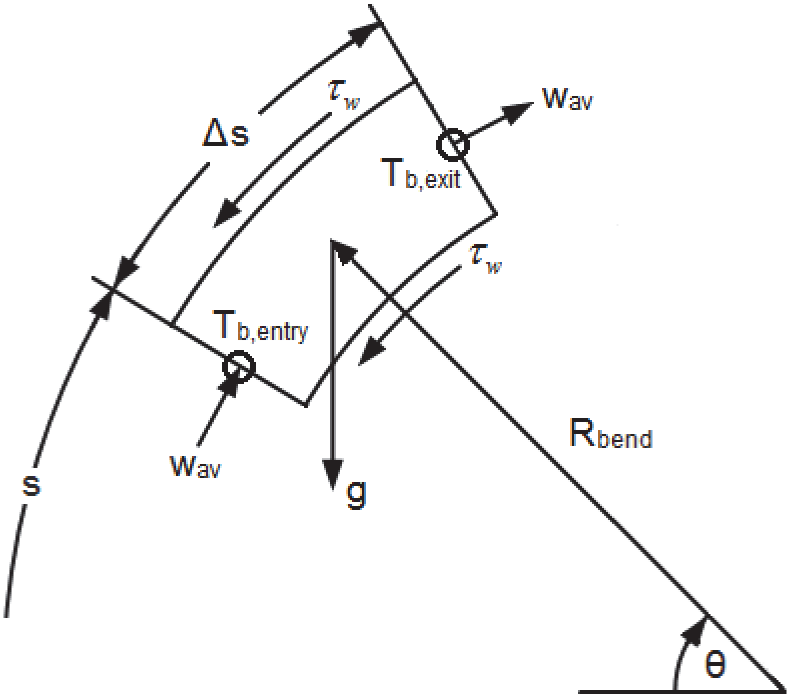

Figure 5.4: Segment of the upper 180º bend of the closed-loop thermosyphon and related notation used in the formulation of the proposed 1-D models.

The velocity profiles in the 1-D segments, such as the one shown in Fig. 5.4, are essentially fully-developed. In each segment, the quasi-one-dimensional (1-D) model equations were solved to obtain the bulk temperatures at the entrance and exit planes, and also the shear stress and Fanning friction factor at the inner surface of the pipe wall, using the procedures that were described in detail in Chapter 2, Section 2.5, and stored. Once the bulk temperatures in all segments of the 1-D portions of the closed-loop thermosyphon were calculated, the values of the effective density of the working fluid were evaluated at the nodes located at the entrance and exit planes of each of the segments (see Fig. 5.4), and stored. The stored values of Fanning friction factor and effective density in each of the segments in the 1-D portions of the closed-loop thermosyphon were used in the numerical evaluation of the overall momentum balance, which was then employed to calculate the average velocity, w_{av}, of the working fluid in the loop (as described in the next section).

5.4 Numerical Evaluation of the Overall Momentum Balance

As was stated in Chapter 2, an overall momentum balance was performed at the conclusion of a loop-wide iteration of the solution procedure of the 1-D/2-D thermosyphon model to determine a reference average velocity of the working fluid, w_{av}. The final form of the equation for this average velocity, Eq. (2.46), is repeated below for convenience:

$$w_{av} = \sqrt{\frac{-\dfrac{r_i}{\rho_{s,ref}} g \oint \rho_s \cos\theta ds}{\oint f_{Fanning} ds}} \tag{5.59}$$

In this equation for w_{av}, the values of the inner pipe radius, r_i, and the magnitude of the gravitational acceleration vector, g, are known (specified), and the latest available value of the reference effective density of the working fluid, $\rho_{s,ref}$, is used. As was stated earlier, the value of $\rho_{s,ref}$ was evaluated at the arithmetic mean of the bulk temperatures at the exits of the left and right vertical legs of the closed-loop thermosyphon, $T_{b,out,heating}$ and $T_{b,out,cooling}$ (as can be seen in Figs. 2.1 and 4.1, these locations correspond to bulk-temperature measurement sections in the experimental set-up). With these values of r_i, g, and $\rho_{s,ref}$, and using the latest available values of the effective density of the work fluid, ρ_s, and the Fanning friction factor, $f_{Fanning}$, stored after solving the aforementioned segmented 1-D model equations and the two-dimensional axisymmetric models of the fluid flow and heat transfer in the vertical heating and cooling sections, the contour integrations on the right-hand side of Eq. (5.59) are evaluated numerically using the following equations:

$$\begin{aligned}\oint \rho_s \cos\theta ds = & \underbrace{\frac{\sum_{i=1}^{N_{HS}} \rho_{s,i} \cos\theta_i V_i}{\pi r_i^2}}_{Vertical\,Heating\,Section} + \underbrace{\sum_{i=2}^{N_{1-D,top}} \frac{\left(\rho_{s,i}\cos\theta_i + \rho_{s,i-1}\cos\theta_{i-1}\right)}{2} \Delta s_{1-D,top}}_{Top\,1-D\,Portion\,of\,the\,Loop} \\ & + \underbrace{\frac{\sum_{i=1}^{N_{CS}} \rho_{s,i} \cos\theta_i V_i}{\pi r_i^2}}_{Vertical\,Cooling\,Section} + \underbrace{\sum_{i=2}^{N_{1-D,bottom}} \frac{\left(\rho_{s,i}\cos\theta_i + \rho_{s,i-1}\cos\theta_{i-1}\right)}{2} \Delta s_{1-D,bottom}}_{Bottom\,1-D\,Portion\,of\,the\,Loop}\end{aligned} \tag{5.60}$$

$$\begin{aligned}\oint f_{Fanning} ds = & \underbrace{\sum_{i=1}^{N_{Wall,HS}} f_{Fanning,i} l_i}_{Vertical\,Heating\,Section} + \underbrace{\sum_{i=2}^{N_{1-D,top}} \frac{\left(f_{Fanning,i} + f_{Fanning,i-1}\right)}{2} \Delta s_{1-D,top}}_{Top\,1-D\,Portion\,of\,the\,Loop} \\ & + \underbrace{\sum_{i=1}^{N_{Wall,CS}} f_{Fanning,i} l_i}_{Vertical\,Cooling\,Section} + \underbrace{\sum_{i=2}^{N_{1-D,bottom}} \frac{\left(f_{Fanning,i} + f_{Fanning,i-1}\right)}{2} \Delta s_{1-D,bottom}}_{Bottom\,1-D\,Portion\,of\,the\,Loop}\end{aligned} \tag{5.61}$$

In Eq. (5.60), N_{HS} and N_{CS} denote the total number of nodes (and control volumes) in the CVFEM meshes that are used to solve the detailed two-dimensional axisymmetric (2-D) models of the fluid flow and heat transfer in the vertical heating and cooling sections, respectively; V_i denotes the volume of the control volume associated with node *i* in the CVFEM mesh; and the values of $\cos\theta_i$ are evaluated only once (as the thermosyphon geometry and the grids remain unchanged in any particular simulation) and stored for later use. In both Eqs. (5.60) and (5.61), $N_{1-D,top}$ and $N_{1-D,bottom}$ represent the total number of nodes (the region between any two adjoining nodes are the segments) in the top and bottom 1-D portions of the closed-loop thermosyphon, respectively; and $\Delta s_{1-D,top}$ and $\Delta s_{1-D,bottom}$ represent the lengths of the segments into which the top and bottom 1-D portions of the closed-loop thermosyphon are divided, respectively. In Eq. (5.61), $N_{Wall,HS}$ and $N_{Wall,CS}$ are the total number of boundary nodes (in the CVFEM meshes) located along the inner surfaces of the pipe wall in the vertical heating and cooling section, respectively; and l_i represents the axial length of the boundary surface of the control volume associated with a boundary node *i* (in the CVFEM meshes). In this context, it should be noted that the area of the boundary face of the control volume associated a boundary node *i* located along the inner surface of the pipe wall in the vertical heating and cooling sections is equal to $2\pi r_i l_i$. It should also be noted that the values of $f_{Fanning,i}$ in the vertical heating and cooling sections of the closed-loop thermosyphons were evaluated using the calculated values of the wall-shear stress (the related procedures are presented in Subsection 5.1.10). Lastly, in both Eqs. (5.60) and (5.61), the trapezoidal rule was used for approximating the integrations over the segments of the 1-D portions of the closed-loop thermosyphon; however, in the vertical heating and cooling sections, piecewise-constant integration is used for consistency reasons, as the values of wall-shear stress yielded by the CVFEM are already averaged over the boundary faces of the control volumes.

5.5 Solution of the 1-D/2-D Thermosyphon Model

An iterative procedure was used to solve the 1-D/2-D model to the closed-loop thermosyphon. This procedure is presented in this section. To set the stage for this presentation, first, a few operational aspects of the thermosyphon (which were discussed in Chapters 2 and 3) and also a relation that was used to provide a starting value of the average velocity of the working fluid in the thermosyphon are briefly reviewed. Following this brief review, the aforementioned iterative procedure for solving the 1-D/2-D model is summarized in a concise point-wise manner.

Following the discussion presented in Chapters 2 and 3, the acronym PMNSCNH is used to denote a partial-melting-no-supercooling-no-hysteresis process, in which the heating is halted when the PCM in all MCPCM particles is in a partially melted state, so the maximum temperature of the slurry does not exceed $T_{max\ PMNSCNH}$ (= 28^{o}C); and then the cooling process is initiated. In a PMNSCNH process, the freezing of the PCM is achieved with no supercooling and there is no hysteresis, so the variations of the effective thermophysical properties of the MCPCM slurries with temperature during the heating process also apply during the subsequent cooling process. The acronym

FMSCWFH is used to indicate a full-melting-supercooling-with-freezing-and-hysteresis process, in which the heating is continued until the PCM in all MCPCM particles is in the fully melted (liquid) state, so the minimum temperature in the slurry exceeds $T_{melting\ completed}$ (= 32.5^{o}C); and then the cooling process is initiated and carried out until all of the PCM is fully frozen, so the maximum temperature of the slurry first dips below $T_{freezing\ SC\ onset}$ (= 18.05^{o}C) and then achieves values under $T_{freezing\ SC\ end}$ (= 15 ^{o}C). As was discussed in Chapter 2, in an FMSCWFH process, because of supercooling that is needed to freeze the PCM and the related hysteresis, it is necessary to use different sets of effective-property correlations for the heating and cooling processes.

As was discussed in Chapter 3, if the increase in the slurry temperature during the heating process is halted between 28.0°C and 32.5°C, and then the cooling process is started, part of the liquid PCM solidifies in the melting-temperature range, but to achieve full solidification, the temperature of the remaining (supercooled) liquid PCM must be lowered to a value equal to or below 15.0°C. For this special case, the effective properties of the MCPCM particles become additionally dependent on the maximum temperature reached during the melting process. This special case was not investigated in the main experiments involving the closed-loop thermosyphon operated with the MCPCM slurries, nor was it investigated in the corresponding numerical simulations undertaken in this work.

Another heating and cooling process of interest involves the following sub-processes: an initial heating process to temperatures beyond $T_{melting\ completed}$ (= 32.5°C), so that full melting of the PCM is achieved; and then a cyclical cooling and heating process that does not involve any temperature below $T_{freezing\ SC\ onset}$ (= 18.06°C), so the PCM remains in a liquid phase throughout. This process, which is referred to as full-melting-no-supercooled-freezing-no-hysteresis (FMNSCFNH), was not used in the main closed-loop thermosyphon experiments, as it does not involve any latent-heat effects during the cyclical heating and cooling process (started after the initial heating process). However, as was discussed in Chapter 3 (Section 3.6), this process was used in a series of special closed-loop thermosyphon experiments and numerical simulations which were undertaken as part of a hybrid technique for determining the rheological properties of the

MCPCM slurries. Additional details of the aforementioned special closed-loop thermosyphon experiments are provided in Appendix C.

In the iterative method for solving the proposed 1-D/2-D model of the closed-loop thermosyphon, it is necessary to specify an initial (or guess) value of the average velocity of the working fluid, w_{av}. In general, this initial value of w_{av} was specified by adapting an analytical solution derived by Bernier and Baliga (1992b) for closed-loop thermosyphons operating with single-phase Newtonian fluids. It is obtained by solving a basic 1-D model in the whole loop, including the heating and cooling sections, thus ignoring the local effects of buoyancy forces on the distributions of the velocity of the working fluid in these sections. This adapted analytical solution is the following:

$$w_{av}^{*} = \left(\frac{q_{heating,total} \, g \, \overline{\beta} \Delta z}{8\pi \overline{c}_{p,s} \overline{\mu}_{s,gen} L_{total,loop}} \right)^{1/2} \tag{5.62}$$

In this equation, w_{av}^{*} is the initial (guess) value of w_{av}; $\overline{\beta}$ is the mean value of the thermal volumetric expansion coefficient evaluated over the expected operational temperature range; $\overline{c}_{p,s}$ denotes an average value of the effective specific heat of the slurry (including the latent heat effects) over the expected operational temperature range; the total length of the closed-loop circuit is denoted as $L_{total,loop}$; and $\overline{\mu}_{s,gen}$ represents the effective dynamic viscosity of the working fluid, evaluated at the mean value of the expected operational temperature range. It should be noted that the initial value of w_{av} does not have an impact on the final (converged) results. However, a proper prescribed value of w_{av}^{*} reduces the number of loop-wide iterations and the total computational effort needed to reach convergence. It should also be noted that in numerical simulations of any particular experimental run of the closed-loop thermosyphon, w_{av}^{*} was set equal to the experimentally determined value of w_{av}.

The iterative solution procedure that was used for solving the proposed 1-D/2-D model of the closed-loop thermosyphon is an extended version of a procedure put forward by Bernier and Baliga (1992b). The steps in this procedure are summarized below.

1. Provide following input parameters: the total heating power input, $q_{heating,total}$; the mass concentration of the slurry, ϕ (if the working fluid is distilled water, ϕ = 0); the cooling water temperature, T_{cool}; and the temperature of the ambient air, T_{∞}.

2. As initial (guess) values, set all temperatures equal to T_{∞} (at the nodes of the CVFEM meshes used in vertical heating and cooling section; at the nodes of the segments of the portions of the thermosyphon in which the 1-D model is used). Set the bulk temperatures at inlet and exit sections of the vertical legs of the thermosyphon, $T_{b,in,heating}$, $T_{b,in,cooling}$, $T_{b,out,heating}$, and $T_{b,out,cooling}$ equal to T_{∞}. Also provide an initial (guess) value of w_{av}, using the above-mentioned Eq. (5.62), in general. In simulations of any particular experimental run, set the initial values of w_{av}, $T_{b,in,heating}$, $T_{b,in,cooling}$, $T_{b,out,heating}$, and $T_{b,out,cooling}$ equal to the corresponding experimentally determined values.

3. Update the value of $\rho_{s,ref}$, the value of the effective density of the working fluid (MCPCM slurries or distilled water) at the arithmetic mean of the latest available values of $T_{b,out,heating}$ and $T_{b,out,cooling}$.

4. Perform the two-dimensional axisymmetric simulation of the fluid flow and heat transfer in the vertical heating section, using the mathematical model and boundary conditions presented in Chapter 2 and the CVFEM presented in Section 5.1. In this simulation, set the inlet temperature equal to a uniform value, $T_{b,in}$, the latest available value of the bulk temperature in the 1-D segment immediately below the vertical heating section. If the thermosyphon is operating with an MCPCM slurry at the working fluid then do the following: in the PMNSCNH or FMSCWFH process, or the first overall iteration of the FMNSCFNH process, calculate the effective thermophysical properties using the correlations pertaining to the heating (melting) process; and in the second or later overall iteration of the FMNSCFNH process,

calculate the effective thermophysical properties using the correlations pertaining to the cooling (freezing) process. If the working fluid is distilled water, then assign properties using the correlations given in Appendix A. When convergence is attained, compute and store the bulk temperature of the working fluid at the exit plane of the post-heating length. Also compute and store the contributions of the vertical heating section to the numerical approximations of the contour integrals in the overall momentum balance, as given in Eqs. 5.60 and 5.61. Check the temperatures in the exit plane of the active heating section, and note the following points if the working fluid is an MCPCM slurry: if the minimum temperature in the slurry exceeds $T_{melting\ completed}$ (= 32.5^{o}C), then the thermosyphon could be operating in the FMSCWFH or FMNSCFNH processes (this has to be determined after Step 6 described below); if the maximum temperature in the slurry is below $T_{max\ PMNSCNH}$ (= 28^{o}C), then the thermosyphon would be operating in the PMNSCNH process.

5. Perform the computations pertaining to the top (upper) 1-D portion of the closed-loop thermosyphon, using the segmented 1-D model and boundary conditions presented in Chapter 2 and the corresponding numerical treatment summarized in Section 5.3. In these calculations, set the inlet bulk temperature equal to the value of the bulk temperature calculated at the exit plane of the post-heating length of the vertical heating section. If the thermosyphon is operating with an MCPCM slurry in the FMSCWFH or FMNSCFNH process, the calculations must be done using correlations for the effective thermophysical properties pertaining to the cooling (freezing) process. If the thermosyphon is operating with an MCPCM slurry in the PMNSCNH process, the calculations must be done using correlations for the effective thermophysical properties pertaining to the heating (melting) process. If the thermosyphon is operating with distilled water, use the correlations given in Appendix A. Compute and store the contributions of this top 1-D portion of the thermosyphon to the numerical approximations of the contour integrals in the overall momentum balance, as given in Eqs. 5.60

and 5.61. Also store the value of the bulk temperature at the exit plane of this top 1-D portion of the thermosyphon.

6. Perform the two-dimensional axisymmetric simulation of the fluid flow and heat transfer in the vertical cooling section, using the mathematical model and boundary conditions presented in Chapter 2 and the CVFEM presented in Section 5.1. In this simulation, set the inlet temperature equal to a uniform value, $T_{b,in}$, the latest available value of the bulk temperature in the 1-D segment immediately above the vertical cooling section. If the thermosyphon is operating with an MCPCM slurry in the FMSCWFH or FMNSCFNH process, use correlations for the effective thermophysical properties pertaining to the cooling (freezing) process; if the thermosyphon is operating with an MCPCM slurry in the PMNSCNH process, use correlations for the effective thermophysical properties pertaining to the heating (melting) process; and if the thermosyphon is operating with distilled water, use the correlations given in Appendix A. When convergence is attained, compute and store the bulk temperature of the working fluid at the exit plane of the post-cooling length. Also compute and store the contributions of the vertical cooling section to the numerical approximations of the contour integrals in the overall momentum balance, as given in Eqs. 5.60 and 5.61. If the working fluid is an MCPCM slurry, check the temperatures in the exit plane of the active cooling section and make note of the following points: if the maximum temperature is below $T_{freezing\,SC\,end}$ (= 15 ^{o}C), then in conjunction with the points made at the end of Step 4 above, determine and note if the thermosyphon is operating in the PMNSCNH or FMSCWFH process; if the minimum temperature is above $T_{freezing\ SC\ onset}$ (= 18.06°C), then in conjunction with the points made at the end of Step 4 above, determine and note if the thermosyphon is operating in the PMNSCNH or FMNSCFNH process.

7. Perform the computations pertaining to the bottom (lower) 1-D portion of the closed-loop thermosyphon, using the segmented 1-D model and boundary

conditions presented in Chapter 2 and the corresponding numerical treatment summarized in Section 5.3. In these calculations, set the inlet temperature equal to the value of the bulk temperature calculated at the exit plane of the post-cooling length of the vertical cooling section. If the working fluid is an MCPCM slurry, then do the following: if the thermosyphon is operating in the PMNSCNH or FMSCWFH process, then calculate the effective thermophysical properties using the correlations pertaining to the heating (melting) process; and if the thermosyphon is operating in the FMNSCFNH process, then calculate the effective thermophysical properties using the correlations pertaining to the cooling (freezing) process. If the working fluid is distilled water, calculate the thermophysical properties using the correlations given in Appendix A. Compute and store the contributions of this bottom 1-D portion of the thermosyphon to the numerical approximations of the contour integrals in the overall momentum balance, as given in Eqs. 5.60 and 5.61. Also store the value of the temperature at the exit plane of this bottom 1-D portion of the thermosyphon.

8. Compute the numerical approximations to the contour integrals in the overall momentum balance, using eqs. (5.60) and (5.61), and then use Eq. (5.59) to compute the new value of the average velocity of the working fluid, $w_{av,new}$, and update the value of w_{av} as follows: $w_{av} = \alpha_{w_{av}} w_{av,new} + \left(1-\alpha_{w_{av}}\right) w_{av}^{*}$, where w_{av}^{*} is the previously available value of w_{av} and $\alpha_{w_{av}}$ is the associated under-relaxation factor ($\alpha_{w_{av}}$ = 0.5 was used in this work). Also update the values of $T_{b,in,heating}$, $T_{b,in,cooling}$, $T_{b,out,heating}$, and $T_{b,out,cooling}$.

9. Check if all user-specified convergence criteria are satisfied. If so, store the values of w_{av}, $T_{b,in,heating}$, $T_{b,in,cooling}$, $T_{b,out,heating}$, $T_{b,out,cooling}$, and other desired results; and stop the computations. If all convergence criteria are not yet satisfied, go to the next step.

10. With the latest available values of w_{av}, $T_{b,in,heating}$, $T_{b,in,cooling}$, $T_{b,out,heating}$, $T_{b,out,cooling}$, and other dependent-variable fields are the new guess values, return to Step 3, and repeat Steps 3 to 9.

The following criteria were used to assess convergence of the iterative solution procedure of the 1-D/2-D thermosyphon model: the absolute values of the relative changes of w_{av} and $T_{b,in,heating}$ (in K) between successive loop-wide iterations were less than 10^{-6}. Convergence of this iterative solution procedure was normally attained in less than 15 loop-wide iterations and required less than two hours of computing on personal computers equipped with Intel quad-core CPUs. In these computations, the convergence of the detailed simulations performed with the CVFEM in the vertical heating and cooling sections was enhanced by initiating the calculations, whenever possible, using a continuation technique. In this technique, the guess (initial) values of the dependent variables were set equal to the corresponding fully-converged values obtained in a previous simulation (with slightly different set of the input parameters, such as $q_{heating,total}$ and ϕ).

The results of the experimental investigations and the numerical solutions of the 1-D/2-D model are presented in the next chapter.

6. Results and Discussion

The results of the experimental investigations and the complementary numerical simulations of the closed-loop thermosyphon, operating with distilled water and MCPCM slurries as the working fluids, are presented and discussed in this chapter. Details of the calculation domain used in the computer simulations based on the proposed 1-D/2-D model, the computational grids used, and the results of grid-independence checks are presented first. Next, the results of complementary experimental and computational investigations of the closed-loop thermosyphon operated with distilled water as the working fluid are presented and discussed. Lastly, the results of complementary experimental and computational investigations of the closed-loop thermosyphon operated with MCPCM slurries as the working fluid are presented and discussed.

6.1 Details of the Calculation Domain, Computational Grids, and Grid-Independence Checks

The calculation domain and its dimensions are presented first in this section. Then, the details of the pattern of the computational grids are presented. After that, grid-independence checks and the selection of an appropriate grid for the final simulations are presented and discussed.

Calculation Domain: The complete fluid-flow passage inside the closed-loop thermosyphon is the full calculation domain. As was discussed in Chapter 4, and schematically illustrated in Fig. 4.1, this thermosyphon was made up of two vertical straight pipes connected together by two vertical 180-degree bends made of the same pipe, each of which consisted of two 90-degree circular bends of the same mean radius, R_{bend}, connected together (at one of their ends) by two opposite fittings of a T-junction. The majority of the fluid-flow circuit of the closed-loop thermosyphon was made of stainless steel tubes, with inner and outer diameters of 10.21 mm and 12.70 mm, respectively. The left and right vertical pipes (see Fig. 4.1) were each 2.198 m long. The active heating length on the left vertical pipe was L_h = 1.000 m, and the active cooling length on the right vertical pipe was L_c = 0.902 m. Each of the four 90-degree circular pipe bends had the same mean radius, R_{bend} = 0.229 m, and each of the top and bottom

180-degree bends was constructed by joining two of the aforementioned 90-degree bends with a 0.128 m long horizontal tube segment of a T-junction. The total length of the fluid-flow circuit, based on the centerline of the tubing, was 6.088 m. A minimum of 0.5 liters of working fluid was required for proper operation of the closed-loop thermosyphon. The center of the active heating portion of the left vertical leg (of the closed-loop thermosyphon) was positioned at a distance Δz = 0.500 m below the center of the active cooling portion of the right vertical leg (see Fig. 4.1).

The dimensions of the various sections of the left and right vertical legs of the closed-loop thermosyphon are given in the schematic illustration in Fig. 6.1. As was discussed in Chapter 2, pre- and post-heating lengths ($L_{h,pre}$ and $L_{h,post}$) were included in the portion of the calculation domain comprising the heating section. The pre-heating length was added to ensure that the local buoyancy effects, which occur mainly in the active heating section of length L_h, do not influence the shape of the fully-developed axial velocity profile in the inlet plane of the heating section. The post-heating length was added to allow the velocity profile of the fluid flow exiting the active heating section across its outlet plane to achieve the shape that characterizes fully-developed flow without local buoyancy effects: for distilled water, which is considered to be a Newtonian fluid, this is the Poiseuille parabola; for the MCPCM slurries, which are modeled as a homogeneous non-Newtonian fluid, the fully-developed profile is given in Eq. (2.29). In a similar vein, pre- and post-cooling lengths ($L_{c,pre}$ and $L_{c,post}$) were added to the portion of the calculation domain comprising the cooling section, in which the active cooling section has a length of L_c. The dimensions of the pre-, post- and active heating lengths were the following: $L_{h,pre}$ = 0.05105 m (5 times the inner pipe diameter), $L_{h,post}$ = 0.500 m, and L_h = 1.000 m, leading to a vertical heating section with a total length of 1.55105 m. The dimensions of the pre-, post- and active cooling lengths were the following: $L_{c,pre}$ = 0.05105 m (again, 5 times the inner pipe diameter), $L_{c,post}$ = 0.500 m, and L_c = 0.9018 m, giving a cooling section with a total length of 1.45285 m. Preliminary computations were done with several different values of these pre- and post- lengths, and the results were used to choose the aforementioned values, which ensured satisfaction of the above-mentioned objectives.

In Fig. 6.1, the portions of the closed-loop thermosyphon that were simulated using the axisymmetric, two-dimensional (2-D) model (described in Chapter 2) and the control-volume finite element method (CVFEM; described in Chapter 5), namely, the vertical heating and cooling sections, are indicated by thick dashed lines; and the top and bottom quasi-one-dimensional (1-D) portions are shown by thinner dashed lines. The locations of the two-dimensional axisymmetric portions, with respect to the sheathed thermocouple probes in the bulk-temperature measurement sections, are also given. Here, it should be noted that the calculation domain includes only the regions corresponding to $0 \le r \le r_i$, where r_i is the inner radius of the pipe ($r_i = D_i / 2 = 5.105$ mm).

Computational Grids: The CVFEM grids that were used to discretize the axisymmetric two-dimensional calculation domains inside the vertical heating and cooling sections had an orthogonal, line-by-line node arrangement. The node distribution was uniform in the *r*-direction and essentially (almost) uniform in the *z*-direction (details given later in this section). First, the uniform node spacing in the *r*-direction, Δr, was determined. Then, an initial (tentative) value of the axial node spacing in the *z*-direction, Δz, was set equal to $\Delta z_{initial} = 16 \cdot \Delta r$. Next, nodes were placed at the axial limits of the active heating and active cooling sections (at $z = l_{h,pre}$ and $z = l_{h,pre} + l_h$ for the heating section; and at $z = l_{c,pre}$ and $z = l_{c,pre} + l_c$ for the cooling section, with respect to the coordinate systems shown in Figs. 2.3 and 2.4), and the other nodes were evenly distributed in the axial direction between these limits, while modifying the value of Δz as little as possible from $\Delta z_{initial}$. Using this slightly modified value of Δz, nodes were first distributed uniformly in the axial direction in the pre- and post-heating and cooling lengths, and then, to obtain ensure calculation domains of the desired lengths (values given in Fig. 6.1), a slight correction was applied over all of these sections, using a geometrical expansion factor, to position the boundary nodes at exactly $z = 0$ and $z = l_{h,pre} + l_h + l_{h,post}$ or $z = l_{c,pre} + l_c + l_{c,post}$. The resulting grids had a uniform node distribution in the *r*-direction and an essentially (almost) uniform node distribution in the *z*-direction (the domain-wide maximum relative difference in the axial node spacing was less than 5%). As was mentioned in Chapter 5, the uniform length of the quasi-one-dimensional segments in the 1-D portions of the closed-loop, Δs, was made essentially (almost) equal to the axial spacing of the grid in heating section.

The 1-D/2-D mathematical model presented in Chapter 2 was used. The effective thermophysical properties of the slurries were prescribed using the correlations given in Chapter 3, and these properties of distilled water were prescribed using the correlations given in Appendix A. The values of the overall heat transfer coefficients, $U_b^{'}$ (= 0.1666 W/m°C), $U_i^{'}$ (=0.17001 W/m°C), and $U_o^{'}$ (=0.17008 W/m°C), needed in the 1-D/2-D model, were determined experimentally (see Chapter 4). The 1-D/2-D model with the aforementioned inputs was solved using the numerical methods and procedures presented and discussed in Chapter 5. The criteria specified in subsection 5.1.12 were used to assess convergence of the iterative solution procedure for the detailed simulations pertaining to the vertical heating and cooling sections. Additionally, convergence of the overall iterative procedure for solving the discretized equations of the proposed 1-D/2-D model was considered to be attained when the absolute values of the relative changes of w_{av} and $T_{b,in,heating}$ in successive iterations (of the overall solution procedure) were less than 10^{-6}, as was discussed in Section 5.5.

After numerous preliminary computations, a baseline grid was chosen for discretizing the calculation domain in the heating section: it had 31 nodes in the radial direction and 571 nodes in the axial direction (including nodes in the pre- and post-heating lengths). The baseline grid chosen for the discretizing the calculation domain in the cooling section was selected in a similar manner: it had 31 and 535 nodes in the radial and axial directions (including nodes in the pre- and post-cooling lengths), respectively. A pattern-preserving grid-refinement procedure was used in the grid-independence checks. As was mentioned in Chapter 5, in this procedure, each triangular element (in the cross-section of the calculation domain) was divided into smaller elements of the same shape, using uniformly-spaced straight lines parallel to each of the three sides and a grid-refinement factor, defined as the ratio of the length of an element edge in the grid under consideration to the length of the corresponding element in the aforementioned baseline grid (thus, the grid-refinement factor for the baseline grid is equal to one).

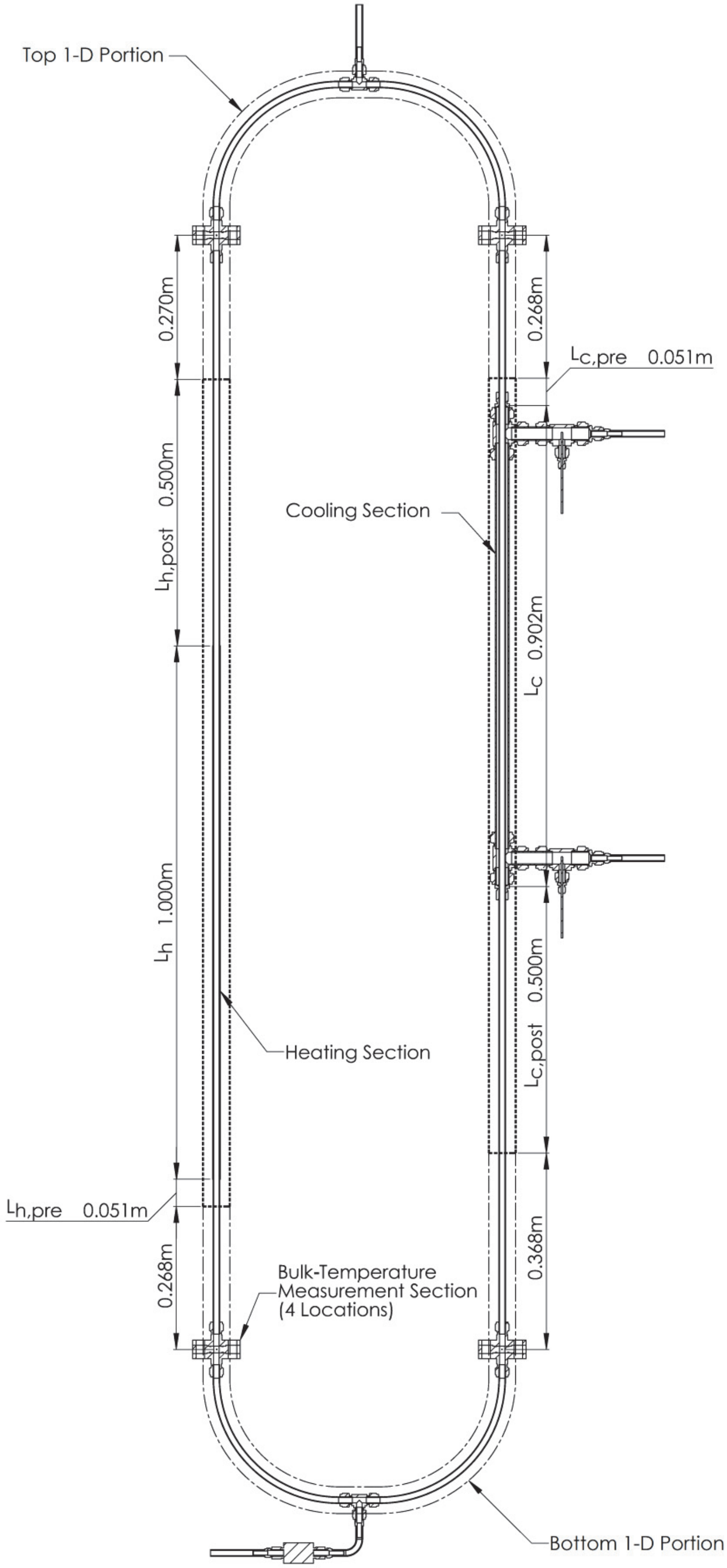

Figure 6.1: Lengths and positions of the calculation domains in the vertical heating and cooling sections of the closed-loop thermosyphon.

Grid-Independence Checks: In the grid-independence checks, three successive pattern-preserving grid refinements were applied to the aforementioned baseline grids in the heating and cooling sections, using grid-refinement factors of 1/2, 1/3 and 1/4. The length of the elements in the 1-D portions of the closed-loop, Δs, were refined in a manner consistent with that used for the grids in the vertical heating and cooling sections. The grid-independence checks were done using the results of numerical simulations of three different experimental runs, one with distilled water (Run 1-W) and two with MCPCM slurries (Runs 1-S and 17-S) as the working fluid. The input parameters for these three experimental runs are listed in Table 6.1. The two runs with the MCPCM slurries corresponded to the full-melting-supercooling-with-freezing-and-hysteresis process, discussed in Chapters 2 and 3, and denoted by the acronym FMSCWFH.

Table 6.1: Experimental runs and corresponding input parameters used in the grid independence studies.

Run	ϕ	$q_{heating,total}$ [W]	T_{cool} [°C]	T_{∞} [°C]
6-W	0% (Distilled water)	60.04	20.02	23.47
1-S	7.471%	54.96	12.99	21.53
17-S	17.50%	35.06	13.08	23.62

In Table 6.1, ϕ represents the mass concentration of MCPCM in the slurry, $q_{heating,total}$ denotes the total power input to the active heating section, T_{cool} is the cooling-water temperature in the active cooling section, and T_{∞} is the ambient air temperature. The focus in this section is on checks to ensure grid-independence of the numerical results. The comparisons of the numerical and experimental results for the three runs listed in Table 6.1, and also for other experimental runs, are presented in subsequent sections of this chapter. The three runs and sets of parameters listed in Table 6.1 were chosen for the grid-checks for the following reasons: of all runs with distilled water as the working fluid, Run 6-W had the highest value of $q_{heating,total}$, so the local buoyancy effects in the vertical heating and cooling sections were the highest, and the corresponding velocity and temperature gradients the steepest; and for the runs with the slurries as the working fluid, Run 1-S involves the highest value of $q_{heating,total}$ and the lowest (non-zero)

MCPCM mass concentration (7.471%), and Run 17-S corresponds to the highest value of $q_{heating,total}$ and the highest MCPCM mass concentration (17.496%).

Simulations were performed for the three runs listed in Table 6.1 using the baseline grids and three other grids, with grid-refinement factors of 1/2, 1/3 and 1/4. The average working-fluid velocity, w_{av}, and the value of bulk temperature at the bulk-temperature measurement section located at the exit of the vertical heating section, $T_{b,out,heating}$, were used to assess the grid independence of the numerical results, and are presented in Table 6.2. The results yielded by the grids with grid-refinement factors of 1/2 and 1/3, and 1/3 and 1/4, were extrapolated to obtain values representative of infinitely-fine grids, and these extrapolated values are reported in Table 6.2. The maximum absolute relative differences between these extrapolated results were 0.0115% for w_{av} and 0.0057% for $T_{b,out,heating}$: in this sense, the extrapolated values obtained using the results yielded by the two finest grids, were considered to be essentially grid-independent.

Table 6.2: Results of grid-independence checks.

Result	Grid-Refinement Factor	Run 6-W	Run 1-S	Run 17-S
w_{av} [m/s]	1 (Baseline Grid)	$1.33121\text{x}10^{-2}$	$6.43265\text{x}10^{-3}$	$3.66524\text{x}10^{-3}$
	1/2	$1.32933\text{x}10^{-2}$	$6.42692\text{x}10^{-3}$	$3.66307\text{x}10^{-3}$
	1/3	$1.32871\text{x}10^{-2}$	$6.42497\text{x}10^{-3}$	$3.66226\text{x}10^{-3}$
	1/4	$1.32843\text{x}10^{-2}$	$6.42401\text{x}10^{-3}$	$3.66187\text{x}10^{-3}$
	Extrapolated (1/2, 1/3)	$1.32822\text{x}10^{-2}$	$6.42341\text{x}10^{-3}$	$3.66161\text{x}10^{-3}$
	Extrapolated (1/3, 1/4)	$1.32806\text{x}10^{-2}$	$6.42277\text{x}10^{-3}$	$3.66137\text{x}10^{-3}$
$T_{b,out,heating}$ [°C]	1 (Baseline Grid)	34.5454	37.4277	38.7268
	1/2	34.5574	37.4454	38.7433
	1/3	34.5618	37.4519	38.7493
	1/4	34.5638	37.4550	38.7524
	Extrapolated (1/2, 1/3)	34.5653	37.4572	38.7541
	Extrapolated (1/3, 1/4)	34.5665	37.4589	38.7563

The results presented in Table 6.2 also showed that the absolute relative differences between the grid-independent values [Extrapolated (1/3, 1/4)] of w_{av} and $T_{b,out,heating}$, and those obtained using the baseline grids (grid-refinement factor of 1), were all less than 0.237% and 0.083%, respectively. Therefore, the above-mentioned baseline grids were considered adequate for all of the final simulations, for runs with both distilled water and the MCPCM slurries as the working fluid.

6.2 Experimental and Numerical Results for Runs with Distilled Water

The experiments performed with distilled water as the working fluid served as a benchmark for the main runs which were undertaken with the MCPCM slurries as the working fluid. The results of these experiments with distilled water as the working fluid also served as an additional check on the validity of the proposed 1-D/2-D model described in Chapter 2, and the numerical methods and procedures described in Chapter 5. These experimental results and the corresponding numerical predictions are presented, compared, and discussed in this section.

6.2.1 Overview of the Experimental and Numerical Runs

Six different experimental runs were conducted with distilled water as the working fluid, using the apparatus and procedures described in Chapter 4, and they were also simulated numerically. The nominal values of the input parameters for these experimental runs are listed in Table 6.3.

Table 6.3: Nominal values of input parameters for the experimental runs conducted with distilled water as the working fluid.

Input Parameters	Values
Total heating power input, $q_{heating,total}$ [W]	10, 20, 30, 40, 50, 60
Cooling water temperature, T_{cool} [°C]	20
Ambient air temperature, T_{∞} [°C]	23.29 to 24.21

6.2.2 Bulk Temperatures and Average Velocity

The specific values of the input parameters for the six experimental runs with distilled water as the working fluid are presented in Table 6.3, along with the corresponding experimental and numerical results for $T_{b,in,heating}$, $T_{b,out,heating}$, $T_{b,in,cooling}$, $T_{b,out,cooling}$, and w_{av}, and also the absolute differences between these results expressed as a percentage of the experimental values. These runs are labeled as N-W, where N denotes the run number and W indicates distilled water as the working fluid. Additional details of the experimental results for all of these runs are provided in Appendix E. The maximum uncertainties in the experimental results are $\pm 0.085\ ^{\mathrm{o}}\mathrm{C}$ for the bulk temperatures and $\pm 5.4\%$ for the average velocity, as was presented and discussed in Chapter 4. In this context, the maximum absolute differences between the experimental and numerical results, expressed as a percentage of the experimental values, namely, 1.39% (equal to $0.31\ ^{\mathrm{o}}\mathrm{C}$) for the bulk temperatures and 4.59% for the average velocity, as reported in Table 6.2, attest to the validity of the 1-D/2-D model described in Chapter 2, and also the numerical methods and procedures described in Chapter 5.

The variations of experimental and numerical results for the average working-fluid velocity, w_{av}, with total power input to the active heating section, $q_{heating,\,total}$, for Runs 1-W to 6-W, are graphically presented in Fig. 6.2. The estimated experimental uncertainties associated with w_{av} are also included this figure in the form of vertical bars, centered about the experimental results. The value of w_{av} increases with increasing value of $q_{heating,\,total}$: the higher power input to the active heating section generates higher increases in the bulk temperature, and, in turn, more pronounced density changes and higher net buoyancy forces over the closed-loop thermosyphon, and these effects lead to higher values of the average working-fluid velocity.

Table 6.4: Input parameters, experimental results, and numerical results for the runs with distilled water as the working fluid.

Run	Input Parameters		Results	$T_{b,in,heating}$ [°C]	$T_{b,out,heating}$ [°C]	$T_{b,in,cooling}$ [°C]	$T_{b,out,cooling}$ [°C]	w_{av} [m/s]
1-W	$q_{heating,total}$ [W]	10.04	Expt.	20.59	25.74	25.65	20.38	$5.67\text{x}10^{-3}$
	T_{cool} [^{o}C]	19.97	Num.	20.67	25.60	25.48	20.38	$5.93\text{x}10^{-3}$
	T_{∞} [^{o}C]	24.11	% Diff.	0.39	0.54	0.66	0	4.59
2-W	$q_{heating,total}$ [W]	20.03	Expt.	20.81	28.12	27.91	20.66	$7.73\text{x}10^{-3}$
	T_{cool} [^{o}C]	19.98	Num.	20.80	27.93	27.72	20.60	$7.95\text{x}10^{-3}$
	T_{∞} [^{o}C]	24.21	% Diff.	0.05	0.68	0.68	0.29	2.85
3-W	$q_{heating,total}$ [W]	29.95	Expt.	21.07	30.06	29.64	20.98	$9.22\text{x}10^{-3}$
	T_{cool} [^{o}C]	20.01	Num.	20.97	29.75	29.44	20.85	$9.46\text{x}10^{-3}$
	T_{∞} [^{o}C]	23.29	% Diff.	0.47	1.03	0.67	0.62	2.60
4-W	$q_{heating,total}$ [W]	40.09	Expt.	21.47	31.78	31.35	21.39	$1.08\text{x}10^{-2}$
	T_{cool} [^{o}C]	20.01	Num.	21.29	31.51	31.17	21.20	$1.09\text{x}10^{-2}$
	T_{∞} [^{o}C]	23.40	% Diff.	0.84	0.85	0.57	0.89	0.93
5-W	$q_{heating,total}$ [W]	49.90	Expt.	21.91	33.33	32.89	21.85	$1.21\text{x}10^{-2}$
	T_{cool} [^{o}C]	20.03	Num.	21.65	33.07	32.71	21.58	$1.21\text{x}10^{-2}$
	T_{∞} [^{o}C]	23.51	% Diff.	1.19	0.78	0.55	1.24	0
6-W	$q_{heating,total}$ [W]	60.04	Expt.	22.28	34.80	34.32	22.25	$1.33\text{x}10^{-2}$
	T_{cool} [^{o}C]	20.02	Num.	21.99	34.55	34.16	21.94	$1.33\text{x}10^{-2}$
	T_{∞} [^{o}C]	23.47	% Diff.	1.30	0.72	0.47	1.39	0

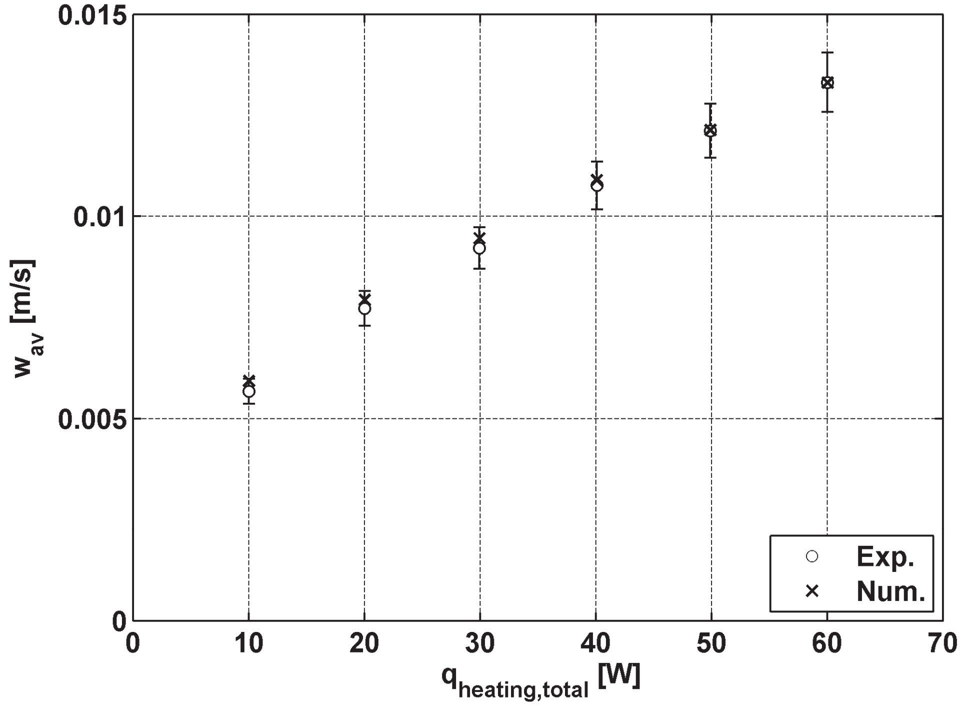

Figure 6.2: Experimental and numerical results for average velocity of the working fluid in the closed-loop thermosyphon for the runs performed with distilled water.

6.2.3 Numerical Predictions of Dimensionless Axial Velocity and Temperature Distributions in the Vertical Heating and Cooling Sections

The variations of the dimensionless axial velocity, w / w_{av}, and temperature, $(T - T_{b,in}) / (T_{b,out} - T_{b,in})$, with the dimensionless radial coordinate, r / r_i, at six different axial locations in the vertical heating and cooling sections are presented in Figs. 6.3 and 6.4, respectively, for Run 6-W. As was noted earlier, and also shown by the input parameters listed in Table 6.4, for the runs with distilled water as the working fluid, Run 6-W had the highest value of $q_{heating,total}$, so the local buoyancy effects in the vertical heating and cooling sections were expected to be the highest, and the corresponding velocity and temperature gradients the steepest. The results shown in Figs. 6.3 and 6.4 confirmed these expectations. These results for the other runs (1-W to 5-W) were qualitatively similar to those for Run 6-W, but the effects of buoyancy were less pronounced.

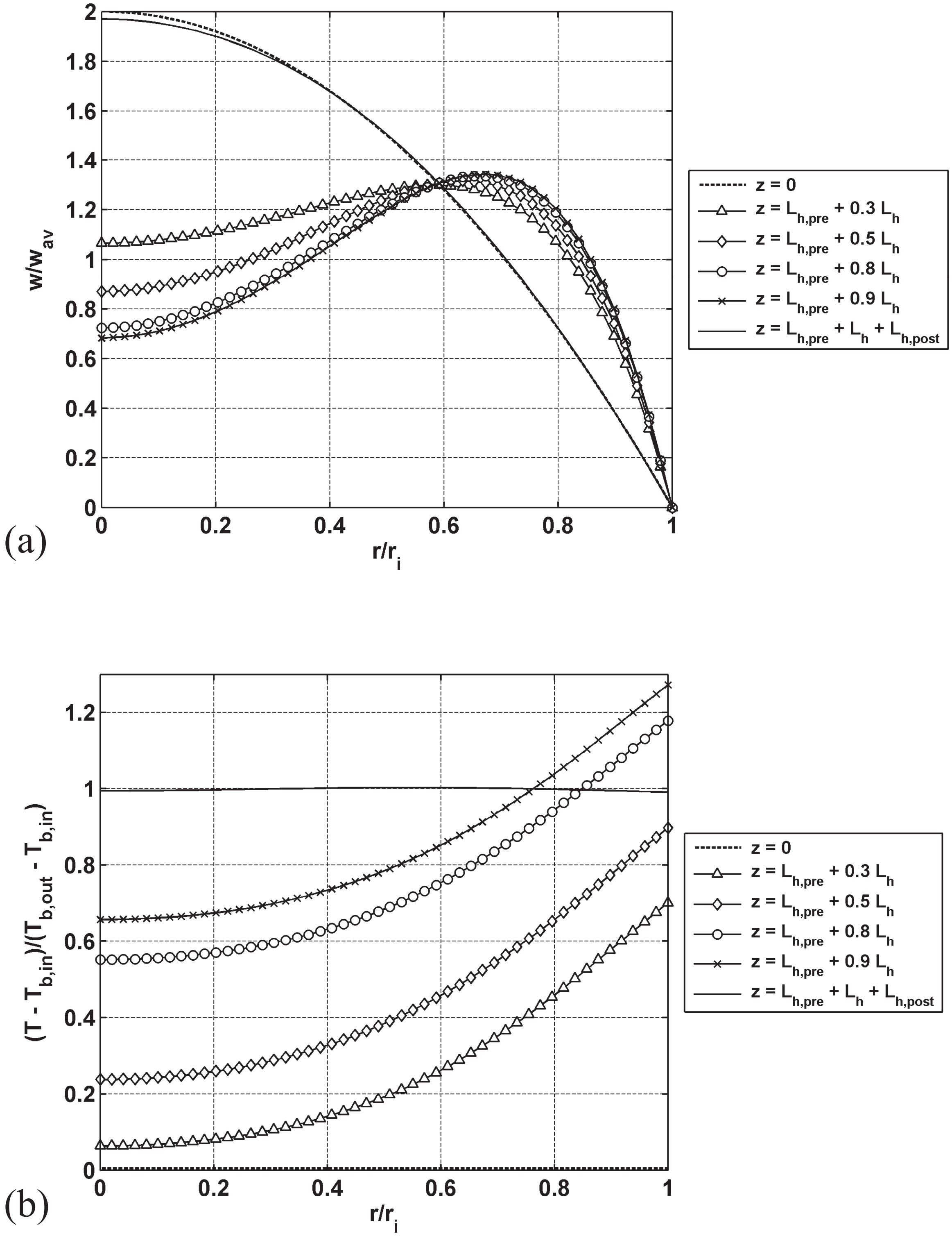

Figure 6.3: Numerical predictions of the distributions of dimensionless (a) axial velocity and (b) temperature in the vertical heating section of the closed-loop thermosyphon operating with distilled water as the working fluid, for Run 6-W.

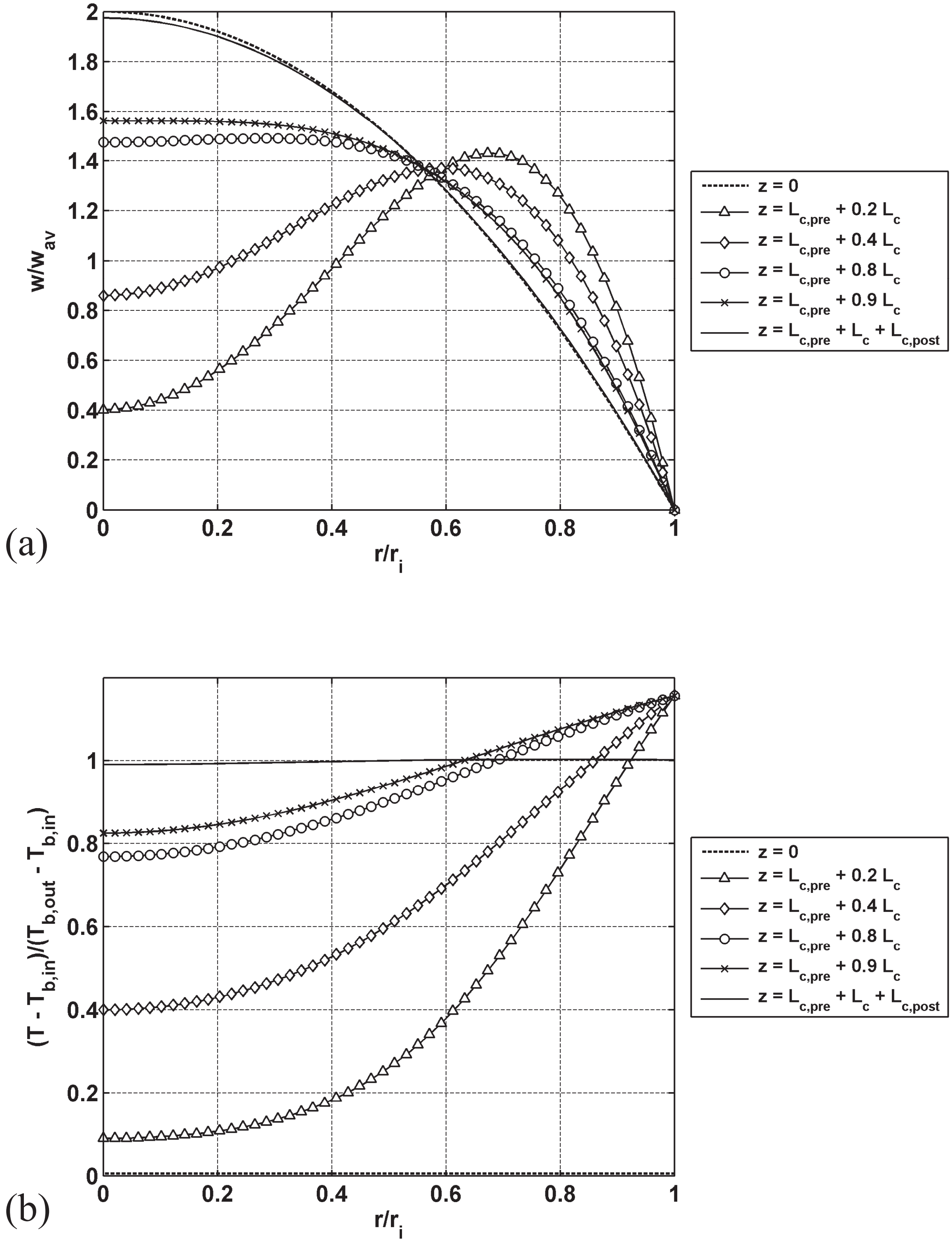

Figure 6.4: Numerical predictions of the distributions of dimensionless (a) axial velocity and (b) temperature in the vertical cooling section of the closed-loop thermosyphon operating with distilled water as the working fluid, for Run 6-W.

The results in Fig. 6.3(a) for the dimensionless axial velocity distribution in the heating section, in which the main flow and the buoyancy forces are both directed vertically upwards (aiding configuration), show the following features: 1) at the inlet to the heating section ($z = 0$; start of the pre-heating length), it is prescribed as the Poiseuille parabola (the pre-heating length was long enough to justify this prescription); 2) it gets increasingly influenced by local buoyancy effects as the fluid travels through the active heating section; 3) in the active heating section, for $z \geq L_{h,pre} + 0.8L_h$, it attains an essentially fully-developed shape (which is different from the Poiseuille parabola, because of the local buoyancy effects); and 4) at the outlet of the heating section ($z = L_{h,pre} + L_h + L_{h,post}$), it reverts back to a shape akin to the Poiseuille parabola, confirming that the post-heating length was long enough to provide this desired result. The results in Fig. 6.3(b) for the dimensionless temperature distribution in the heating section show the following features: 1) at the inlet to the heating section, it is uniform and essentially zero, as the inlet temperature was set equal to $T_{b,in}$ (again, the pre-heating length was long enough to justify this prescription); 2) it gets increasingly influenced by local buoyancy effects as the fluid travels through the active heating section; 3) in the active heating section, for $z \geq L_{h,pre} + 0.8L_h$, it attains an essentially fully-developed shape for the thermal boundary condition imposed in this section (same shape, but temperature at all *r* locations increases essentially linearly with *z*); and 4) at the outlet of the heating section ($z = L_{h,pre} + L_h + L_{h,post}$), it is essentially uniform again, but at a value of one (unity), indicating that $T = T_{b,out}$ for $0 \leq r \leq r_i$, and confirming that the post-heating length was long enough to provide this desired result.

The results in Fig. 6.4(a) for the dimensionless axial velocity distributions in the cooling section, in which the main flow and the buoyancy forces are both directed vertically downwards (aiding configuration), show features that are similar to those discussed above for the heating section. However, the dimensionless temperature distributions presented in Fig. 6.4(b), while indicating the influence of buoyancy (aiding configuration), are different from those in Fig. 6.3(b), because the thermal boundary condition in the active cooling section corresponds to essentially uniform wall temperature ($T_{r=r_i} = T_{cool}$), while it corresponds to essentially uniform heat flux in the active heating section.

6.2.4 Axial Distributions of the Temperature of the Outer Surface of the Tube Wall in the Active Heating Section

As was discussed in Chapter 4, the outer surface of the tube wall in the active heating section was instrumented with 40 calibrated thermocouples, evenly distributed over its length (L_h = 1m). The experimental and numerical results for the axial distributions of the temperature of the outer surface of the tube wall in the active heating section are plotted in Fig. 6.5 for all six runs of the closed-loop thermosyphon with distilled water as the working fluid (Runs 1-W to 6-W; for input parameters, see Table 6.2). *In Fig. 6.5, z = 0 m corresponds to the start of the active heating section.*

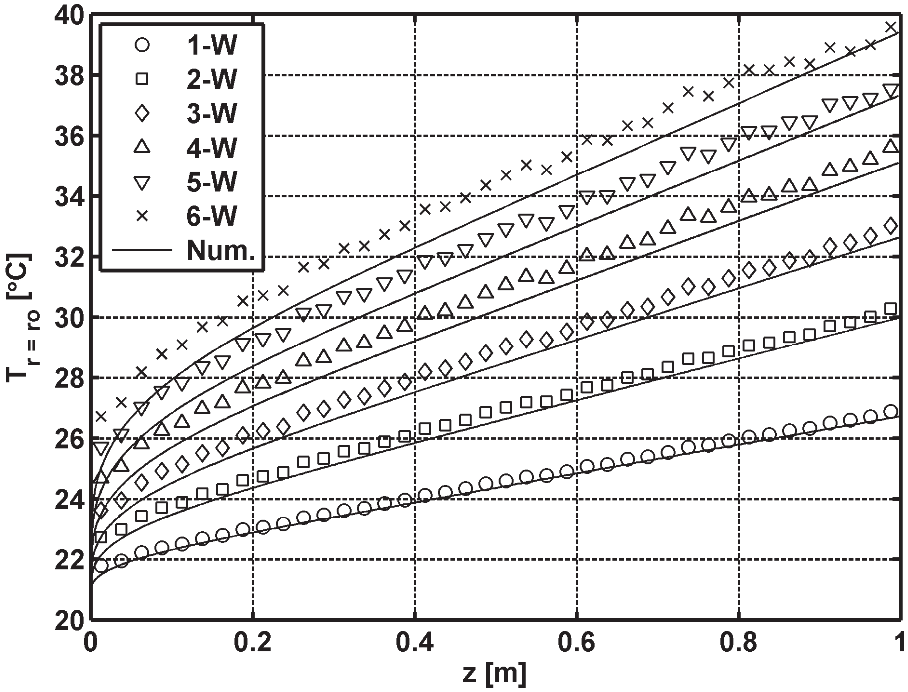

Figure 6.5: Experimental and numerical result for the axial distributions of the temperature of the outer surface of the tube wall in the active heating section of the closed-loop thermosyphon operated with distilled water as the working fluid.

The experimental uncertainty of the experimental results plotted in Fig. 6.5 is ±0.063°C (see Subsection 4.6.2 in Chapter 4). The error bands corresponding to this uncertainty would be slightly smaller than the size of the symbols used to indicate the experimental data points in Fig. 6.5, thus they are not included in this figure. The agreement between the experimental and numerical results shown in this figure is very good for Runs 1-W, 2-W and 3-W, which correspond to lower values of the total power input to the active heating section ($q_{heating,total}$), and also quite good for Runs 4-W, 5-W, and 6-W, which correspond to higher values of $q_{heating,total}$.

In Fig. 6.5, the results for Run 6-W (highest power input to the active heating section) shows the following features: (1) the plot of $T_{r=r_o}$ vs. z in the range $0 \le z \le 0.4\,\mathrm{m}$ indicates the developing region, it rises quite steeply at the start of this region in a nonlinear manner, and then approaches a linear distribution; and (2) the plot of $T_{r=r_o}$ vs. z plot in the range $z > 0.4\,\mathrm{m}$ is essentially linear, indicating a fully-developed region, which is also indicated by the results presented in Fig. 6.3. The results presented in Fig. 6.5 for the other runs (1-W to 5-W) are qualitatively similar to those for Run 6-W, but the length of the developing region is smaller for lower values of $q_{heating,total}$.

6.3 Experimental and Numerical Results for Runs with MCPCM Slurries

The experimental and numerical results for the runs performed with the MCPCM slurries as the working fluid in the closed-loop thermosyphon are presented, compared, and discussed first in this section. As will be seen, these results and comparisons establish the validity of the 1-D/2-D model described in Chapter 2, and also of the numerical methods and procedures described in Chapter 5. Following the presentation of these results and comparisons, the numerical results obtained for some of the runs by assuming Newtonian behavior of the MCPCM slurries (ignoring their actual non-Newtonian behavior) are compared to the corresponding experimental results: as will be seen in this context too, these simulations and comparisons underscore the importance of accurately modeling the actual non-Newtonian rheological behavior of the MCPCM slurries.

6.3.1 Overview of the Experiments and Numerical Runs

Eighteen different experimental runs were conducted with the MCPCM slurries as the working fluid, using the apparatus and procedures described in Chapter 4, and they were also simulated numerically. Two of the experimental runs, corresponding to the lowest and highest values of the mass concentration of the MCPCM and the corresponding highest values of the total power input to the active heating section were completely rerun (from scratch), to establish the repeatability of the experimental results. The nominal values of the input parameters for these experimental runs are listed in Table 6.5. The runs with nominal values of total heating power input ($q_{heating,total}$) in the range 26.5W to 55.0W corresponded to the full-melting-supercooling-with-freezing-and-hysteresis process, which was fully discussed in Chapters 2 and 3, and is denoted by the acronym FMSCWFH; and those with nominal values of $q_{heating,total}$ in the range 3.7W to 12.3W corresponded to the partial-melting-no-supercooling-no-hysteresis process, which, again, was fully discussed in Chapters 2 and 3, and is denoted by the acronym PMNSCNH. The nominal value of the cooling water temperature used in the active cooling section, T_{cool}, was maintained at 13°C in the FMSCWFH processes, and at 13°C and also 19.5°C in the PMNSCNH processes.

Table 6.5: Nominal values of input parameters for the experimental runs conducted with the MCPCM slurries as the working fluid.

Input Parameters	Values
MCPCM mass concentration ϕ	7.5%, 10%, 12.5%, 15%, 17.5%
Total heating power input, $q_{heating,total}$ [W]	26.5 to 55.0 (FMSCWFH process) 3.7 to 12.3 (PMNSCNH process)
Cooling water temperature, T_{cool} [°C]	13 (FMSCWFH and PMNSCNH processes) and 19.5 (PMNSCNH process)
Ambient air temperature, T_{∞} [°C]	21.08 to 24.87

6.3.2 Bulk Temperatures and Average Velocity

The specific values of the input parameters for the 18 experimental runs (plus two repeatability runs) with MCPCM slurries as the working fluid are presented in Tables 6.6 (for ϕ = 7.471%), 6.7 (for ϕ = 9.997%), 6.8 (for ϕ = 12.49%), 6.9 (for ϕ = 14.95%), and 6.10 (for ϕ = 17.5%), along with the corresponding experimental and numerical results for $T_{b,in,heating}$, $T_{b,out,heating}$, $T_{b,in,cooling}$, $T_{b,out,cooling}$, and w_{av}, and also the absolute differences between these results expressed as a percentage of the experimental values. These runs are labeled as N-S, where N denotes the run number and S indicates MCPCM slurries as the working fluid. Runs 1-Sr and 17-Sr denote reruns of Runs 1-S and 17-S, which were undertaken to establish repeatability of the experimental results. Again, these repeatability runs were done for the minimum and maximum values of the mass concentration of the MCPCM in the slurries, at the corresponding maximum values of the total power input in the active heating section ($q_{heating,total}$). Additional details of the experimental results for all of these runs are provided in Appendix E.

The maximum uncertainties in the experimental results are $\pm 0.085\ ^{o}\mathrm{C}$ for the bulk temperatures and $\pm 5.4\%$ for the average velocity (see Chapter 4). However, it should be noted that for Runs 12-S and 16-S, in which the mass concentration of the MCPCM was ϕ = 12.5% and 14.95%, respectively, and which were run in the partial-melting-no-supercooling-no-hysteresis (PMNSCNH) process, the total power input to the active heating section was quite low. Thus, for these runs (12-S and 16-S), and also for other runs with relatively low values of $q_{heating,total}$ (< 10W), the relative errors caused by the rates of heat losses or gain from the ambient air could become rather high, and, as a result, the uncertainties in the experimentally determined values of average velocity, w_{av}, are expected to be greater than $\pm 5.4\%$. Similarly, for the runs with the highest mass concentration of the MCPCM (Runs 17-S and 18-S; for which ϕ = 17.5%), the effective dynamic viscosity of the slurries is quite high: thus, the reliability and accuracy of the techniques that were used to determine the relative consistency index, m, and the flow behaviour index, n, in the relation for the effective dynamic viscosity, Eq. (3.15) in

Chapter 3, were compromised a bit at ϕ = 17.5%; and thus the accuracy of the related numerical predictions for these slurries is also adversely affected.

For the highest value of ϕ (= 17.50%), the thermosyphon was not operated in the partial-melting-no-supercooling-no-hysteresis (PMNSCNH) process, as the values of $q_{heating,total}$ for which the maximum slurry temperature did not exceed 28ºC in the active heating section were too low. Thus, for ϕ = 17.5%, the runs were conducted only in the full-melting-supercooling-with-freezing-and-hysteresis (FMSCWFH) process.

Table 6.6: Input parameters, experimental results, and numerical results for runs with an MCPCM slurry of mass concentration 7.471% as the working fluid: Runs 1-S to 2S correspond to FMSCWFH; and Runs 3-S and 4-S correspond to PMNSCNH.

Run	Input Parameters		Results	$T_{b,in,heating}$ [°C]	$T_{b,out,heating}$ [°C]	$T_{b,in,cooling}$ [°C]	$T_{b,out,cooling}$ [°C]	w_{av} [m/s]
1-S	$q_{heating,total}$ [W]	54.96	Expt.	15.06	37.16	36.21	14.78	$6.44\text{x}10^{-3}$
	T_{cool} [ºC]	12.99	Num.	15.29	37.43	36.25	14.81	$6.43\text{x}10^{-3}$
	T_{∞} [ºC]	21.53	% Diff.	1.53	0.73	0.11	0.20	0.16
1-Sr	$q_{heating,total}$ [W]	55.07	Expt.	15.25	37.30	36.41	14.92	$6.50\text{x}10^{-3}$
	T_{cool} [ºC]	13.07						
	T_{∞} [ºC]	22.57						
2-S	$q_{heating,total}$ [W]	41.02	Expt.	14.74	33.62	32.90	14.32	$5.56\text{x}10^{-3}$
	T_{cool} [ºC]	12.97	Num.	15.00	33.68	32.71	14.36	$5.62\text{x}10^{-3}$
	T_{∞} [ºC]	22.07	% Diff.	1.76	0.18	0.58	0.28	1.08
3-S	$q_{heating,total}$ [W]	12.28	Expt.	14.81	26.34	26.05	14.06	$2.99\text{x}10^{-3}$
	T_{cool} [ºC]	12.96	Num.	15.35	26.50	25.99	14.20	$3.03\text{x}10^{-3}$
	T_{∞} [ºC]	22.05	% Diff.	3.65	0.61	0.23	1.00	1.34
4-S	$q_{heating,total}$ [W]	7.308	Expt.	19.61	26.71	26.14	19.82	$2.36\text{x}10^{-3}$
	T_{cool} [ºC]	19.58	Num.	20.04	26.67	25.89	19.82	$2.47\text{x}10^{-3}$
	T_{∞} [ºC]	21.08	% Diff.	2.19	0.15	0.96	0	4.66

Table 6.7: Input parameters, experimental results, and numerical results for runs with an MCPCM slurry of mass concentration 9.997% as the working fluid: Runs 5-S and 6-S correspond to FMSCWFH; and Runs 7-S and 8-S correspond to PMNSCNH.

Run	Input Parameters		Results	$T_{b,in,heating}$ [°C]	$T_{b,out,heating}$ [°C]	$T_{b,in,cooling}$ [°C]	$T_{b,out,cooling}$ [°C]	w_{av} [m/s]
5-S	$q_{heating,total}$ [W]	45.07	Expt.	15.19	37.18	36.06	14.59	5.18x10^{-3}
	T_{cool} [°C]	12.99	Num.	15.34	36.84	35.56	14.63	5.31x10^{-3}
	T_{∞} [°C]	22.66	% Diff.	0.99	0.91	1.39	0.27	2.51
6-S	$q_{heating,total}$ [W]	33.37	Expt.	14.93	33.22	32.26	14.27	4.50x10^{-3}
	T_{cool} [°C]	12.99	Num.	15.10	32.98	31.88	14.29	4.61x10^{-3}
	T_{∞} [°C]	22.38	% Diff.	1.14	0.72	1.18	0.14	2.44
7-S	$q_{heating,total}$ [W]	9.701	Expt.	15.57	26.47	26.04	14.34	2.45x10^{-3}
	T_{cool} [°C]	12.98	Num.	15.95	26.55	26.02	14.54	2.48x10^{-3}
	T_{∞} [°C]	22.50	% Diff.	2.44	0.30	0.08	1.39	1.22
8-S	$q_{heating,total}$ [W]	5.457	Expt.	20.11	26.53	25.94	19.99	1.88x10^{-3}
	T_{cool} [°C]	19.54	Num.	20.38	26.54	25.72	19.99	1.90x10^{-3}
	T_{∞} [°C]	21.75	% Diff.	1.34	0.04	0.85	0	1.06

As was stated earlier, the checks on the repeatability of the experimental results were done with the following set of runs: Runs 1-S and 1-Sr; and Runs 17-S and 17-Sr. These repeatability checks show that maximum discrepancy in the bulk temperature results is 2.73% (or $0.42\,^{\circ}\mathrm{C}$) and occurs for Runs 17-S and 17-Sr; and for the average velocity of the working fluid, the maximum discrepancy is 0.93% and occurs for Runs 1-S and 1-Sr. It should be noted again that these repeatability runs were done with the lowest and highest values of the mass concentration of the MCPCM and the corresponding highest values of the total power input to the active heating section, and chosen runs were re-run from scratch (completely redone). In this context, the aforementioned discrepancies were considered quite reasonable and acceptable.

Table 6.8: Input parameters, experimental results, and numerical results for runs with an MCPCM slurry of mass concentration 12.49% as the working fluid: Runs 9-S and 10-S correspond to FMSCWFH; and Runs 11-S and 12-S correspond to PMNSCNH.

Run	Input Parameters		Results	$T_{b,in,heating}$ [°C]	$T_{b,out,heating}$ [°C]	$T_{b,in,cooling}$ [°C]	$T_{b,out,cooling}$ [°C]	w_{av} [m/s]
9-S	$q_{heating,total}$ [W]	42.33	Expt.	15.06	37.39	36.12	14.56	$4.67\text{x}10^{-3}$
	T_{cool} [^{o}C]	13.08	Num.	15.42	37.85	36.22	14.66	$4.66\text{x}10^{-3}$
	T_{∞} [^{o}C]	22.18	% Diff.	2.39	1.23	0.28	0.69	0.21
10-S	$q_{heating,total}$ [W]	31.95	Expt.	14.82	33.42	32.34	14.27	$4.12\text{x}10^{-3}$
	T_{cool} [^{o}C]	13.09	Num.	15.26	33.96	32.56	14.39	$4.09\text{x}10^{-3}$
	T_{∞} [^{o}C]	22.02	% Diff.	2.88	1.59	0.68	0.83	0.73
11-S	$q_{heating,total}$ [W]	8.315	Expt.	15.75	26.72	26.35	14.67	$2.04\text{x}10^{-3}$
	T_{cool} [^{o}C]	13.05	Num.	16.46	26.68	26.12	14.86	$2.14\text{x}10^{-3}$
	T_{∞} [^{o}C]	22.67	% Diff	4.51	0.15	0.87	1.30	4.90
12-S	$q_{heating,total}$ [W]	5.066	Expt.	20.04	26.83	26.34	20.11	$1.61\text{x}10^{-3}$
	T_{cool} [^{o}C]	19.62	Num.	20.68	26.76	25.98	20.20	$1.72\text{x}10^{-3}$
	T_{∞} [^{o}C]	22.22	% Diff	3.19	0.26	1.37	0.45	6.83

The results presented in Tables 6.6 to 6.10 show that the maximum absolute differences between the experimental and numerical results, expressed as a percentage of the experimental values, are 4.51% (equal to $0.71\,^{o}\mathrm{C}$) for the bulk temperatures (corresponding to Run 11-S) and 9.16% for the average velocity (pertaining to Run 16-S). These differences are higher than those encountered in the simulations with distilled water as the working fluid. However, as was discussed in the previous paragraph, the experimental results for Runs 11-S and 16-S, and also for some other runs with $q_{heating,total}$ < 10 W, may incorporate higher uncertainties than those mentioned earlier, and the numerical predictions for Runs 17-S and 18-S may have been compromised because of uncertainties in the related empirically determined values of the effective dynamic viscosity. Therefore, in Tables 6.6 – 6.10, if only the runs with $q_{heating,total} \geq$ 10W are considered as reliable enough for checks on the numerical predictions, and also Runs 17-S and 18-S are not considered in such checks, then the maximum absolute differences between the experimental and numerical results, expressed as a percentage of the experimental values, are 3.65% (equal to $0.54\ ^{o}\mathrm{C}$) for the bulk temperatures (corresponding to Run 3-S) and 2.51% for the average velocity (pertaining to Run 5-S). In this context, the accuracies of the 1-D/2-D model described in Chapter 2, and the numerical methods and procedures described in Chapter 5, were considered quite acceptable.

Table 6.9: Input parameters, experimental results, and numerical results for runs with an MCPCM slurry of mass concentration 14.95% as the working fluid: Runs 13-S and 14-S correspond to FMSCWFH; and Runs 15-S and 16-S correspond to PMNSCNH.

Run	Input Parameters		Results	$T_{b,in,heating}$ [°C]	$T_{b,out,heating}$ [°C]	$T_{b,in,cooling}$ [°C]	$T_{b,out,cooling}$ [°C]	w_{av} [m/s]
13-S	$q_{heating,total}$ [W]	37.95	Expt.	15.78	37.96	36.60	14.75	$4.22\text{x}10^{-3}$
	T_{cool} [^{o}C]	13.00	Num.	16.07	38.67	37.09	14.90	$4.15\text{x}10^{-3}$
	T_{∞} [^{o}C]	25.24	% Diff.	1.84	1.87	1.33	1.02	1.66
14-S	$q_{heating,total}$ [W]	27.52	Expt.	15.67	33.45	32.48	14.53	$3.68\text{x}10^{-3}$
	T_{cool} [^{o}C]	13.00	Num.	16.00	34.21	32.96	14.68	$3.61\text{x}10^{-3}$
	T_{∞} [^{o}C]	24.87	% Diff.	2.11	2.27	1.48	1.03	1.90
15-S	$q_{heating,total}$ [W]	6.508	Expt.	17.08	26.84	26.60	15.29	$1.85\text{x}10^{-3}$
	T_{cool} [^{o}C]	12.97	Num.	17.53	26.90	26.58	15.44	$1.88\text{x}10^{-3}$
	T_{∞} [^{o}C]	24.56	% Diff.	2.63	0.22	0.08	0.98	1.62
16-S	$q_{heating,total}$ [W]	3.692	Expt.	21.23	27.00	26.40	20.65	$1.31\text{x}10^{-3}$
	T_{cool} [^{o}C]	19.57	Num.	21.45	26.77	26.18	20.62	$1.43\text{x}10^{-3}$
	T_{∞} [^{o}C]	23.60	% Diff.	1.04	0.85	0.83	0.15	9.16

Table 6.10: Input parameters, experimental results, and numerical results for runs with an MCPCM slurry of mass concentration 17.50% as the working fluid: Runs 17-S, 17-Sr, and 18-S all correspond to FMSCWFH.

Run	Input Parameters		Results	$T_{b,in,heating}$ [°C]	$T_{b,out,heating}$ [°C]	$T_{b,in,cooling}$ [°C]	$T_{b,out,cooling}$ [°C]	w_{av} [m/s]
17-S	$q_{heating,total}$ [W]	35.06	Expt.	15.38	37.37	35.88	14.64	$3.78\text{x}10^{-3}$
	T_{cool} [^{o}C]	13.08	Num.	15.94	38.73	36.68	14.81	$3.67\text{x}10^{-3}$
	T_{∞} [^{o}C]	23.62	% Diff.	3.64	3.64	2.23	1.16	2.91
17-Sr	$q_{heating,total}$ [W]	35.13	Expt.	14.96	36.81	35.26	14.41	$3.77\text{x}10^{-3}$
	T_{cool} [^{o}C]	13.08						
	T_{∞} [^{o}C]	22.18						
18-S	$q_{heating,total}$ [W]	26.54	Expt.	15.32	33.48	32.36	14.46	$3.35\text{x}10^{-3}$
	T_{cool} [^{o}C]	13.06	Num.	15.97	34.73	33.05	14.68	$3.24\text{x}10^{-3}$
	T_{∞} [^{o}C]	23.62	% Diff.	4.24	3.73	2.13	1.52	3.28

The variations of experimental and numerical results for the average working-fluid velocity, w_{av}, with total power input to the active heating section, $q_{heating,\,total}$, for MCPCM concentrations of 7.471% and 9.997% (Runs 1-S to 8-S) are presented graphically in Fig. 6.6, those for MCPCM concentrations of 12.49%, 14.95%, and 17.50% (Runs 9-S to 18-S) are presented graphically in Fig. 6.7. The estimated experimental uncertainties associated with w_{av} are also included these figure in the form of vertical bars, centered about the experimental results.

The data points located in the right-halves of Figs. 6.6 and 6.7 pertain to the runs conducted in the full-melting-supercooling-with-freezing-and-hysteresis (FMSCWFH) process; and the data points in the left-halves of these figures correspond to runs done in the partial-melting-no-supercooling-no-hysteresis (PMNSCNH) process. For the runs done in the FMSCWFH process, the values of $q_{heating,total}$ required to completely melt the MCPCM particles, by achieving a minimum slurry temperature greater than 32.5ºC at the exit of the active heating section, are quite high; thus the related buoyancy effects are stronger (due to the larger temperature and density changes), which, in turn, induce higher values of the average velocity of the working fluid. On the other hand, for runs done in the PMNSCNH process, it is necessary to keep the values of $q_{heating,total}$ low enough to ensure that the maximum slurry temperature does not exceed 28.0ºC at the exit of the active heating section; thus the buoyancy effects and the induced values of the average velocity of the working fluid are relatively smaller.

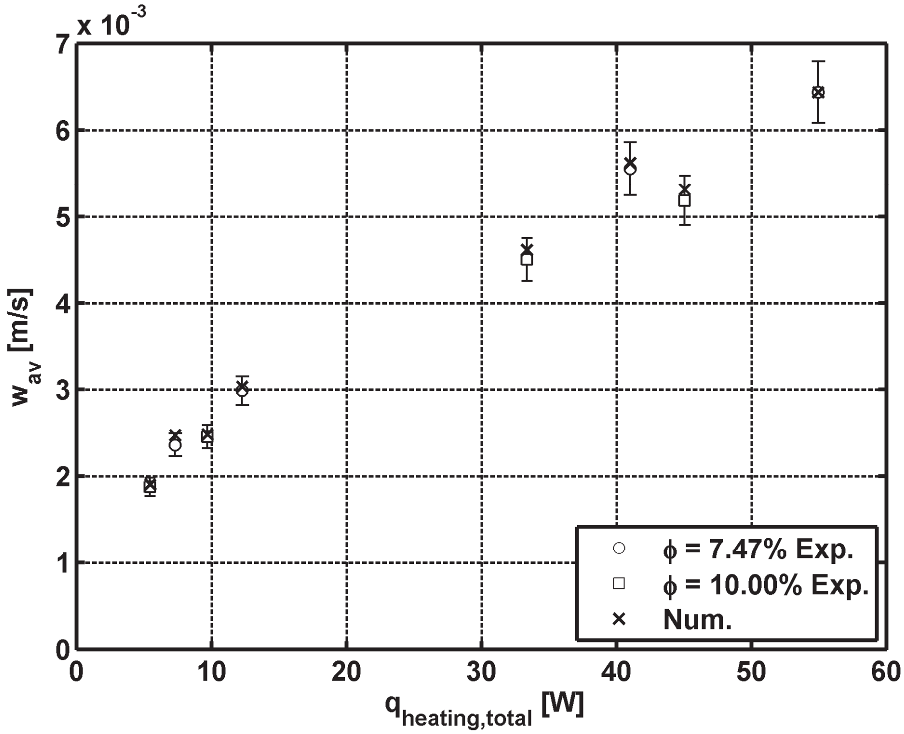

Figure 6.6: Experimental and numerical results for average velocity of the working fluid in the closed-loop thermosyphon for the runs performed with slurries of MCPCM mass concentrations 7.471% and 9.997% (Runs 1-S to 8-S).

As can be seen from the results presented in Figs. 6.6 and 6.7, the average velocity, w_{av}, generally decreases as the mass concentration of the slurry, ϕ , is increased (for comparable values of $q_{heating,total}$). This decrease in average velocity is mainly caused by the overall increase of the effective dynamic viscosity of the slurry, as the relative consistency index, m, increases strongly at relatively high values of ϕ (see Fig. 3.15). It should also be noted that at high values of ϕ, the overall buoyancy force driving the flow of the slurry in the thermosyphon is also high, due to the strong decrease of ρ_s associated with the melting of the PCM. Thus, the results presented in Tables 6.6 – 6.10 and in Figs. 6.6 and 6.7 show that for the MCPCM slurries and the closed-loop thermosyphon studied in this work, the aforementioned increase of the overall buoyancy force at high values of ϕ was less important than the related increase of the effective dynamic viscosity.

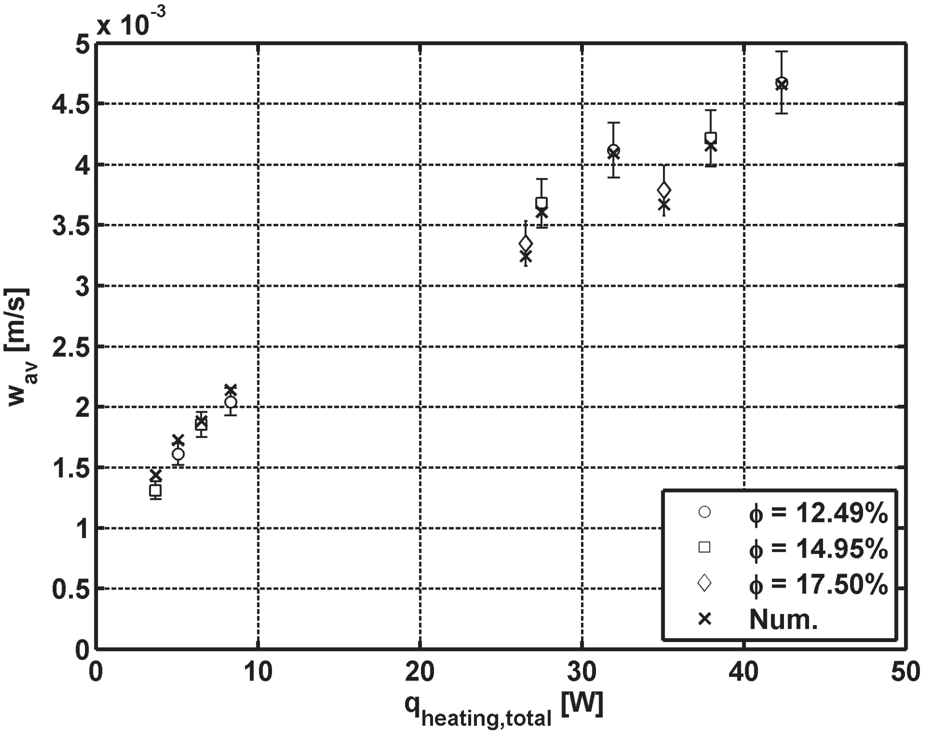

Figure 6.7: Experimental and numerical results for average velocity of the working fluid in the closed-loop thermosyphon for the runs performed with slurries of MCPCM mass concentrations 12.49%, 14.95%, and 17.50% (Runs 9-S to 18-S).

6.3.3 Numerical Predictions of Dimensionless Axial Velocity and Temperature Distributions in the Vertical Heating and Cooling Sections

The variations of the dimensionless axial velocity, w / w_{av}, and temperature, $(T - T_{b,in}) / (T_{b,out} - T_{b,in})$, with the dimensionless radial coordinate, r / r_i, at six different axial locations in the vertical heating and cooling sections are presented in Figs. 6.8 and 6.9, respectively, for Run 9-S. As can be seen from the input parameters in Tables 6.6 to 6.10 for the runs with slurries, ϕ = 12.49% is an intermediate value; and $q_{heating,total}$ = 42.33W is the highest power input for this value of mass concentration of MCPCM. So the local buoyancy effects in the vertical heating and cooling sections were expected to be quite high, and the corresponding velocity and temperature gradients quite steep, along with appreciable effects of buoyancy and the PCM latent heat. The results shown in Figs. 6.8 and 6.9 confirm these expectations. These results for the other runs with the MCPCM slurries are qualitatively similar to those for Run 9-S, with the effects of the aforementioned phenomena less or more pronounced.

The results in Fig. 6.8(a) for the dimensionless axial velocity distribution in the heating section, in which the main flow and the buoyancy forces are both directed vertically upwards (aiding configuration), show the following features: 1) at the inlet to the heating section ($z = 0$; start of the pre-heating length) it is set equal to the fully-developed velocity profile (without local buoyancy effects) for non-Newtonian flows, as prescribed in Eq. (2.29), as the pre-heating length was long enough to justify this prescription; 2) it gets increasingly influenced by local buoyancy and latent-heat heat effects as the fluid travels through the active heating section; 3) in the active heating section, for $z \geq L_{h,pre} + 0.8L_h$, it attains shapes that are not influenced by latent-heat effects (as the PCM has fully melted before $z = L_{h,pre} + 0.8L_h$); and 4) at the outlet of the heating section ($z = L_{h,pre} + L_h + L_{h,post}$), it reverts back to a shape essentially akin to the fully-developed velocity profile (without local buoyancy effects) for non-Newtonian flows, as prescribed in Eq. (2.29), confirming that the post-heating length was long enough to provide this desired result.

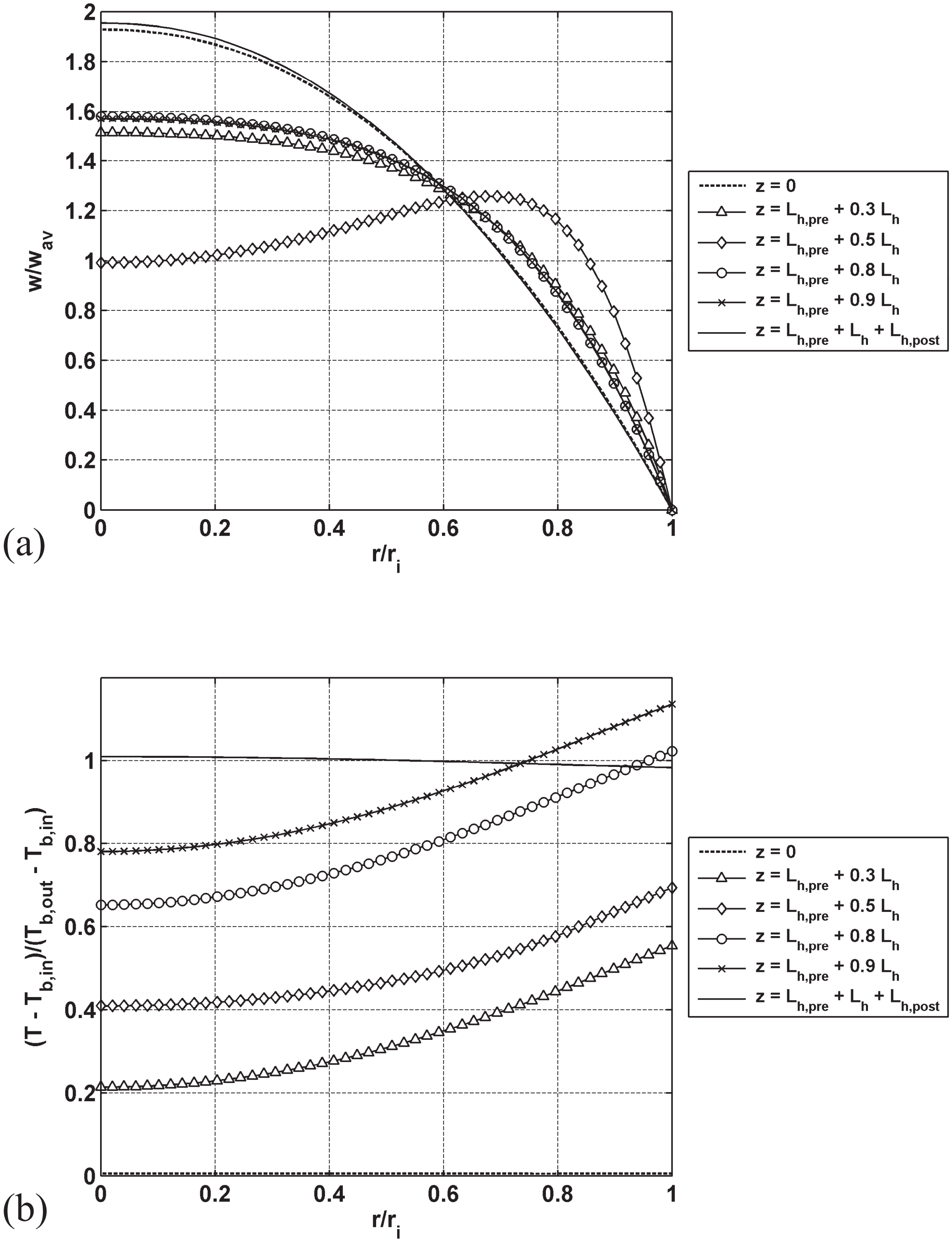

Figure 6.8: Numerical predictions of the distributions of dimensionless (a) axial velocity and (b) temperature in the vertical heating section of the closed-loop thermosyphon operating with a slurry of ϕ = 12.49% as the working fluid, for Run 9-S.

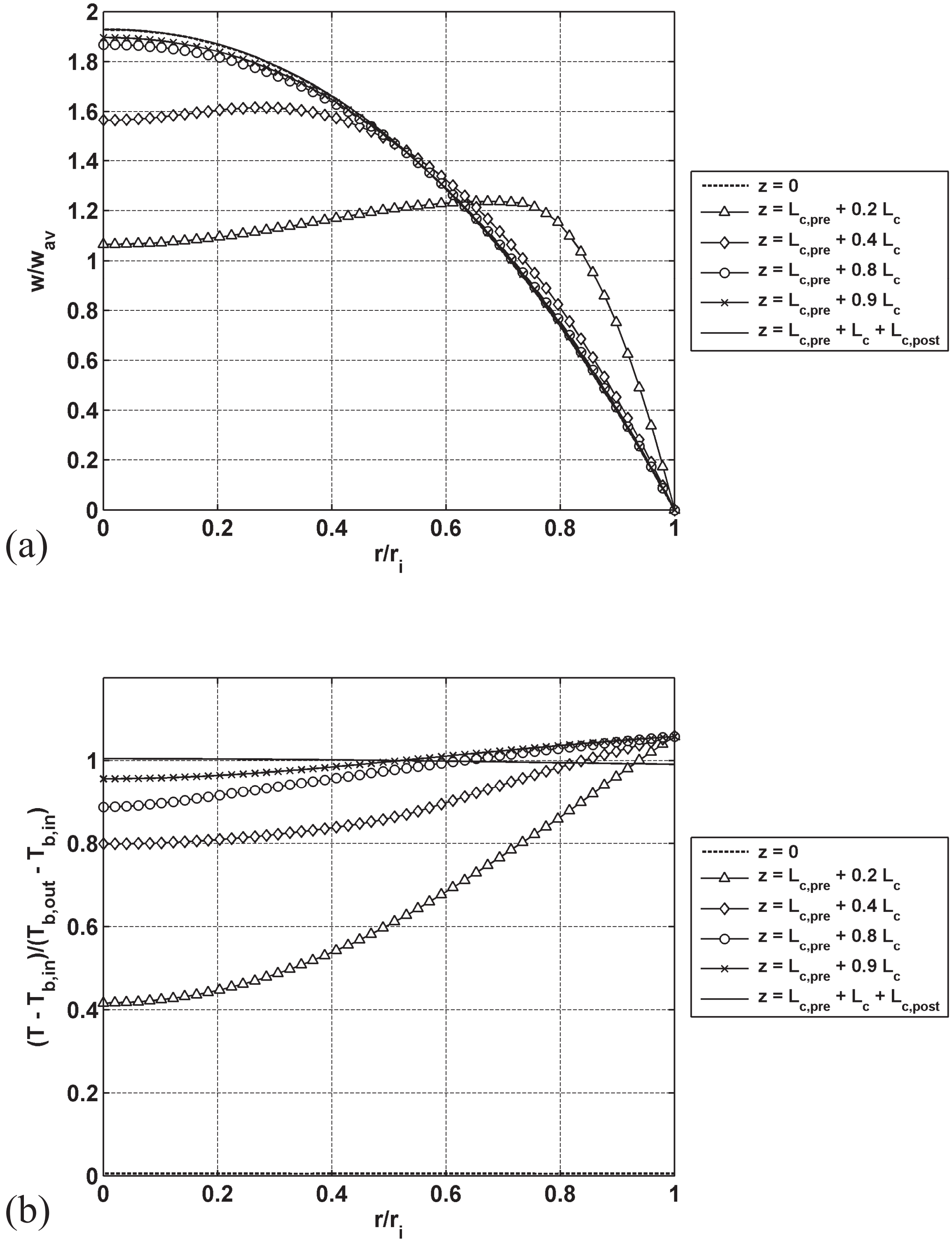

Figure 6.9: Numerical predictions of the distributions of dimensionless (a) axial velocity and (b) temperature in the vertical cooling section of the closed-loop thermosyphon operating with a slurry of ϕ = 12.49% as the working fluid, for Run 9-S.

The results in Fig. 6.8(b) for the dimensionless temperature distribution in the heating section show the following features: 1) at the inlet to the heating section, it is uniform and essentially zero, as the inlet temperature was set equal to $T_{b,in}$ (the pre-heating length was long enough to justify this prescription); 2) it gets increasingly influenced by local buoyancy and latent-heat effects as the fluid travels through the active heating section; 3) in the active heating section, for $z \geq L_{h,pre} + 0.8L_h$, it attains an essentially fully-developed shape for the thermal boundary condition imposed in this section (same shape, but temperature at all *r* locations increases essentially linearly with *z*); and 4) at the outlet of the heating section ($z = L_{h,pre} + L_h + L_{h,post}$), it is essentially uniform again, but at a value of one (unity), indicating that $T = T_{b,out}$ for $0 \leq r \leq r_i$, and confirming that the post-heating length was long enough to provide this desired result.

The results in Fig. 6.9(a) for the dimensionless axial velocity distributions in the cooling section, in which the main flow and the buoyancy forces are both directed vertically downwards (aiding configuration), show features that are similar to those discussed above for the heating section. However, the dimensionless temperature distributions presented in Fig. 6.9(b), while indicating the influence of buoyancy (aiding configuration), are different from those in Fig. 6.9(b), because the thermal boundary condition in the active cooling section corresponds to essentially uniform wall temperature ($T_{r=r_i}$ = T_{cool}), while it corresponds to essentially uniform heat flux in the active heating section.

6.3.4 Axial Distributions of the Temperature of the Outer Surface of the Tube Wall in the Active Heating Section

The experimental and numerical results for the axial distributions of the temperature of the outer surface of the tube wall, $T_{r=r_o}$, in the active heating section are plotted in Fig. 6.10 for ϕ = 7.471% (Runs 1-S to 4-S); in Fig. 6.11 for ϕ = 9.997% (Runs 5-S to 8-S); in Fig. 6.12 for ϕ = 12.49% (Runs 9-S to 12-S); in Fig. 6.13 for ϕ = 14.95% (Runs 13-S to 16-S); and in Fig. 6.14 for ϕ = 17.50% (Runs 17-S and 18-S). *In Figs. 6.10 to 6.14, z = 0 m corresponds to the start of the active heating section.*

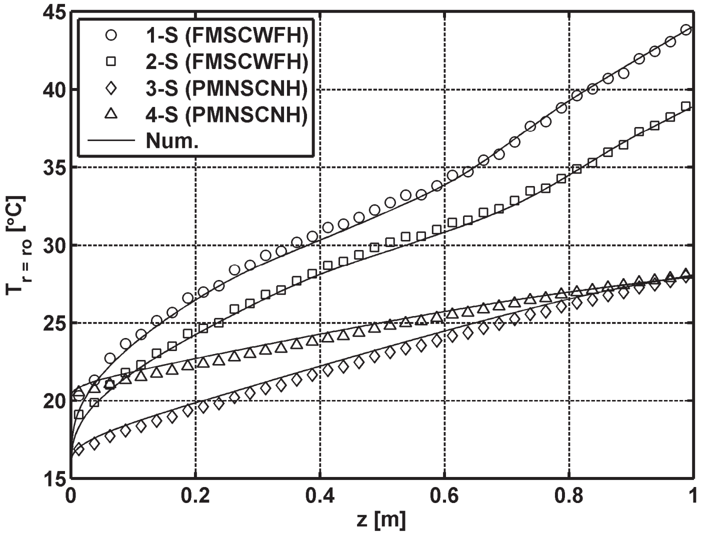

Figure 6.10: Experimental and numerical result for the axial distributions of the temperature of the outer surface of the tube wall in the active heating section of the closed-loop thermosyphon operated with MCPCM slurries of mass concentration 7.471%.

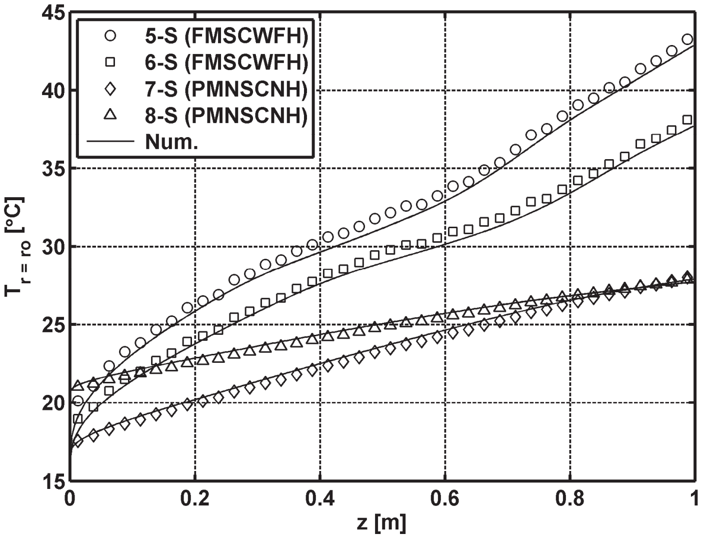

Figure 6.11: Experimental and numerical result for the axial distributions of the temperature of the outer surface of the tube wall in the active heating section of the closed-loop thermosyphon operated with MCPCM slurries of mass concentration 9.997%.

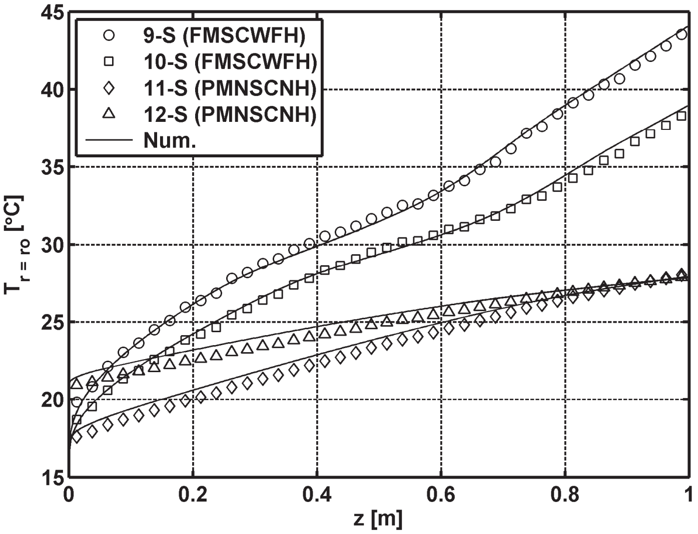

Figure 6.12: Experimental and numerical result for the axial distributions of the temperature of the outer surface of the tube wall in the active heating section of the closed-loop thermosyphon operated with MCPCM slurries of mass concentration 12.49%.

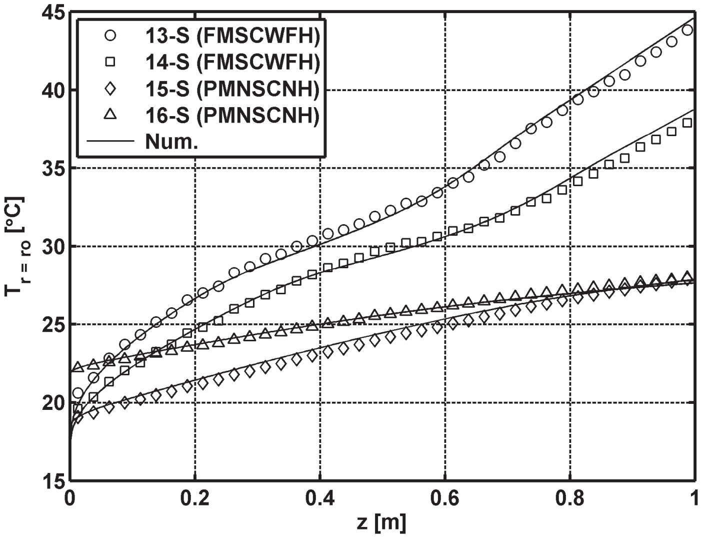

Figure 6.13: Experimental and numerical result for the axial distributions of the temperature of the outer surface of the tube wall in the active heating section of the closed-loop thermosyphon operated with MCPCM slurries of mass concentration 14.95%.

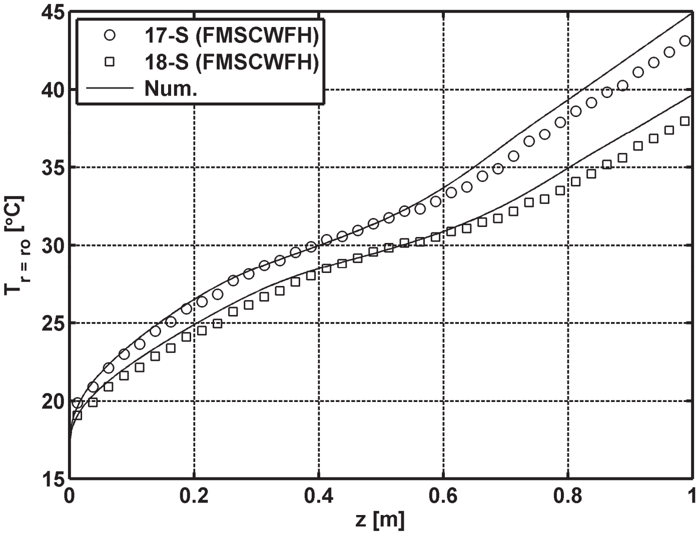

Figure 6.14: Experimental and numerical result for the axial distributions of the temperature of the outer surface of the tube wall in the active heating section of the closed-loop thermosyphon operated with MCPCM slurries of mass concentration 17.50%.

The experimental uncertainty of the experimental results plotted in Figs. 6.10 to 6.14 is ±0.063°C (see Subsection 4.6.2 in Chapter 4). The error bands corresponding to this uncertainty would be slightly smaller than the size of the symbols used to indicate the experimental data points in these figures, so they are not included in them. The agreement between the experimental and numerical results shown in this figure is very good for the runs corresponding to Figs. 6.10 to 6.13, and it is good for runs pertaining to Fig. 6.14 (Run 17-S and 18-S; with ϕ = 17.5% and the highest values of the effective dynamic viscosity of the slurry; and the related uncertainties discussed in Subsection 6.3.1). Thus, these comparisons also validate the proposed 1-D/2-D model, and the proposed numerical methods and procedures.

The $T_{r=r_o}\, vs.z$ plots in Figs. 6.10 to 6.14 for the runs conducted in the full-melting-supercooling-with-freezing-and-hysteresis (FMSCWFH) process have the following features: in the region $0 \le z \le 0.6\,\mathrm{m}$ (roughly), the joint (and coupled) effects of the developing flow, buoyancy, and latent heat of the PCM during the solid-liquid phase-change phenomenon cause these plots to be nonlinear; the region $0.6\,\mathrm{m} < z \le 0.8\,\mathrm{m}$ (roughly) corresponds to sensible heating of the slurry (as the melting of the PCM is fully completed before the start of this region), and the plots indicate a second region of development for this condition; and for $z > 0.8\,\mathrm{m}$ (roughly), these plots are almost linear, indicating an essentially fully-developed regime (with local buoyancy effects) in this region of the active heating section. The $T_{r=r_o}\, vs.\, z$ plots in Figs. 6.10 to 6.14 for the runs conducted in the partial-melting-no-supercooling-no-hysteresis (PMNSCNH) process exhibit the joint (and coupled) effects of the developing flow, buoyancy, and latent heat of the PCM during the solid-liquid phase-change phenomenon, causing these plots to be nonlinear throughout the active heating section, $0 \le z \le 1.0\,\mathrm{m}$.

6.3.5 Assessment of the Importance of Accounting for non-Newtonian Behavior

In this subsection, the importance of accounting for the non-Newtonian behavior of the MCPCM slurries is demonstrated by presenting the results obtained by assuming these slurries are Newtonian fluids, comparing these results with experimental results for the same runs, and discussing the related inaccuracies. For the simulations in which the behavior of slurries was approximated as Newtonian, their effective dynamic viscosity was assumed to be independent of the local rate of strain and expressed as follows:

$$\mu_s = \mu_{H_2O} \cdot f\left(\phi\right) \tag{6.1}$$

In this equation, μ_{H_2O} denotes the dynamic viscosity of distilled water (a Newtonian fluid; μ_{H_2O} is evaluated at the local temperature of the working fluid), and $f\left(\phi\right)$ is a function of the mass concentration of MCPCM in the slurry. Such a model of the effective dynamic viscosity of MCPCM slurries has been used in previous studies of forced and mixed convection heat transfer with these slurries as the working fluid [Goel et al. (1994), Inaba et al. (2004), Scott (2006)]. For this model, the relative dynamic viscosity data measured with the glass capillary-tube viscometers (as described in Chapter 3) were curve-fitted solely with respect to the mass concentration of the MCPCM, without taking into account any dependence on the rate of strain. The resulting curve-fit is given in the following equation:

$$\mu_s = \mu_{H_2O}\left(4.1759\text{x}10^{-3}\phi^3 - 4.8413\text{x}10^{-2}\phi^2 + 84.132\phi + 1\right) \tag{6.2}$$

Equation (6.2) for the effective dynamic viscosity was used in the 1-D/2-D model presented in Chapter 2, along with the correlations presented in Chapter 3 for the other effective thermophysical properties of the slurries, and the numerical methods and procedures out forward in Chapter 5, to simulate the following experimental runs (see Tables 6.5, 6.6, and 6.10 for full details of the input parameters): for ϕ = 7.471% (the lowest MCPCM mass concentration of the slurries considered in this work), Runs 1-S and 2-S (full-melting-supercooling-with-freezing-and-hysteresis, or FMSCWFH, process), and Runs 3-S and 4-S (partial-melting-no-supercooling-no-hysteresis, or PMNSCNH, process); and for ϕ = 17.50% (the highest MCPCM mass concentration of the slurries considered in this work), Runs 17-S and 18-S (full-melting-supercooling-with-freezing-and-hysteresis, or FMSCWFH, process). The calculation domains and grids presented and discussed in Section 6.1 were also used in these simulations. The numerical predictions of the average velocity yielded by these simulations for Runs 1-S and 17-S are presented along with the corresponding experimental results in Fig. 6.15.

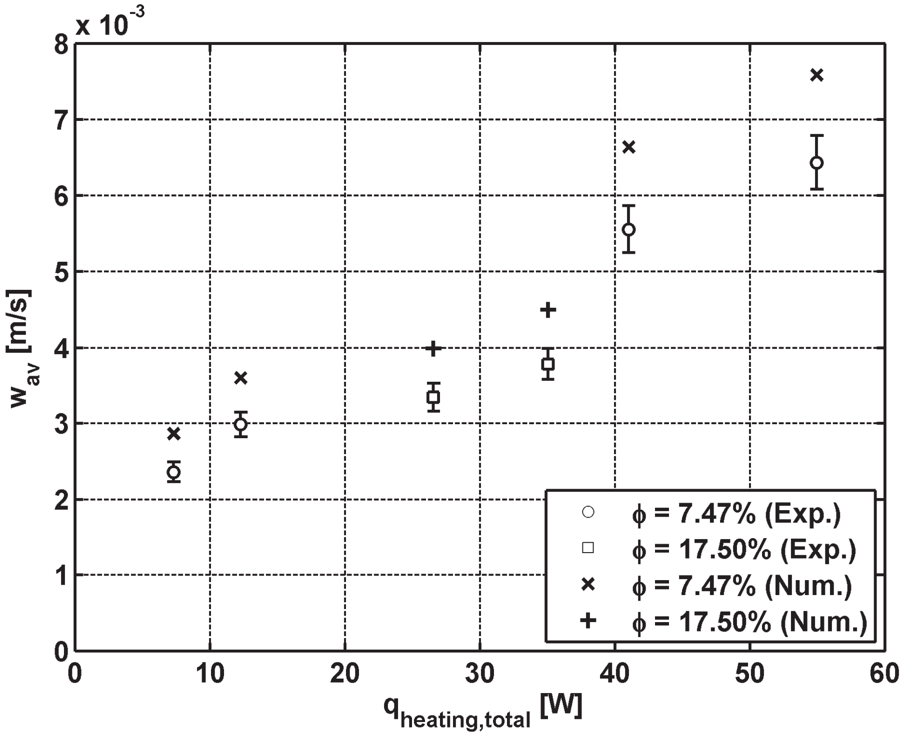

Figure 6.15: Numerical predictions obtained by assuming the MCPCM slurries behave as a Newtonian fluid and experimental results for average velocity of the working fluid.

As shown by the results presented in Fig. 6.15, the numerical results for w_{av} obtained by assuming that the MCPCM slurries behave as a Newtonian fluid are all substantially higher than the corresponding experimental results (well outside the experimental error bands). As was discussed in Chapter 3, the values of the rate of strain in the MCPCM slurries flowing through the glass capillary-tube viscometers used in this work were one to two orders of magnitude greater than the values that prevailed in the closed-loop thermosyphon experiments. Since the MCPCM slurries are slightly (yet non-negligibly) shear-thinning, the effective dynamic viscosity values would be significantly higher in the thermosyphon than in the glass capillary-tube viscometers. Thus, if the MCPCM slurries are wrongly assumed to behave as a Newtonian fluid and the data obtained with glass capillary-tube viscometers are interpreted and correlated accordingly, and the related correlations are used in the numerical simulations, the values of effective dynamic viscosity would be generally underestimated compared to the actual values prevailing in the closed-loop thermosyphon experiments. Hence, in such numerical simulations, the values of shear stress along the inner surface of the closed-loop thermosyphon are under-predicted and the values of w_{av} are significantly over-predicted compared to the corresponding experimental values.

The experimental results and the corresponding numerical predictions (obtained assuming the slurries behave as a Newtonian fluid) for the axial distributions of the temperature of the outer surface of the tube wall, $T_{r=r_o}$, in the active heating section are plotted in Fig. 6.16 and 6.17 for ϕ = 7.471% (Runs 1-S to 4-S) and ϕ = 17.50% (Runs 17-S and 18-S), respectively. It should be noted that *in these figures, z = 0 m corresponds to the start of the active heating section*. These results again show that the agreement between the numerical predictions and the experimental results is poor, especially near the exit of the heating section. The outer wall temperature distributions are under-predicted, mostly because of the over-predicted values of w_{av} (as shown in Fig. 6.15).

When the results presented in Figs. 6.15, 6.16, and 6.17 are examined in the context of those presented earlier in Subsections 6.3.2 and 6.3.4 (Figs. 6.6, 6.7, and 6.10

to 6.14), the importance of accounting for the non-Newtonian behavior of the MCPCM slurries used in this work is clearly established.

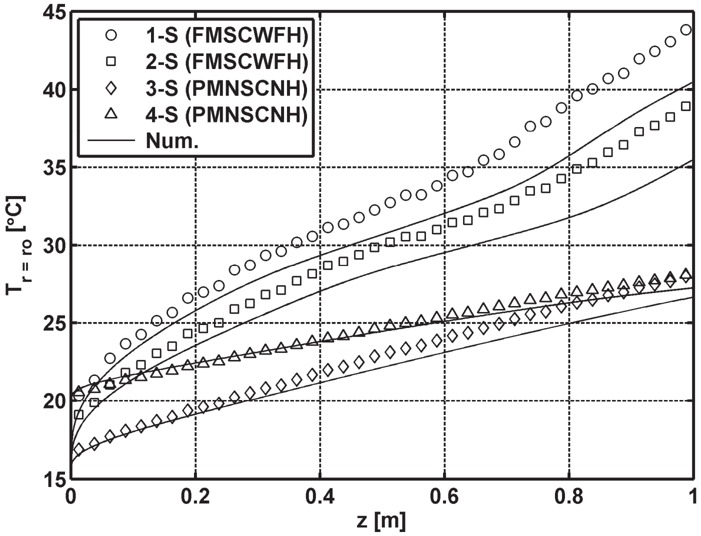

Figure 6.16: Numerical predictions obtained by assuming the MCPCM slurries behave as a Newtonian fluid and experimental results for the axial distributions of the temperature of the outer surface of the pipe wall in the active heating section of the closed-loop thermosyphon, for ϕ = 7.471%.

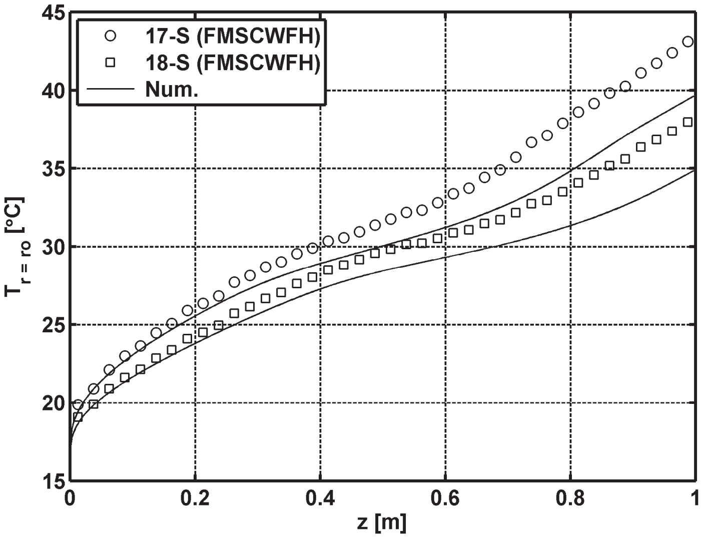

Figure 6.17: Numerical predictions obtained by assuming the MCPCM slurries behave as a Newtonian fluid and experimental results for the axial distributions of the temperature of the outer surface of the pipe wall in the active heating section of the closed-loop thermosyphon, for ϕ = 17.50%.

7. Conclusion

This last chapter is composed of two sections: first, a review of the thesis and its main contributions (indicated using *italics* font) are presented; and second, some extensions of this work are proposed.

7.1 Review of the Thesis and its Contributions

The main focus of the research work presented in this thesis was on complementary computational and experimental investigations of steady, laminar, fluid flow and heat transfer in a closed-loop thermosyphon having vertical heating and cooling sections, and operating with slurries of a microencapsulated phase-change material (MCPCM) suspended in distilled water.

In Chapter 1, the motivation and main goals of the work, an overview of the microencapsulated phase-change material and the slurries, and the objectives of this work were discussed. A review of the published literature on the topics related to this work was also presented.

In Chapter 2, a cost-effective 1-D/2-D model, which involves an amalgamation of two-dimensional axisymmetric and quasi-one-dimensional models of the steady fluid flow and heat transfer in the vertical (heating and cooling) sections and the other portions of the closed-loop thermosyphon, respectively, was proposed, concentrating on the theoretical considerations and aspects on which this model is based. For the two-dimensional axisymmetric part of this model, a homogeneous approach to the modeling of the flow of MCPCM slurries and the related heat transfer was shown to be applicable and elaborated. This two-dimensional model takes into account the slight shear-thinning, non-Newtonian, behavior of the MCPCM slurries. *The integration of a simple, but effective, non-Newtonian rheological model of the MCPCM slurries with a general formulation of the aforementioned homogenous model of the fluid flow and heat transfer phenomena is considered as one of the main contributions of this thesis*. Additional theoretical considerations, such as the overall momentum balance which allows the evaluation of the average velocity of the working fluid in the closed-loop thermosyphon, were also presented and discussed in Chapter 2.

The results of investigations which were undertaken to determine the effective thermophysical properties of the MCPCM slurries used in this work were presented in Chapter 3. The experimental apparatus and instrumentation used for measuring and characterizing the effective specific heat and phase-change behavior of the MCPCM particles, and the effective density and the effective dynamic viscosity of the slurries, were presented, along with the proposed experimental procedures. Experiments were conducted to obtain effective thermophysical property data for both the heating (melting) and cooling (freezing) processes. The experimental data were used to propose correlations for the effective thermophysical properties of the MCPCM slurries, in forms which facilitated their incorporation in the proposed 1-D/2-D model of the closed-loop thermosyphon. *The full characterization of the phase-change behavior of the MCPCM slurries used in this work, including an evaluation of their supercooling requirement and the related hysteresis effects, and the approach that was used to prescribe the effective thermophysical properties pertaining to particular heating, cooling, and phase-change processes, are among the main contributions of this thesis*. *Also, to the author's best knowledge, this is the first investigation of effective thermophysical properties of MCPCM slurries in which the effects of the aforementioned hysteresis associated with the supercooling requirement were measured and correlated precisely.* Lastly, an approach was proposed for the determination of the rheological behavior of the slurries. This approach involves a combination of a modified version of the 1-D/2-D model, measurements using glass capillary-tube viscometers, and experimental results obtained with the thermosyphon apparatus operated with the MCPCM slurries in the fully-melted-no-freezing mode. *This approach to the determination of the non-Newtonian rheological behavior of the MCPCM slurries and a proposed correlation for their effective dynamic viscosity is also considered to be one of the main contributions of this work.*

The thermosyphon apparatus and the procedures which were used in the main experimental investigations of this work were presented in Chapter 4. *The design, construction, testing, and use of this apparatus are also considered as a part of the main contributions of this work.*

In Chapter 5, the numerical methods and procedures proposed for solving the proposed 1-D/2-D model of the closed loop thermosyphon were presented. The formulation of a co-located equal-order control-volume finite element method (CVFEM), which was used to solve the steady, two-dimensional axisymmetric model of the fluid flow and heat transfer phenomena in the vertical heating and cooling sections, was presented, along with results of two test problems which were used to validate it. The proposed CVFEM incorporates improved formulations of the discretized pressure equation and boundary treatments for incompressible fluid flow. *This CVFEM and the aforementioned improved formulations are considered to be important contributions of this thesis*. They have been published in a journal article by the author of this thesis and his supervisor, in the context of two-dimensional planar problems [Lamoureux and Baliga (2011), in *Numerical Heat Transfer, Part B: Fundamentals*]. Lastly, the numerical evaluation of the overall momentum balance and an overall iterative solution procedure for the proposed 1-D/2-D model of the closed-loop thermosyphon were presented in this chapter.

The main results of the complementary numerical and experimental investigations of the closed-loop thermosyphon, operated with distilled water and the MCPCM slurries, were presented and discussed in Chapter 6 (a detailed presentation of the experimental results is provided in Appendix E). *To the best knowledge of the author, this work constitutes the first complementary numerical and experimental investigation of closed-loop thermosyphons operated with MCPCM slurries as the working fluid.* The numerical and experimental results showed good agreement, attesting to the validity of the proposed 1-D/2-D model and the proposed numerical methods and procedures. *The results and discussions presented in this chapter, with special attention to full-melting-supercooling-with-freezing-and-hysteresis (FMSCWFH) and partial-melting-no-supercooling-no-hysteresis (PMNSCNH) processes, are also considered as important contributions of this thesis.* Lastly, the importance of accounting for the non-Newtonian behavior of the MCPCM slurries was assessed, by undertaking additional simulations in which a Newtonian behavior of the slurries was assumed and comparing the related results to corresponding experimental results obtained in this work. These results and comparisons clearly established the importance of accounting for the non-Newtonian behavior of the MCPCM slurries used in this work.

7.2 Suggested Extensions of this Work

In this final section of the thesis, a few suggestions for extensions of this work are proposed below.

It would be interesting to extend the proposed 1-D/2-D thermosyphon model to a 1-D/3-D version for the simulation of closed-loop thermosyphons in which three-dimensional fluid flow and heat transfer phenomena occur in the heating and cooling sections. For example, such an extended 1-D/3-D model could be used for investigating and designing closed-loop thermosyphons in which the heating and cooling sections are inclined (rather than vertical) or have complex geometries.

The proposed 1-D/2-D model of closed-loop thermosyphons could be amalgamated with optimization techniques, such as genetic algorithms or gradient-based methods, and then used to propose optimized designs of such devices. Similarly, the proposed 1-D/2-D model in conjunction with an optimization technique could be used to tailor the effective thermophysical properties of the MCPCM slurries for specific applications (thereby leading to designs with optimized working fluids).

Extending the proposed 1-D/2-D model for applications involving transitional or turbulent flow regimes would be an interesting and challenging undertaking. Proposing an accurate and cost-effective model of the potential dampening or enhancing effects of the MCPCM particles on the turbulence is an example of one of the challenges associated with such an extension.

Further investigations aiming to reduce the effective dynamic viscosity of MCPCM slurries at moderate to relatively high mass concentrations, using small quantities of suitable additives (such as surfactants) or other approaches, would constitute worthwhile efforts. Slurries with relatively high MCPCM mass concentration, but effective dynamic viscosity values that are not too different from those of water, would be very attractive in applications involving forced, natural, or mixed convection heat transfer processes.

Endeavors seeking to reduce or eliminate the supercooling requirement of the encapsulated PCMs, such as the work of Fan et al. (2004), without significantly compromising its latent heat of fusion, could lead to valuable contributions. The resulting MCPCM particles and slurries would allow a more flexible range of operational temperatures, as supercooling would be significantly reduced or no longer required.

Although particle migration or segregation from the carrier liquid was not an issue in this work, actual closed-loop thermosyphons and similar devices operating with MCPCM slurries could be afflicted by such issues, as they could remain inoperative for prolonged periods of time. Thus, efforts to mitigate particle migration and overall separation of the slurry constituents at rest would be valuable. Such efforts could also include the design of passive inflow devices that promote mixing of the MCPCM particles with the carrier fluid upon start-up of the application and also during operation.

The author would like to conclude with the hope that this work would prove useful to some practicing engineers and other researchers, and also encourage them to pursue some of the above-mentioned extensions.

References

Acharya, S., Baliga, B.R., Karki, K., Murthy, J.Y., Prakash, C. and Vanka, S.P. (2007), Pressure-Based Finite Volume Methods in Computational Fluid Dynamics, *ASME J. Heat Transfer*, Vol. 129, pp. 407-424.

Acrivos, A. (1995), "Shear-Induced Particle Diffusion in Concentrated Suspensions of Noncolloidal Particles", *Journal of Rheology*, Vol. 39, Bingham Award Lecture – 1994, pp. 813-826.

Ahuja, A.S. (1975), "Augmentation of Heat Transport in Laminar Flow of Polystyrene Suspensions. I. Experiments and Results", *Journal of Applied Physics*, Vol. 46, No. 8, pp. 3408-3416.

Alvarado, J.L, Marsh, C., Sohn, C., Phetteplace, G. and Newell, T. (2007), "Thermal Performance of Microencapsulated Phase Change Material Slurry in Turbulent Flow Under Constant Heat Flux", *Int. J. Heat and Mass Transfer*, Vol. 50, pp. 1938-1952.

Alvarado, J.L., Marsh, C., Sohn, C., Vilceus, M., Hock, V., Phetteplace, G. and Newell, T. (2006), "Characterization of Supercooling Suppression of Microencapsulated Phase Change Material by Using DSC", *J. Thermal Analysis and Calorimetry*, Vol. 86, pp. 505-509.

Aung, W. (1987), "Mixed Convection in Internal Flow", in *Handbook of Single-Phase Convective Heat Transfer*, S. Kakac, R.K. Shah and W. Aung (Editors), Wiley, New York, Chapter 15, pp. 15.1-15.51.

Bagnold, R.A. (1954), "Experiments on a Gravity Free Dispersion of Large Solid Spheres in a Newtonian Fluid Under Shear", *Proc. Royal Society of London*, Series A, Vol. 225, pp. 49-63.

Bagnold, R.A. (1956), "The Flow of Cohesionless Grains in Fluids", *Philosophical Transactions of the Royal Society of London*, Series A, Vol. 249, pp. 235-297.

Bai, F. and Lu, W.Q. (2003), "Numerical Analysis of Laminar Forced Convection Heat Transfer in Microencapsulated Phase Change Material Suspensions", *Journal of Enhanced Heat Transfer*, Vol. 10, pp. 311-322.

Baliga, B.R. (1997), "Control-Volume Finite Element Methods for Fluid Flow and Heat Transfer", in W.J. Minkowycz and E.M. Sparrow (Editors), *Advances in Numerical Heat Transfer*, Taylor & Francis, Washington D.C., Vol. 1, Chapter 3, pp. 97-135.

Baliga, B.R. and Atabaki, N. (2006), "Control-Volume-Based Finite Difference and Finite Element Methods", in W.J. Minkowycz, E.M. Sparrow and J.Y. Murthy (Editors), *Handbook of Numerical Heat Transfer*, 2nd Ed., Chapter 6, John Wiley & Sons, New York.

Baliga, B.R. and Patankar, S.V. (1980), “A New Finite Element Formulation for Convection-Diffusion Problems”, *Numerical Heat Transfer*, Vol. 3, pp. 393-409.

Baliga, B.R. and Patankar, S.V. (1983), “A Control-Volume Finite Element Method for Two-Dimensional Fluid Flow and Heat Transfer”, *Numerical Heat Transfer*, Vol. 6, pp. 245-261.

Batchelor, G.K. (1974), “Transport Properties of Two-Phase Materials with Random Structure”, *Annual Review of Fluid Mechanics*, Vol. 6, pp. 227-255.

Benne, K.S. and Homan, K.O. (2008), “Dynamics of a Closed-Loop Thermosyphon Incorporating Thermal Storage”, *Numerical Heat Transfer, Part A*, Vol. 54, pp. 235-254.

Bergles, A.E. (2003), “High-Flux Processes Through Enhanced Heat Transfer”, *Proc. Rohsenow Symposium on Future Trends in Heat Transfer*, MIT, Massachusetts, U.S.A.

Bernier, M.A. and Baliga, B.R. (1992a), “Conjugate Conduction and Laminar Mixed Convection in Vertical Pipes for Upward Flow and Uniform Wall Heat Flux”, *Numerical Heat Transfer, Part A*, Vol .21, pp. 313-332.

Bernier, M.A. and Baliga, B.R. (1992b), “A 1-D/2-D Model and Experimental Results for a Closed-Loop Thermosyphon with Vertical Heat Transfer Sections”, *International Journal of Heat and Mass Transfer*, Vol. 35, No. 11, pp. 2969-2982.

Bird, R.B., Armstrong, R.C, Hassager, O. (1987), *Dynamics of Polymeric Liquids, Vol. 1*, 2nd Ed., Wiley, New York.

Bird, R.B., Stewart, W.E. and Lightfoot, E.N. (2002), *Transport Phenomena*, 2nd Ed., John Wiley, New York.

Blevins, R.D. (1984), *Applied Fluid Dynamics Handbook*, Van Nostrand Reinhold Company, New York.

Bouré, J.A. and Delhaye, J.M. (1982), “General Equations and Two-Phase Flow Modeling”, *Handbook of Multiphase Systems*, Section 1.2, G. Hetsroni (Editor), McGraw-Hill Book Company, New York.

Brennen, C.E. (2005), *Fundamentals of Multiphase Flow*, Cambridge University Press, Cambridge, U.K.

Cammarata, L., Fichera, A. and Pagano, A. (2004), “Controlling Natural Convection in a Closed Thermosyphon Using Neural Networks”, *Heat and Mass Transfer*, Vol. 40, pp. 525-531.

Campbell, C.S. (1990), “Rapid Granular Flows”, *Annual Review of Fluid Mechanics*, Vol. 22, pp. 57-92.

Charunyakorn, P., Sengupta, S. and Roy, S.K. (1991), "Forced Convection Heat Transfer in Microencapsulated Phase Change Material Slurries: Flow in Circular Ducts", *Int. J. Heat and Mass Transfer*, Vol. 34, pp. 819-833.

Chen, B., Wang, X., Zeng, R., Zhang, Y., Wang, X., Niu, J., Li, Y. and Di, H. (2008), "An Experimental Study of Convective Heat Transfer with Microencapsulated Phase Change Material Suspension: Laminar Flow in a Circular Tube under Constant Heat Flux", *Experimental Thermal and Fluid Science*, Vol. 32, pp. 1638-1646.

Chhabra, R.P. and Richardson, J.F. (1999), *Non-Newtonian Flow in the Process Industries: Fundamentals and Engineering Applications*, Butterworth-Heinemann, Boston, USA.

Churchill, S.W. and Usagi, R. (1972), "A General Expression for the Correlation of Rates of Transfer and Other Phenomena", *AIChE Journal*, Vol. 18, pp. 1121-1128.

Churchill, S.W. (1977), "A Comprehensive Correlating Equation for Buoyancy-Induced Flow in Channels", *Letters in Heat and Mass Transfer*, Vol. 4, pp. 193-199.

Colvin, D.P. and Mulligan, J.C. (1987), "Microencapsulated phase-change for storage of heat", *NASA Tech Brief MFS-27198*, George C. Marshall Space Flight Center, AL.

Costa, V.A.F., Oliveira, L.A. and Baliga, B.R. (2007), "On First- and Second-Order Mass-Weighted Schemes for Control-Volume Finite Element Methods", *Proc. 5th International Conference on Computational Heat and Mass Transfer*, pp. 378-384, Canmore, Alberta, Canada, June 18-22.

Costa, V.A.F., Oliveira, L.A. and Figueiredo, A.R. (1995), "A Control-Volume-Based Finite Element Method for Three-Dimensional Incompressible Turbulent Fluid Flow, Heat Transfer and Related Phenomena", *Int. J. Numerical Methods in Fluids*, Vol. 21, pp. 591-613.

Cox, R.G. and Mason, S.G. (1971), "Suspended Particles in Fluid Flow through Tubes", *Annual Review of Fluid Mechanics*, Vol. 4, pp. 291-316.

Crapiste, G.H., Rotstein, E. and Whitaker, S. (1973), "General Closure Scheme for the Method of Volume Averaging", *Chemical Engineering Science*, Vol. 41, pp. 227-235.

Crowe, C.T. (1982), "Review – Numerical Models for Dilute Gas-Particle Flows", *ASME Journal of Fluids Engineering*, Vol. 104, pp. 297-303.

Crowe, C.T. (1991), "The State-of-the-Art in the Development of Numerical Models for Dispersed Phase Flows", *Proc. International Conference on Multiphase Flows 1991*, Tsukuba, Japan, pp. 49-60.

Crowe, C.T. (2006), *Multiphase Flow Handbook*, Taylor & Francis, Boca Raton, Florida.

Crowe, C.T., Sommerfeld, M. and Tsuji, Yutaka (1998), "Multiphase Flows with Droplets and Particles", CRC Press, Boca Raton.

Darby, R. (1986), "Hydrodynamics of Slurries and Suspensions", *Encyclopedia of Fluid Mechanics*, Vol. 5, Chapter 2, N.P. Cheremisinoff (Editor), Gulf Publishing Company, Houston, Texas.

Datta, P., Sengupta, S. and Roy, S.K. (1992), "Natural Convection Heat Transfer in an Enclosure with Suspensions of Microencapsulated Phase Change Materials," *ASME-HTD*, *General Papers in Heat Transfer*, Vol. 204, pp. 133-241.

Davis, L.P. and Perona, J.J. (1971), "Development of Free Convection Flow of a Gas in a Heated Vertical Open Tube", *Int. Journal of Heat and Mass Transfer*, Vol. 14, pp. 889-903.

Desrayaud, G, Fichera, A. and Marcoux, M. (2006), "Numerical Investigation of Natural Circulation in a 2D-Annular Closed-Loop Thermosyphon", *Int. Journal of Heat and Fluid Flow*, Vol. 27, pp. 154-166.

Drew, D.A. (1983), "Mathematical Modeling of Two-Phase Flow", *Annual Review of Fluid Mechanics*, Vol. 15, pp. 261-291.

Drew, D.A. and Lahey Jr., R.T. (1993), "Analytical Modeling of Multiphase Flow", *Particulate Two-Phase Flow*, Chapter 16, M.C. Roco (Editor), Butterworth-Heinemann, Boston.

Durst, F., Milojevic, D. and Schönung, B. (1984), "Eulerian and Lagrangian Predictions of Particulate Two-Phase Flows: a Numerical Study", *Appl. Math. Modelling*, Vol. 8, pp. 101-115.

Dyer, J.R. (1975), "The Development of Laminar Natural-Convective Flow in a Vertical Uniform Heat Flux Duct", *Int. J. Heat mass Transfer*, Vol. 18, pp. 1455-1465.

Dyer, J.R. (1978), "Natural-Convective Flow Through a Vertical Duct with a Restricted Entry", *Int. J. Heat Mass Transfer*, Vol. 21, pp. 1341-1354.

Eckert, E.R.G. and Diaguila, A.J. (1954), "Convective Heat Transfer for Mixed, Free and Forced Flow Through Tubes", *Journal of Heat Transfer*, Vol. 76, pp. 497-504.

Eckert, E.R.G. and Drake, R.M. (1972), *Analysis of Heat and Mass Transfer*, McGraw-Hill, New-York.

Einstein, A. (1906), "Eine Neue Bestimmung der Molekül-Dimensionen", *Annalen der Physik*, Vol. 19, pp. 289-306.

Elenbaas, W. (1942a), "Heat Dissipation of Parallel Plates by Free Convection", *Physica*, Vol. 9, pp. 1-28.

Elenbaas, W. (1942b), "The Dissipation of Heat by Free Convection – the Inner Surface of Vertical Tubes of Different Shapes of Cross-Section", *Physica*, Vol. 9, pp. 865-874.

Elkouh, N. and Baliga, B.R. (1995), “Effect of Variable Properties on Natural Convection in Water near its Density Inversion Temperature, *Proc. 30th National Heat Transfer Conference*, Portland, Oregon, August 6-8, HTD-Vol. 33, pp. 53-63.

Fan, L.S. and Zhu, C. (1998), *Principles of Gas-Solid Flows*, Cambridge University Press, Cambridge, U.K.

Fan, Y.F., Zhang, X.X., Wang, X.C., Li, J. and Zhu, Q.B. (2004), “Super-Cooling Prevention of Microencapsulated Phase Change Material”, *Thermochimica Acta*, Vol. 413, pp. 1-6.

Ferguson, J. and Kembłowski, Z. (1991), *Applied Fluid Rheology*, Elsevier, New York.

Ferziger, J.H. and Perić, M. (1999), *Computational Methods for Fluid Dynamics*, 2nd Ed., Springer, New York.

Fichera, A. and Pagano, A. (2002), “Neural Network-Based Prediction of the Oscillating Behaviour of a Closed Loop Thermosyphon”, *Int. Journal of Heat and Mass Transfer*, Vol. 45, pp. 3875- 3884.

Finlayson, B.A. (1972), *The Method of Weighted Residuals and Variational Principles*, Academic Press, New York.

Friedmann, M., Gillis, J. and Liron, N. (1968), “Laminar Flow in a Pipe at Low and Moderate Reynolds Numbers”, *Applied Scientific Research*, Vol. 19, pp. 426-438.

Gaul, L., Kogl, M. and Wagner, M. (2003), *Boundary Element Methods for Engineers and Scientists*, Springer, Berlin, Germany.

Gidaspow, D. (1994), *Multiphase Flow and Fluidization*, Academic Press, Boston.

Goel, M., Roy, S.K. and Sengupta, S. (1994), “Laminar Forced Convection Heat Transfer in Microencapsulated Phase Change Material Suspensions”, *Int. Journal of Heat and Mass Transfer*, Vol. 37, No. 4, pp. 593-604.

Greif, R. (1988), “Natural Circulation Loops”, *ASME J. Heat Transfer*, Vol. 110, pp. 1243-1258.

Gresho, P.M. and Sani, R.L. (2000), *Incompressible Flow and the Finite Element Method: Volume 2, Isothermal Laminar Flow*, John Wiley & Sons, New York.

Gupta, S.N. and Mishra, P. (1975), “Isothermal Laminar Flow of Non-Newtonian Fluids through Helical Coils”, *Indian Journal of Technology*, Vol. 13, pp. 245.

Haar, L., Gallagher, J.S. and Kell, G.S. (1984), *NBS/NRC Steam Tables: Thermodynamic and transport properties and computer programs for vapor and liquid states of water in SI units*, Taylor & Francis, Washington DC..

Haider, S.I. and Nakayama, W. (2002), "A Natural Circulation Model of the Closed Loop, Two-Phase Thermosyphon for Electronics Cooling", *ASME Journal of Heat Transfer*, Vol. 124, pp. 881-890.

Hallman, T.M. (1958), "Combined Forced and Free Convection in a Vertical Tube", *Ph.D. Thesis*, Purdue University.

Harlow, F.H. and Welch, J.E. (1965), "Numerical Calculation of Time-Dependent Viscous Incompressible Flow of Fluid with Free Surface", *Phys. Fluids*, Vol. 8, pp. 2182-2189.

Hartnett, J.P., Irvine, T.F. and Cho, Y.I. (1964 – 2010), *Advances in Heat Transfer*, Vols. 1-42.

Ho, C.J. (2004), "A Continuum Model for Transport Phenomena in Convective Flow of Solid-Liquid Phase Change Material Suspensions", *Applied Mathematical Modelling*, Vol. 29, No. 9, pp. 805-817.

Ho, C.J., Chiu, S.Y. and Lin, J.F. (2005), "Heat Transfer Characteristics of a Rectangular Natural Circulation Loop Containing Solid-Liquid Phase-Change Material Suspensions", *Int. Journal of Numerical Methods for Heat & Fluid Flow*, Vol. 15, No. 5, pp. 441-461.

Ho, C.J., Huang, J.B., Tsai, P.S. and Yang, Y.M. (2010), "Preparation and Properties of Hybrid Water-Based Suspension of Al_2O_3 Nanoparticles and MEPCM Particles as Functional Forced Convection Fluid", *Int. Communications in Heat and Mass Transfer*, Vol. 37, pp. 490-494.

Holman, J.P. (2011), *Experimental Methods for Engineers*, 8th Ed., McGraw-Hill, New York.

Hu, X. and Zhang, Y. (2002), "Novel Insight and Numerical Analysis of Convective Heat Transfer Enhancement with Microencapsulated Phase Change Material Slurries: Laminar Flow in a Circular Tube with Constant Heat Flux", *Int. Journal of Heat and Mass Transfer*, Vol. 45, pp. 3163-3172.

Hsu, C.F. and Patankar, S.V. (1982), "Analysis of Laminar Non-Newtonian Flow and Heat Transfer in Curved Tubes", *AIChE Journal*, Vol. 28, pp. 610-616.

Inaba, H. (2000), "New Challenge in Advanced Thermal Energy Transportation Using Functionally Thermal Fluids", *Int. Journal of Thermal Science*, Vol. 39, pp. 991-1003.

Inaba, H., Kim, M.J. and Horibe, A. (2004), "Melting Heat Transfer Characteristics of Microencapsulated Phase Change Material Slurries with Plural Microcapsules Having Different Diameters", *ASME J. Heat Transfer*, Vol. 126, pp. 558-565.

Incropera, F.P. and DeWitt, D.P. (2002), *Fundamentals of Heat and Mass Transfer*, 5th Ed., John Wiley and Sons, New York.

Japikse, D. (1973), "Advances in Thermosyphon Technology", *Advances in Heat Transfer*, Vol. 9, pp. 1-111.

Jeffrey, D.J. and Acrivos, A. (1976), "The Rheological Properties of Suspensions of Rigid Particles", *AIChE Journal*, Vol. 22, pp. 417-432.

Jiang, T.S., Kim, M.H., Kremesec Jr., V.J. and Slattery, J.C. (1986), "The Local Volume-Averaged Equations of Motion for a Suspension of Non-Neutrally Buoyant Spheres", *Chem. Eng. Comm.*, Vol. 50, pp. 1-30.

Johnson, P.C. and Jackson, R. (1987), "Frictional-Collisional Equations of Motion for Particulate Flows with Applications to Chutes and Shear Cells", *Journal of Fluid Mechanics*, Vol. 176, pp. 67-93.

Kakac, S., Shah, R.K. and Aung, W. (1987), *Handbook of Single-Phase Convective Heat Transfer*, Wiley, New York.

Karniadakis, G. and Sherwin, S.J. (2005), *Spectral/hp Element Method for Computational Fluid Dynamics*, 2nd Ed., Oxford University Press, Oxford, U.K.

Karnis, A., Goldsmith, H.L. and Mason, S.G. (1966), "The Flow of Suspensions Through Tubes V. Inertial Effects", *Canadian Journal of Chemical Engineering*, Vol. 44, pp. 181-193.

Katz, L. (1967), "Natural Convection Heat Transfer with Fluids using Suspended Particles which Undergo Phase Change", *Ph.D. Thesis*, Massachusetts Institute of Technology, Cambridge, MA.

Kaviany, M. (2001), *Principles of Convective Heat Transfer*, 2nd Ed., Mechanical Engineering Series, Springer-Verlag, New York.

Kays, W.M. and Crawford, M.E. (1993), *Convective Heat and Mass Transfer*, 3rd Ed., McGraw-Hill, New York.

Kays, W.M. and London, A.L. (1964), *Compact Heat Exchangers*, 2nd Ed., McGraw-Hill, New York.

Kays, W.M. and Perkins, H.C. (1973), "Forced Convection, Internal Flow in Ducts", *Handbook of Heat Transfer*, W.M. Rohsenow and J. P. Hartness (Editors), Section 7, pp. 7-1 to 7-193.

Kline, S.J. and McClintock, F.A. (1953), "Describing Uncertainties in Single-Sample Experiments", *Mechanical Engineering*, January 1953, pp. 3-8.

Krieger, J.M. (1972), "Rheology of Monodisperse Lattices", *Advances in Colloid and Interface Science*, Vol. 3, pp. 111-136.

Krieger, J.M. and Dougherty, T.J. (1959), "A Mechanism for Non-Newtonian Flow in Suspensions of Rigid Spheres", *Trans. Soc. Rheol.*, *Journal of Rheology*, Vol. 3, pp. 137-152.

Küçüka, S. and Başaran, T. (2007), “Laminar Flow Modelling of a Thermosyphon Loop at Specified Wall Temperatures”, *Heat and Mass Transfer*, Vol. 43, pp. 1293-1302.

Lagana, A. (1997), “Mixed Convection Heat Transfer in Vertical, Horizontal and Inclined Pipes”, *M.Sc. Thesis*, McGill University, Montreal, Quebec, Canada.

Lamoureux, A. and Baliga, B.R. (2011), “Improved Formulations of the Discretized Pressure Equation and Boundary Treatments in Co-Located Equal-Order Control-Volume Finite-Element Methods for Incompressible Fluid Flow”, *Numerical Heat Transfer Part B: Fundamentals*, Vol. 59, pp. 442-472.

Leal, L.G. (1973), “On the Effective Conductivity of Dilute Suspensions of Spherical Drops in the Limit of Low Particle Peclet Numbers”, *Chemical Engineering Communications*, Vol. 1, pp. 21-31.

Leblanc, G.E., Secco, R.A. and Kostic, M. (1998), “Viscosity Measurements”, in John G. Webster (Editor), *The Measurement, Instrumentation and Sensors Handbook*, Chapter 30, CRC Press, Boca Raton.

Lee, W.S., Chen, B.R. and Chen, S.L. (2006), “Latent Heat Storage in a Two-Phase Thermosyphon Solar Water Heater”, *J. Solar Energy Engineering*, Vol. 128, pp. 69-76.

Liang, S.F., Vidal. A. and Acrivos, A. (1969), “Buoyancy-Driven Convection in Cylindrical Geometries”, *Journal of Fluid Mechanics*, Vol. 36, Part 2, pp. 239-256.

Masson, C. (1993), “Numerical Prediction of Gas-Solid Particle Flows over a Wide Range of Concentration in Irregular Geometries”, *Ph.D. Thesis*, McGill University, Montreal, Quebec, Canada.

Masson, C. and Baliga, B.R. (1994), “A Control-Volume Finite Element Method for Dilute Gas-Solid Particle Flows”, *Computers & Fluids*, Vol. 23, No. 8, pp. 1073-1096.

Masson, C., Saabas, H.J. and Baliga, B.R. (1994), “Co-Located Equal-Order Control-Volume Finite Element Method for Two-Dimensional Axisymmetric Incompressible Fluid Flow”, *International Journal for Numerical Methods in Fluids,* Vol. 18, pp. 1-26.

Masson, C. and Baliga, B.R. (1998), “Simulation of Gas-Solid Particle Flows over a Wide Range of Concentration”, *Int. Journal for Numerical Methods in Fluids*, Vol. 28, pp. 1441-1479.

Maude, A.D. and Whitmore, R.L. (1958), “A Generalized Theory of Sedimentation”, *British Journal of Applied Physics*, Vol. 9, pp. 477-482.

Maxwell, J. C. (1954), *A Treatise on Electricity and Magnetism*, 3rd Ed., Vol. 1, Dover Publications Inc., New York.

Maydanik, Y.F. (2005), “Loop Heat Pipes”, *Appl. Thermal Eng.*, Vol. 25, pp. 635-657.

Metais, B. and Eckert, E.R.G. (1964), “Forced, Mixed and Free Convection Regimes”, *Journal of Heat Transfer*, Vol. 86, pp. 295-296.

Metzner, A.B. and Reed, J.C. (1955), “Flow of Non-Newtonian Fluids – Correlations of the Laminar, Transition and Turbulent-flow Regions”, *A.I.Ch.E. Journal*, Vol. 1, pp. 434-440.

Minkowycz, W.J. and Sparrow, E.M. (1997), *Advances in Numerical Heat Transfer*, Vol. 1, Taylor and Francis, Washington D.C.

Minkowycz, W.J. and Sparrow, E.M. (2000), *Advances in Numerical Heat Transfer*, Vo. 2, Taylor and Francis, Washington D.C.

Minkowycz, W.J., Sparrow, E.M. and Murthy, J.Y. (2006), *Handbook of Numerical Heat Transfer*, 2nd Ed., John Wiley & Sons, New York.

Mooney, M. (1951), “The Viscosity of a Concentrated Suspension of Spherical Particles”, *Journal of Colloid Science*, Vol. 6, pp. 161-170.

Mudawar, I. (2003), “Assessment of High-Heat-Flux Thermal Management Schemes”, *Proc. Rohsenow Symposium on Future Trends in Heat Transfer*, MIT, Massachusetts, U.S.A.

Mulligan, J.C., Colvin, D.P. and Bryant, Y.G. (1996), “Microencapsulated Phase-Change Material Suspensions for Heat Transfer in Spacecraft Thermal Systems”, *Journal of Spacecraft and Rockets*, Vol. 33, No. 2, pp. 278-284.

Murthy, J.Y., Minkowycz, W.J., Sparrow, E.M. and Mathur, S.R. (2006), “Survey of Numerical Methods”, in J.W. Minkowycz, E.M. Sparrow, and J.Y. Murthy (Editors), *Handbook of Numerical Heat Transfer*, 2nd Ed., Chap. 1, John Wiley & Sons, New York.

Na, M.K., Jeon, J.S. and Kwak, H.Y. (2001), “Experimental Study on Closed-Loop Two-Phase Thermosyphon Devices for Cooling MCMs”, *Heat Transfer Engineering*, Vol. 22, pp. 29-39.

Naterer, G.F. (2003), “Heat Transfer in Single and Multiphase Systems”, CRC Press, Boca Raton.

Nir, A. and Acrivos, A. (1974), “Experiments on the Effective Viscosity of Concentrated Suspensions of Solid Spheres”, *Int. Journal of Multiphase Flow*, Vol. 1, pp. 373-381.

Nir, A. and Acrivos, A. (1976), “The Effective Thermal Conductivity of Sheared Suspensions”, *Journal of Fluid Mechanics*, Vol. 78, pp. 33-48.

Oosthuizen, P.H. and Naylor, D. (1999), *An Introduction to Convective Heat Transfer Analysis*, McGraw-Hill, New York.

Ottino, J.M. and Khakhar, D.V. (2000), “Mixing and Segregation of Granular Materials”, *Annual Review of Fluid Mechanics*, Vol. 32, pp. 55-91.

Parent, M.G., Van Der Meer, T.H. and Hollands, K.G.T. (1990), "Natural Convection Heat Exchangers in Solar Water Heating Systems: Theory and Experiment", *Solar Energy*, Vol. 45, pp. 43-52.

Patankar, S.V. (1980), *Numerical Heat Transfer and Fluid Flow*, Hemisphere, Washington, D.C.

Patankar, S.V. and Spalding, D.B. (1972), "A Calculation Procedure for Heat, Mass, and Momentum Transfer in Three-Dimensional Parabolic Flows", *Int. J. Heat Mass Transfer*, Vol. 15, pp. 1767-1806.

Peyret, R. (2002), *Spectral Methods for Incompressible Viscous Flow*, Springer, Berlin, Germany.

Prakash, C. and Patankar, S.V. (1985), "A Control-Volume-Based Finite-Element Method for Solving the Navier-Stokes Equations Using Equal-order Velocity-Pressure Interpolation", *Numerical Heat Transfer*, Vol. 8, pp. 259-280.

Press, W.H., Teukolsky, S.A., Vetterling, W.T., and Flannery, B.P. (1992), *Numerical Recipes in FORTRAN*, 2nd Ed., Cambridge University Press, U.K., pp. 678-683.

Raithby, G.D. (1976), "Skew Upstream Differencing Schemes for Problems Involving Fluid Flow", *Comp. Methods in Applied Mechanics and Engineering*, Vol. 9, pp. 153-164.

Raithby, G.D. and Hollands, K.G.T. (1975), "A General Method of Obtaining Approximate Solutions to Laminar and Turbulent Free Convection Problems", *Advances in Heat Transfer*, Vol. 11, Academic Press, New York, pp. 264-315.

Raithby, G.D. and Hollands, K.G.T. (1985), "Natural Convection", *Handbook of Heat Transfer Fundamentals*, W.M. Rohsenow, J.P. Hartnett and E.N. Ganic (Editors), McGraw-Hill, New York.

Reddy, J.N. and Gartling, D.K. (1994), *The Finite Element Method in Heat Transfer and Fluid Dynamics*, CRC Press, Boca Raton, Florida.

Rhie, C.M. and Chow, W.L. (1983), "Numerical Study of the Turbulent Flow Past an Airfoil with Trailing Edge Separation", *AIAA Journal*, Vol. 21, pp. 1525-1532.

Richardson L.F. (1910), The Approximate Arithmetical Solution by Finite Differences of Physical Problems Involving Differential Equations with Application to a Masonry Dam, *Transc. Royal Society of London*, Series A, Vol. 210, pp. 307-357.

Roache, P.J. (1998), *Fundamentals of Computational Fluid Dynamics*, Hermosa Publishers, Albuquerque, New Mexico.

Rohsenow, W.M., Harnett, J.P. and Cho, Y.I. (1998), *Handbook of Heat Transfer*, 3rd Ed., McGraw-Hill, New York.

Roy, S.K. and Avanic, B.L. (2001), "Turbulent Heat Transfer with Phase Change Material Suspensions", *Int. Journal of Heat and Mass Transfer*, Vol. 44, pp. 2277-2285.

Roy, S.K. and Sengupta, S. (1991), "An Evaluation of Phase Change Microcapsules for Use in Enhanced Heat Transfer Fluids", *Int. Communications of Heat and Mass Transfer*, Vol. 18, pp. 495-507.

Saabas, H.J. and Baliga, B.R. (1994), "A Co-located Equal-Order Control-Volume Finite Element Method for Multidimensional, Incompressible Fluid Flow, Part I: Formulation", *Numerical Heat Transfer*, Part B, Vol. 26, pp. 381-407.

Savage, S.B. (1984), "The Mechanics of Rapid Granular Flows," *Advances in Applied Mechanics*, Vol. 24, pp. 289-366.

Savage, S.B. (1998), "Analyses of Slow High-Concentration Flows of Granular Materials", *Journal of Fluid Mechanics*, Vol. 377, pp. 1-26.

Schaflinger, U. (Editor) (1966), "Flow of Particles in Suspensions", *International Centre for Mechanical Sciences* – Courses and Lectures, No. 370, Springer Wien, New York.

Schneider, G.E. and Raw, M.J. (1986), "A Skewed, Positive Influence Coefficient Upwinding Procedure for Control-Volume-Based-Finite-Element Convection-Diffusion Computation", *Numerical Heat Transfer*, Vol. 9, pp. 1-26.

Scott, D.A. (2006), "Heat Transfer in Pipes Conveying Slurries of Microencapsulated Phase-Change Materials in Water", *Ph.D. Thesis*, McGill University, Montreal, Canada.

Scott, D.A., Lamoureux, A. and Baliga, B.R. (2010), "Computational Investigation of Laminar Mixed Convection in a Vertical Pipe with Slurries of a Microencapsulated Phase-Change Material in Distilled Water", *Proc. 2010 ASME International Heat Transfer Conference (IHTC-14)*, Washington, D.C., pp. 1-12.

Shah, R.K. (1975), "Thermal Entry Length Solutions for the Circular Tube and Parallel Plates", *Proc. 3rd National Heat and Mass Transfer Conference*, Indian Inst. Technol., Bombay, Vol. 1, paper No. HMT-11-75.

Shah, R.K. and London, A.L. (1978), "Laminar Flow Forced Convection in Ducts", *Advances in Heat Transfer, Supplement 1*, Academic Press, New York.

Shilei, L., Guohui, F., Neng, Z. and Li, D. (2007), "Experimental Study and Evaluation of Latent Heat Storage in Phase Change Material Wallboards", *Energy & Bldg.*, Vol. 39, pp. 1088-1091.

Sieder, E.N. and Tate, G.E. (1936), "Heat Transfer and Pressure Drop of Liquids in Tubes", *Industrial and Engineering Chemistry*, Vol. 28, No. 12, pp. 1429-1434.

Sinton, D.A. and Baliga, B.R. (2003), “Computational Modelling of Continuous Casting”, *Proc. 2003 ASME International Mechanical Engineering Congress & Exposition (IMECE’03)*, Paper No. IMECE2003-43967, Washington, D.C., pp. 1-13.

Slattery, J.C. (1981), *Momentum, Energy and Mass Transfer in Continua*, 2nd Ed., Krieger, Huntington, N.Y.

Sohn, C.W. and Chen, M.M. (1981), “Microconvective Thermal Conductivity in Disperse Two-Phase Mixtures as Observed in a Low Velocity Couette Flow Experiment”, *Journal of Heat Transfer*, Vol. 103, pp. 47-51.

Sommerfeld, M. and Huber, N. (1999), “Experimental Analysis and Modelling of Particle-Wall Collisions”, *Int. Journal of Multiphase Flows*, Vol. 25, pp. 1457-1489.

Spalding, D.B. (1972), “A Novel Finite-Difference Formulation for Differential Expressions Involving Both First and Second Derivatives”, *Int. J. Numerical Methods in Engineering*, Vol. 4, pp. 551-559.

Spalding, D.B. (1978), “Numerical Computation of Multiphase Flows”, Workshop lecture notes, Purdue University.

Stein, H.N. (1986), “Rheological Behavior of Suspensions”, *Encyclopedia of Fluid Mechanics*, Chapter 1, N.P. Cheremisinoff (Editor), Gulf Publishing Company, Houston, Texas, pp. 3-48.

Stewart, H.B. and Wendroff, B. (1984), “Two-Phase Flow: Models and Methods”, *Journal of Computational Physics*, Vol. 56, pp. 363.

Tannehill, J.C., Anderson, D.A., and Pletcher, R.H. (1997), *Computational Fluid Mechanics and Heat Transfer*, 2nd Ed., Taylor and Francis, Washington D.C.

Tavoularis, J.P. (2005), *Measurements in Fluid Mechanics*, Cambridge University Press, Cambridge, U.K.

Tran, L.D., Masson, C. and Smaïli, A. (2006), “A Stable Second-Order Mass-Weighted Upwind Scheme for Unstructured Meshes”, *Int. J. Numerical Methods in Fluids*, Vol. 51, pp. 749-771.

Vand, V. (1945), “Theory of Viscosity of Concentrated Suspensions”, *Nature*, Vol. 155, pp. 364-365.

Venditti, D.A. (1998), “An h-Adaptive Control-Volume Finite Element Method for Steady, Two-Dimensional Fluid Flow and Heat Transfer”, *M. Eng. Thesis*, McGill University, Montreal, Quebec, Canada.

Venditti, D.A. and Baliga, B.R. (1998), “An h-Adaptive Strategy for CVFEM Simulations of Viscous Incompressible Flow”, *Proc. 6th Annual Conference of the Computational Fluid Dynamics Society of Canada (CFD 98)*, pp. VIII-65-VIII-70, Quebec City, Canada.

Wang, M., Tsuji, T. and Nagano, Y. (1994), "Mixed Convection with Flow Reversal in the Thermal Entrance Region of Horizontal and Vertical Pipes", *Int. J. Heat Mass Transfer*, Vol. 37, No. 15, pp. 2305-2319.

Wang, X., Niu, J., Li, Y., Wang, X., Chen, B., Zeng, R., Song, Q. and Zhang, Y. (2007), "Flow and Heat Transfer Behaviors of Phase Change Material Slurries in a Horizontal Circular Tube", *Int. Journal of Heat and Mass Transfer*, Vol. 50, pp. 2480-2491.

Wang, X., Niu, J., Li, Y., Zhang, Y., Wang., X., Chen, B., Zeng, R. and Song, Q. (2008), "Heat Transfer of Microencapsulated PCM Slurry Flow in a Circular Tube", *AIChE Journal*, Vol. 54, pp. 1110-1120.

Wang, X., Zhang, Y. and Hu, X. (2004), "Turbulent Heat Transfer Enhancement of Microencapsulated Phase Change Material Slurries with Constant Wall Heat Flux", *Journal of Enhanced Heat Transfer*, Vol. 11, pp. 13-22.

Whitaker, S. (1973), "The Transport Equations for Multi-Phase Systems", *Chemical Engineering Science*, Vol. 29, pp. 139-147.

Whitaker, S. (1999), *The Method of Volume Averaging*, Kluwer, Dordrecht, Netherlands.

White, F. M. (1991), *Viscous Fluid Flow*, McGraw-Hill, New York.

White, F. M. (1998), *Fluid Mechanics*, 4th Ed., McGraw-Hill College, New York.

Yamagishi, Y., Sugeno, T., Takashi, I., Tkeuchi, H. and Pyatenko, A.T. (1996), "An Evaluation of Microencapsulated PCM for Use in Cold Energy Transportation Medium", *Proc. IECEC*, Washington DC, pp. 2077-2083.

Yamagishi, Y., Takeuchi, H., Pyatenko, A.T. and Kayukawa, N. (1999), "Characteristics of Microencapsulated PCM Slurry as a Heat-Transfer Fluid", *AIChE J.*, Vol. 45, pp. 696-707.

Yang, R., Xu, H. and Zhang, Y. (2003), "Preparation Physical Property and Thermal Physical Property of Phase Change Microcapsule Slurry and Phase-Change Emulsions", *Solar Energy Materials & Solar Cells*, Vol. 80, pp. 405-416.

Yovanovich, N.M., Teertstra, P. and Muzychka, Y.S. (2002), "Natural Convection Inside Vertical Isothermal Ducts of Constant Arbitrary Cross Section", *Journal of Thermophysics and Heat Transfer*, Vol. 16, pp. 116-121.

Zeldin, B. and Schmidt, F.W. (1972), "Developing Flow with Combined Forced-Free Convection in an Isothermal Vertical Tube", *Journal of Heat Transfer*, Vol. 94, pp. 211-223.

Zhang, H., Wang, X. and Wu, D. (2010), “Silica Encapsulation of n-Octadecane Via Sol-Gel Process: a Novel Microencapsulated Phase-Change Material with Enhanced Thermal Conductivity and Performance”, *Journal of Colloid and Interface Science*, Vol. 343, pp. 246-255.

Zhang, Y. and Faghri, A. (1995), “Analysis of Forced Convection Heat Transfer in Microencapsulated Phase Change Material Suspensions”, *J. Thermophysics and Heat Transfer*, Vol. 9, pp. 727-732.

Zhang, Y., Hu, X. and Wang, X. (2003), “Theoretical Analysis of Convective Heat Transfer Enhancement of Microencapsulated Phase Change Material Slurries”, *Heat and Mass Transfer*, Vol. 40, pp. 59-66.

Zienkiewicz, O.C. and Taylor, R.L. (2000a), *Finite Element Method: Volume 2, Fluid Dynamics*, 5th Ed., Butterworth-Heinemann, Elsevier, New York.

Zienkiewicz, O.C. and Taylor, R.L. (2000b), *The Finite Element Method: Volume 3, Fluid Dynamics*, 5th Ed., McGraw-Hill, London.

Zimmels, Y. (1986), “Accelerated and Steady Particle Flows in Newtonian Fluids”, *Encyclopedia of Fluid Mechanics*, Vol. 5, Chapter 3, N.P. Cheremisinoff (Editor), Gulf Publishing Company, Houston, Texas, pp. 93-117.

Zvirin, Y. (1981), “A Review of Natural Circulation Loops in Pressurized Water Reactors and Other Systems”, *Nuclear Engineering and Design*, Vol. 67, pp. 203-225.

Appendix A: Thermophysical Properties of Water

The correlations presented in this Appendix were used to evaluate the thermophysical properties of water. These correlations were obtained by using the least-squares technique to fit polynomial functions to reference data found in the published literature. The curve fits presented below can be used to calculate the thermophysical properties of water for temperatures between 5ºC to 55ºC.

The correlated density data was taken from the NBS/NRC Steam Tables [Haar et al. (1984)]. The absolute maximum relative difference between the density values predicted by the curve fit and the reference data was 0.035%. The reference data used to obtain the curve fits for the thermal conductivity, the dynamic viscosity, and the specific heat were taken from Incropera and DeWitt (2002). The absolute maximum relative differences between the values predicted by the curve fits and the reference data were 0.2%, 1%, and 0.1% for the thermal conductivity, dynamic viscosity, and specific heat of water, respectively.

In the following correlations, T is expressed in ºC.

Density, ρ_{H_2O} [in kg/m^3]:

$$\rho_{H_2O} = 1000.6 - 4.2086\text{x}10^{-2}\,T - 4.1413\text{x}10^{-3}\,T^2$$

Thermal conductivity, k_{H_2O} [in W/mºC]:

$$k_{H_2O} = 0.5694 + 1.829\text{x}10^{-3}\,T - 7.053\text{x}10^{-6}\,T^2$$

Dynamic viscosity, μ_{H_2O} [in kg/m-s]:

$$\mu_{H_2O} = 1.700\text{x}10^{-3} - 4.624\text{x}10^{-5}\,T + 6.427\text{x}10^{-7}\,T^2 - 3.566\text{x}10^{-9}\,T^3$$

Specific heat, c_{p,H_2O} [in J/kgºC]:

$$c_{p,H_2O} = 4211.0 - 2.313T + 4.953\text{x}10^{-2}\,T^2 - 3.007\text{x}10^{-4}\,T^3$$

Appendix B: Effective Thermophysical Properties of MCPCM Particles and Slurries

Density, ρ_s*:*

The effective density of the MCPCM slurries is evaluated using Eq. (3.2):

$$\frac{1}{\rho_s} = \frac{\phi}{\rho_{MCPCM}} + \frac{(1-\phi)}{\rho_{H_2O}}$$

In this equation, the density of water ρ_{H_2O} is obtained using the correlation presented in Appendix A. The effective density of the MCPCM particles is calculated using Eq. (3.4) and Eq. (3.5), where T is in ºC and ρ_{MCPCM} in kg/m^3:

Monotonic heating (melting) process:

For $5\,^{\circ}\mathrm{C} \le T \le 25.9\,^{\circ}\mathrm{C}$:
$$\rho_{MCPCM} = -6.157\text{x}10^{-2}T^2 - 1.564\text{x}10^{-1}T + 9.717\text{x}10^2$$
For $25.9\,^{\circ}\mathrm{C} < T \le 29.85\,^{\circ}\mathrm{C}$:
$$\rho_{MCPCM} = 2.083T^3 - 1.739\text{x}10^2T^2 + 4.812\text{x}10^3T - 4.3256\text{x}10^4$$
For $29.85\,^{\circ}\mathrm{C} < T \le 55\,^{\circ}\mathrm{C}$:
$$\rho_{MCPCM} = 3.977\text{x}10^{-3}T^2 - 1.258T + 8.876\text{x}10^2$$

Monotonic cooling (freezing) process:

For $5\,^{\circ}\mathrm{C} \le T \le 18.05\,^{\circ}\mathrm{C}$:
$$\rho_{MCPCM} = -6.157\text{x}10^{-2}T^2 - 1.564\text{x}10^{-1}T + 9.717\text{x}10^2$$
For $18.05\,^{\circ}\mathrm{C} < T \le 19.21\,^{\circ}\mathrm{C}$:
$$\rho_{MCPCM} = 1.049\text{x}10^2T^3 - 5.868\text{x}10^3T^2 + 1.092\text{x}10^5T - 6.7582\text{x}10^5$$
For $19.21^{\circ}\mathrm{C} < T \le 55\,^{\circ}\mathrm{C}$:
$$\rho_{MCPCM} = 3.977\text{x}10^{-3}T^2 - 1.258T + 8.876\text{x}10^2$$

Thermal conductivity, k_s *:*

The effective thermal conductivity of the MCPCM slurries is evaluated using Maxwell's equation [Eq. (3.6)]:

$$\frac{k_s}{k_{H_2O}} = \frac{2k_{H_2O} + k_{MCPCM} + 2\varphi\left(k_{MCPCM} - k_{H_2O}\right)}{2k_{H_2O} + k_{MCPCM} - \varphi\left(k_{MCPCM} - k_{H_2O}\right)}$$

In this equation, φ denotes the volume concentration of the MCPCM particles, which can be computed using Eq. (3.7):

$$\varphi = \phi\left(\frac{\rho_s}{\rho_{MCPCM}}\right)$$

The value of k_{H_2O} is evaluated using the correlation iven in Appendix A, and k_{MCPCM} is determined by adapting the results of Scott (2006), as follows [see. Eqs. (3.9) and (3.10)]:

Monotonic heating (melting) process:

For $5\,^{\circ}\mathrm{C} \le T \le 28.64\,^{\circ}\mathrm{C}$:
$k_{MCPCM} = 0.171\,\mathrm{W/m°C}$
For $28.64\,^{\circ}\mathrm{C} < T \le 55\,^{\circ}\mathrm{C}$:
$k_{MCPCM} = 0.097\,\mathrm{W/m°C}$

Monotonic cooling (freezing) process:

For $5\,^{\circ}\mathrm{C} \le T \le 18.06\,^{\circ}\mathrm{C}$:
$k_{MCPCM} = 0.171\,\mathrm{W/m°C}$
For $18.06\,^{\circ}\mathrm{C} < T \le 55\,^{\circ}\mathrm{C}$:
$k_{MCPCM} = 0.097\,\mathrm{W/m°C}$

Dynamic viscosity, μ_s:

The effective dynamic viscosity of the MCPCM slurries studied in this work obeys a power-law behavior and is calculated with the following relation [see Eq. (3.15)]:

$$\eta_s = \frac{\mu_s}{\mu_{H_2O}} = m\,\dot{\gamma}^{n-1}$$

In this equation, n is the flow behaviour index, m is the relative consistency index (with respect to water), and $\dot{\gamma}$ represents the magnitude of the local rate of strain. The dynamic viscosity of water, μ_{H_2O}, is evaluated using the correlation given in Appendix A. The values of n and m are computed using Eqs. (3.22) and (3.23), as follows (n is dimensionless and m is expressed in s^{n-1}):

$$n = -1.132\text{x}10^3\phi^4 + 3.979\text{x}10^2\phi^3 - 4.068\text{x}10^1\phi^2 + 1$$

$$m = 1.297\text{x}10^3\phi^3 + 7.451\text{x}10^2\phi^2 + 7.044\text{x}10^1\phi + 1$$

Lastly, for two-dimensional axisymmetric flows, the magnitude of the local rate of strain is computed using Eq. (3.24):

$$\dot{\gamma} = \sqrt{\frac{1}{2}\left[2\left(\frac{\partial v}{\partial z} + \frac{\partial w}{\partial r}\right)^2 + 4\left(\frac{v}{r}\right)^2 + 4\left(\frac{\partial v}{\partial r}\right)^2 + 4\left(\frac{\partial w}{\partial z}\right)^2\right]}$$

Specific heat, $c_{p,MCPCM}$ *:*

The effective specific heat of the MCPCM slurries, $c_{p,s}$, is calculated using Eq. (3.11), as follows:

$$c_{p,s} = \phi c_{p,MCPCM} + (1-\phi) c_{p,H_2O}$$

The specific heat of water is evaluated using the correlation given in Appendix A. The effective specific heat of the MCPCM particles is calculated using the correlations given in Eqs. (3.13) and (3.14), where $c_{p,MCPCM}$ is in kJ/kg°C and *T* is in °C:

Monotonic heating (melting) process:

$$\begin{aligned}
&\text{For } 5\,^{\circ}\text{C} \le T \le 20\,^{\circ}\text{C}:\\
&c_{p,MCPCM} = 2.442\text{x}10^{-6}(T-5)^5 - 6.210\text{x}10^{-5}(T-5)^4\\
&\qquad +8.517\text{x}10^{-4}(T-5)^3 - 1.982\text{x}10^{-3}(T-5)^2\\
&\qquad +4.451\text{x}10^{-2}(T-5) + 2.016\\
&\text{For } 20\,^{\circ}\text{C} < T \le 27\,^{\circ}\text{C}:\\
&c_{p,MCPCM} = 2.726\text{x}10^{-3}(T-20)^5 - 1.925\text{x}10^{-2}(T-20)^4\\
&\qquad +6.910\text{x}10^{-2}(T-20)^3 - 4.970\text{x}10^{-2}(T-20)^2\\
&\qquad +4.556\text{x}10^{-1}(T-20) + 3.823\\
&\text{For } 27\,^{\circ}\text{C} < T \le 28.66\,^{\circ}\text{C}:\\
&c_{p,MCPCM} = 1.037(T-27)^2 + 1.740\text{x}10^{1}(T-27) + 27.87\\
&\text{For } 28.66\,^{\circ}\text{C} < T \le 28.72\,^{\circ}\text{C}:\\
&c_{p,MCPCM} = -4.164\text{x}10^{2}(T-28.66)^2 + 2.582\text{x}10^{1}(T-28.66)\\
&\qquad +59.60\\
&\text{For } 28.72\,^{\circ}\text{C} < T \le 28.9\,^{\circ}\text{C}:\\
&c_{p,MCPCM} = -2.951\text{x}10^{2}(T-28.72) + 59.65\\
&\text{For } 28.9\,^{\circ}\text{C} < T \le 29.1\,^{\circ}\text{C}:\\
&c_{p,MCPCM} = 3.079\text{x}10^{2}(T-28.9)^4 - 4.791\text{x}10^{2}(T-28.9)^3\\
&\qquad +2.741\text{x}10^{2}(T-28.9)^2 - 6.245\text{x}10^{1}(T-28.9)\\
&\qquad +6.533\\
&\text{For } 29.1\,^{\circ}\text{C} < T \le 55\,^{\circ}\text{C}:\\
&c_{p,MCPCM} = 1.620\text{x}10^{-3}(T-29.1) + 1.668
\end{aligned}$$

Monotonic cooling (freezing) process:

$$
\begin{aligned}
&\text{For } 5\,^{\text{o}}\text{C} \le T \le 15\,^{\text{o}}\text{C}:\\
c_{p,MCPCM} &= 2.442\text{x}10^{-6}\left(T-5\right)^5 - 6.210\text{x}10^{-5}\left(T-5\right)^4\\
&\quad +8.517\text{x}10^{-4}\left(T-5\right)^3 - 1.982\text{x}10^{-3}\left(T-5\right)^2\\
&\quad +4.451\text{x}10^{-2}\left(T-5\right) + 2.016
\end{aligned}
$$

$$
\begin{aligned}
&\text{For } 15^{\text{o}}\,\text{C} < T \le 16.35\,^{\text{o}}\text{C}:\\
c_{p,MCPCM} &= 1.609\text{x}10^{1}\left(T-15\right)^5 - 3.072\text{x}10^{1}\left(T-15\right)^4\\
&\quad +2.053\text{x}10^{1}\left(T-15\right)^3 - 3.719\left(T-15\right)^2\\
&\quad +6.414\text{x}10^{-1}\left(T-15\right) + 2.738
\end{aligned}
$$

$$
\begin{aligned}
&\text{For } 16.35\,^{\text{o}}\text{C} < T \le 16.9\,^{\text{o}}\text{C}:\\
c_{p,MCPCM} &= -4.900\text{x}10^{2}\left(T-16.35\right)^3 + 4.763\text{x}10^{2}\left(T-16.35\right)^2\\
&\quad +5.861\text{x}10^{1}\left(T-16.35\right) + 17.41
\end{aligned}
$$

$$
\begin{aligned}
&\text{For } 16.9\,^{\text{o}}\text{C} < T \le 17.3\,^{\text{o}}\text{C}:\\
c_{p,MCPCM} &= 1.612\text{x}10^{2}\left(T-16.9\right)^4 + 3.276\text{x}10^{2}\left(T-16.9\right)^3\\
&\quad -5.434\text{x}10^{2}\left(T-16.9\right)^2 + 1.752\text{x}10^{2}\left(T-16.9\right)\\
&\quad +1.122\text{x}10^{2}
\end{aligned}
$$

$$
\begin{aligned}
&\text{For } 17.3\,^{\text{o}}\text{C} < T \le 18.0\,^{\text{o}}\text{C}:\\
c_{p,MCPCM} &= 2.665\text{x}10^{2}\left(T-17.3\right)^3 - 2.863\text{x}10^{2}\left(T-17.3\right)^2\\
&\quad -7.699\text{x}10^{1}\left(T-17.3\right) + 1.204\text{x}10^{2}
\end{aligned}
$$

$$
\begin{aligned}
&\text{For } 18.0\,^{\text{o}}\text{C} < T \le 18.7\,^{\text{o}}\text{C}:\\
c_{p,MCPCM} &= 1.746\text{x}10^{2}\left(T-18.0\right)^4 - 3.327\text{x}10^{2}\left(T-18.0\right)^3\\
&\quad +2.405\text{x}10^{2}\left(T-18.0\right)^2 - 8.807\text{x}10^{1}\left(T-18.0\right)\\
&\quad +17.62
\end{aligned}
$$

$$
\begin{aligned}
&\text{For } 18.7\,^{\text{o}}\text{C} < T \le 55\,^{\text{o}}\text{C}:\\
c_{p,MCPCM} &= 1.620\text{x}10^{-3}\left(T-18.7\right) + 1.651
\end{aligned}
$$

Although the latents heats of melting and freezing of the MCPCM particles are not directly needed in the calculations undertaken in this work, they can be evaluated using Eq. (3.12), as follows (in kJ/kg):

$$
\begin{aligned}
\lambda_{melting,s} &= \lambda_{melting,MCPCM} \cdot \phi = 129.5 \cdot \phi\\
\lambda_{freezing,s} &= \lambda_{freezing,MCPCM} \cdot \phi = 134.0 \cdot \phi
\end{aligned}
$$

Effective specific enthalpy and function F(T):

The effective specific enthalpy of the MCPCM slurries can be evaluated using the following relations:

$$i_s = \phi i_{MCPCM} + \left(1-\phi\right) i_{H_2O}$$
$$i_{MCPCM} = \int_{T_{ref}}^{T} c_{p,MCPCM} dT + i_{MCPCM,ref}$$
$$i_{H_2O} = \int_{T_{ref}}^{T} c_{p,H_2O} dT + i_{H_2O,ref}$$

In this equation, T_{ref} denotes a suitable reference temperature; and $i_{MCPCM,ref}$ and $i_{H_2O,ref}$ are the reference values of the specific enthalpies of the MCPCM particles and water, respectively, evaluated at T_{ref}. Since differences (or variations) of the effective specific enthalpy are important (and not its absolute value), the reference values $i_{MCPCM,ref}$ and $i_{H_2O,ref}$ are set equal to the convenient value of zero at the reference temperature T_{ref}. A reference temperature value of 5°C was chosen, as it corresponds to the lower-temperature limit of the proposed correlations for the effective thermophysical properties. The relation for i_{H_2O} is the following, where i_{H_2O} is in kJ/kg, *T* is in °C, and T_{ref} = 5°C:

$$i_{H_2O} = -7.5175\text{x}10^{-8} T^4 + 1.6510\text{x}10^{-5} T^3 - 1.1565\text{x}10^{-3} T^2 + 4.2110T - 21.028$$

The relations for calculating the effective specific enthalpy of the MCPCM particles were obtained by performing suitable integrations of the effective specific heat correlations listed previously. It should be noted that two sets of relations are presented: one for the monotonic heating (melting) process and another for the monotonic cooling (freezing) process. Outside the PCM melting and freezing temperature ranges, the values predicted by these relations are essentially equal (within machine precision), as is to be expected. However, within the phase-change temperature range of the MCPCM particles, the effective specific enthalpy of the MCPCM particles depends on the state of the PCM, thus explaining the need for two different sets of relations, one for each phase-change process. In the following relations, i_{MCPCM} is in kJ/kg and *T* is in °C (note: T_{ref} = 5°C).

Monotonic heating (melting) process:

For $5\ ^{\mathrm{o}}\mathrm{C} \le T \le 20\ ^{\mathrm{o}}\mathrm{C}$:

$$\begin{aligned} i_{MCPCM} = {} & 4.0696\text{x}10^{-7}\left(T-5\right)^6 - 1.2420\text{x}10^{-5}\left(T-5\right)^5 \\ & +2.1292\text{x}10^{-4}\left(T-5\right)^4 - 6.6059\text{x}10^{-4}\left(T-5\right)^3 \\ & +2.2256\text{x}10^{-2}\left(T-5\right)^2 + 2.0162\left(T-5\right) + 0 \end{aligned}$$

For $20\ ^{\mathrm{o}}\mathrm{C} < T \le 27\ ^{\mathrm{o}}\mathrm{C}$:

$$\begin{aligned} i_{MCPCM} = {} & 4.5436\text{x}10^{-4}\left(T-20\right)^6 - 3.8509\text{x}10^{-3}\left(T-20\right)^5 \\ & +1.7274\text{x}10^{-2}\left(T-20\right)^4 - 1.6566\text{x}10^{-2}\left(T-20\right)^3 \\ & +2.2782\text{x}10^{-1}\left(T-20\right)^2 + 3.8229\left(T-20\right) + 39.005 \end{aligned}$$

For $27\ ^{\mathrm{o}}\mathrm{C} < T \le 28.66\ ^{\mathrm{o}}\mathrm{C}$:

$$i_{MCPCM} = 3.4556\text{x}10^{-1}\left(T-27\right)^3 + 8.6990\left(T-27\right)^2 + 27.866\left(T-27\right) + 1.0146\text{x}10^2$$

For $28.66\ ^{\mathrm{o}}\mathrm{C} < T \le 28.72\ ^{\mathrm{o}}\mathrm{C}$:

$$\begin{aligned} i_{MCPCM} = {} & -1.3881\text{x}10^2\left(T-28.66\right)^3 + 12.911\left(T-28.66\right)^2 \\ & +59.603\left(T-28.66\right) + 1.7326\text{x}10^2 \end{aligned}$$

For $28.72\ ^{\mathrm{o}}\mathrm{C} < T \le 28.9\ ^{\mathrm{o}}\mathrm{C}$:

$$i_{MCPCM} = -1.4756\text{x}10^2\left(T-28.72\right)^2 + 59.653\left(T-28.72\right) + 1.7686\text{x}10^2$$

For $28.9\ ^{\mathrm{o}}\mathrm{C} < T \le 29.1\ ^{\mathrm{o}}\mathrm{C}$:

$$\begin{aligned} i_{MCPCM} = {} & 61.573\left(T-28.9\right)^5 - 1.1978\text{x}10^2\left(T-28.9\right)^4 \\ & +91.378\left(T-28.9\right)^3 - 31.225\left(T-28.9\right)^2 \\ & +6.5330\left(T-28.9\right) + 1.8281\text{x}10^2 \end{aligned}$$

For $29.1\ ^{\mathrm{o}}\mathrm{C} < T \le 55\ ^{\mathrm{o}}\mathrm{C}$:

$$i_{MCPCM} = 8.0978\text{x}10^{-4}\left(T-29.1\right)^2 + 1.6679\left(T-29.1\right) + 1.8343\text{x}10^2$$

Monotonic cooling (freezing) process:

$$\begin{aligned}
&\text{For } 5\,^{\circ}\text{C} \le T \le 15\,^{\circ}\text{C}:\\
&i_{MCPCM} = 4.0697\text{x}10^{-7}\left(T-5\right)^{6} - 1.2420\text{x}10^{-5}\left(T-5\right)^{5}\\
&\qquad +2.1292\text{x}10^{-4}\left(T-5\right)^{4} - 6.6059\text{x}10^{-4}\left(T-5\right)^{3}\\
&\qquad +2.2256\text{x}10^{-2}\left(T-5\right)^{2} + 2.0162\left(T-5\right) + 0
\end{aligned}$$

$$\begin{aligned}
&\text{For } 15^{\circ}\text{C} < T \le 16.35\,^{\circ}\text{C}:\\
&i_{MCPCM} = 2.6809\left(T-15\right)^{6} - 6.1449\left(T-15\right)^{5}\\
&\qquad +5.1323\left(T-15\right)^{4} - 1.2397\left(T-15\right)^{3}\\
&\qquad +3.2071\text{x}10^{-1}\left(T-15\right)^{2} + 2.7381\left(T-15\right) + 23.021
\end{aligned}$$

$$\begin{aligned}
&\text{For } 16.35\,^{\circ}\text{C} < T \le 16.9\,^{\circ}\text{C}:\\
&i_{MCPCM} = -1.2251\text{x}10^{2}\left(T-16.35\right)^{4} + 1.5875\text{x}10^{2}\left(T-16.35\right)^{3}\\
&\qquad +29.305\left(T-16.35\right)^{2} + 17.410\left(T-16.35\right) + 29.973
\end{aligned}$$

$$\begin{aligned}
&\text{For } 16.9\,^{\circ}\text{C} < T \le 17.3\,^{\circ}\text{C}:\\
&i_{MCPCM} = 32.241\left(T-16.9\right)^{5} + 81.906\left(T-16.9\right)^{4}\\
&\qquad -1.8113\text{x}10^{2}\left(T-16.9\right)^{3} + 87.576\left(T-16.9\right)^{2}\\
&\qquad +1.1218\text{x}10^{2}\left(T-16.9\right) + 63.616
\end{aligned}$$

$$\begin{aligned}
&\text{For } 17.3\,^{\circ}\text{C} < T \le 18.0\,^{\circ}\text{C}:\\
&i_{MCPCM} = 66.625\left(T-17.3\right)^{4} - 95.438\left(T-17.3\right)^{3}\\
&\qquad -38.497\left(T-17.3\right)^{2} + 1.2039\text{x}10^{2}\left(T-17.3\right) + 1.13336\text{x}10^{2}
\end{aligned}$$

$$\begin{aligned}
&\text{For } 18.0\,^{\circ}\text{C} < T \le 18.7\,^{\circ}\text{C}:\\
&i_{MCPCM} = 34.925\left(T-18.0\right)^{5} - 83.174\left(T-18.0\right)^{4}\\
&\qquad +80.182\left(T-18.0\right)^{3} - 44.032\left(T-18.0\right)^{2}\\
&\qquad +17.617\left(T-18.0\right) + 1.6201\text{x}10^{2}
\end{aligned}$$

$$\begin{aligned}
&\text{For } 18.7\,^{\circ}\text{C} < T \le 55\,^{\circ}\text{C}:\\
&i_{MCPCM} = 8.0978\text{x}10^{-4}\left(T-18.7\right)^{2} + 1.6511\left(T-18.7\right) + 1.6617\text{x}10^{2}
\end{aligned}$$

Next, the function $F\left(T\right)$, which is introduced in the energy equation to take into account the strong variation with temperature of the effective specific heat, is evaluated. Starting with Eq. (2.22), the effective specific enthalpy is related to $F\left(T\right)$ as follows:

$$
\begin{aligned}
& i_s = c_{p,s,ref}\int_{T_{ref}}^{T}\left[1+f\left(t\right)\right]dT + i_{s,ref} = c_{p,s,ref}\left[\left(T-T_{ref}\right)+F\left(T\right)\right]+i_{s,ref} \\
& where: F\left(T\right)=\int_{T_{ref}}^{T} f\left(t\right)dT \quad and \quad c_{p,s,ref} = \phi c_{p,MCPCM}\Big|_{T_{ref}} + \left(1-\phi\right)c_{p,H_2O}\Big|_{T_{ref}}
\end{aligned}
$$

The function $F\left(T\right)$ can then be computed as follows ($i_{s,ref}$ = 0, as the reference enthalpies of water and the MCPCM particles are both set equal to zero at T_{ref}):

$$
\begin{aligned}
& i_s = \phi i_{MCPCM} + \left(1-\phi\right)i_{H_2O} = c_{p,s,ref}\left[\left(T-T_{ref}\right)+F\left(T\right)\right]+i_{s,ref} \\
& \frac{\phi i_{MCPCM} + \left(1-\phi\right)i_{H_2O}}{c_{p,s,ref}} = \left[\left(T-T_{ref}\right)+F\left(T\right)\right] \\
& F\left(T\right) = \frac{\phi i_{MCPCM} + \left(1-\phi\right)i_{H_2O}}{c_{p,s,ref}} - \left(T-T_{ref}\right)
\end{aligned}
$$

Appendix C: Thermosyphon Experiments used in a Technique for Determining the Rheological Properties of the MCPCM Slurries

As was described in Chapter 3, a hybrid technique was used in this work for determining the rheological properties of the MCPCM slurries. This technique involves a combination of raw data from measurements with glass capillary-tube viscometers, measurements from closed-loop thermosyphon experiments undertaken specially in this context, and complementary numerical simulations (using a modified version of the 1-D/2-D model described in Chapter 2). The rheological properties determined with this technique were the values of the relative consistency index, *m*, and the flow behaviour index, *n*, needed in Eq. (3.15) for the calculation of η_s, the effective relative viscosity of the slurry (the effective dynamic viscosity of the slurry, μ_s, normalized by the dynamic viscosity of distilled water, μ_{H_2O}, at the same temperature). Details of the special closed-loop thermosyphon experiments which were undertaken to obtain inputs for this hybrid technique are provided in this appendix.

The special closed-loop thermosyphon experiments used in the above-mentioned hybrid technique were done with the MCPCM slurries operating in the full-melting-no-supercooled-freezing-no-hysteresis (FMNSCFNH) process, discussed earlier in Section 3.5. For each value of the MCPCM mass concentration in the slurries, the values of *m* and *n* were calculated using inputs (to the above-mentioned hybrid technique) from the above-mentioned special thermosyphon experiments, conducted in the aforementioned FMNSCFNH process. The proposed hybrid technique for determining the values of *m* and *n* was inspired by a similar procedure employed by Nir and Acrivos (1974) to deduce the effective dynamic viscosity of slurries at near-zero rates of strain using inputs from complementary experimental and computational investigations of natural convection in an enclosure.

The parameters of the special closed-loop thermosyphon experiments which were undertaken to provide inputs to the proposed hybrid technique for determining *m* and *n* are listed in the following table. Again, it should be noted that each run of these special experiments was done with the MCPCM slurries operating in a full-melting-no-supercooled-freezing-no-hysteresis (FMNSCFNH) process.

Run	ϕ	$q_{heating,total}$ [W]	T_{cool} [°C]	T_{∞} [°C]	w_{av} [m/s]
1	7.471%	29.01	22.05	22.58	$4.120\text{x}10^{-3}$
2	9.997%	20.00	22.02	23.18	$3.138\text{x}10^{-3}$
3	12.49%	20.17	21.97	22.60	$2.531\text{x}10^{-3}$
4	14.95%	15.02	22.06	23.36	$1.902\text{x}10^{-3}$
5	17.50%	12.15	22.03	22.85	$1.407\text{x}10^{-3}$

As was discussed in Chapter 3, it was assumed in this work that the effective dynamic viscosity of the MCPCM slurries is essentially unaffected by the state (solid or liquid) of the encapsulated PCM. Therefore, the special closed-loop thermosyphon experiments were undertaken with the MCPCM slurries operating in the full-melting-no-supercooled-freezing-no-hysteresis (FMNSCFNH) process, in which relatively higher heating-power inputs, $q_{heating,total}$, are required, so the relative uncertainties associated with minor heat losses to the ambient are reduced.

The values of n yielded by the proposed hybrid technique for each of the aforementioned five runs are presented in the next table.

Run	ϕ	n
1	7.471%	0.9072
2	9.997%	0.8962
3	12.49%	0.8500
4	14.95%	0.8309
5	17.50%	0.7809

A least-square method was used with the above-mentioned values of n to obtain the following fourth-order polynomial curve-fit:

$$n = -1.132\text{x}10^3\phi^4 + 3.979\text{x}10^2\phi^3 - 4.068\text{x}10^1\phi^2 + 1$$

For each value of MCPCM mass concentration, the above-mentioned correlation for n and corrected effective relative viscosity data (see related details in Chapter 3) were used in Eq. (3.15) to obtain the corresponding values of the relative consistency index, m. These values of m are presented in the table below.

ϕ	m [$\text{s}^{\text{n-1}}$]
7.471%	11.25
9.997%	16.21
12.49%	24.26
14.95%	32.74
17.50%	43.04

Using these results in a least-squares procedure, the following correlation for m (in $\text{s}^{\text{n-1}}$) was obtained:

$$m = 1.297\text{x}10^3\phi^3 + 7.451\text{x}10^2\phi^2 + 7.044\text{x}10^1\phi + 1$$

Appendix D: Thermocouple Calibration Curves

As explained in Chapter 4, 3rd or 4th order polynomial functions were curve-fitted and used to relate the output voltage of each thermocouple (and sheathed thermocouple probe) to a temperature value. The polynomial functions have the following generic form, for a given thermocouple [see Eq. (4.2)]:

$$T_{measured} = a_n V^n + a_{n-1} V^{n-1} + \ldots + a_1 V^1 + a_0$$

In this equation, $T_{measured}$ is the temperature measured by the thermocouple in ºC, a represent the polynomial coefficients and V denotes the voltage output of the thermocouple in mV. The values of the coefficients a pertaining to each thermocouple are listed in the table below. The type and function of each thermocouple and sheathed thermocouple probe are also given (in the following table, TC stands for thermocouple while 1/16P and 1/8P denote stainless steel sheathed thermocouple probes having the corresponding diameters in inches).

#	Function	Type	a_4	a_3	a_2	a_1	a_0
1	$T_{r=r_0}$ #1	TC	N/A	1.4259×10^{-2}	-2.9974×10^{-1}	1.7279×10^{1}	6.7142×10^{-2}
2	$T_{r=r_0}$ #2	TC	N/A	1.4001×10^{-2}	-3.0052×10^{-1}	1.7290×10^{1}	4.2974×10^{-2}
3	$T_{r=r_0}$ #3	TC	N/A	1.4811×10^{-2}	-3.0561×10^{-1}	1.7298×10^{1}	3.9519×10^{-2}
4	$T_{r=r_0}$ #4	TC	N/A	1.5050×10^{-2}	-3.0671×10^{-1}	1.7291×10^{1}	3.7413×10^{-2}
5	$T_{r=r_0}$ #5	TC	N/A	1.4469×10^{-2}	-3.0078×10^{-1}	1.7286×10^{1}	4.2752×10^{-2}
6	$T_{r=r_0}$ #6	TC	N/A	1.4030×10^{-2}	-2.9856×10^{-1}	1.7292×10^{1}	3.2304×10^{-2}
7	$T_{r=r_0}$ #7	TC	N/A	1.7437×10^{-2}	-3.2146×10^{-1}	1.7319×10^{1}	2.5972×10^{-2}
8	$T_{r=r_0}$ #8	TC	N/A	1.8875×10^{-2}	-3.2893×10^{-1}	1.7324×10^{1}	3.1995×10^{-2}
9	$T_{r=r_0}$ #9	TC	N/A	8.8309×10^{-3}	-2.6876×10^{-1}	1.7244×10^{1}	5.2175×10^{-2}
10	$T_{r=r_0}$ #10	TC	N/A	1.3742×10^{-2}	-3.0087×10^{-1}	1.7290×10^{1}	3.6747×10^{-2}

11	$T_{r=r_0}$ #11	TC	N/A	1.7186×10^{-2}	-3.1679×10^{-1}	1.7313×10^{1}	2.2479×10^{-2}
12	$T_{r=r_0}$ #12	TC	N/A	1.8389×10^{-2}	-3.2462×10^{-1}	1.7323×10^{1}	1.7293×10^{-2}
13	$T_{r=r_0}$ #13	TC	N/A	1.1212×10^{-2}	-2.8789×10^{-1}	1.7269×10^{1}	2.6615×10^{-2}
14	$T_{r=r_0}$ #14	TC	N/A	1.5549×10^{-2}	-3.0840×10^{-1}	1.7297×10^{1}	3.2700×10^{-3}
15	$T_{r=r_0}$ #15	TC	N/A	1.6020×10^{-2}	-3.1524×10^{-1}	1.7299×10^{1}	3.4361×10^{-3}
16	$T_{r=r_0}$ #16	TC	N/A	1.0443×10^{-2}	-2.7785×10^{-1}	1.7258×10^{1}	5.8018×10^{-6}
17	$T_{r=r_0}$ #17	TC	N/A	1.3368×10^{-2}	-2.9757×10^{-1}	1.7274×10^{1}	8.9952×10^{-4}
18	$T_{r=r_0}$ #18	TC	N/A	1.1141×10^{-2}	-2.8373×10^{-1}	1.7257×10^{1}	-1.0628×10^{-2}
19	$T_{r=r_0}$ #19	TC	N/A	1.8634×10^{-2}	-3.1904×10^{-1}	1.7295×10^{1}	-2.4430×10^{-2}
20	$T_{r=r_0}$ #20	TC	N/A	9.9640×10^{-3}	-2.7717×10^{-1}	1.7250×10^{1}	-8.2974×10^{-3}
21	$T_{r=r_0}$ #21	TC	N/A	1.3794×10^{-2}	-3.0072×10^{-1}	1.7298×10^{1}	-2.1128×10^{-1}
22	$T_{r=r_0}$ #22	TC	N/A	1.3570×10^{-2}	-3.0202×10^{-1}	1.7304×10^{1}	-2.1535×10^{-1}
23	$T_{r=r_0}$ #23	TC	N/A	1.4602×10^{-2}	-3.0449×10^{-1}	1.7301×10^{1}	-2.1444×10^{-1}
24	$T_{r=r_0}$ #24	TC	N/A	1.6514×10^{-2}	-3.0943×10^{-1}	1.7299×10^{1}	-2.2965×10^{-1}
25	$T_{r=r_0}$ #25	TC	N/A	1.2933×10^{-2}	-2.9600×10^{-1}	1.7295×10^{1}	-2.1828×10^{-1}
26	$T_{r=r_0}$ #26	TC	N/A	1.7912×10^{-2}	-3.2076×10^{-1}	1.7327×10^{1}	-2.3851×10^{-1}
27	$T_{r=r_0}$ #27	TC	N/A	1.4712×10^{-2}	-3.0584×10^{-1}	1.7307×10^{1}	-2.3167×10^{-1}
28	$T_{r=r_0}$ #28	TC	N/A	1.5101×10^{-2}	-3.0771×10^{-1}	1.7313×10^{1}	-2.3870×10^{-1}
29	$T_{r=r_0}$ #29	TC	N/A	1.4493×10^{-2}	-3.0473×10^{-1}	1.7301×10^{1}	-2.2935×10^{-1}
30	$T_{r=r_0}$ #30	TC	N/A	1.5591×10^{-2}	-3.0981×10^{-1}	1.7310×10^{1}	-2.3575×10^{-1}
31	$T_{r=r_0}$ #31	TC	N/A	1.5675×10^{-2}	-3.1244×10^{-1}	1.7314×10^{1}	-2.4269×10^{-1}
32	$T_{r=r_0}$ #32	TC	N/A	1.6121×10^{-2}	-3.1478×10^{-1}	1.7323×10^{1}	-2.5164×10^{-1}
33	$T_{r=r_0}$ #33	TC	N/A	1.6331×10^{-2}	-3.1347×10^{-1}	1.7303×10^{1}	-2.5385×10^{-1}
34	$T_{r=r_0}$ #34	TC	N/A	1.6340×10^{-2}	-3.1388×10^{-1}	1.7319×10^{1}	-2.7520×10^{-1}
35	$T_{r=r_0}$ #35	TC	N/A	1.4568×10^{-2}	-3.0491×10^{-1}	1.7302×10^{1}	-2.8086×10^{-1}

36	$T_{r=r_0}$ #36	TC	N/A	1.4876x10^{-2}	-3.0655x10^{-1}	1.7306x10^{1}	-2.8883x10^{-1}
37	$T_{r=r_0}$ #37	TC	N/A	1.4887x10^{-2}	-3.0703x10^{-1}	1.7309x10^{1}	-2.9866x10^{-1}
38	$T_{r=r_0}$ #38	TC	N/A	1.4639x10^{-2}	-3.0391x10^{-1}	1.7296x10^{1}	-2.9364x10^{-1}
39	$T_{r=r_0}$ #39	TC	N/A	1.9741x10^{-2}	-3.2722x10^{-1}	1.7317x10^{1}	-3.0641x10^{-1}
40	$T_{r=r_0}$ #40	TC	N/A	1.1744x10^{-2}	-2.8688x10^{-1}	1.7270x10^{1}	-2.9136x10^{-1}
41	$T_{\infty,top}$	TC	N/A	1.2930x10^{-2}	-2.9514x10^{-1}	1.7278x10^{1}	4.0477x10^{-2}
42	$T_{\infty,bottom}$	TC	N/A	1.5895x10^{-2}	-3.1085x10^{-1}	1.7307x10^{1}	2.1879x10^{-2}
43	Spare	TC	N/A	1.5511x10^{-2}	-3.0959x10^{-1}	1.7303x10^{1}	2.2752x10^{-2}
44	Spare	TC	N/A	1.5859x10^{-2}	-3.1182x10^{-1}	1.7306x10^{1}	1.9951x10^{-2}
45	Spare	TC	N/A	1.5658x10^{-2}	-3.1117x10^{-1}	1.7307x10^{1}	1.5642x10^{-2}
46	Spare	TC	N/A	9.9580x10^{-3}	-2.7874x10^{-1}	1.7254x10^{1}	2.4186x10^{-2}
47	Spare	TC	N/A	1.7814x10^{-2}	-3.2078x10^{-1}	1.7317x10^{1}	8.1437x10^{-3}
48	Spare	TC	N/A	1.7682x10^{-2}	-3.2071x10^{-1}	1.7318x10^{1}	9.2238x10^{-3}
49	Spare	1/16P	-2.3319x10^{-2}	1.6137x10^{-1}	-5.9909x10^{-1}	1.7479x10^{1}	1.7746x10^{-2}
50	Spare	1/16P	N/A	-1.9797x10^{-2}	-1.4265x10^{-1}	1.7069x10^{1}	1.1142x10^{-1}
51	$T_{b,in,cooling}$	1/16P	N/A	-1.6599x10^{-2}	-1.5639x10^{-1}	1.7100x10^{1}	7.5886x10^{-2}
52	Spare	1/16P	N/A	-2.4518x10^{-2}	-1.1196x10^{-1}	1.7034x10^{1}	9.6458x10^{-2}
53	$T_{b,out,cooling}$	1/16P	N/A	-5.5970x10^{-3}	-2.2232x10^{-1}	1.7229x10^{1}	-2.1426x10^{-2}
54	$T_{b,in,heating}$	1/16P	N/A	6.6780x10^{-5}	-2.3661x10^{-1}	1.7207x10^{1}	5.6939x10^{-3}
55	$T_{b,out,heating}$	1/16P	N/A	6.3454x10^{-3}	-2.6129x10^{-1}	1.7192x10^{1}	4.0336x10^{-2}
56	Spare	1/16P	-1.5665x10^{-2}	9.7962x10^{-2}	-4.4612x10^{-1}	1.7393x10^{1}	-7.8818x10^{-2}
57	Spare	1/8P	-4.6068x10^{-3}	3.8672x10^{-2}	-3.5931x10^{-1}	1.7419x10^{1}	-1.7163x10^{-1}
58	Spare	1/8P	N/A	-3.2794x10^{-4}	-2.4550x10^{-1}	1.7296x10^{1}	-1.3661x10^{-1}
59	$T_{cool,in}$	1/8P	N/A	7.7975x10^{-4}	-2.4539x10^{-1}	1.7249x10^{1}	-8.4093x10^{-2}
60	$T_{cool,out}$	1/8P	N/A	-3.1059x10^{-3}	-2.3093x10^{-1}	1.7255x10^{1}	-1.1328x10^{-1}

Appendix E: Experimental Results

In this Appendix, the experimental results are listed in the form of data tables for all experimental runs. In these tables, the temperatures are given in ºC, voltages in V, currents in A, heating power inputs in W, and average velocities in m/s. The voltage applied across the nichrome-wire heater was measured using the voltmeter integrated in the data acquisition unit (*Hewlett-Packard* 3497A), and it is denoted as $V_{heating}$; while $I_{heating}$ denotes the electrical current passing through the heater, and it was measured using the HP3478A multimeter. It should be noted that the value of the total heating power input, $q_{heating,total}$, was computed by taking the time-mean value (over the duration of the data sampling) of the instantaneous product of $V_{heating}$ and $I_{heating}$.

The data obtained in the experimental runs performed with distilled water as the working fluid are presented first. After that, the data pertaining to the experimental runs conducted with the MCPCM slurries as the working fluid are presented.

Run 1-W, Distilled Water					
$T_{r=r_0}$ #1	21.79	$T_{r=r_0}$ #21	24.60	$T_{\infty,top}$	25.02
$T_{r=r_0}$ #2	21.95	$T_{r=r_0}$ #22	24.73	$T_{\infty,bottom}$	23.21
$T_{r=r_0}$ #3	22.21	$T_{r=r_0}$ #23	24.77	T_{∞}	24.11
$T_{r=r_0}$ #4	22.38	$T_{r=r_0}$ #24	24.90	$T_{b,in,heating}$	20.59
$T_{r=r_0}$ #5	22.50	$T_{r=r_0}$ #25	25.07	$T_{b,out,heating}$	25.74
$T_{r=r_0}$ #6	22.68	$T_{r=r_0}$ #26	25.14	$T_{b,in,cooling}$	25.65
$T_{r=r_0}$ #7	22.78	$T_{r=r_0}$ #27	25.30	$T_{b,out,cooling}$	20.38
$T_{r=r_0}$ #8	22.97	$T_{r=r_0}$ #28	25.39	$T_{cool,in}$	19.96
$T_{r=r_0}$ #9	23.06	$T_{r=r_0}$ #29	25.54	$T_{cool,out}$	19.98
$T_{r=r_0}$ #10	23.16	$T_{r=r_0}$ #30	25.71	T_{cool}	19.97
$T_{r=r_0}$ #11	23.37	$T_{r=r_0}$ #31	25.77	$V_{heating}$	34.691
$T_{r=r_0}$ #12	23.46	$T_{r=r_0}$ #32	25.91	$I_{heating}$	0.28952
$T_{r=r_0}$ #13	23.61	$T_{r=r_0}$ #33	26.04	$q_{heating,total}$	10.044
$T_{r=r_0}$ #14	23.69	$T_{r=r_0}$ #34	26.12	w_{av}	$5.6671\text{x}10^{-3}$
$T_{r=r_0}$ #15	23.84	$T_{r=r_0}$ #35	26.25		
$T_{r=r_0}$ #16	23.97	$T_{r=r_0}$ #36	26.32		
$T_{r=r_0}$ #17	24.12	$T_{r=r_0}$ #37	26.50		
$T_{r=r_0}$ #18	24.21	$T_{r=r_0}$ #38	26.59		
$T_{r=r_0}$ #19	24.34	$T_{r=r_0}$ #39	26.71		
$T_{r=r_0}$ #20	24.50	$T_{r=r_0}$ #40	26.88		

Run 2-W, Distilled Water					
$T_{r=r_0}$ #1	22.72	$T_{r=r_0}$ #21	27.00	$T_{\infty,top}$	25.06
$T_{r=r_0}$ #2	22.98	$T_{r=r_0}$ #22	27.18	$T_{\infty,bottom}$	23.36
$T_{r=r_0}$ #3	23.42	$T_{r=r_0}$ #23	27.21	T_{∞}	24.21
$T_{r=r_0}$ #4	23.70	$T_{r=r_0}$ #24	27.42	$T_{b,in,heating}$	20.81
$T_{r=r_0}$ #5	23.88	$T_{r=r_0}$ #25	27.67	$T_{b,out,heating}$	28.12
$T_{r=r_0}$ #6	24.16	$T_{r=r_0}$ #26	27.74	$T_{b,in,cooling}$	27.91
$T_{r=r_0}$ #7	24.31	$T_{r=r_0}$ #27	28.00	$T_{b,out,cooling}$	20.66
$T_{r=r_0}$ #8	24.62	$T_{r=r_0}$ #28	28.10	$T_{cool,in}$	19.96
$T_{r=r_0}$ #9	24.74	$T_{r=r_0}$ #29	28.34	$T_{cool,out}$	19.99
$T_{r=r_0}$ #10	24.86	$T_{r=r_0}$ #30	28.61	T_{cool}	19.98
$T_{r=r_0}$ #11	25.21	$T_{r=r_0}$ #31	28.64	$V_{heating}$	49.001
$T_{r=r_0}$ #12	25.33	$T_{r=r_0}$ #32	28.86	$I_{heating}$	0.40885
$T_{r=r_0}$ #13	25.57	$T_{r=r_0}$ #33	29.06	$q_{heating,total}$	20.034
$T_{r=r_0}$ #14	25.66	$T_{r=r_0}$ #34	29.15	w_{av}	$7.7317\text{x}10^{-3}$
$T_{r=r_0}$ #15	25.88	$T_{r=r_0}$ #35	29.34		
$T_{r=r_0}$ #16	26.06	$T_{r=r_0}$ #36	29.42		
$T_{r=r_0}$ #17	26.31	$T_{r=r_0}$ #37	29.71		
$T_{r=r_0}$ #18	26.42	$T_{r=r_0}$ #38	29.83		
$T_{r=r_0}$ #19	26.60	$T_{r=r_0}$ #39	30.01		
$T_{r=r_0}$ #20	26.84	$T_{r=r_0}$ #40	30.27		

Run 3-W, Distilled Water					
$T_{r=r_0}$ #1	23.61	$T_{r=r_0}$ #21	29.02	$T_{\infty,top}$	23.78
$T_{r=r_0}$ #2	23.94	$T_{r=r_0}$ #22	29.25	$T_{\infty,bottom}$	22.80
$T_{r=r_0}$ #3	24.54	$T_{r=r_0}$ #23	29.24	T_{∞}	23.29
$T_{r=r_0}$ #4	24.91	$T_{r=r_0}$ #24	29.51	$T_{b,in,heating}$	21.07
$T_{r=r_0}$ #5	25.13	$T_{r=r_0}$ #25	29.85	$T_{b,out,heating}$	30.06
$T_{r=r_0}$ #6	25.51	$T_{r=r_0}$ #26	29.91	$T_{b,in,cooling}$	29.64
$T_{r=r_0}$ #7	25.68	$T_{r=r_0}$ #27	30.23	$T_{b,out,cooling}$	20.98
$T_{r=r_0}$ #8	26.08	$T_{r=r_0}$ #28	30.34	$T_{cool,in}$	19.98
$T_{r=r_0}$ #9	26.23	$T_{r=r_0}$ #29	30.65	$T_{cool,out}$	20.03
$T_{r=r_0}$ #10	26.37	$T_{r=r_0}$ #30	31.00	T_{cool}	20.01
$T_{r=r_0}$ #11	26.83	$T_{r=r_0}$ #31	30.99	$V_{heating}$	59.922
$T_{r=r_0}$ #12	26.96	$T_{r=r_0}$ #32	31.28	$I_{heating}$	0.49974
$T_{r=r_0}$ #13	27.26	$T_{r=r_0}$ #33	31.55	$q_{heating,total}$	29.946
$T_{r=r_0}$ #14	27.37	$T_{r=r_0}$ #34	31.63	w_{av}	$9.2241\text{x}10^{-3}$
$T_{r=r_0}$ #15	27.64	$T_{r=r_0}$ #35	31.86		
$T_{r=r_0}$ #16	27.85	$T_{r=r_0}$ #36	31.93		
$T_{r=r_0}$ #17	28.18	$T_{r=r_0}$ #37	32.32		
$T_{r=r_0}$ #18	28.30	$T_{r=r_0}$ #38	32.46		
$T_{r=r_0}$ #19	28.51	$T_{r=r_0}$ #39	32.67		
$T_{r=r_0}$ #20	28.81	$T_{r=r_0}$ #40	33.01		

Run 4-W, Distilled Water					
$T_{r=r_0}$ #1	24.67	$T_{r=r_0}$ #21	31.05	$T_{\infty,top}$	23.73
$T_{r=r_0}$ #2	25.05	$T_{r=r_0}$ #22	31.32	$T_{\infty,bottom}$	23.06
$T_{r=r_0}$ #3	25.80	$T_{r=r_0}$ #23	31.26	T_{∞}	23.40
$T_{r=r_0}$ #4	26.25	$T_{r=r_0}$ #24	31.59	$T_{b,in,heating}$	21.47
$T_{r=r_0}$ #5	26.51	$T_{r=r_0}$ #25	32.01	$T_{b,out,heating}$	31.78
$T_{r=r_0}$ #6	26.96	$T_{r=r_0}$ #26	32.05	$T_{b,in,cooling}$	31.35
$T_{r=r_0}$ #7	27.15	$T_{r=r_0}$ #27	32.42	$T_{b,out,cooling}$	21.39
$T_{r=r_0}$ #8	27.64	$T_{r=r_0}$ #28	32.53	$T_{cool,in}$	19.98
$T_{r=r_0}$ #9	27.80	$T_{r=r_0}$ #29	32.91	$T_{cool,out}$	20.04
$T_{r=r_0}$ #10	27.96	$T_{r=r_0}$ #30	33.33	T_{cool}	20.01
$T_{r=r_0}$ #11	28.53	$T_{r=r_0}$ #31	33.28	$V_{heating}$	69.342
$T_{r=r_0}$ #12	28.65	$T_{r=r_0}$ #32	33.62	$I_{heating}$	0.57816
$T_{r=r_0}$ #13	29.03	$T_{r=r_0}$ #33	33.95	$q_{heating,total}$	40.091
$T_{r=r_0}$ #14	29.13	$T_{r=r_0}$ #34	34.01	w_{av}	$1.0768\text{x}10^{-2}$
$T_{r=r_0}$ #15	29.45	$T_{r=r_0}$ #35	34.27		
$T_{r=r_0}$ #16	29.68	$T_{r=r_0}$ #36	34.33		
$T_{r=r_0}$ #17	30.09	$T_{r=r_0}$ #37	34.82		
$T_{r=r_0}$ #18	30.20	$T_{r=r_0}$ #38	34.96		
$T_{r=r_0}$ #19	30.45	$T_{r=r_0}$ #39	35.20		
$T_{r=r_0}$ #20	30.79	$T_{r=r_0}$ #40	35.59		

Run 5-W, Distilled Water					
$T_{r=r_0}$ #1	25.71	$T_{r=r_0}$ #21	32.92	$T_{\infty,top}$	23.77
$T_{r=r_0}$ #2	26.14	$T_{r=r_0}$ #22	33.23	$T_{\infty,bottom}$	23.25
$T_{r=r_0}$ #3	27.02	$T_{r=r_0}$ #23	33.12	T_{∞}	23.51
$T_{r=r_0}$ #4	27.55	$T_{r=r_0}$ #24	33.51	$T_{b,in,heating}$	21.91
$T_{r=r_0}$ #5	27.83	$T_{r=r_0}$ #25	34.00	$T_{b,out,heating}$	33.33
$T_{r=r_0}$ #6	28.36	$T_{r=r_0}$ #26	34.01	$T_{b,in,cooling}$	32.89
$T_{r=r_0}$ #7	28.56	$T_{r=r_0}$ #27	34.44	$T_{b,out,cooling}$	21.85
$T_{r=r_0}$ #8	29.13	$T_{r=r_0}$ #28	34.55	$T_{cool,in}$	19.99
$T_{r=r_0}$ #9	29.30	$T_{r=r_0}$ #29	34.98	$T_{cool,out}$	20.06
$T_{r=r_0}$ #10	29.46	$T_{r=r_0}$ #30	35.46	T_{cool}	20.03
$T_{r=r_0}$ #11	30.13	$T_{r=r_0}$ #31	35.36	$V_{heating}$	77.372
$T_{r=r_0}$ #12	30.25	$T_{r=r_0}$ #32	35.75	$I_{heating}$	0.64497
$T_{r=r_0}$ #13	30.69	$T_{r=r_0}$ #33	36.13	$q_{heating,total}$	49.903
$T_{r=r_0}$ #14	30.78	$T_{r=r_0}$ #34	36.16	w_{av}	$1.2117\text{x}10^{-2}$
$T_{r=r_0}$ #15	31.13	$T_{r=r_0}$ #35	36.45		
$T_{r=r_0}$ #16	31.39	$T_{r=r_0}$ #36	36.49		
$T_{r=r_0}$ #17	31.87	$T_{r=r_0}$ #37	37.05		
$T_{r=r_0}$ #18	31.96	$T_{r=r_0}$ #38	37.11		
$T_{r=r_0}$ #19	32.23	$T_{r=r_0}$ #39	37.24		
$T_{r=r_0}$ #20	32.59	$T_{r=r_0}$ #40	37.53		

Run 6-W, Distilled Water					
$T_{r=r_0}$ #1	26.72	$T_{r=r_0}$ #21	34.69	$T_{\infty,top}$	23.71
$T_{r=r_0}$ #2	27.18	$T_{r=r_0}$ #22	35.03	$T_{\infty,bottom}$	23.22
$T_{r=r_0}$ #3	28.19	$T_{r=r_0}$ #23	34.86	T_{∞}	23.47
$T_{r=r_0}$ #4	28.78	$T_{r=r_0}$ #24	35.30	$T_{b,in,heating}$	22.28
$T_{r=r_0}$ #5	29.09	$T_{r=r_0}$ #25	35.86	$T_{b,out,heating}$	34.80
$T_{r=r_0}$ #6	29.68	$T_{r=r_0}$ #26	35.84	$T_{b,in,cooling}$	34.32
$T_{r=r_0}$ #7	29.88	$T_{r=r_0}$ #27	36.32	$T_{b,out,cooling}$	22.25
$T_{r=r_0}$ #8	30.54	$T_{r=r_0}$ #28	36.42	$T_{cool,in}$	19.98
$T_{r=r_0}$ #9	30.72	$T_{r=r_0}$ #29	36.91	$T_{cool,out}$	20.07
$T_{r=r_0}$ #10	30.88	$T_{r=r_0}$ #30	37.45	T_{cool}	20.02
$T_{r=r_0}$ #11	31.65	$T_{r=r_0}$ #31	37.30	$V_{heating}$	84.880
$T_{r=r_0}$ #12	31.76	$T_{r=r_0}$ #32	37.74	$I_{heating}$	0.70737
$T_{r=r_0}$ #13	32.27	$T_{r=r_0}$ #33	38.17	$q_{heating,total}$	60.041
$T_{r=r_0}$ #14	32.35	$T_{r=r_0}$ #34	38.16	w_{av}	1.3316×10^{-2}
$T_{r=r_0}$ #15	32.73	$T_{r=r_0}$ #35	38.44		
$T_{r=r_0}$ #16	33.01	$T_{r=r_0}$ #36	38.36		
$T_{r=r_0}$ #17	33.56	$T_{r=r_0}$ #37	38.90		
$T_{r=r_0}$ #18	33.64	$T_{r=r_0}$ #38	38.77		
$T_{r=r_0}$ #19	33.93	$T_{r=r_0}$ #39	38.99		
$T_{r=r_0}$ #20	34.34	$T_{r=r_0}$ #40	39.58		

Run 1-S, ϕ = 7.471%					
$T_{r=r_0}$ #1	20.33	$T_{r=r_0}$ #21	32.72	$T_{\infty,top}$	23.68
$T_{r=r_0}$ #2	21.31	$T_{r=r_0}$ #22	33.21	$T_{\infty,bottom}$	19.39
$T_{r=r_0}$ #3	22.71	$T_{r=r_0}$ #23	33.22	T_{∞}	21.53
$T_{r=r_0}$ #4	23.65	$T_{r=r_0}$ #24	33.80	$T_{b,in,heating}$	15.06
$T_{r=r_0}$ #5	24.25	$T_{r=r_0}$ #25	34.46	$T_{b,out,heating}$	37.16
$T_{r=r_0}$ #6	25.14	$T_{r=r_0}$ #26	34.71	$T_{b,in,cooling}$	36.21
$T_{r=r_0}$ #7	25.66	$T_{r=r_0}$ #27	35.44	$T_{b,out,cooling}$	14.78
$T_{r=r_0}$ #8	26.58	$T_{r=r_0}$ #28	35.82	$T_{cool,in}$	12.95
$T_{r=r_0}$ #9	26.97	$T_{r=r_0}$ #29	36.61	$T_{cool,out}$	13.03
$T_{r=r_0}$ #10	27.37	$T_{r=r_0}$ #30	37.63	T_{cool}	12.99
$T_{r=r_0}$ #11	28.38	$T_{r=r_0}$ #31	37.95	$V_{heating}$	81.203
$T_{r=r_0}$ #12	28.71	$T_{r=r_0}$ #32	38.81	$I_{heating}$	0.67685
$T_{r=r_0}$ #13	29.34	$T_{r=r_0}$ #33	39.60	$q_{heating,total}$	54.963
$T_{r=r_0}$ #14	29.60	$T_{r=r_0}$ #34	40.04	w_{av}	6.4357x10^{-3}
$T_{r=r_0}$ #15	30.18	$T_{r=r_0}$ #35	40.70		
$T_{r=r_0}$ #16	30.56	$T_{r=r_0}$ #36	41.03		
$T_{r=r_0}$ #17	31.14	$T_{r=r_0}$ #37	41.97		
$T_{r=r_0}$ #18	31.35	$T_{r=r_0}$ #38	42.44		
$T_{r=r_0}$ #19	31.76	$T_{r=r_0}$ #39	43.06		
$T_{r=r_0}$ #20	32.26	$T_{r=r_0}$ #40	43.83		

Run 1-Sr (Repeatability Run), ϕ = 7.471%					
$T_{r=r_0}$ #1	20.61	$T_{r=r_0}$ #21	32.82	$T_{\infty,top}$	24.67
$T_{r=r_0}$ #2	21.57	$T_{r=r_0}$ #22	33.31	$T_{\infty,bottom}$	20.47
$T_{r=r_0}$ #3	22.96	$T_{r=r_0}$ #23	33.31	T_{∞}	22.57
$T_{r=r_0}$ #4	23.88	$T_{r=r_0}$ #24	33.88	$T_{b,in,heating}$	15.25
$T_{r=r_0}$ #5	24.47	$T_{r=r_0}$ #25	34.55	$T_{b,out,heating}$	37.30
$T_{r=r_0}$ #6	25.35	$T_{r=r_0}$ #26	34.80	$T_{b,in,cooling}$	36.41
$T_{r=r_0}$ #7	25.87	$T_{r=r_0}$ #27	35.52	$T_{b,out,cooling}$	14.92
$T_{r=r_0}$ #8	26.78	$T_{r=r_0}$ #28	35.88	$T_{cool,in}$	13.02
$T_{r=r_0}$ #9	27.16	$T_{r=r_0}$ #29	36.69	$T_{cool,out}$	13.11
$T_{r=r_0}$ #10	27.56	$T_{r=r_0}$ #30	37.76	T_{cool}	13.07
$T_{r=r_0}$ #11	28.56	$T_{r=r_0}$ #31	38.08	$V_{heating}$	81.274
$T_{r=r_0}$ #12	28.88	$T_{r=r_0}$ #32	38.93	$I_{heating}$	0.67754
$T_{r=r_0}$ #13	29.50	$T_{r=r_0}$ #33	39.71	$q_{heating,total}$	55.067
$T_{r=r_0}$ #14	29.74	$T_{r=r_0}$ #34	40.15	w_{av}	6.5026x10^{-3}
$T_{r=r_0}$ #15	30.31	$T_{r=r_0}$ #35	40.80		
$T_{r=r_0}$ #16	30.68	$T_{r=r_0}$ #36	41.12		
$T_{r=r_0}$ #17	31.25	$T_{r=r_0}$ #37	42.06		
$T_{r=r_0}$ #18	31.47	$T_{r=r_0}$ #38	42.53		
$T_{r=r_0}$ #19	31.88	$T_{r=r_0}$ #39	43.14		
$T_{r=r_0}$ #20	32.38	$T_{r=r_0}$ #40	43.92		

Run 2-S, ϕ = 7.471%					
$T_{r=r_0}$ #1	19.08	$T_{r=r_0}$ #21	30.19	$T_{\infty,top}$	24.13
$T_{r=r_0}$ #2	19.87	$T_{r=r_0}$ #22	30.54	$T_{\infty,bottom}$	20.01
$T_{r=r_0}$ #3	21.01	$T_{r=r_0}$ #23	30.56	T_{∞}	22.07
$T_{r=r_0}$ #4	21.79	$T_{r=r_0}$ #24	30.99	$T_{b,in,heating}$	14.74
$T_{r=r_0}$ #5	22.30	$T_{r=r_0}$ #25	31.45	$T_{b,out,heating}$	33.62
$T_{r=r_0}$ #6	23.03	$T_{r=r_0}$ #26	31.59	$T_{b,in,cooling}$	32.90
$T_{r=r_0}$ #7	23.50	$T_{r=r_0}$ #27	32.09	$T_{b,out,cooling}$	14.32
$T_{r=r_0}$ #8	24.29	$T_{r=r_0}$ #28	32.33	$T_{cool,in}$	12.93
$T_{r=r_0}$ #9	24.64	$T_{r=r_0}$ #29	32.84	$T_{cool,out}$	13.00
$T_{r=r_0}$ #10	25.00	$T_{r=r_0}$ #30	33.47	T_{cool}	12.97
$T_{r=r_0}$ #11	25.86	$T_{r=r_0}$ #31	33.62	$V_{heating}$	70.132
$T_{r=r_0}$ #12	26.22	$T_{r=r_0}$ #32	34.24	$I_{heating}$	0.58491
$T_{r=r_0}$ #13	26.80	$T_{r=r_0}$ #33	34.86	$q_{heating,total}$	41.020
$T_{r=r_0}$ #14	27.08	$T_{r=r_0}$ #34	35.27	w_{av}	$5.5553\text{x}10^{-3}$
$T_{r=r_0}$ #15	27.67	$T_{r=r_0}$ #35	35.95		
$T_{r=r_0}$ #16	28.12	$T_{r=r_0}$ #36	36.41		
$T_{r=r_0}$ #17	28.67	$T_{r=r_0}$ #37	37.28		
$T_{r=r_0}$ #18	28.94	$T_{r=r_0}$ #38	37.67		
$T_{r=r_0}$ #19	29.36	$T_{r=r_0}$ #39	38.22		
$T_{r=r_0}$ #20	29.85	$T_{r=r_0}$ #40	38.93		

Run 3-S, ϕ = 7.471%					
$T_{r=r_0}$ #1	16.88	$T_{r=r_0}$ #21	23.10	$T_{\infty,top}$	24.13
$T_{r=r_0}$ #2	17.23	$T_{r=r_0}$ #22	23.35	$T_{\infty,bottom}$	19.97
$T_{r=r_0}$ #3	17.70	$T_{r=r_0}$ #23	23.53	T_{∞}	22.05
$T_{r=r_0}$ #4	18.07	$T_{r=r_0}$ #24	23.84	$T_{b,in,heating}$	14.81
$T_{r=r_0}$ #5	18.35	$T_{r=r_0}$ #25	24.15	$T_{b,out,heating}$	26.34
$T_{r=r_0}$ #6	18.69	$T_{r=r_0}$ #26	24.34	$T_{b,in,cooling}$	26.05
$T_{r=r_0}$ #7	18.95	$T_{r=r_0}$ #27	24.66	$T_{b,out,cooling}$	14.06
$T_{r=r_0}$ #8	19.36	$T_{r=r_0}$ #28	24.92	$T_{cool,in}$	12.94
$T_{r=r_0}$ #9	19.58	$T_{r=r_0}$ #29	25.22	$T_{cool,out}$	12.97
$T_{r=r_0}$ #10	19.80	$T_{r=r_0}$ #30	25.53	T_{cool}	12.96
$T_{r=r_0}$ #11	20.21	$T_{r=r_0}$ #31	25.71	$V_{heating}$	38.348
$T_{r=r_0}$ #12	20.48	$T_{r=r_0}$ #32	26.03	$I_{heating}$	0.32012
$T_{r=r_0}$ #13	20.79	$T_{r=r_0}$ #33	26.28	$q_{heating,total}$	12.276
$T_{r=r_0}$ #14	21.00	$T_{r=r_0}$ #34	26.47	w_{av}	2.9849x10^{-3}
$T_{r=r_0}$ #15	21.34	$T_{r=r_0}$ #35	26.74		
$T_{r=r_0}$ #16	21.64	$T_{r=r_0}$ #36	26.94		
$T_{r=r_0}$ #17	21.95	$T_{r=r_0}$ #37	27.25		
$T_{r=r_0}$ #18	22.18	$T_{r=r_0}$ #38	27.43		
$T_{r=r_0}$ #19	22.47	$T_{r=r_0}$ #39	27.66		
$T_{r=r_0}$ #20	22.85	$T_{r=r_0}$ #40	27.96		

Run 4-S, ϕ = 7.471%					
$T_{r=r_0}$ #1	20.53	$T_{r=r_0}$ #21	24.79	$T_{\infty,top}$	23.14
$T_{r=r_0}$ #2	20.75	$T_{r=r_0}$ #22	24.96	$T_{\infty,bottom}$	19.01
$T_{r=r_0}$ #3	21.06	$T_{r=r_0}$ #23	25.09	T_{∞}	21.08
$T_{r=r_0}$ #4	21.31	$T_{r=r_0}$ #24	25.29	$T_{b,in,heating}$	19.61
$T_{r=r_0}$ #5	21.51	$T_{r=r_0}$ #25	25.51	$T_{b,out,heating}$	26.71
$T_{r=r_0}$ #6	21.73	$T_{r=r_0}$ #26	25.63	$T_{b,in,cooling}$	26.14
$T_{r=r_0}$ #7	21.91	$T_{r=r_0}$ #27	25.85	$T_{b,out,cooling}$	19.82
$T_{r=r_0}$ #8	22.19	$T_{r=r_0}$ #28	26.04	$T_{cool,in}$	19.57
$T_{r=r_0}$ #9	22.36	$T_{r=r_0}$ #29	26.24	$T_{cool,out}$	19.58
$T_{r=r_0}$ #10	22.50	$T_{r=r_0}$ #30	26.44	T_{cool}	19.58
$T_{r=r_0}$ #11	22.78	$T_{r=r_0}$ #31	26.56	$V_{heating}$	29.592
$T_{r=r_0}$ #12	22.98	$T_{r=r_0}$ #32	26.79	$I_{heating}$	0.24695
$T_{r=r_0}$ #13	23.19	$T_{r=r_0}$ #33	26.95	$q_{heating,total}$	7.308
$T_{r=r_0}$ #14	23.33	$T_{r=r_0}$ #34	27.07	w_{av}	$2.3598\text{x}10^{-3}$
$T_{r=r_0}$ #15	23.55	$T_{r=r_0}$ #35	27.25		
$T_{r=r_0}$ #16	23.79	$T_{r=r_0}$ #36	27.39		
$T_{r=r_0}$ #17	23.99	$T_{r=r_0}$ #37	27.59		
$T_{r=r_0}$ #18	24.14	$T_{r=r_0}$ #38	27.70		
$T_{r=r_0}$ #19	24.34	$T_{r=r_0}$ #39	27.85		
$T_{r=r_0}$ #20	24.61	$T_{r=r_0}$ #40	28.05		

Run 5-S, ϕ = 9.997%					
$T_{r=r_0}$ #1	20.11	$T_{r=r_0}$ #21	32.14	$T_{\infty,top}$	23.40
$T_{r=r_0}$ #2	21.06	$T_{r=r_0}$ #22	32.59	$T_{\infty,bottom}$	21.92
$T_{r=r_0}$ #3	22.35	$T_{r=r_0}$ #23	32.67	T_{∞}	22.66
$T_{r=r_0}$ #4	23.24	$T_{r=r_0}$ #24	33.22	$T_{b,in,heating}$	15.19
$T_{r=r_0}$ #5	23.82	$T_{r=r_0}$ #25	33.84	$T_{b,out,heating}$	37.18
$T_{r=r_0}$ #6	24.66	$T_{r=r_0}$ #26	34.14	$T_{b,in,cooling}$	36.06
$T_{r=r_0}$ #7	25.21	$T_{r=r_0}$ #27	34.88	$T_{b,out,cooling}$	14.59
$T_{r=r_0}$ #8	26.07	$T_{r=r_0}$ #28	35.35	$T_{cool,in}$	12.96
$T_{r=r_0}$ #9	26.48	$T_{r=r_0}$ #29	36.17	$T_{cool,out}$	13.03
$T_{r=r_0}$ #10	26.90	$T_{r=r_0}$ #30	37.14	T_{cool}	12.99
$T_{r=r_0}$ #11	27.86	$T_{r=r_0}$ #31	37.53	$V_{heating}$	73.532
$T_{r=r_0}$ #12	28.23	$T_{r=r_0}$ #32	38.34	$I_{heating}$	0.61295
$T_{r=r_0}$ #13	28.84	$T_{r=r_0}$ #33	39.06	$q_{heating,total}$	45.071
$T_{r=r_0}$ #14	29.13	$T_{r=r_0}$ #34	39.50	w_{av}	5.1819×10^{-3}
$T_{r=r_0}$ #15	29.70	$T_{r=r_0}$ #35	40.15		
$T_{r=r_0}$ #16	30.10	$T_{r=r_0}$ #36	40.51		
$T_{r=r_0}$ #17	30.62	$T_{r=r_0}$ #37	41.36		
$T_{r=r_0}$ #18	30.85	$T_{r=r_0}$ #38	41.87		
$T_{r=r_0}$ #19	31.26	$T_{r=r_0}$ #39	42.50		
$T_{r=r_0}$ #20	31.77	$T_{r=r_0}$ #40	43.26		

Run 6-S, ϕ = 9.997%					
$T_{r=r_0}$ #1	18.94	$T_{r=r_0}$ #21	29.77	$T_{\infty,top}$	23.11
$T_{r=r_0}$ #2	19.70	$T_{r=r_0}$ #22	30.08	$T_{\infty,bottom}$	21.66
$T_{r=r_0}$ #3	20.75	$T_{r=r_0}$ #23	30.15	T_{∞}	22.38
$T_{r=r_0}$ #4	21.49	$T_{r=r_0}$ #24	30.54	$T_{b,in,heating}$	14.93
$T_{r=r_0}$ #5	21.99	$T_{r=r_0}$ #25	30.95	$T_{b,out,heating}$	33.22
$T_{r=r_0}$ #6	22.67	$T_{r=r_0}$ #26	31.08	$T_{b,in,cooling}$	32.26
$T_{r=r_0}$ #7	23.15	$T_{r=r_0}$ #27	31.55	$T_{b,out,cooling}$	14.27
$T_{r=r_0}$ #8	23.89	$T_{r=r_0}$ #28	31.80	$T_{cool,in}$	12.96
$T_{r=r_0}$ #9	24.26	$T_{r=r_0}$ #29	32.27	$T_{cool,out}$	13.01
$T_{r=r_0}$ #10	24.63	$T_{r=r_0}$ #30	32.84	T_{cool}	12.99
$T_{r=r_0}$ #11	25.44	$T_{r=r_0}$ #31	33.03	$V_{heating}$	63.255
$T_{r=r_0}$ #12	25.83	$T_{r=r_0}$ #32	33.62	$I_{heating}$	0.52749
$T_{r=r_0}$ #13	26.37	$T_{r=r_0}$ #33	34.21	$q_{heating,total}$	33.366
$T_{r=r_0}$ #14	26.69	$T_{r=r_0}$ #34	34.62	w_{av}	$4.5009\text{x}10^{-3}$
$T_{r=r_0}$ #15	27.26	$T_{r=r_0}$ #35	35.26		
$T_{r=r_0}$ #16	27.73	$T_{r=r_0}$ #36	35.73		
$T_{r=r_0}$ #17	28.24	$T_{r=r_0}$ #37	36.52		
$T_{r=r_0}$ #18	28.54	$T_{r=r_0}$ #38	36.90		
$T_{r=r_0}$ #19	28.96	$T_{r=r_0}$ #39	37.44		
$T_{r=r_0}$ #20	29.44	$T_{r=r_0}$ #40	38.11		

Run 7-S, ϕ = 9.997%					
$T_{r=r_0}$ #1	17.54	$T_{r=r_0}$ #21	23.46	$T_{\infty,top}$	23.24
$T_{r=r_0}$ #2	17.88	$T_{r=r_0}$ #22	23.72	$T_{\infty,bottom}$	21.75
$T_{r=r_0}$ #3	18.31	$T_{r=r_0}$ #23	23.91	T_{∞}	22.50
$T_{r=r_0}$ #4	18.64	$T_{r=r_0}$ #24	24.17	$T_{b,in,heating}$	15.57
$T_{r=r_0}$ #5	18.90	$T_{r=r_0}$ #25	24.46	$T_{b,out,heating}$	26.47
$T_{r=r_0}$ #6	19.23	$T_{r=r_0}$ #26	24.66	$T_{b,in,cooling}$	26.04
$T_{r=r_0}$ #7	19.50	$T_{r=r_0}$ #27	24.96	$T_{b,out,cooling}$	14.34
$T_{r=r_0}$ #8	19.86	$T_{r=r_0}$ #28	25.19	$T_{cool,in}$	12.97
$T_{r=r_0}$ #9	20.08	$T_{r=r_0}$ #29	25.47	$T_{cool,out}$	12.98
$T_{r=r_0}$ #10	20.32	$T_{r=r_0}$ #30	25.78	T_{cool}	12.98
$T_{r=r_0}$ #11	20.70	$T_{r=r_0}$ #31	25.95	$V_{heating}$	34.093
$T_{r=r_0}$ #12	20.96	$T_{r=r_0}$ #32	26.24	$I_{heating}$	0.28454
$T_{r=r_0}$ #13	21.25	$T_{r=r_0}$ #33	26.47	$q_{heating,total}$	9.701
$T_{r=r_0}$ #14	21.47	$T_{r=r_0}$ #34	26.67	w_{av}	$2.4535\text{x}10^{-3}$
$T_{r=r_0}$ #15	21.80	$T_{r=r_0}$ #35	26.91		
$T_{r=r_0}$ #16	22.08	$T_{r=r_0}$ #36	27.09		
$T_{r=r_0}$ #17	22.37	$T_{r=r_0}$ #37	27.36		
$T_{r=r_0}$ #18	22.61	$T_{r=r_0}$ #38	27.55		
$T_{r=r_0}$ #19	22.89	$T_{r=r_0}$ #39	27.75		
$T_{r=r_0}$ #20	23.23	$T_{r=r_0}$ #40	27.99		

Run 8-S, ϕ = 9.997%					
$T_{r=r_0}$ #1	21.02	$T_{r=r_0}$ #21	24.91	$T_{\infty,top}$	22.82
$T_{r=r_0}$ #2	21.21	$T_{r=r_0}$ #22	25.06	$T_{\infty,bottom}$	20.69
$T_{r=r_0}$ #3	21.48	$T_{r=r_0}$ #23	25.19	T_{∞}	21.75
$T_{r=r_0}$ #4	21.70	$T_{r=r_0}$ #24	25.36	$T_{b,in,heating}$	20.11
$T_{r=r_0}$ #5	21.88	$T_{r=r_0}$ #25	25.55	$T_{b,out,heating}$	26.53
$T_{r=r_0}$ #6	22.09	$T_{r=r_0}$ #26	25.67	$T_{b,in,cooling}$	25.94
$T_{r=r_0}$ #7	22.26	$T_{r=r_0}$ #27	25.87	$T_{b,out,cooling}$	19.99
$T_{r=r_0}$ #8	22.51	$T_{r=r_0}$ #28	26.04	$T_{cool,in}$	19.53
$T_{r=r_0}$ #9	22.66	$T_{r=r_0}$ #29	26.21	$T_{cool,out}$	19.54
$T_{r=r_0}$ #10	22.81	$T_{r=r_0}$ #30	26.39	T_{cool}	19.54
$T_{r=r_0}$ #11	23.05	$T_{r=r_0}$ #31	26.51	$V_{heating}$	25.573
$T_{r=r_0}$ #12	23.25	$T_{r=r_0}$ #32	26.71	$I_{heating}$	0.21340
$T_{r=r_0}$ #13	23.44	$T_{r=r_0}$ #33	26.85	$q_{heating,total}$	5.457
$T_{r=r_0}$ #14	23.57	$T_{r=r_0}$ #34	26.97	w_{av}	$1.8747\text{x}10^{-3}$
$T_{r=r_0}$ #15	23.78	$T_{r=r_0}$ #35	27.12		
$T_{r=r_0}$ #16	23.99	$T_{r=r_0}$ #36	27.26		
$T_{r=r_0}$ #17	24.17	$T_{r=r_0}$ #37	27.43		
$T_{r=r_0}$ #18	24.33	$T_{r=r_0}$ #38	27.53		
$T_{r=r_0}$ #19	24.50	$T_{r=r_0}$ #39	27.66		
$T_{r=r_0}$ #20	24.76	$T_{r=r_0}$ #40	27.83		

Run 9-S, ϕ = 12.49%					
$T_{r=r_0}$ #1	19.81	$T_{r=r_0}$ #21	32.06	$T_{\infty,top}$	24.01
$T_{r=r_0}$ #2	20.82	$T_{r=r_0}$ #22	32.52	$T_{\infty,bottom}$	20.35
$T_{r=r_0}$ #3	22.12	$T_{r=r_0}$ #23	32.62	T_{∞}	22.18
$T_{r=r_0}$ #4	23.03	$T_{r=r_0}$ #24	33.14	$T_{b,in,heating}$	15.06
$T_{r=r_0}$ #5	23.64	$T_{r=r_0}$ #25	33.76	$T_{b,out,heating}$	37.39
$T_{r=r_0}$ #6	24.50	$T_{r=r_0}$ #26	34.10	$T_{b,in,cooling}$	36.12
$T_{r=r_0}$ #7	25.08	$T_{r=r_0}$ #27	34.83	$T_{b,out,cooling}$	14.56
$T_{r=r_0}$ #8	25.95	$T_{r=r_0}$ #28	35.31	$T_{cool,in}$	13.04
$T_{r=r_0}$ #9	26.38	$T_{r=r_0}$ #29	36.15	$T_{cool,out}$	13.11
$T_{r=r_0}$ #10	26.84	$T_{r=r_0}$ #30	37.16	T_{cool}	13.08
$T_{r=r_0}$ #11	27.79	$T_{r=r_0}$ #31	37.58	$V_{heating}$	71.257
$T_{r=r_0}$ #12	28.18	$T_{r=r_0}$ #32	38.41	$I_{heating}$	0.59408
$T_{r=r_0}$ #13	28.77	$T_{r=r_0}$ #33	39.13	$q_{heating,total}$	42.332
$T_{r=r_0}$ #14	29.09	$T_{r=r_0}$ #34	39.64	w_{av}	$4.6742\text{x}10^{-3}$
$T_{r=r_0}$ #15	29.66	$T_{r=r_0}$ #35	40.31		
$T_{r=r_0}$ #16	30.05	$T_{r=r_0}$ #36	40.69		
$T_{r=r_0}$ #17	30.54	$T_{r=r_0}$ #37	41.56		
$T_{r=r_0}$ #18	30.79	$T_{r=r_0}$ #38	42.13		
$T_{r=r_0}$ #19	31.19	$T_{r=r_0}$ #39	42.80		
$T_{r=r_0}$ #20	31.66	$T_{r=r_0}$ #40	43.54		

Run 10-S, ϕ = 12.49%					
$T_{r=r_0}$ #1	18.67	$T_{r=r_0}$ #21	29.81	$T_{\infty,top}$	23.96
$T_{r=r_0}$ #2	19.51	$T_{r=r_0}$ #22	30.15	$T_{\infty,bottom}$	20.09
$T_{r=r_0}$ #3	20.58	$T_{r=r_0}$ #23	30.22	T_{∞}	22.02
$T_{r=r_0}$ #4	21.33	$T_{r=r_0}$ #24	30.58	$T_{b,in,heating}$	14.82
$T_{r=r_0}$ #5	21.85	$T_{r=r_0}$ #25	30.97	$T_{b,out,heating}$	33.42
$T_{r=r_0}$ #6	22.57	$T_{r=r_0}$ #26	31.14	$T_{b,in,cooling}$	32.34
$T_{r=r_0}$ #7	23.08	$T_{r=r_0}$ #27	31.60	$T_{b,out,cooling}$	14.27
$T_{r=r_0}$ #8	23.82	$T_{r=r_0}$ #28	31.83	$T_{cool,in}$	13.07
$T_{r=r_0}$ #9	24.20	$T_{r=r_0}$ #29	32.30	$T_{cool,out}$	13.11
$T_{r=r_0}$ #10	24.63	$T_{r=r_0}$ #30	32.89	T_{cool}	13.09
$T_{r=r_0}$ #11	25.45	$T_{r=r_0}$ #31	33.10	$V_{heating}$	61.896
$T_{r=r_0}$ #12	25.85	$T_{r=r_0}$ #32	33.67	$I_{heating}$	0.51622
$T_{r=r_0}$ #13	26.39	$T_{r=r_0}$ #33	34.25	$q_{heating,total}$	31.952
$T_{r=r_0}$ #14	26.76	$T_{r=r_0}$ #34	34.74	w_{av}	4.1168x10^{-3}
$T_{r=r_0}$ #15	27.36	$T_{r=r_0}$ #35	35.40		
$T_{r=r_0}$ #16	27.80	$T_{r=r_0}$ #36	35.83		
$T_{r=r_0}$ #17	28.32	$T_{r=r_0}$ #37	36.60		
$T_{r=r_0}$ #18	28.64	$T_{r=r_0}$ #38	37.10		
$T_{r=r_0}$ #19	29.05	$T_{r=r_0}$ #39	37.67		
$T_{r=r_0}$ #20	29.50	$T_{r=r_0}$ #40	38.28		

Run 11-S, ϕ = 12.49%					
$T_{r=r_0}$ #1	17.59	$T_{r=r_0}$ #21	23.58	$T_{\infty,top}$	24.52
$T_{r=r_0}$ #2	17.92	$T_{r=r_0}$ #22	23.84	$T_{\infty,bottom}$	20.82
$T_{r=r_0}$ #3	18.34	$T_{r=r_0}$ #23	24.04	T_{∞}	22.67
$T_{r=r_0}$ #4	18.67	$T_{r=r_0}$ #24	24.30	$T_{b,in,heating}$	15.75
$T_{r=r_0}$ #5	18.94	$T_{r=r_0}$ #25	24.59	$T_{b,out,heating}$	26.72
$T_{r=r_0}$ #6	19.27	$T_{r=r_0}$ #26	24.80	$T_{b,in,cooling}$	26.35
$T_{r=r_0}$ #7	19.54	$T_{r=r_0}$ #27	25.09	$T_{b,out,cooling}$	14.67
$T_{r=r_0}$ #8	19.90	$T_{r=r_0}$ #28	25.33	$T_{cool,in}$	13.05
$T_{r=r_0}$ #9	20.14	$T_{r=r_0}$ #29	25.60	$T_{cool,out}$	13.06
$T_{r=r_0}$ #10	20.39	$T_{r=r_0}$ #30	25.90	T_{cool}	13.05
$T_{r=r_0}$ #11	20.76	$T_{r=r_0}$ #31	26.08	$V_{heating}$	31.560
$T_{r=r_0}$ #12	21.03	$T_{r=r_0}$ #32	26.35	$I_{heating}$	0.26345
$T_{r=r_0}$ #13	21.32	$T_{r=r_0}$ #33	26.58	$q_{heating,total}$	8.315
$T_{r=r_0}$ #14	21.56	$T_{r=r_0}$ #34	26.77	w_{av}	2.0388×10^{-3}
$T_{r=r_0}$ #15	21.89	$T_{r=r_0}$ #35	27.00		
$T_{r=r_0}$ #16	22.17	$T_{r=r_0}$ #36	27.18		
$T_{r=r_0}$ #17	22.46	$T_{r=r_0}$ #37	27.43		
$T_{r=r_0}$ #18	22.71	$T_{r=r_0}$ #38	27.61		
$T_{r=r_0}$ #19	22.99	$T_{r=r_0}$ #39	27.79		
$T_{r=r_0}$ #20	23.33	$T_{r=r_0}$ #40	28.02		

Run 12-S, ϕ = 12.49%					
$T_{r=r_0}$ #1	20.91	$T_{r=r_0}$ #21	24.94	$T_{\infty,top}$	24.50
$T_{r=r_0}$ #2	21.12	$T_{r=r_0}$ #22	25.11	$T_{\infty,bottom}$	19.94
$T_{r=r_0}$ #3	21.39	$T_{r=r_0}$ #23	25.25	T_{∞}	22.22
$T_{r=r_0}$ #4	21.60	$T_{r=r_0}$ #24	25.41	$T_{b,in,heating}$	20.04
$T_{r=r_0}$ #5	21.79	$T_{r=r_0}$ #25	25.61	$T_{b,out,heating}$	26.83
$T_{r=r_0}$ #6	22.01	$T_{r=r_0}$ #26	25.75	$T_{b,in,cooling}$	26.34
$T_{r=r_0}$ #7	22.20	$T_{r=r_0}$ #27	25.94	$T_{b,out,cooling}$	20.11
$T_{r=r_0}$ #8	22.44	$T_{r=r_0}$ #28	26.10	$T_{cool,in}$	19.61
$T_{r=r_0}$ #9	22.60	$T_{r=r_0}$ #29	26.28	$T_{cool,out}$	19.62
$T_{r=r_0}$ #10	22.77	$T_{r=r_0}$ #30	26.47	T_{cool}	19.62
$T_{r=r_0}$ #11	23.03	$T_{r=r_0}$ #31	26.59	$V_{heating}$	24.635
$T_{r=r_0}$ #12	23.21	$T_{r=r_0}$ #32	26.77	$I_{heating}$	0.20563
$T_{r=r_0}$ #13	23.41	$T_{r=r_0}$ #33	26.91	$q_{heating,total}$	5.066
$T_{r=r_0}$ #14	23.57	$T_{r=r_0}$ #34	27.05	w_{av}	1.6072x10^{-3}
$T_{r=r_0}$ #15	23.79	$T_{r=r_0}$ #35	27.20		
$T_{r=r_0}$ #16	23.99	$T_{r=r_0}$ #36	27.31		
$T_{r=r_0}$ #17	24.18	$T_{r=r_0}$ #37	27.48		
$T_{r=r_0}$ #18	24.35	$T_{r=r_0}$ #38	27.60		
$T_{r=r_0}$ #19	24.54	$T_{r=r_0}$ #39	27.72		
$T_{r=r_0}$ #20	24.78	$T_{r=r_0}$ #40	27.88		

Run 13-S, ϕ = 14.95%					
$T_{r=r_0}$ #1	20.60	$T_{r=r_0}$ #21	32.28	$T_{\infty,top}$	25.60
$T_{r=r_0}$ #2	21.58	$T_{r=r_0}$ #22	32.74	$T_{\infty,bottom}$	24.88
$T_{r=r_0}$ #3	22.82	$T_{r=r_0}$ #23	32.88	T_{∞}	25.24
$T_{r=r_0}$ #4	23.71	$T_{r=r_0}$ #24	33.41	$T_{b,in,heating}$	15.78
$T_{r=r_0}$ #5	24.31	$T_{r=r_0}$ #25	34.04	$T_{b,out,heating}$	37.96
$T_{r=r_0}$ #6	25.14	$T_{r=r_0}$ #26	34.42	$T_{b,in,cooling}$	36.60
$T_{r=r_0}$ #7	25.71	$T_{r=r_0}$ #27	35.17	$T_{b,out,cooling}$	14.75
$T_{r=r_0}$ #8	26.54	$T_{r=r_0}$ #28	35.70	$T_{cool,in}$	12.97
$T_{r=r_0}$ #9	26.98	$T_{r=r_0}$ #29	36.56	$T_{cool,out}$	13.03
$T_{r=r_0}$ #10	27.42	$T_{r=r_0}$ #30	37.53	T_{cool}	13.00
$T_{r=r_0}$ #11	28.30	$T_{r=r_0}$ #31	37.93	$V_{heating}$	67.473
$T_{r=r_0}$ #12	28.67	$T_{r=r_0}$ #32	38.70	$I_{heating}$	0.56245
$T_{r=r_0}$ #13	29.21	$T_{r=r_0}$ #33	39.39	$q_{heating,total}$	37.950
$T_{r=r_0}$ #14	29.48	$T_{r=r_0}$ #34	39.90	w_{av}	$4.2150\text{x}10^{-3}$
$T_{r=r_0}$ #15	29.98	$T_{r=r_0}$ #35	40.57		
$T_{r=r_0}$ #16	30.33	$T_{r=r_0}$ #36	40.97		
$T_{r=r_0}$ #17	30.79	$T_{r=r_0}$ #37	41.84		
$T_{r=r_0}$ #18	31.03	$T_{r=r_0}$ #38	42.42		
$T_{r=r_0}$ #19	31.41	$T_{r=r_0}$ #39	43.09		
$T_{r=r_0}$ #20	31.89	$T_{r=r_0}$ #40	43.82		

Run 14-S, ϕ = 14.95%					
$T_{r=r_0}$ #1	19.55	$T_{r=r_0}$ #21	29.92	$T_{\infty,top}$	25.26
$T_{r=r_0}$ #2	20.34	$T_{r=r_0}$ #22	30.21	$T_{\infty,bottom}$	24.47
$T_{r=r_0}$ #3	21.33	$T_{r=r_0}$ #23	30.28	T_{∞}	24.87
$T_{r=r_0}$ #4	22.04	$T_{r=r_0}$ #24	30.61	$T_{b,in,heating}$	15.67
$T_{r=r_0}$ #5	22.54	$T_{r=r_0}$ #25	30.97	$T_{b,out,heating}$	33.45
$T_{r=r_0}$ #6	23.22	$T_{r=r_0}$ #26	31.14	$T_{b,in,cooling}$	32.48
$T_{r=r_0}$ #7	23.71	$T_{r=r_0}$ #27	31.56	$T_{b,out,cooling}$	14.53
$T_{r=r_0}$ #8	24.41	$T_{r=r_0}$ #28	31.80	$T_{cool,in}$	12.97
$T_{r=r_0}$ #9	24.79	$T_{r=r_0}$ #29	32.25	$T_{cool,out}$	13.02
$T_{r=r_0}$ #10	25.20	$T_{r=r_0}$ #30	32.81	T_{cool}	13.00
$T_{r=r_0}$ #11	25.96	$T_{r=r_0}$ #31	33.03	$V_{heating}$	57.442
$T_{r=r_0}$ #12	26.35	$T_{r=r_0}$ #32	33.57	$I_{heating}$	0.47906
$T_{r=r_0}$ #13	26.87	$T_{r=r_0}$ #33	34.13	$q_{heating,total}$	27.518
$T_{r=r_0}$ #14	27.21	$T_{r=r_0}$ #34	34.60	w_{av}	$3.6765\text{x}10^{-3}$
$T_{r=r_0}$ #15	27.75	$T_{r=r_0}$ #35	35.19		
$T_{r=r_0}$ #16	28.16	$T_{r=r_0}$ #36	35.60		
$T_{r=r_0}$ #17	28.62	$T_{r=r_0}$ #37	36.32		
$T_{r=r_0}$ #18	28.90	$T_{r=r_0}$ #38	36.79		
$T_{r=r_0}$ #19	29.26	$T_{r=r_0}$ #39	37.32		
$T_{r=r_0}$ #20	29.65	$T_{r=r_0}$ #40	37.90		

Run 15-S, ϕ = 14.95%					
$T_{r=r_0}$ #1	19.04	$T_{r=r_0}$ #21	24.18	$T_{\infty,top}$	25.01
$T_{r=r_0}$ #2	19.32	$T_{r=r_0}$ #22	24.41	$T_{\infty,bottom}$	24.10
$T_{r=r_0}$ #3	19.68	$T_{r=r_0}$ #23	24.58	T_{∞}	24.56
$T_{r=r_0}$ #4	19.96	$T_{r=r_0}$ #24	24.79	$T_{b,in,heating}$	17.08
$T_{r=r_0}$ #5	20.19	$T_{r=r_0}$ #25	25.04	$T_{b,out,heating}$	26.84
$T_{r=r_0}$ #6	20.48	$T_{r=r_0}$ #26	25.22	$T_{b,in,cooling}$	26.60
$T_{r=r_0}$ #7	20.71	$T_{r=r_0}$ #27	25.46	$T_{b,out,cooling}$	15.29
$T_{r=r_0}$ #8	21.03	$T_{r=r_0}$ #28	25.66	$T_{cool,in}$	12.97
$T_{r=r_0}$ #9	21.23	$T_{r=r_0}$ #29	25.89	$T_{cool,out}$	12.98
$T_{r=r_0}$ #10	21.46	$T_{r=r_0}$ #30	26.13	T_{cool}	12.97
$T_{r=r_0}$ #11	21.77	$T_{r=r_0}$ #31	26.29	$V_{heating}$	27.922
$T_{r=r_0}$ #12	22.00	$T_{r=r_0}$ #32	26.51	$I_{heating}$	0.23307
$T_{r=r_0}$ #13	22.25	$T_{r=r_0}$ #33	26.69	$q_{heating,total}$	6.508
$T_{r=r_0}$ #14	22.46	$T_{r=r_0}$ #34	26.86	w_{av}	1.8514x10^{-3}
$T_{r=r_0}$ #15	22.74	$T_{r=r_0}$ #35	27.05		
$T_{r=r_0}$ #16	22.98	$T_{r=r_0}$ #36	27.19		
$T_{r=r_0}$ #17	23.23	$T_{r=r_0}$ #37	27.40		
$T_{r=r_0}$ #18	23.44	$T_{r=r_0}$ #38	27.55		
$T_{r=r_0}$ #19	23.68	$T_{r=r_0}$ #39	27.69		
$T_{r=r_0}$ #20	23.98	$T_{r=r_0}$ #40	27.87		

Run 16-S, ϕ = 14.95%					
$T_{r=r_0}$ #1	22.17	$T_{r=r_0}$ #21	25.63	$T_{\infty,top}$	24.15
$T_{r=r_0}$ #2	22.34	$T_{r=r_0}$ #22	25.77	$T_{\infty,bottom}$	23.05
$T_{r=r_0}$ #3	22.57	$T_{r=r_0}$ #23	25.88	T_{∞}	23.60
$T_{r=r_0}$ #4	22.76	$T_{r=r_0}$ #24	26.02	$T_{b,in,heating}$	21.23
$T_{r=r_0}$ #5	22.92	$T_{r=r_0}$ #25	26.18	$T_{b,out,heating}$	27.00
$T_{r=r_0}$ #6	23.11	$T_{r=r_0}$ #26	26.29	$T_{b,in,cooling}$	26.40
$T_{r=r_0}$ #7	23.28	$T_{r=r_0}$ #27	26.44	$T_{b,out,cooling}$	20.65
$T_{r=r_0}$ #8	23.49	$T_{r=r_0}$ #28	26.57	$T_{cool,in}$	19.56
$T_{r=r_0}$ #9	23.63	$T_{r=r_0}$ #29	26.72	$T_{cool,out}$	19.57
$T_{r=r_0}$ #10	23.78	$T_{r=r_0}$ #30	26.86	T_{cool}	19.57
$T_{r=r_0}$ #11	23.99	$T_{r=r_0}$ #31	26.96	$V_{heating}$	21.033
$T_{r=r_0}$ #12	24.16	$T_{r=r_0}$ #32	27.11	$I_{heating}$	0.17555
$T_{r=r_0}$ #13	24.33	$T_{r=r_0}$ #33	27.21	$q_{heating,total}$	3.692
$T_{r=r_0}$ #14	24.47	$T_{r=r_0}$ #34	27.32	w_{av}	$1.3092\text{x}10^{-3}$
$T_{r=r_0}$ #15	24.65	$T_{r=r_0}$ #35	27.43		
$T_{r=r_0}$ #16	24.83	$T_{r=r_0}$ #36	27.53		
$T_{r=r_0}$ #17	24.99	$T_{r=r_0}$ #37	27.65		
$T_{r=r_0}$ #18	25.13	$T_{r=r_0}$ #38	27.74		
$T_{r=r_0}$ #19	25.29	$T_{r=r_0}$ #39	27.83		
$T_{r=r_0}$ #20	25.50	$T_{r=r_0}$ #40	27.96		

Run 17-S, ϕ = 17.50%					
$T_{r=r_0}$ #1	19.87	$T_{r=r_0}$ #21	31.75	$T_{\infty,top}$	25.47
$T_{r=r_0}$ #2	20.88	$T_{r=r_0}$ #22	32.18	$T_{\infty,bottom}$	21.78
$T_{r=r_0}$ #3	22.12	$T_{r=r_0}$ #23	32.32	T_{∞}	23.62
$T_{r=r_0}$ #4	23.00	$T_{r=r_0}$ #24	32.80	$T_{b,in,heating}$	15.38
$T_{r=r_0}$ #5	23.62	$T_{r=r_0}$ #25	33.38	$T_{b,out,heating}$	37.37
$T_{r=r_0}$ #6	24.45	$T_{r=r_0}$ #26	33.73	$T_{b,in,cooling}$	35.88
$T_{r=r_0}$ #7	25.05	$T_{r=r_0}$ #27	34.42	$T_{b,out,cooling}$	14.64
$T_{r=r_0}$ #8	25.88	$T_{r=r_0}$ #28	34.90	$T_{cool,in}$	13.05
$T_{r=r_0}$ #9	26.34	$T_{r=r_0}$ #29	35.71	$T_{cool,out}$	13.10
$T_{r=r_0}$ #10	26.82	$T_{r=r_0}$ #30	36.67	T_{cool}	13.08
$T_{r=r_0}$ #11	27.71	$T_{r=r_0}$ #31	37.10	$V_{heating}$	64.848
$T_{r=r_0}$ #12	28.12	$T_{r=r_0}$ #32	37.89	$I_{heating}$	0.54070
$T_{r=r_0}$ #13	28.68	$T_{r=r_0}$ #33	38.61	$q_{heating,total}$	35.063
$T_{r=r_0}$ #14	29.00	$T_{r=r_0}$ #34	39.16	w_{av}	3.7834x10^{-3}
$T_{r=r_0}$ #15	29.53	$T_{r=r_0}$ #35	39.82		
$T_{r=r_0}$ #16	29.89	$T_{r=r_0}$ #36	40.25		
$T_{r=r_0}$ #17	30.34	$T_{r=r_0}$ #37	41.11		
$T_{r=r_0}$ #18	30.57	$T_{r=r_0}$ #38	41.72		
$T_{r=r_0}$ #19	30.93	$T_{r=r_0}$ #39	42.40		
$T_{r=r_0}$ #20	31.37	$T_{r=r_0}$ #40	43.12		

Run 17-Sr (Repeatability Run), ϕ = 17.50%					
$T_{r=r_0}$ #1	19.31	$T_{r=r_0}$ #21	31.43	$T_{\infty,top}$	24.74
$T_{r=r_0}$ #2	20.32	$T_{r=r_0}$ #22	31.84	$T_{\infty,bottom}$	19.62
$T_{r=r_0}$ #3	21.56	$T_{r=r_0}$ #23	31.95	T_{∞}	22.18
$T_{r=r_0}$ #4	22.46	$T_{r=r_0}$ #24	32.42	$T_{b,in,heating}$	14.96
$T_{r=r_0}$ #5	23.09	$T_{r=r_0}$ #25	32.96	$T_{b,out,heating}$	36.81
$T_{r=r_0}$ #6	23.93	$T_{r=r_0}$ #26	33.29	$T_{b,in,cooling}$	35.26
$T_{r=r_0}$ #7	24.53	$T_{r=r_0}$ #27	33.94	$T_{b,out,cooling}$	14.41
$T_{r=r_0}$ #8	25.37	$T_{r=r_0}$ #28	34.38	$T_{cool,in}$	13.06
$T_{r=r_0}$ #9	25.84	$T_{r=r_0}$ #29	35.15	$T_{cool,out}$	13.10
$T_{r=r_0}$ #10	26.33	$T_{r=r_0}$ #30	36.08	T_{cool}	13.08
$T_{r=r_0}$ #11	27.24	$T_{r=r_0}$ #31	36.51	$V_{heating}$	64.916
$T_{r=r_0}$ #12	27.67	$T_{r=r_0}$ #32	37.33	$I_{heating}$	0.54120
$T_{r=r_0}$ #13	28.26	$T_{r=r_0}$ #33	38.08	$q_{heating,total}$	35.133
$T_{r=r_0}$ #14	28.61	$T_{r=r_0}$ #34	38.65	w_{av}	$3.7663\text{x}10^{-3}$
$T_{r=r_0}$ #15	29.18	$T_{r=r_0}$ #35	39.31		
$T_{r=r_0}$ #16	29.57	$T_{r=r_0}$ #36	39.74		
$T_{r=r_0}$ #17	30.03	$T_{r=r_0}$ #37	40.61		
$T_{r=r_0}$ #18	30.27	$T_{r=r_0}$ #38	41.22		
$T_{r=r_0}$ #19	30.62	$T_{r=r_0}$ #39	41.89		
$T_{r=r_0}$ #20	31.06	$T_{r=r_0}$ #40	42.62		

Run 18-S, ϕ = 17.50%					
$T_{r=r_0}$ #1	19.06	$T_{r=r_0}$ #21	29.83	$T_{\infty,top}$	25.58
$T_{r=r_0}$ #2	19.88	$T_{r=r_0}$ #22	30.12	$T_{\infty,bottom}$	21.67
$T_{r=r_0}$ #3	20.88	$T_{r=r_0}$ #23	30.20	T_{∞}	23.62
$T_{r=r_0}$ #4	21.62	$T_{r=r_0}$ #24	30.51	$T_{b,in,heating}$	15.32
$T_{r=r_0}$ #5	22.14	$T_{r=r_0}$ #25	30.87	$T_{b,out,heating}$	33.48
$T_{r=r_0}$ #6	22.84	$T_{r=r_0}$ #26	31.05	$T_{b,in,cooling}$	32.36
$T_{r=r_0}$ #7	23.37	$T_{r=r_0}$ #27	31.47	$T_{b,out,cooling}$	14.46
$T_{r=r_0}$ #8	24.08	$T_{r=r_0}$ #28	31.70	$T_{cool,in}$	13.04
$T_{r=r_0}$ #9	24.49	$T_{r=r_0}$ #29	32.15	$T_{cool,out}$	13.08
$T_{r=r_0}$ #10	24.93	$T_{r=r_0}$ #30	32.71	T_{cool}	13.06
$T_{r=r_0}$ #11	25.71	$T_{r=r_0}$ #31	32.93	$V_{heating}$	56.413
$T_{r=r_0}$ #12	26.13	$T_{r=r_0}$ #32	33.48	$I_{heating}$	0.47055
$T_{r=r_0}$ #13	26.66	$T_{r=r_0}$ #33	34.05	$q_{heating,total}$	26.545
$T_{r=r_0}$ #14	27.03	$T_{r=r_0}$ #34	34.55	w_{av}	$3.3452 \text{x} 10^{-3}$
$T_{r=r_0}$ #15	27.60	$T_{r=r_0}$ #35	35.15		
$T_{r=r_0}$ #16	28.02	$T_{r=r_0}$ #36	35.59		
$T_{r=r_0}$ #17	28.49	$T_{r=r_0}$ #37	36.33		
$T_{r=r_0}$ #18	28.79	$T_{r=r_0}$ #38	36.83		
$T_{r=r_0}$ #19	29.15	$T_{r=r_0}$ #39	37.37		
$T_{r=r_0}$ #20	29.55	$T_{r=r_0}$ #40	37.98		